

PHYSICAL PROCESSES AROUND GALACTIC NUCLEI

INAUGURAL-DISSERTATION

zur
Erlangung des Doktorgrades
der Mathematisch-Naturwissenschaftlichen Fakultät
der Universität zu Köln



vorgelegt von

HARSHITHA KRISHNA MURTHY BHAT
aus Bengaluru, Indien

Köln, 2022

Berichterstatter (Gutachter) / *Reviewer*:

Prof. Dr. Andreas Eckart

Prof. Dr. Lucas Labadie

Prof. Dr. Anton Zensus

Tag der mündlichen Prüfung / *Day of oral examination*:

08.03.2023

Erscheinungsjahr / *Year of publication*:

2023

This dissertation has been accepted by the Faculty of Mathematics and Natural Sciences of the University of Cologne.

Abstract

Supermassive Black Holes (SMBHs) located at the center of the galaxies and their activities in their immediate surroundings impact the properties and evolution of their host galaxy. This influence can be attributed to various factors, including radiation pressure, the interaction of radio plasma with Interstellar Medium (ISM), Active Galactic Nucleus outflows, and/or relativistic jets that inject energy and transport gas from the center to the other regions of the galaxy. In my thesis, I explore the physical processes and interactions in three different black hole environments: AGNs with HMBHs, the Galactic Centre, and Green Pea/Bean galaxies with fading AGNs.

Black holes with masses over $10^{10}M_{\odot}$ have ionizing UV spectra that create broad and narrow emission lines in quasars by interacting with the surrounding medium. We examined if this phenomenon introduces a statistical bias against detecting Hypermassive black holes (HMBH). We used a correlation between L_X/L_{UV} to create spectral energy distributions for black holes with masses $10^6 - 10^{12}M_{\odot}$. This set of SEDs was then used in the photoionization code CLOUDY to predict emission line strengths of numerous clouds using the ‘locally optimally emitting cloud’ model. We discovered that the commonly used optical lines $H\beta$ and $H\alpha$ decline rapidly at higher BH masses. Instead, the UV lines O VI 1034 Å and C IV 1549 Å are better suited to detect HMBH. Using the ratio of the narrow emission lines in BPT diagrams, we found that HMBH may be misclassified as star-forming galaxies instead of AGN.

We studied the Galactic Center using MIR emission, observing dust features along the mini-spiral and detecting several resolved filaments and clumps. We report the proper motions, temperatures, spectral indices, and flux densities of these sources. We also identified stream-like motion of extended clumps along the mini-spiral, and MIR counterparts of the radio tail components of the IRS7 source. Additionally, we analyzed the shape and orientation of the extended

late-type IRS3 star, which is consistent with the ALMA sub-mm detection of the source.

We studied 'Green Peas' or 'Green Beans' galaxies with strong [OIII] 5007Å emissions. We selected high [OIII] emitting galaxies from a larger sample and conducted LBT-MODS long-slit spectroscopy on the 12 closest sources. We found that there is no preferential direction for NLR extension, indicating no impact of jets on the EELR. The extension in [OII] is extended much further along the galactic plane when compared to [OIII].

Contents

Abstract	i
Contents	iii
1 Introduction	1
1.1 The Galactic Center	1
1.1.1 The Supermassive Black Hole in the Galactic Center	2
1.1.2 Nuclear Stellar Cluster	3
1.1.3 The Interstellar Medium	4
1.2 Active Galactic Nuclei	7
1.2.1 AGN geometry and Unification Scheme	8
1.2.2 Spectral Energy Distribution	9
1.3 Observational Techniques	10
1.3.1 VISIR at Very Large Telescope	10
1.3.2 MODS at Large Binocular Telescope	12
2 Paper I - Observational diagnostics of Hypermassive Black Holes	13
3 Paper II - Mid-Infrared observations of Galactic Centre	33
4 Paper III - Influence of Jets on [OIII] Extensions in Green Pea/Bean Galaxies	55
5 Summary and Conclusions	81
Bibliography	85
List of Figures	91
List of Acronyms	93

Acknowledgements	95
Declaration	97
Eingebundene Manuskripte in Vorbereitung:	98
Curriculum Vitae	99

1 Introduction

Black Holes (BHs) are one of the most mysterious objects in our Universe. The concept of BHs (called *dark stars* or *frozen stars* back then) and its theoretical speculations existed long before we knew them as real astrophysical objects. There are three main categories of BHs: i. *stellar mass black holes* ($M_{BH} \sim 5 - 10sM_{\odot}$), which are created at the end stage of the evolution of massive stars; ii. *intermediate-mass Black Holes (IMBHs)* ($M_{BH} \sim 100s - 10^5 M_{\odot}$), found in the centers of globular clusters; iii. *Supermassive Black Holes (SMBHs)* ($M_{BH} \geq 10^5 M_{\odot}$), found in the centers of galaxies.

We now know that most of the galaxies harbor a SMBH at their center (including the Milky Way) and studying the SMBH environment is crucial in understanding the current galaxy evolution schemes. The SMBH grows by feeding onto the Interstellar Medium (ISM) of the host galaxy but the process is inhibited by the feedback from galactic nuclei in the form of radiation and outflows/jets. In the following chapter, I will give a short overview of the two different cases of BH environment; the Galactic center (GC) and the Active Galactic Nuclei (AGNs) along with the observational techniques used in obtaining the data for this thesis.

1.1 The Galactic Center

At the distance of ~ 8 kpc, the SMBH at the center of our Galaxy is the only one that has been studied with such extensive detail. Our closest neighbour, the Andromeda galaxy (M31) is at a distance of 780 kpc i.e., 100 times further. Therefore, the GC is the highest spatially resolvable galactic nucleus in the universe and proves to be a unique laboratory to study physical processes such as star formation & dynamics, physics of the interstellar medium, accretion emissions, etc. In the optical and ultraviolet (UV) domain, the GC is obscured by

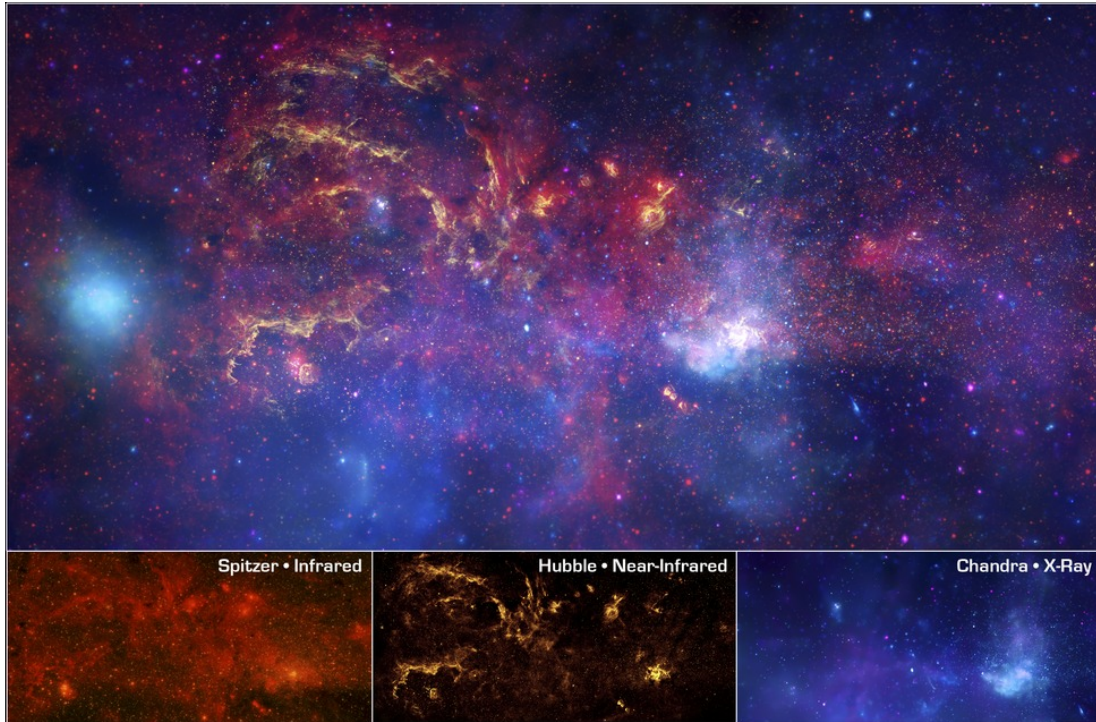


Figure 1.1: Composite image of the Galactic Centre using images from the Spitzer Space Telescope, the Hubble Space Telescope, and the Chandra X-ray observatory. The bright spot in the middle of the image is where the SMBH is situated. Image credit: NASA/JPL-Caltech/ESA/CXC/STScI

large gas and dust lanes along the line of sight. Therefore, central regions are only observable in the radio, Infrared (IR), and X-ray regimes (Fig. 1.1).

In this section, I will discuss some of the important components of the GC that are relevant to this thesis (especially Paper II). The GC is discussed extensively in various textbooks and review articles, the information here relies on Eckart et al. (2005); Genzel et al. (2010).

1.1.1 The Supermassive Black Hole in the Galactic Center

In the early 1960s, many distant luminous Quasars (QSOs) were discovered with the advent of radio astronomy. To account for their enormous energy outputs, Lynden-Bell (1969); Lynden-Bell and Rees (1971) predicted that most galactic nuclei, including the centre of Milky Way, might harbor SMBHs, which in most cases are less active (or inactive) than in QSOs. This led to the first detection of a non-thermal compact radio source, Sgr A* at the centre of our Galaxy (Balick and Brown (1974); see Goss et al. (2003) for historical details). The first detection of Sgr A* using Very Long Baseline Interferometry (VLBI) came from Lo et al. (1975), who derived an upper limit for the source size to be 0.02" at 3.7cm using 242 km baseline. They reported a flux density of 0.6 Jy at 3.7 cm with indications of variability. The first successful IR observations of the

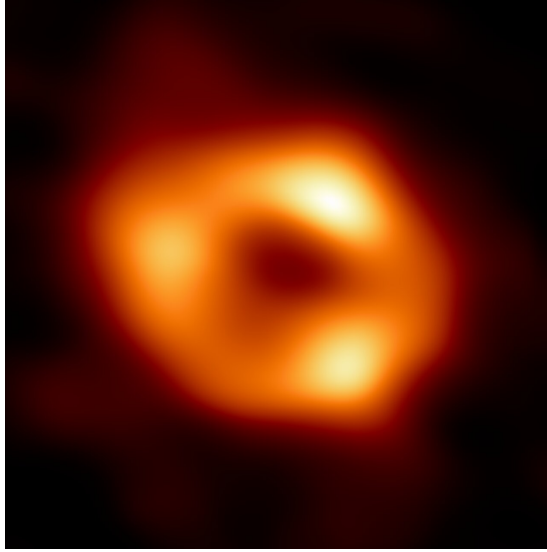


Figure 1.2: The very first image of the SMBH ‘shadow’ at the center of Milky Way produced by Event Horizon Telescope Collaboration. Image credit: EHT collaboration

Galactic centre came from [Becklin and Kleinmann \(1968\)](#) who could resolve the compact Nuclear stellar cluster (NSC) at $2.2\mu\text{m}$. Even though the variability of Sgr A* indicated the scaled-down quasar activity, the strongest proof for the existence of SMBH came from studying the Keplerian stellar motions around Sgr A* ([Eckart and Genzel, 1996, 1997](#); [Ghez et al., 1998](#); [Gillessen et al., 2017](#); [Parsa et al., 2017](#)). In 2022, [Event Horizon Telescope Collaboration et al. \(2022\)](#) provided the first direct evidence for the presence of SMBH by publishing an image of the SMBH ‘shadow’ at the centre of the Milky Way (Fig. 1.2), using a global interferometric array of eight telescopes operating at a wavelength of $\lambda = 1.3\text{mm}$. The mass of SMBH associated with the Sgr A* is estimated to be about $M_{BH} \sim 4 \times 10^6 M_{\odot}$ and is at a distance of about $\sim 8\text{kpc}$ from us.

1.1.2 Nuclear Stellar Cluster

For decades, Near Infrared (NIR) observations have shown a high density of bright sources very close to Sgr A*, revealing the photospheric emission of the stars. Their density profile is consistent with the scenario of an extremely dense cluster with SMBH at its centre. However, resolving and tracing their individual orbits only became possible with technical advancements like Speckle imaging and Adaptive Optics (AO) on large telescopes. The angular resolution has improved by more than an order of magnitude (up to $\sim 40\text{mas}$) and the sensitivity by 3 to 5 magnitudes (to $K_s \sim 16$) (Fig. 1.3).

There is a significantly low number of late-type stars and a large number of early-type stars in the NSC. Early NIR spectroscopy of NSC had suggested that the bright stars such as IRS 7, 13, 16, etc. are late-type giants, supergiants and

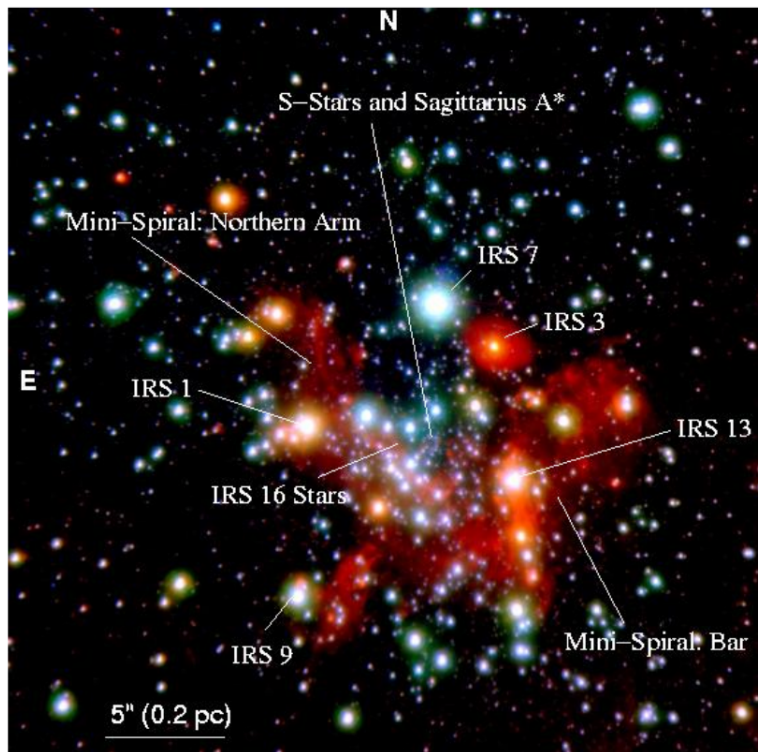


Figure 1.3: Multi-wavelength image (using H , K , L' bands) of the central parsec of GC observed at NACO/ESO VLT. Image credit: University of Cologne

Asymptotic Giant Branch (AGB) stars (Becklin and Neugebauer, 1975). This was typical for a stellar cluster like NSC. However, spectroscopic observations in the 1990s revealed that some of these bright stars are indeed hot early-type stars (Krabbe et al., 1995; Genzel et al., 1996; Tanner et al., 2006). Modeling their stellar atmosphere showed that these ‘HeI-stars’ are post-main-sequence, blue super-giants and Wolf-Rayet (WR) stars (2-8 Myrs old) and Zero-Age Main-Sequence (ZAMS) stars ($30-100 M_{\odot}$) and are able to ionize surrounding Helium due to their high surface temperatures of around $20,000-30,000$ K (Najarro et al., 1997; Martins et al., 2007). They produce strong interstellar winds with velocities up to 1000 km s^{-1} and heavy mass losses of $10^{-5} - 10^{-4} M_{\odot}/\text{yr}$. Many of these stars interact with the ISM and the radiation in the GC to form bow-shock sources (Tanner et al., 2005). In Paper II, we discuss some of the interesting consequences of such stars in a dynamical environment like GC.

1.1.3 The Interstellar Medium

The gravitational influence of the central SMBH is up to $3-5$ pc (Alexander, 2005). High angular resolution observations show the presence of a ring of dense clumpy molecular and neutral gas and warm dust called the Circumnuclear disc (CND) at the border of the influence, extending from $\sim 1.5 - 7 \text{ pc}$. The CND is estimated to have a mass of a few $10^6 M_{\odot}$ (Becklin et al., 1982; Herrnstein and Ho, 2002) and consists of dense clouds of molecular gas (up

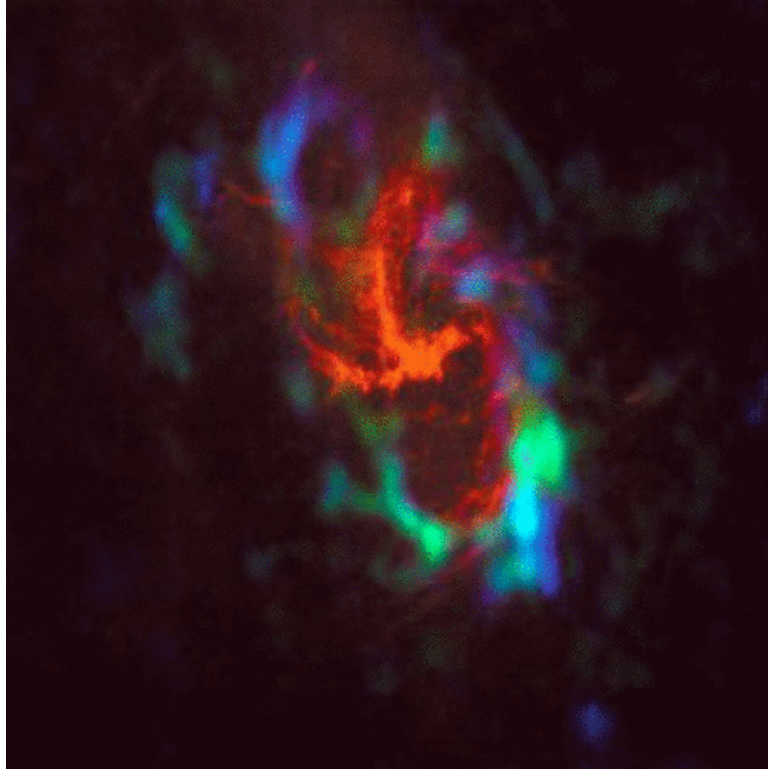


Figure 1.4: Multi-wavelength image of the inner few pc of the Galactic centre. Integrated line emission in HCN 4-3 (green: SMA, [Montero-Castaño et al. \(2009\)](#)) and HCN 1-0 (blue: OVRO, [Christopher et al. \(2005\)](#)), highlight the neutral gas in CND whereas the 6 cm radio continuum emission (red: [Lo and Claussen \(1983\)](#)) highlights the ionised gas in the mini-spiral. Image credit: [Genzel et al. \(2010\)](#)

to 10^7cm^{-3} [Guesten et al. \(1987\)](#); [Wright et al. \(2001\)](#)). It encloses an ionized central cavity which has a much lower mean gas density within $\sim 1 - 1.5 \text{pc}$ radius with a total mass of $\sim 60 M_{\odot}$ ([Lo and Claussen, 1983](#); [Blank et al., 2016](#)).

At the inner edge of the CND, there is a system of orbiting ionised clumpy streamers extending inwards (called *mini-spiral*) (Highlighted by 6cm radio continuum emission (red) in Fig. 1.4). Mini-spiral consists of 3 distinct arms called western, eastern, and northern arms. The western arm has a near-circular orbit similar to the neutral gas in CND, whereas the eastern and northern arms penetrate deep into the ionised cavity and reach up to a few arcseconds from Sgr A*. The streamers are estimated to transfer material into central few arcseconds at the inflow rate of $\sim 10^{-3} M_{\odot}$ ([Genzel et al., 1994](#)) and are photoionized by the UV radiation coming from the young massive stars present in the central parsec of the GC ([Martins et al., 2007](#)).

There have been several studies on the kinematics of mini-spiral. [Vollmer and Duschl \(2000\)](#) derived the 3D model to describe the bulk motion of the mini-spiral in three different planes using the data cube of [Ne II] line ($12.8 \mu\text{m}$). [Paumard et al. \(2004\)](#) showed that the Northern arm is a weak continuous

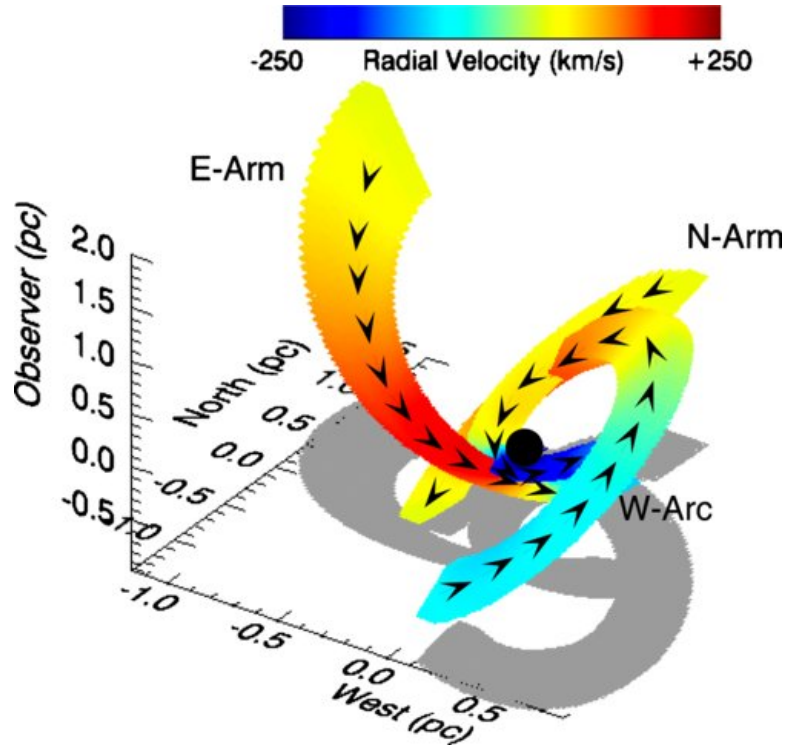


Figure 1.5: The 3-D view of the kinematics and structure of the mini-spiral around the Sgr A* (black sphere) as discussed in Zhao et al. (2010). The arrows indicate the direction of the streamers along the orbits and the colour represents the radial velocity and the grey shadow indicates their projection onto the sky plane.

surface that is drawn into a narrow stream as it reaches Sgr A*. With multi-epoch Very Large Array (VLA) observations using the H92 α and H30 α lines, Zhao et al. (2009, 2010) confirmed that the streamers can be modeled as a system of three bundles of quasi-Keplerian orbits in the potential dominated by the Sgr A* (Fig. 1.5). The orbital planes of the northern arm and the western arc are nearly co-planar, while the eastern arm plane is perpendicular to them.

While the model of *tidally stretched gas filaments* orbiting the central SMBH describes most of the dynamics of the mini-spiral, there are notable exceptions (Yusef-Zadeh et al., 1998; Paumard et al., 2004). These peculiar motions could be the results of cloud-cloud collisions or ionised gas interactions with the stellar winds (called bow-shocks, Peißker et al. (2019, 2020)). There are also indications for a central, partially collimated outflow that would explain the motions of some of the thin filaments in the region (Mužić et al., 2007). The discussions on the outflows and dynamics of mini-spiral are dealt with in more detail in Paper II.

1.2 Active Galactic Nuclei

A galactic nucleus is considered to be active (or **AGN**) if the radiation from the compact nuclear region far outshines the stellar radiation coming from the rest of the galaxy. The study of **AGNs** has a rich and century-long history. They were first detected when **Fath (1909)** studied the optical spectra of a few spiral ‘nebulae’ including NGC1068 (now known as M77). NGC1068 showed very prominent emission lines and had a diffuse nucleus. In the next decades, more such sources were discovered. **Slipher (1917)** studied the source later along with other similar sources like NGC4151 and found unusually strong and broad high-excitation emission lines.

Seyfert (1943) was the first to study these sources systematically using their optical spectra and showed that some of the galaxies (or ‘extragalactic nebulae’ as they were called then) had very broad nuclear emission lines. As a result, a certain class of **AGNs** are called *Seyfert galaxies* in his honor. The major breakthrough, however, came from the advancements in radio astronomy as it led to the discoveries of discrete bright radio sources (**Bolton et al., 1949**) and they were soon associated with star-like optical counterparts (called *quasi-stellar radio sources* or **QSOs**, **Schmidt (1963)**) with strong and high-redshifted emission lines. It was only with **Khachikian and Weedman (1974)**, that Seyferts were first suspected to be related with **QSOs**.

It is now believed that the enormous energy released in an **AGN** is a result of the accretion of surrounding matter onto the **SMBH** at the centre of the galaxy. Even though a **SMBH** exists at the core of all galaxies, it is the present rate of accretion that distinguishes between a normal galaxy and an active galaxy. During the episodes of activity in **SMBH**’s lifetime, the gravitational potential of the accreting gas is converted into radiative (radiative mode) or kinetic energy (jet mode). Observationally, an object is classified as **AGN** if it satisfies one or more of the following criteria:

1. It emits enormous amounts of energy from the compact nuclear regions beyond what is expected through stellar processes for that particular type of galaxy.
2. Its centre shows a distinct signature of non-stellar flat Spectral Energy Distribution (**SED**) throughout the spectrum
3. Its spectrum exhibits strong high-excitation emission lines, whose line ratios indicate the presence of hard ionizing radiation.
4. It shows variations in line and/or continuum emission in short time scales

Due to this broad physical definition and observational criteria, a wide variety of objects fall under the classification of **AGN** and would require further sub-

This section largely follows from **Peterson (1997)**; **Netzer (2013)**

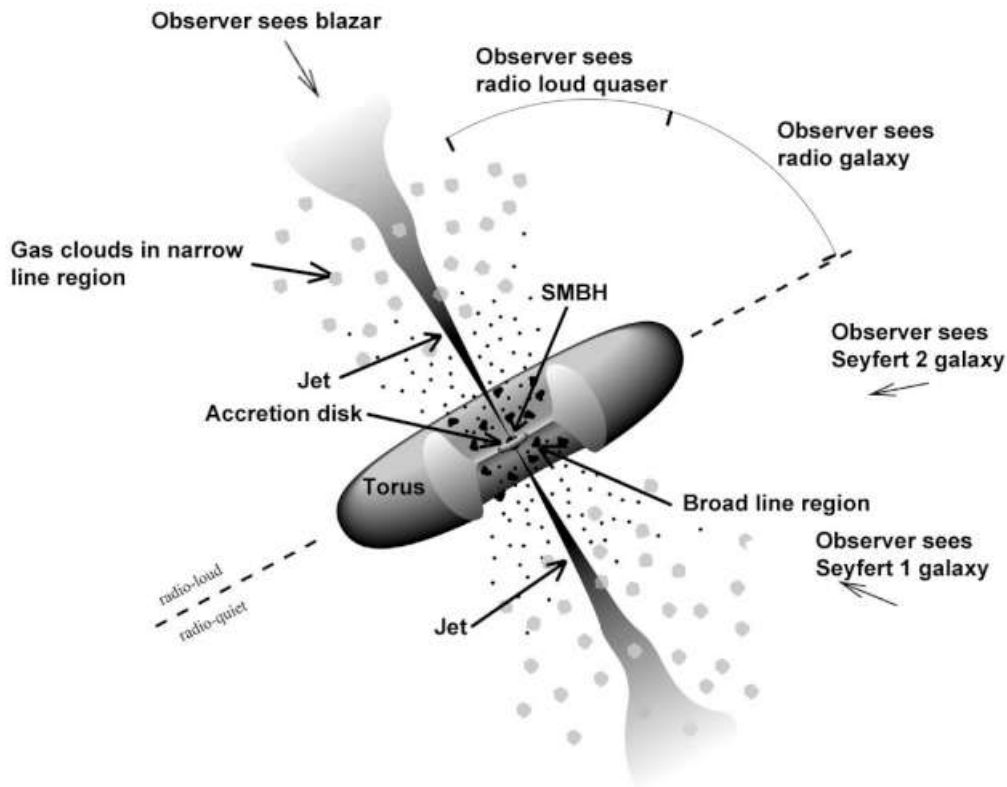


Figure 1.6: A schematic representation of the Unified model of the AGN. Image credit: <https://fermi.gsfc.nasa.gov/science/eteu/agn>

classification.

1.2.1 AGN geometry and Unification Scheme

The AGN unification model argues that all AGNs are similar in their intrinsic properties and the large diversity in the observed properties is due to different orientations/viewing angles. A schematic diagram of the simplified geometric unification model is presented in Fig. 1.6.

According to the model, a SMBH is at the centre accreting material from an optically thick geometrically thin *accretion disc*. The infalling matter loses energy and angular momentum through friction as it reaches the inner parts of the disc. The inner parts of the disc reach temperatures up to $10^5 K$ resulting in thermal emission mainly in the UV and Optical regions, giving rise to the *blue bump* in the SED. These photons are further re-emitted in X-rays through inverse Compton scattering in the hot corona that surrounds the disc.

At a distance of about 10-100 light days from the centre, the region is filled with high density ($\sim 10^{10} cm^{-3}$), dust-free gas clouds that are moving roughly in Keplerian orbits and are called *Broad Line Regions (BLRs)*. Outside the BLRs up to a few hundred parsecs away, there are regions with lower-density lower-

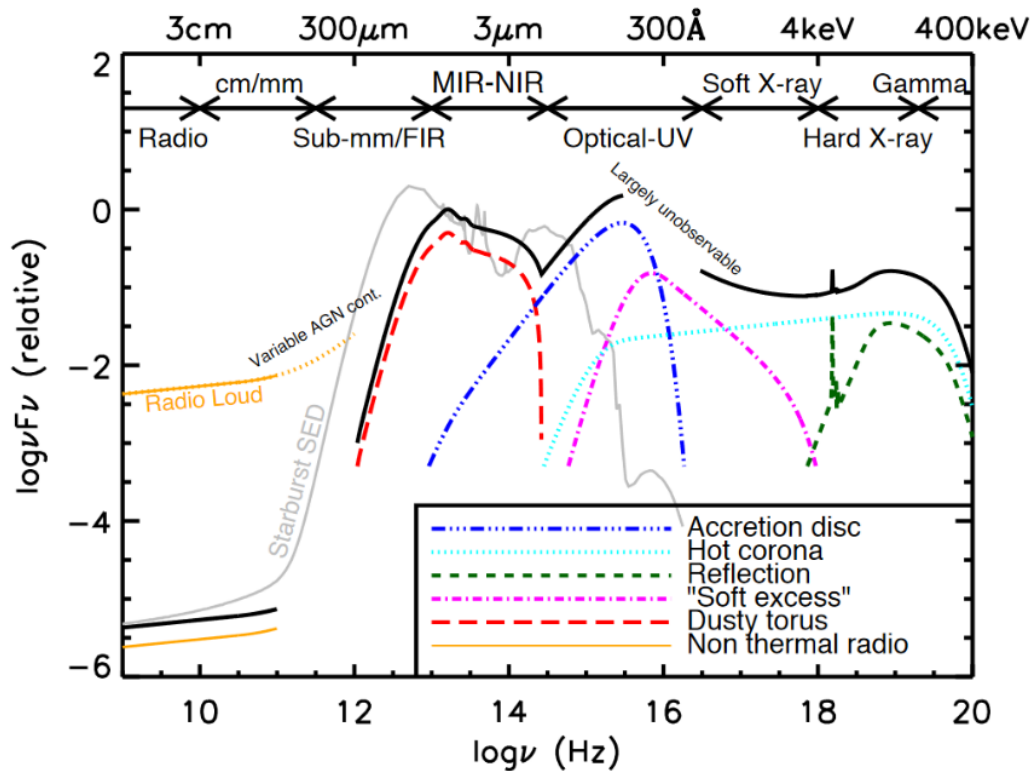


Figure 1.7: A schematic representation of *AGN SED* along with individual components that correspond to different physical processes. Image credit: Panda (2021), adapted from Padovani et al. (2017)

velocity ionized gas and are called *Narrow Line Regions (NLRs)*. Due to their low densities, *NLRs* are where most of the forbidden emission lines are produced.

There is a dusty torus surrounding the entire central region extending up to 0.1-10 pc. It is one of the most important structures for describing the differences between the different types of AGN. When the *BLRs* are obscured by the torus, an AGN appears to be Type II whereas, when viewed at a greater inclination it appears to be Type I.

1.2.2 Spectral Energy Distribution

The characteristic spectral signatures of AGNs, are easily observed in several wavelength regimes. This is partially the reason for the very large number of classes and sub-classes in AGN. Fig. 1.7 is a schematic representation of an *AGN SED* covering the entire range from radio to X-ray frequencies. Various physical processes at different distances are responsible for the observed broad band *SED* and relative contributions of these components can vary drastically for different classes of AGN.

Radio observations: The radio regime is dominated by the synchrotron emis-

sion (ultra-relativistic electrons in a magnetic field) coming from the radio jets. This non-thermal radiation is well represented by a single power law, $F_\nu \propto \nu^\alpha$, where F_ν is the flux density at frequency ν and α is the spectral index used to classify the sources into *flat-spectrum radio sources* ($\alpha < 0.5$) and *steep-spectrum radio sources*. ($\alpha > 0.5$).

Infrared observations: The Infrared emission in an AGN is dominated by the reprocessed radiation by the ‘dusty torus’. This emission dominates the AGN SED from ~ 1 micron to up to a few 10s of microns. Mid-Infrared (MIR) luminosities are tightly correlated with X-ray luminosities and hence can be used as AGN signature when X-rays are obscured.

Optical and UV observations: The UV-Optical emission of AGNs (or the ‘big blue bump’) is the thermal radiation from the accretion disc. According to the standard theory of accretion discs (geometrically thin optically thick discs, Shakura and Sunyaev (1973)), this radiation can be modeled as the sum of continuous local blackbodies of different temperatures along the annuli of the disc. A simplified expression to calculate the temperature of the annulus at a distance R is given by Peterson (1997) as,

$$T(R) = 3.5 \times 10^5 (\eta)^{\frac{1}{4}} \left(\frac{\dot{m}}{\dot{m}_{\text{Edd}}} \right)^{\frac{1}{4}} \left(\frac{M_{\text{BH}}}{10^8 M_\odot} \right)^{-\frac{1}{4}} \left(\frac{R}{R_s} \right)^{-\frac{3}{4}} \text{ K}$$

where M_{BH} is the mass of the central black hole accreting at the rate of \dot{m} , \dot{m}_{Edd} is its Eddington accretion rate, and $R_s = 2GM_{\text{BH}}/c^2$ is the Schwarzschild radius. G is the gravitational constant and c is the velocity of light.

X-ray observations: Most AGNs are very powerful X-ray emitters covering the energy range from about 0.5 keV to 10 keV. The X-ray emission is mostly the result of inverse Compton scattering of UV-Optical photons by hot corona surrounding the accretion disc (Haardt and Maraschi, 1991). The soft X-ray spectrum of type-I AGNs is usually filled with strong narrow absorption lines along with a strong X-ray continuum. Type-II AGNs on the other hand has an obscured X-ray continuum and shows narrow emission lines. Usually, a single power-law of the form $L_\nu \propto \nu^{-\alpha_{\text{OX}}}$ where $\alpha_{\text{OX}} \sim 0.7-0.9$ is used to fit the spectrum over the range of 0.2-20 keV (Beckmann et al., 2009).

1.3 Observational Techniques

1.3.1 VISIR at Very Large Telescope

MIR data for Paper II was obtained at the European Southern Observatory (ESO)’s Very Large Telescope (VLT) using VLT Imager and Spectrometer for the mid-InfraRed (VISIR). VLT is situated on top of Cerro Paranal at an altitude of 2635m in the Chilean Atacama desert and is ideal for optical and infrared

observations as it is one of the driest places on earth. It is also the most suitable ground-based telescope to observe the Galactic Centre as it is visible from the southern hemisphere. The telescope consists of four Unit Telescopes (UTs) (Antu, Kueyen, Melipal, and Yepun) with primary mirrors of 8.2 m diameter and four movable 1.8 m diameter Auxiliary Telescopes and can be combined to form a large interferometer (Very Large Telescope Interferometer (VLTI)). VISIR is mounted on UT-3 and provides diffraction-limited imaging at high sensitivity in two MIR wavelength bands: the N-band ($8 - 13\mu\text{m}$) and the Q-band ($16.5 - 24.5\mu\text{m}$).

The main drawback in using ground-based telescopes for MIR observations is the bright thermal background from both the atmosphere and the telescope. To avoid internal background contamination, the VISIR detectors are cooled down to a few Kelvins. To account for the external thermal background from the telescope and the sky, a technique called *chopping/nodding* is performed (Fig. 1.8). Chopping is when the images are taken at two positions, i.e. on-source image and off-source image by rapidly moving the secondary mirror of the telescope. The sky and telescope background can be removed by subtracting both images. However, there is an additional optical path difference introduced due to the change in the position of the secondary mirror. This additional background is suppressed by moving the entire telescope to an off-source position called nod-position where again the same chopping cycle is repeated.

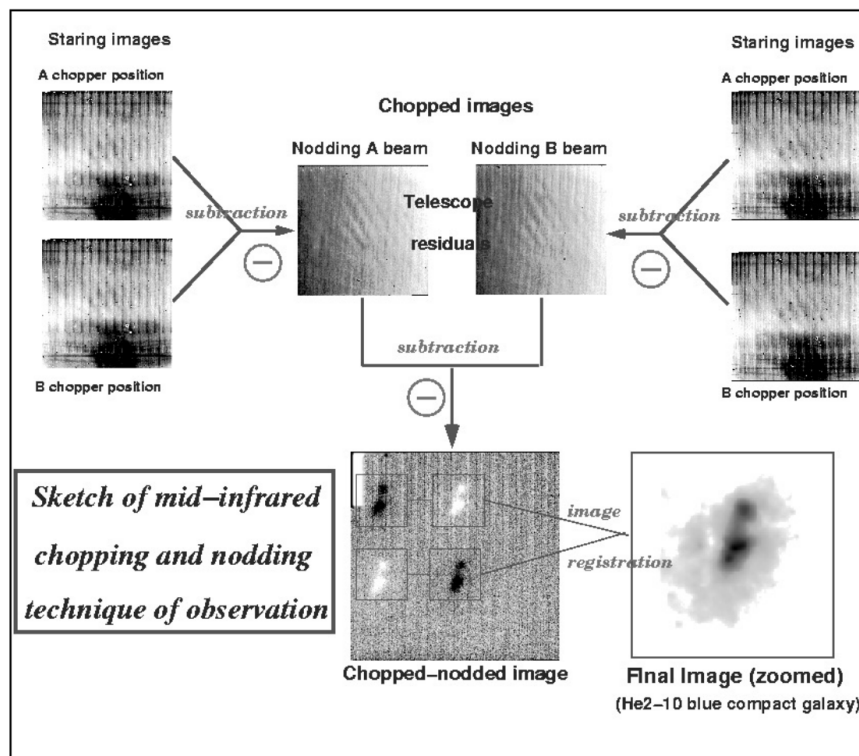


Figure 1.8: Chopping and nodding technique on observations. Image credit:ESO VISIR user manual.

1.3.2 MODS at Large Binocular Telescope

The optical long-slit spectroscopic data for Paper III was carried out at the Large Binocular Telescope (LBT) located at Mt. Graham International Observatory in Arizona, USA at an altitude of 3221 m. As the name suggests, LBT is a binocular telescope with two identical circular 8.4 m wide mirrors, resulting in the combined collecting area equivalent to a single circular 11.8 m mirror. The mirrors are mounted on a common altitude-azimuth mounting and are separated by 14.4 m, enabling interferometric observations (22.8 m baseline). In addition to the binocular design, AO is implemented in LBT using adaptive Gregorian secondary mirrors, providing wide Field of View (FoV), high angular resolution observations with high sensitivity.

The Multi-Object Double Spectrograph (MODS) was utilized for the long-slit observations. MODS is a set of identical low- to medium-resolution spectrographs spanning wavelengths from UV to near-IR (320nm-1100nm). Each spectrograph has a 6" x 6" field of view, with a dichroic element located below the slit dividing the beam at 565nm into optimized red and blue channels.

The resulting spectral frames underwent flat-correction, and bias-correction, and were combined utilizing the MODS CCD Reduction pipeline. Pyraf scripts were utilized for calibrations, background subtraction, and 1-D spectra extraction, adapted from standard IRAF routines. Wavelength and flux calibration spectra were also obtained alongside the scientific observations, calibrated using Ne, Hg, Kr, Xe, and Ar lamps. Each observational run included spectroscopic standard stars for flux calibration, with all calibration spectra undergoing the same reduction process. Finally, MODS1 and MODS2 channels and different dithered positions were reduced and combined to obtain the spectra

Paper I - Observational diagnostics of Hypermassive Black Holes

Recent discoveries of bright QSOs at $z > 6$, powered by accretion onto BHs with masses $10^8 - 10^{10} M_{\odot}$ have challenged our understanding of the formation and evolution of SMBHs. The discovery of more such SMBHs would put serious constraints on the current models for seed black holes. Finding even one BH with $M_{BH} \geq 10^{11} M_{\odot}$ at high red-shift ($z > 6$) would pose serious challenges for the current black hole evolution theories, requiring either highly super-Eddington accretion or supermassive seed black holes.

In this work, we simulated the observational diagnostics of such Hypermassive Black Holes (HMBHs). We predict observable emission line ratios and/or their detection limits for AGNs with $M_{BH} > 10^9 M_{\odot}$. We use the photo-ionization code CLOUDY (Ferland et al., 1998) to look for the line strengths of the prominent UV-Optical Broad and Narrow Emission Lines for $M_{BH} = 10^6 - 10^{12} M_{\odot}$ to see how these line strengths evolve as we move from the usually observed mass range to the hyper-massive ones. We find that the emission lines are intrinsically weaker because of the very different SEDs of the HMBHs and hence affected the observational diagnostics.

The results are reported in the following peer-reviewed article published in the *Monthly Notices of the Royal Astronomical Society*.

Credit: H. K. Bhat, S. Chakravorty, D. Sengupta, M. Elvis et. al., MNRAS 497, 2992B (2020). Reproduced with the permission of ©Oxford University Press.

Hypermassive black holes have faint broad and narrow emission lines¹⁴

Harshitha K. Bhat,^{1,2,3*} Susmita Chakravorty,⁴ Dhrubojoyoti Sengupta,⁵ Martin Elvis,⁶
Sudeb Ranjan Datta,⁴ Nirupam Roy,⁴ Caroline Bertemes^{6,7}, Gary Ferland⁸ and Savithri H. Ezhikode⁹

¹Department of Physics, St. Joseph's College, 36 Lalbagh Road, Bangalore 560027, India

²I. Physikalisches Institut der Universität zu Köln, Zùlpicher Str 77, D-50937 Köln, Germany

³Max-Planck-Institut für Radioastronomie, Auf dem Hügel 69, D-53121 Bonn, Germany

⁴Department of Physics, Indian Institute of Science, Bangalore 560012, India

⁵Presidency University, 86/1 College Street, Kolkata 700073, India

⁶Harvard-Smithsonian Center for Astrophysics, 60 Garden Street, Cambridge, MA 02138, USA

⁷Department of Physics, University of Bath, Claverton Down, Bath BA2 7AY, UK

⁸Department of Physics and Astronomy, University of Kentucky, Lexington, KY 40506, USA

⁹Inter-University Centre for Astronomy & Astrophysics (IUCAA), Ganeshkhind, Pune 411007, India

Accepted 2020 July 2. Received 2020 June 16; in original form 2019 August 28

ABSTRACT

The extreme ultraviolet region (EUV) provides most of the ionization that creates the high equivalent width (EW) broad and narrow emission lines (BELs and NELs) of quasars. Spectra of hypermassive Schwarzschild black holes (HMBHs; $M_{\text{BH}} \geq 10^{10} M_{\odot}$) with α -discs, decline rapidly in the EUV suggesting much lower EWs. Model spectra for BHs of mass 10^6 – $10^{12} M_{\odot}$ and accretion rates $0.03 \leq L_{\text{bol}}/L_{\text{Edd}} \leq 1.0$ were input to the CLOUDY photoionization code. BELs become ~ 100 times weaker in EW from $M_{\text{BH}} \sim 10^8 M_{\odot}$ to $M_{\text{BH}} \sim 10^{10} M_{\odot}$. The high-ionization BELs (O VI 1034 Å, C IV 1549 Å, and He II 1640 Å) decline in EW from $M_{\text{BH}} \geq 10^6 M_{\odot}$, reproducing the Baldwin effect, but regain EW for $M_{\text{BH}} \geq 10^{10} M_{\odot}$. The low-ionization lines (Mg II 2798 Å, H β 4861 Å, and H α 6563 Å) remain weak. Lines for maximally spinning HMBHs behave similarly. Line ratio diagrams for the BELs show that high O VI/H β and low C IV/H α may pick out HMBH, although O VI is often hard to observe. In NEL BPT diagrams, HMBHs lie among star-forming regions, except for highly spinning, high accretion rate HMBHs. In summary, the BELs expected from HMBHs would be hard to detect using the current optical facilities. From 100 to $10^{12} M_{\odot}$, the emission lines used to detect active galactic nuclei (AGNs) only have high EW in the 10^6 – $10^9 M_{\odot}$ window, where most AGNs are found. This selection effect may be distorting reported distributions of M_{BH} .

Key words: accretion, accretion discs – black hole physics – line: formation – galaxies: active – quasars: emission lines – quasars: supermassive black holes.

1 INTRODUCTION

Active galactic nuclei (AGNs) are the central regions of galaxies that host supermassive black holes (SMBHs) that are actively accreting surrounding material. They have been an exciting field of research in Astrophysics for a long time now (Netzer 2015, and references therein). The gravitational potential energy of the infalling matter is converted into radiation that photoionizes both the unresolvable nearby ($\lesssim 0.1$ pc, to the BH) and more distant ($\lesssim 100$ pc, partially resolvable in near AGNs) gas that then re-emit as broad and narrow emission lines (BELs and NELs), respectively, in the optical and UV regions. The NELs usually have Doppler widths ≤ 500 km s⁻¹ and arise in relatively low density ($\sim 10^3$ cm⁻³) gas. BELs have Doppler widths ~ 1000 – 10000 km s⁻¹ and arise in higher density gas ($\sim 10^9$ cm⁻³) as determined by absence of certain forbidden lines. Such large Doppler widths in the BELs suggest that the broad-line regions (BLRs) are in deep gravitational potential where Keplerian velocities are often > 1 per cent c , which makes BELs very important

in understanding the central source. Furthermore, the presence of BELs is an indicator of AGN activity.

Studying the BELs and NELs in AGNs and using them to understand fundamental properties, particularly the mass, of the associated black holes (BHs) is a well-established method. New data from more and more sensitive multiwavelength campaigns suggest the presence of hypermassive black holes (HMBHs; $M_{\text{BH}} \geq 10^{10} M_{\odot}$) that are extreme and/or unusual for AGNs (e.g. Fan et al. 2001; Mortlock et al. 2011; Wu et al. 2015). King (2015) gives a maximum theoretical limit for M_{BH} through luminous accretion as $\sim 5 \times 10^{10} M_{\odot}$ for typical parameters. Of the $> 10^5$ quasars known, only a few tens have BH masses $> 10^{10} M_{\odot}$ (Natarajan & Treister 2009; Ichikawa & Inayoshi 2017). This scarcity may be because they are rare, or perhaps cannot grow any larger. Discovery of more HMBH will put serious constraints on the current models for seed BHs. (Volonteri 2012; Johnson et al. 2013; Natarajan 2014; Latif & Ferrara 2016). Finding even one BH with $M_{\text{BH}} \geq 10^{11} M_{\odot}$ at high redshift ($z > 6$) would pose serious challenges for the existing BH evolution theories, requiring either highly super-Eddington accretion or supermassive seed BHs.

Here, we investigate whether this paucity of HMBH could be a selection effect due to the cooler temperatures of alpha-disc accretion

* E-mail: harshikikkeri@gmail.com

discs at high masses. We were motivated by the striking results for low-mass ($<10^5 M_{\odot}$) BHs by Chakravorty, Elvis & Ferland (2014), who found that BLR emission is drastically (factor >10 for $H\beta$ 4861 Å) and quite suddenly (in <1 dex in mass from 10^5 to $10^4 M_{\odot}$) reduced as the discs become too hot and overionize gas moving at Keplerian speeds $>1000 \text{ km s}^{-1}$. A complementary effect is expected as the discs become too cool (in case of HMBHs) to photoionize the gas to produce the typical BLR emission lines. That cooler accretion discs would result in weaker line emission, was first investigated analytically by Laor & Davis (2011). Hence, we can expect that the emission lines will be weaker for HMBHs. Here, we make a detailed investigation of the predicted BLR and narrow-line region (NLR) equivalent widths (EWs) as a function of HMBH mass.

As the mass estimates for AGNs come from the detection of BELs in the UV and optical region of the AGN spectra, we wanted to know if the same methods of detection are possible for HMBHs. Therefore, we investigate the predicted EWs of few prominent BELs over a wide range of BH masses ($M_{\text{BH}} = 10^6\text{--}10^{12} M_{\odot}$) and accretion rates ($L_{\text{bol}}/L_{\text{Edd}} = 0.03\text{--}1$), to see if there is a decrease in intrinsic line strengths among these BELs, making such BHs very hard to be discovered with our current standard detection methods. See Section 5.

The strengths of the BELs and NELs depend on the ionizing spectral energy distribution (SED), which in turn depends on the fundamental properties of the BH: its mass and the rate at which it is accreting matter. Larger BHs have cooler maximum temperatures. At some mass the ionizing photons they emit will drop, potentially weakening their BELs and NELs to the point of undetectability. Investigating whether this happens for HMBHs is the purpose of this paper. The mass accretion rate (\dot{m}) can be related to the ratio between the bolometric luminosity (L_{bol}) of the accretion disc of accreted matter around the BH, to the classical Eddington luminosity L_{Edd} of the BH. In Section 2, we shall show the details of how we have related the accretion rate with $L_{\text{bol}}/L_{\text{Edd}}$. Thus, throughout the paper, the accretion rate will be represented by $L_{\text{bol}}/L_{\text{Edd}}$.

Since we are interested in the higher end of the BH masses, we could not rely on the conventional method of assuming broken power laws to construct the broad-band SEDs of the BHs (Tananbaum et al. 1979; Lusso & Risaliti 2016). In Section 2, we elaborate on the methods adopted to properly link the different components of the AGN SED, while being careful about the mass evolution of these inter-relations.

Unlike BELs, NELs are not necessarily signatures of AGN activity. Dynamically (velocity widths), NELs are very similar to the emission lines of star-forming regions (SFRs), planetary nebulae, and even supernova remnants, as the photoionization equilibrium in all these regions is achieved at around same temperatures ($T \sim 10^4 \text{ K}$). To distinguish between NELs from all these different astrophysical objects, BPT diagrams (Baldwin, Phillips & Terlevich 1981) were made as an attempt to have diagnostic diagrams for NELs in SMBH. Using our predicted strengths of NELs, we also investigate the line ratios of HMBHs on BPT diagrams. See Section 6. Since the BPT diagrams are well-tested tools to find NELs, in AGNs, we extend the same logic to look at BELs. Since now we are looking at a much wider range of physical parameters of the BHs, we do not expect the broad lines to show intensity variations within a standard small range anymore. See Section 7.2 for the interesting consequences of mass and accretion rate variation on the line ratios of different BELs.

In this study, we have used the photoionization code called CLOUDY¹ (Ferland et al. 2017), to predict the emission line strengths

as a function of M_{BH} and $L_{\text{bol}}/L_{\text{Edd}}$. The physical parameters used for the CLOUDY calculations are mentioned in detail in Section 3. To model the gas/clouds that produce the BELs and NELs, we use the ‘locally optimally emitting cloud (LOC)’ model (Baldwin et al. 1995), which suggests that the emission lines are produced optimally – that each line is produced most efficiently within a narrow range of density and incident light flux. The history of this model and how we use it in this paper have been detailed in Section 4.

2 SPECTRAL ENERGY DISTRIBUTION

2.1 The radiation from the accretion disc

The main source of energy in AGNs is the conversion of gravitational potential energy of the accreting matter into radiation. This radiation from the accretion disc around the BH, peaks in the extreme ultraviolet region (EUV, 10–100 eV). The SED of AGNs is broad-band, extending from radio wavelengths to gamma rays. However, for the study of photoionized gas, the range from optical UV to soft X-rays matters most, because these photons ionize the gas present in the central $\sim 100 \text{ pc}$ of the AGN. Observationally there is uncertainty in the shape of the SED of the radiation from the accretion disc near its peak, due to absorption of EUV radiation by Galactic neutral gas and dust. Therefore, observations below 10 eV and above 100 eV have to be used to reconstruct the unobserved part of SEDs.

According to standard theory of accretion discs (Shakura & Sunyaev 1973; Frank, King & Raine 2002), radiation from the accretion disc can be modelled as the sum of all the local blackbodies emitted by different annuli of the disc. By knowing the temperature of the innermost stable annulus of the disc, temperature of all the subsequent rings can be estimated. A simplified form of the temperature of the annulus at radius R is given by equation (3.19) of Peterson (1997) (also see the ‘larger’ approximation of equation (5.43) of Frank et al. 2002). The same equation can be rewritten as

$$T(R) = 3.5 \times 10^5 (\eta)^{-\frac{1}{4}} \left(\frac{\dot{m}}{\dot{m}_{\text{Edd}}} \right)^{\frac{1}{4}} \left(\frac{M_{\text{BH}}}{10^8 M_{\odot}} \right)^{-\frac{1}{4}} \left(\frac{R}{R_s} \right)^{-\frac{3}{4}} \text{ K.} \quad (1)$$

M_{BH} is the mass of the central BH, \dot{m} is its mass accretion rate, while \dot{m}_{Edd} is the Eddington mass accretion rate. $R_s = 2GM_{\text{BH}}/c^2$ is the Schwarzschild radius, G being the gravitational constant, and c the velocity of light. η is the accretion efficiency factor, which relates

$$L = \eta \dot{m} c^2, \quad (2)$$

L being the luminosity emitted from the disc (both surfaces, top and bottom).

A standard model for the spectral component of a non-spinning accretion disc is available as a package called DISKBB in XSPEC² (Mitsuda et al. 1984; Makishima et al. 1986). The two inputs required by DISKBB are $T(R_{\text{in}})$ (which can be derived from 1) and the normalization A_{dbb} , given by

$$A_{\text{dbb}} = \left\{ \frac{R_{\text{in}}/\text{km}}{D/(10 \text{ kpc})} \right\}^2 \cos \theta \quad (3)$$

for a BH observed at a distance D ($=100 \text{ Mpc}$ throughout this paper) whose line of sight makes an angle θ ($=30^\circ$ throughout this paper, unless otherwise mentioned) to the normal to the plane of the disc. R_{in} is the distance of the innermost stable annulus of the accretion disc from the central BH.

¹<http://www.nublado.org/>

²<https://heasarc.gsfc.nasa.gov/docs/xanadu/xspec/>

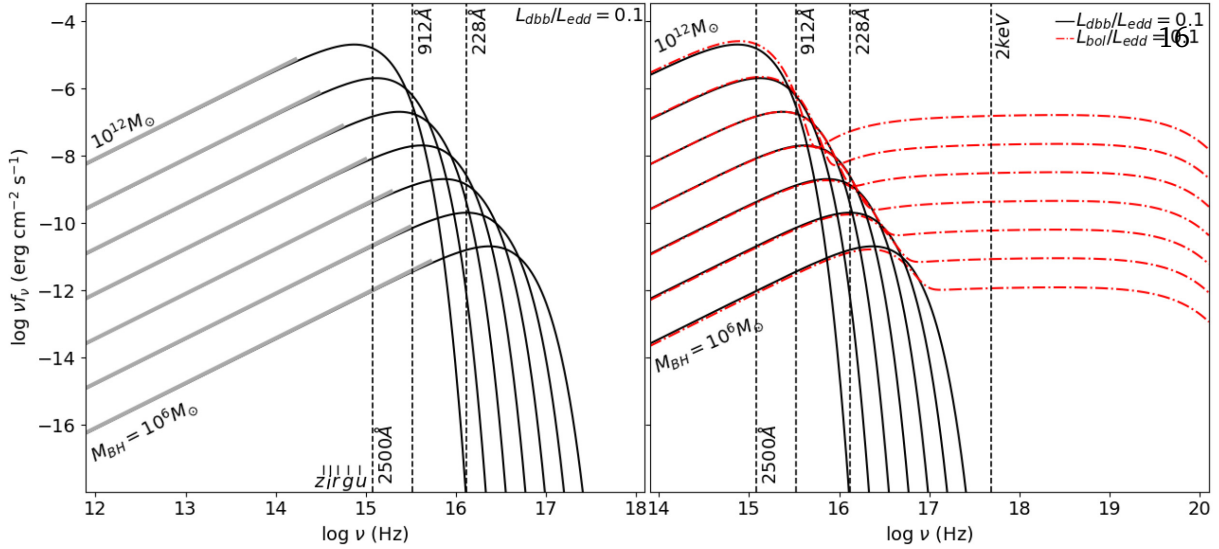


Figure 1. Left-hand panel: The SEDs of the radiation from the accretion disc around the super to hypermassive black holes. The SEDs are calculated using the package DISKBB within XSPEC. All the BHs here, are accreting at the rate $L_{\text{dbb}}/L_{\text{Edd}} = 0.1$ and the different lines correspond to different BH masses from $M_{\text{BH}} = 10^6$ to $10^{12} M_\odot$ at steps of 1 dex. The grey thicker lines highlight the region of the SED where $f_\nu \sim \nu^{1/3}$. Note that the traditionally (since Tananbaum et al. 1979) important wavelength 2500 Å does not fall in the grey part of the SED, unless $M_{\text{BH}} \lesssim 10^8 M_\odot$. We have also marked the positions of the centres of the five filters of SDSS, namely *u*, *g*, *r*, *i*, and *z*. Right-hand panel: The complete AGN SED from optical to X-rays (red dotted and dashed lines), but consisting of only the components from the central regions – the DISKBB component, and the power-law component. The procedure of appropriately adding these two components to get the complete SED is elaborately described in Section 2. Note that the solid black curves still correspond to $L_{\text{dbb}}/L_{\text{Edd}} = 0.1$, whereas the dotted and dashed red curves correspond to $L_{\text{bol}}/L_{\text{Edd}} = 0.1$. For details of this distinction, refer to Sections 2.1 and 2.3.

To decide the value of $T(R_{\text{in}})$ for a BH of mass M_{BH} , we have to consider the value of η carefully. Zimmerman et al. (2005) discuss that the DISKBB assumes a non-zero torque at the inner boundary of the accretion disc (also see Gierlinski et al. 1999), which they refer to as the ‘standard torque’ scenario. In this scenario, the total luminosity of the disc is

$$L = \frac{3G\dot{m}M_{\text{BH}}}{2R_{\text{in}}} \quad (4)$$

(equation 10 of Zimmerman et al. 2005). Thus, using equations (2) and (4), we see that η is dependent on the choice of R_{in} that we make

$$\eta = \frac{3GM_{\text{BH}}}{2c^2 R_{\text{in}}}. \quad (5)$$

For this paper, we adopt, $R_{\text{in}} = 3 R_s = 6GM_{\text{BH}}/c^2$, for the non-spinning BH. Hence, $\eta = 0.25$.

With the above-mentioned definitions and assumptions, we have used the DISKBB in version 11.3 of XSPEC to generate the SED (in flux $-f_\nu|_{\text{dbb}}$) of the radiation from one surface of the accretion disc. We can then obtain the luminosity from one surface of the disc, by multiplying with a factor of πD^2 and integrating over ν . We have verified using $\theta = 0$, in equation (3), that the ratio of 2 times this luminosity, to the Eddington luminosity is $\simeq \dot{m}/\dot{m}_{\text{Edd}}$ used in equation (1). The factor 2 is to account for emission from both sides of the disc.

After understanding this method of generating models for accretion disc radiation, we proceed to produce SEDs for the accretion disc, for a wide range of BH masses – $M_{\text{BH}} = 10^6 - 10^{12} M_\odot$ – at steps of 0.25 dex. For demonstration, in the left-hand panel of Fig. 1, we plot the SEDs for the different masses (as labelled), but all of them for $L_{\text{dbb}}/L_{\text{Edd}} = 0.1$ (solid black lines), where L_{dbb} is the luminosity obtained by integrating the accretion disc SED (from DISKBB in XSPEC) through the entire energy range of 1 μm –200 keV, and then

converting from flux to luminosity through a factor of πD^2 . The drop in ionizing photons between the H ionization edge (912 Å) and the He ionization edge (228 Å) is large towards high masses. Note that the peak of the SEDs shifts towards the lower energies (or larger wavelengths) for heavier BHs. Even the SDSS filters (marked at the bottom of Fig. 1, left-hand panel) will probe a different part of the accretion disc for $M_{\text{BH}} \geq 10^9 M_\odot$, than that for standard mass BHs. Even for BHs with $M_{\text{BH}} = 10^8 M_\odot$ at redshift $z \geq 3$, these SDSS filters slide away from the $f_\nu \sim \nu^{1/3}$ region (which for each SED is highlighted by the thicker grey lines).

For most of the paper, we avoid the additional complication of the spin of the BH. However, a spinning BH will have a harder SED shape in the photoionizing energy bands than a non-spinning BH of the same mass. Hence, after deriving the results for non-spinning SMBH, we perform an initial comparison of Schwarzschild and spinning BHs in Section 8.

2.2 The non-thermal radiation

In the energy range of 2–10 keV, AGNs have a non-thermal spectral component that is ascribed to inverse Comptonization of some of the disc photons by the hot coronal plasma surrounding the BH (Czerny & Elvis 1987; Lightman & Zdziarski 1987; Coppi 1992; Haardt & Maraschi 1993; Beloborodov 1999; Coppi 1999). This spectral component can be modelled using a power-law $f(\nu) \sim \nu^{-\alpha}$, where α is the spectral index (Arnaud 1996; Zdziarski, Johnson & Magdziarz 1996; Życki, Done & Smith 1999).

The power law becomes a significant component in photoionizing the BEL ions, especially for HMBH SEDs, because the HMBH DISKBB moves to lower energies.

Empirically α depends on L_{bol} (Lu & Yu 1999; Wang, Watarai & Mineshige 2004; Shemmer et al. 2006), though there is not complete consensus (Trakhtenbrot et al. 2017). Brightman et al. (2013) give a

Table 1. Maximum M_{BH} for which 2500 Å falls on the linear part of their SED.

$\frac{L_{\text{bol}}}{L_{\text{Edd}}}$	$\log\left(\frac{M_{\text{BH}}}{M_{\odot}}\right)$
0.03	7.75
0.1	8.25
0.3	9.00
1.0	9.25

phenomenological relation between the spectral index and L_{bol} as

$$\Gamma = \alpha + 1 = (0.32 \pm 0.05) \times \log\left(\frac{L_{\text{bol}}}{L_{\text{Edd}}}\right) + (2.27 \pm 0.06), \quad (6)$$

where L_{bol} is the total ‘observed’ luminosity between 1 μ and hard X-rays (200 keV). Note that the entire 1 μ to 200 keV range cannot be observed – sometimes because of the natural extinction (by Galactic dust and neutral hydrogen) in the ∼10–200 eV; and sometimes because of bad data in other wavelengths, for the samples that Brightman et al. (2013) considered. Hence, they had made judicious extrapolations and modelling, where required. We then define L_{bol} as the sum of the luminosities from both the SED components – the accretion disc and the power law, in the same energy range. Using equation (6), we see that the spectral indices for power-law components will be 0.78, 0.95, 1.10, and 1.27, respectively, for the different $L_{\text{bol}}/L_{\text{Edd}} = 0.03, 0.1, 0.3,$ and 1.0 ratios that we plan to investigate in this paper. Note that, in this paper, we shall use $L_{\text{bol}}/L_{\text{Edd}}$ as proxy for the accretion rate. Using these spectral energy indices, we construct power-law component and introduce exponential cut-offs at both the ends

$$f(\nu) \sim \nu^{-\alpha} \times e^{-\frac{10\text{eV}}{\nu}} \times e^{-\frac{\nu}{200\text{keV}}}. \quad (7)$$

Once the power-law component is constructed, we need to devise a scheme for its relative normalization with respect to the DISKBB component.

2.3 The multicomponent broad-band AGN SED

Conventionally, the nominal UV to X-ray slope, $\alpha_{\text{OX}} = -0.384 \log(L_{2\text{keV}}/L_{2500\text{Å}})$ (Tananbaum et al. 1979) is used to relate the luminosities at 2500 Å and 2 keV, where the accretion disc radiation predominantly determines the luminosity at 2500 Å, while the X-rays at 2 keV mostly comes from the power-law component. For the BHs in the ‘standard AGN mass range’, $M_{\text{BH}} \lesssim 10^8 M_{\odot}$, and $L_{\text{bol}}/L_{\text{Edd}} \gtrsim 0.1$, 2500 Å falls on the part of the DISKBB SED, where $f_{\nu} \sim \nu^{1/3}$ (thick highlighted grey lines in the left-hand panel of Fig. 1). However, for HMBHs the peak of the DISKBB emission moves to lower energies and $f_{\nu} \sim \nu^{1/3}$ may not be satisfied at 2500 Å, as demonstrated in the left-hand panel of Fig. 1. The highest possible BH mass, for which 2500 Å deviates from $f_{\nu} \sim \nu^{1/3}$, is also a function of the accretion rate, $L_{\text{bol}}/L_{\text{Edd}}$. For the different $L_{\text{bol}}/L_{\text{Edd}}$ ratios, used in this paper, in Table 1, we have listed the values of the highest mass for which 2500 Å, in the corresponding SEDs, falls on the $f_{\nu} \sim \nu^{1/3}$ part of the DISKBB SED. Thus, for HMBHs, 2500 Å represents a physically different part of the accretion disc than in case of the standard mass BHs. The reason we pay due attention to the nature of the SED at 2500 Å, is because this wavelength has been used as a reference wavelength in many multiwavelength AGN SEDs, even for the more recent, robust, SED investigations, where UV and optical luminosities are related to each other. Lusso & Risaliti (2016) examined a large sample of 159 AGNs and found a tight relationship

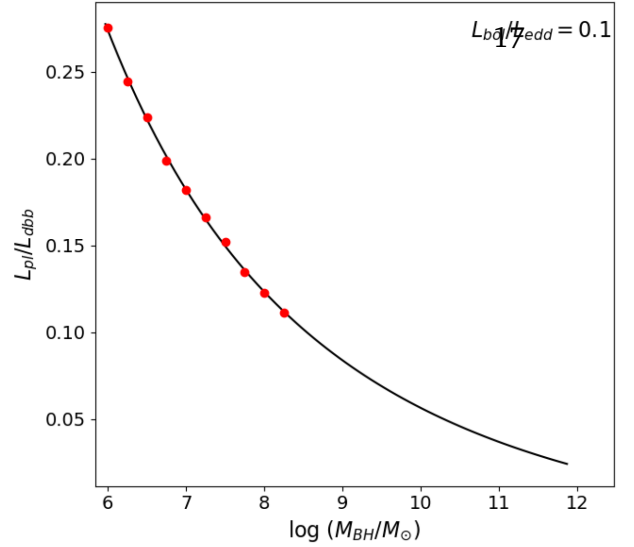


Figure 2. $L_{\text{pl}}/L_{\text{dbb}}$ ratios as a function of mass ratios for $L_{\text{bol}}/L_{\text{Edd}} = 0.1$. Red circles are the ratios obtained by using equation (8) to derive $L_{2\text{keV}}$. The red circle with the highest mass represents the highest mass BH for which 2500 Å falls within the $f_{\nu} \sim \nu^{1/3}$ part of the SED. Black line represents the best-fitting curve through the red circles and is further extrapolated to find the $L_{\text{pl}}/L_{\text{dbb}}$ ratios for higher masses, using the fit function equation (9).

between the luminosities at 2500 Å and 2 keV.

$$\log(L_{2\text{keV}}) = 0.638 \times \log(L_{2500\text{Å}}) + 7.074. \quad (8)$$

While they use the same wavelengths, as used by the definition of α_{OX} , this form of the relationship directly relates the observables, namely the fluxes.

For each $L_{\text{bol}}/L_{\text{Edd}}$, we first choose the range of M_{BH} for which the 2500 Å falls on the part of the DISKBB SED, where $f_{\nu} \sim \nu^{1/3}$. For example, as seen from Fig. 1 (left-hand panel) and Table 1, for $L_{\text{dbb}}/L_{\text{Edd}} = 0.1$ this mass range corresponds to $M_{\text{BH}} = 10^6 - 10^{8.25} M_{\odot}$. For each of these SEDs, we then scale the power-law component relative to the DISKBB as follows. For each value of M_{BH} , we start with $L_{\text{dbb}}/L_{\text{Edd}} = \text{desired } L_{\text{bol}}/L_{\text{Edd}} = 0.1$ (say). The XSPEC generated DISKBB spectra give us the value of $L_{2500\text{Å}}$. Thus, we can use that value in equation (8) to derive $L_{2\text{keV}}$, which gives us the required normalization for the power-law component. We add the luminosity L_{dbb} in the DISKBB and the luminosity L_{pl} in the normalized power-law component and check if $L_{\text{bol}}/L_{\text{Edd}} = 0.1$. If $L_{\text{bol}}/L_{\text{Edd}} \neq 0.1$, then we iterate by changing $L_{\text{dbb}}/L_{\text{Edd}}$ slightly, and repeating the process. The iteration continues, until, for the given M_{BH} , we achieve $L_{\text{bol}}/L_{\text{Edd}} = (L_{\text{dbb}} + L_{\text{pl}})/L_{\text{Edd}} = 0.1$. At this stage, we calculate the luminosity (L_{pl}) in the power-law component and the luminosity in the (L_{dbb}) in the DISKBB component, whence we can derive the ratio $L_{\text{pl}}/L_{\text{dbb}}$. In Fig. 2, the red circles correspond to the mass range for which the ratio $L_{\text{pl}}/L_{\text{dbb}}$ was derived using the aforementioned method. The solid black line joining the red circles is then extrapolated using a smooth, power series extrapolation

$$\frac{L_{\text{pl}}}{L_{\text{dbb}}} = \frac{a_1}{\frac{M_{\text{BH}}}{M_{\odot}}} + \frac{a_2}{\left(\frac{M_{\text{BH}}}{M_{\odot}} - b_2\right)^2}, \quad (9)$$

where the values of constants are provided in Table 2. Thus, for the higher mass BHs, as well, we get the scaling of the power-law component relative to the DISKBB component, which can then be used to construct the corresponding SEDs. We have thus, built a suite of SEDs (100 of them) for $L_{\text{bol}}/L_{\text{Edd}} = 0.03, 0.1, 0.3, 1.0$ with the

Table 2. Constants of the $\log\left(\frac{M_{\text{BH}}}{M_{\odot}}\right) - \frac{L_{\text{pl}}}{L_{\text{dbb}}}$ best-fitting equation.

$\frac{L_{\text{bol}}}{L_{\text{Edd}}}$	a_1	a_2	b_2
0.03	-8.21633	165.093	-3.58592
0.1	-1.35708	21.282	-0.523004
0.3	-1.30806	23.599	-2.24452
1.0	-0.674781	12.5449	-2.31223

Table 3. BEL parameter ranges.

	Min	Max	Δ
$\log \Phi(\text{H})$	18	24	0.5
$\log n_{\text{H}}$	8	14	0.5
$\log N_{\text{H}}$	21	23	0.5

range of mass varying from $M_{\text{BH}} = 10^6$ to $10^{12} M_{\odot}$ in intervals of 0.25 dex. The right-hand panel of Fig. 1 shows the optical to X-rays SEDs (red dotted and dashed lines) obtained thus, for $L_{\text{bol}}/L_{\text{Edd}} = 0.1$, where the steeply falling (relative to the power law) higher energy tails of the DISKBB are shown in solid black lines. Above $M_{\text{BH}} \sim 10^9 M_{\odot}$ the power law dominates the main ionizing continuum relevant for the BEL ions. For lower accretion rate ($L_{\text{bol}}/L_{\text{Edd}} < 0.1$) this statement is true for even lower BH mass.

One might argue that equation (8) does not distinguish between SMBHs and HMBHs and so this equation should be used directly, even for the HMBHs and we should not extrapolate. However, these extrapolations, which become important only for the HMBHs, are based on the physics of accretion discs. Further, in Appendix, we show that if we had directly used equation (8) for the highest masses, the differences in the results would be minor, and effectively has no difference in the qualitative inferences.

3 PHOTOIONIZATION CALCULATION

For each of 100 SEDs (25 masses \times 4 $L_{\text{bol}}/L_{\text{Edd}}$ values), we use the C17.00 version of CLOUDY³ (Ferland et al. 2017), to calculate the EWs of many emission lines for a wide range of the parameters $\Phi(\text{H})$, n_{H} , and N_{H} . $\Phi(\text{H})$ is the ionizing incident photon flux $\Phi(\text{H}) = Q(\text{H})/4\pi r^2$, where $Q(\text{H})$ is the number of hydrogen ionizing photons.

Though CLOUDY gives EW of each line as a function of $\Phi(\text{H})$, n_{H} , the parameter $\Phi(\text{H})$ can easily be interchanged by r . Hence, we can express (following Hazy 2) that the flux of the emission line from a cloud of density n_{H} and at a distance r is

$$F(r, n_{\text{H}}) \sim \text{EW}(r, n_{\text{H}}) \frac{\nu F_{\nu}^c}{\lambda}, \quad (10)$$

where λ is the central wavelength of the line and νF_{ν}^c is the incident continuum at λ . $F(r, n_{\text{H}})$ can then be used in equation (12) to calculate the total line luminosity L_{line} , as described in the next section.

For the calculation of BELs, the parameters are stepped over a grid of values as shown in Table 3, a total of 845 CLOUDY runs (for each SED). These ranges are based on Baldwin et al. (1995), Korista et al. (1997a), and the range of N_{H} on Chakravorty et al. (2014). We have calculated the EWs of all the 42 prominent quasar emission lines listed in Korista et al. (1997a), out of which only 5 strongest lines are demonstrated here.

³<http://www.nublado.org/>

Table 4. NEL parameter ranges.

	Min	Max	Δ
$\log \Phi(\text{H})$	10	20	0.5
$\log n_{\text{H}}$	2	10	0.5
$\log N_{\text{H}}$	21	23	0.5

For the calculation of NELs, the ranges in Table 4 were used. We adopted these ranges based on Ferguson et al. (1997). We have calculated the EWs of all the 23 prominent NELs listed in Ferguson et al. (1997), out of which only 6 strongest lines are demonstrated here. For NELs, the presence of dust can play some role in determining the gas composition and hence the strength of lines. Ferguson et al. (1997) demonstrate the effect of the presence of dust in detail. However, they also find a combination of parameters, where the dust-free gas produces very similar line strengths (matching observations) as a dusty gas. For the sake of simplicity, we adopt those parameters and work with dust-free gas for the NELs. The appropriate parameters are discussed in more detail in Section 6.

Thus for the total number of SEDs explored in this paper, along with the calculations for each of the physical parameters of the gas properties $\Phi(\text{H})$, n_{H} , and N_{H} , we ran a total of 256 240 CLOUDY models. For SEDs with low accretion rate, we have done CLOUDY calculations only up to $M_{\text{BH}} = 10^{11.5} M_{\odot}$ due to numerical convenience. This huge theoretical data set was then used to calculate the optimal line strengths as discussed in Section 4.

4 LOCALLY OPTIMALLY EMITTING CLOUDS

Strong BELs are the identifying feature of AGNs and study of them gives information on their central engine. The BELs are also used to estimate the chemical composition of the hosting galaxy and their EWs are even used in estimating the BH mass.

Photoionization models of the BLR are extremely relevant to the study of AGNs (Netzer, Laor & Gondhalekar 1992). Early BLR models were quite limited and used to assume the lines were emitted by the single gas cloud, one with a single ionization parameter, column density, and gas density (Kwan & Krolik 1981). These models became untenable when reverberation mapping observations showed the presence of a wide distribution of emission-line cloud properties with distance from the ionizing continuum. This development prompted a multicloud model with a wide range of spatial and density distributions (Baldwin et al. 1995).

The LOC model was introduced by Baldwin et al. (1995). This model established that any given BEL is most intensely emitted by gas with a particularly narrow range of ionization parameter and density and thus a weighted average over spatial and density distribution includes the gas with optimal parameters for each of the observed lines. Ferguson et al. (1997) further extended this model to predict the line strengths of NELs.

The total line luminosity emitted by the entire set of clouds at various radial distances and densities is given by

$$L_{\text{line}} \propto \int \int r^2 F(r, n_{\text{H}}) f(r) g(n_{\text{H}}) dn_{\text{H}} dr, \quad (11)$$

where $f(r)$ and $g(n_{\text{H}})$ are the spatial and density distribution functions, respectively. For simplicity, we assume them to be power laws as in Ferguson et al. (1997). We have further normalized the L_{line} over the entire spatial and density distribution functions.

$$L_{\text{line}} = 0.24 \frac{\int \int r^2 F(r, n_{\text{H}}) r^{\gamma} n_{\text{H}}^{\beta} dn_{\text{H}} dr}{\int \int r^{\gamma} n_{\text{H}}^{\beta} dn_{\text{H}} dr} \quad (12)$$

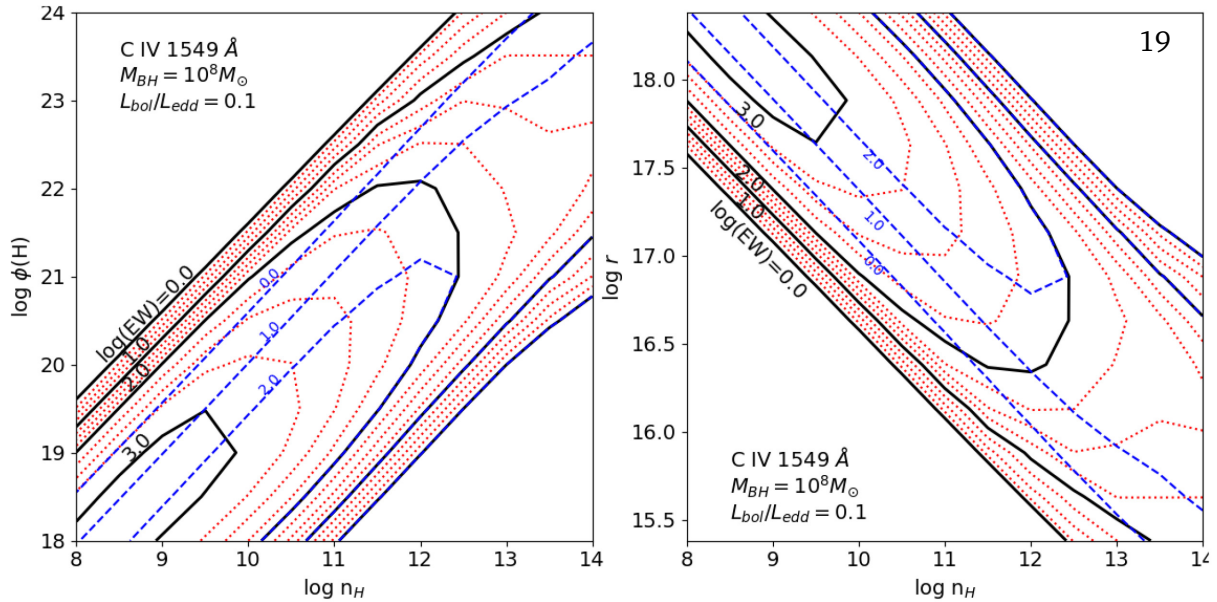


Figure 3. Contour plot for EW of C IV (1549 Å) in the $n_{\text{H}}-\Phi(\text{H})$ plane (left-hand panel) and $n_{\text{H}}-R_{\text{cloud}}$ plane (right-hand panel). The solid black lines are contours at steps of 1 dex and dotted red lines are at the steps of 0.25 dex, for $\log N_{\text{H}} = 23$. The dashed blue lines are contours at steps of 1 dex, for $\log N_{\text{H}} = 21$. Originally, Baldwin et al. (1995) and Korista et al. (1997) presented the efficiency of line emission for different BELs as a function of n_{H} and Φ (as in the left-hand panel). Ferguson et al. (1997) made a similar study on NELs; efficiency was presented as a function of n_{H} and R_{cloud} (as in the right-hand panel) instead. For the sake of consistency, between the BEL and NEL analysis we stick to R_{cloud} instead of Φ , throughout the rest of this paper. Here, we represent both planes, to demonstrate that it is a mere inversion of the contours, when the y -parameter of the plane is changed from Φ to R .

Similarly, the weighted average of the EWs (\mathcal{EW}) of each line emitted by the entire set of clouds at various radial distances and densities is calculated using

$$\mathcal{EW} = 0.24 \frac{\int \int \text{EW}(r, n_{\text{H}}) r^{\gamma} n_{\text{H}}^{\beta} dn_{\text{H}} dr}{\int \int r^{\gamma} n_{\text{H}}^{\beta} dn_{\text{H}} dr}. \quad (13)$$

The successes and the limitations of LOC model are discussed in detail by Leighly & Casebeer (2007). Limitations of LOC model include that (i) some parameters, like the spatial and density indices cannot be physically interpreted and (ii) a number of physical effects are not included in the model, a significant one being self-shielding. However, for the purpose of this paper, the LOC model is sufficient.

The factor 0.24 in equations (12) and (13) represents a nominal constant covering factor for the broad-line emitting clouds (following Leighly & Casebeer 2007, see Fig. 1). Covering fraction is a very complex issue, varying from source to source. Hence its theoretical generalization over a wide range of mass and accretion rates of BHs is difficult and beyond the scope of this paper. Hence we maintain this value of 0.24 throughout the paper, even for narrow-line emitting clouds. Please note that any different constant covering factor would simply scale the $\log(\mathcal{EW})$ s in the vertical direction, in our subsequent Figures, altering none of the trends demonstrated. Further, a constant covering factor will absolutely have no effect of the line ratios, presented later.

5 BROAD EMISSION LINES

From the CLOUDY photoionization calculations, we derive EWs for all the prominent BELs. The EWs are measured relative to the incident continuum at 1215 Å which is then normalized to the central wavelength of each line. In Fig. 3, we represent the isocontours of calculated EWs (in log) for C IV 1549 Å, one of the strongest known BELs on the $\log n_{\text{H}}-\log \Phi(\text{H})$ (left-hand panel) and $\log n_{\text{H}}-\log r$ (right-

hand panel) planes for $M_{\text{BH}} = 10^{8.0} M_{\odot}$ and $L_{\text{bol}}/L_{\text{Edd}} = 0.1$. We see that our (solid black and dotted red) contour plots match closely with the contours presented in Baldwin et al. (1995) and Korista et al. (1997a), for $\log N_{\text{H}} = 23$. The slight quantitative differences are expected because the earlier authors used a slightly different SED compared to the one that is used to get Fig. 3. The diagonal lines in the contours with a slope of 45° are of constant ionization parameter $U = \Phi(H)/cn_{\text{H}}$, which is a measure of the recombination rate at the face of the cloud. C IV being a collisionally excited line shows a band of constant U lines where there is efficient emission. At high n_{H} and $\Phi(H)$, contours start to turn over indicating thermal heating of the gas instead of photoionization. To understand the effects of column density, we point to the isocontours for $\log N_{\text{H}} = 21$ in dashed blue line, in Fig. 3. When compared to the solid black $\log N_{\text{H}} = 23$ contours (at same 1 dex separation), the ones with lower N_{H} show that for highly ionized gas, we need high column density gas to yield emission lines of any reasonable strength. In Fig. 4, we represent the contour for $M_{\text{BH}} = 10^{11} M_{\odot}$ to compare the efficiency of line emission at higher masses. While the highest EW achieved for the $M_{\text{BH}} = 10^8 M_{\odot}$ SED is $10^{2.5}$, that for the $M_{\text{BH}} = 10^{11} M_{\odot}$ SED is $10^{1.25}$. Thus, everything else remaining the same, the line becomes fainter by 1.25 dex.

To assess the contribution from all the clouds spread across a range of distance and having a range of density, we apply the LOC model mentioned in Section 4 for our calculations. We use equation (12) and equation (13) over the entire range of r and n_{H} . Baldwin (1997) suggested that the L_{line} is only weakly sensitive to the radial and column density distributions as long as γ in equation (12) is > -1 . Baldwin (1997) further shows that $\beta = -1$ is strongly suggested by observations which is further confirmed by Hamann et al. (2002). Therefore, we use a constant power index of -1 for both, n_{H} and r in our calculations to get L_{line} and \mathcal{EW} . Fig. 5 shows the resultant $\log(\mathcal{EW})$ as a function of M_{BH} for the BEL C IV 1549 Å, for $L_{\text{bol}}/L_{\text{Edd}} = 0.1$ (red dotted line).

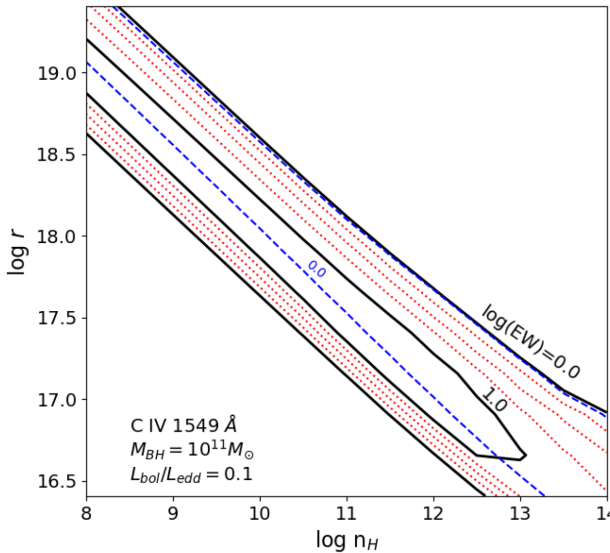


Figure 4. Contour plot for EW of C IV (1549 Å) in the $n_{\text{H}}-R_{\text{cloud}}$ plane for $M_{\text{BH}} = 10^{11} M_{\odot}$. The efficiency of the line emission has decreased greatly when compared to $M_{\text{BH}} = 10^8 M_{\odot}$ (Fig. 3). The different line styles and colours represent the same variation of physical parameters as in Fig. 3.

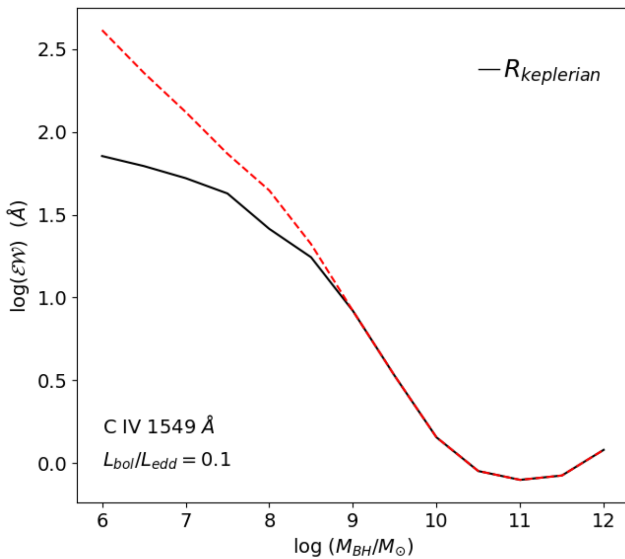


Figure 5. $\mathcal{E}\mathcal{W}$ of C IV (1549 Å) as a function of M_{BH}/M_{\odot} . Dashed line represents $\mathcal{E}\mathcal{W}$ calculated using LOC integration (equation 13). The black solid line represents $\mathcal{E}\mathcal{W}$ after limiting the outermost radius of cloud with $v_{\text{min}} = 1000 \text{ km s}^{-1}$.

At 10^4 K , thermal widths are only about 10 km s^{-1} . The observed widths in BELs ($\gtrsim 10 \text{ km s}^{-1}$) should therefore be due to organized high velocity flows of clouds with Keplerian, or at least, virialized velocities. This allows us to define maximum radius for BLR as

$$R_{\text{Keplerian}} = GM_{\text{BH}}/v_{\text{min}}^2, \quad (14)$$

where v_{min} is the lowest observed velocity of the cloud. Introducing $R_{\text{Keplerian}}$ cut-off within CLOUDY calculated line strengths, results in a significant change in $\mathcal{E}\mathcal{W}$ at the lower mass end as in Chakravorty et al. (2014). In Fig. 5, the black solid line corresponds to $\mathcal{E}\mathcal{W}$ after imposing a lower limit at $v_{\text{min}} \geq 1000 \text{ km s}^{-1}$. For the rest

of the paper, we will always calculate $\mathcal{E}\mathcal{W}$ and L_{line} for (all) BELs, maintaining this lower limit of v_{min} . 20

In the different panels of Fig. 6, we extend the calculation and show how the line strength $\mathcal{E}\mathcal{W}$ of six of the prominent BELs such as O VI 1034 Å, C IV 1549 Å, He II 1640 Å, Mg II 2798 Å, H β 4861 Å, and H α 6563 Å vary when accretion rate is varied over the range $0.03 \leq L_{\text{bol}}/L_{\text{Edd}} \leq 1.0$.

For C IV 1549 Å (top middle panel of Fig. 6) at $L_{\text{bol}}/L_{\text{Edd}} = 0.1$, the $\mathcal{E}\mathcal{W} = 26$ for the $10^8 M_{\odot}$ BH, which is in excellent agreement with what fig. 1 of Leighly & Casebeer (2007) predicts for the same emission line, for the nominal model (with $C_f = 0.24$). The $\mathcal{E}\mathcal{W}$ of this line remains quite constant for $10^6 M_{\odot} < \text{BH} < 10^8 M_{\odot}$ and then drops quickly to 1 per cent of the peak by $\sim 10^{10} M_{\odot}$. O VI 1034 Å, He II 1640 Å, and Mg II 2798 Å all show similar ~ 2 dex decrease in $\mathcal{E}\mathcal{W}$ from 10^8 to $10^{10} M_{\odot}$. H β 4861 Å and H α 6563 Å show similar behaviour from 10^9 to $10^{11} M_{\odot}$.

In Fig. 6, notice the distinction between the $\mathcal{E}\mathcal{W}$ profiles of the high-ionization O VI, C IV, and He II (top panels) to those of the low-ionization Mg II, H β , and H α lines (bottom panels). The low-ionization lines maintain quite constant $\mathcal{E}\mathcal{W}$ up to $\sim 10^{10} M_{\odot}$ while the high-ionization lines begin to drop in $\mathcal{E}\mathcal{W}$ by $\sim 10^8 M_{\odot}$, for the BHs with accretion rate $L_{\text{bol}}/L_{\text{Edd}} = 0.1$. The aforementioned mass ranges mentioned for the $\mathcal{E}\mathcal{W}$ profiles vary when the accretion rate changes, but the qualitative behaviour of the different lines remains the same. Also, the high ionization profiles decrease with increase of mass, up to a critical value of BH mass, hit a minimum and then invert the trend and start increasing with mass. On the other hand, the low-ionization lines profiles show increase (or almost constant values) of $\mathcal{E}\mathcal{W}$ with mass increase, hit a maximum and then drops with increase in mass. Such differing evolution of the $\mathcal{E}\mathcal{W}$ s will also have consequences on how the luminosities of these lines would evolve as a function of the BH mass, particularly at the high-mass end.

We take C IV 1549 Å as a representative of the high-ionization lines and H α 6563 Å as a representative of the low-ionization lines and plot their luminosities as a function of mass in Fig. 7. At the high-mass end, while the luminosity of the C IV line remains constant, the luminosity of H α line drops, sometimes by even an order of magnitude. Thus, the low-ionization lines are not the best tracers to look for while searching for the HMBH using the current optical telescopes. This result has implications for the most commonly done BH searches that rely on optical surveys like SDSS, which in their turn, rely heavily on the H β 4861 Å and H α 6563 Å lines. However, the results presented here may serve as a benchmark for emission-line studies, using the next-generation 30 m class optical telescopes.

The distinction between the behaviour of the high- and the low-ionization lines is readily understood from Fig. 8. The ionization potentials (IP) of O V and C III, which would result in the formation of O VI and C IV ions, are the highest, among the BEL ions/elements discussed. Note that the IP of these ions are at an interesting energy range – one where the accretion disc is more dominant for the SEDs of the lower mass ($M_{\text{BH}} \lesssim 10^8 M_{\odot}$) BHs, but the power-law radiation component is more dominant for the higher mass BHs. For each ion (high-ionization lines), the narrow mass range, where the transition of the relative dominance happens, is where the $\mathcal{E}\mathcal{W}$ turns over. For ions (low-ionization lines), where there is no significant switch of the dominating SED component, the $\mathcal{E}\mathcal{W}$ simply declines with an increase in BH mass. In fact, for the H α and H β lines with neutral, but excited Hydrogen, of course IP is not the deciding factor. Hence, they follow the simple rationale that the $\mathcal{E}\mathcal{W}$ increases with the mass (and hence the luminosity) of the BH until their line energies go above the $f(\nu) \sim \nu^{1/3}$ part of the BH SED – which happens because the accretion disc peak and hence the $\nu^{1/3}$ (part of the SED) recedes to

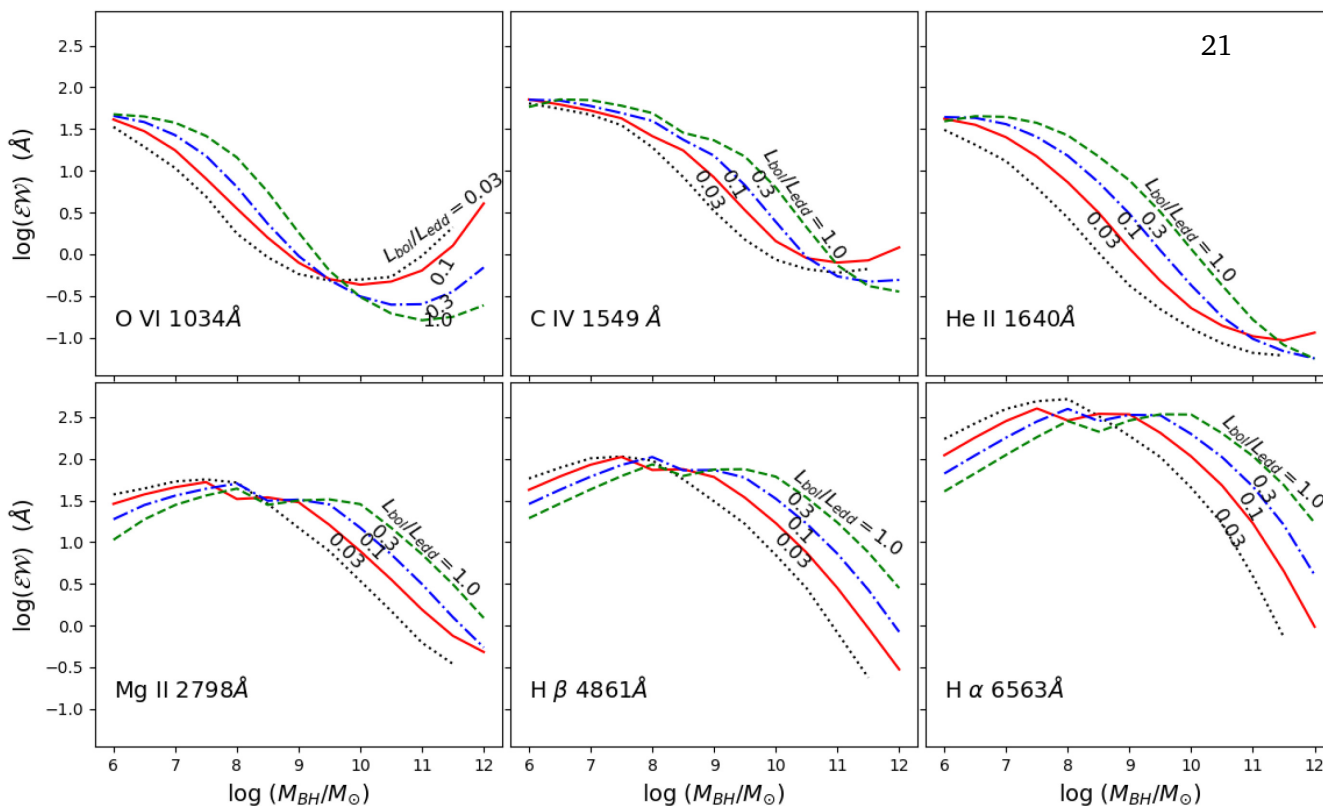


Figure 6. Evolution of \mathcal{EW} of few prominent BELs over range of masses and accretion rates.

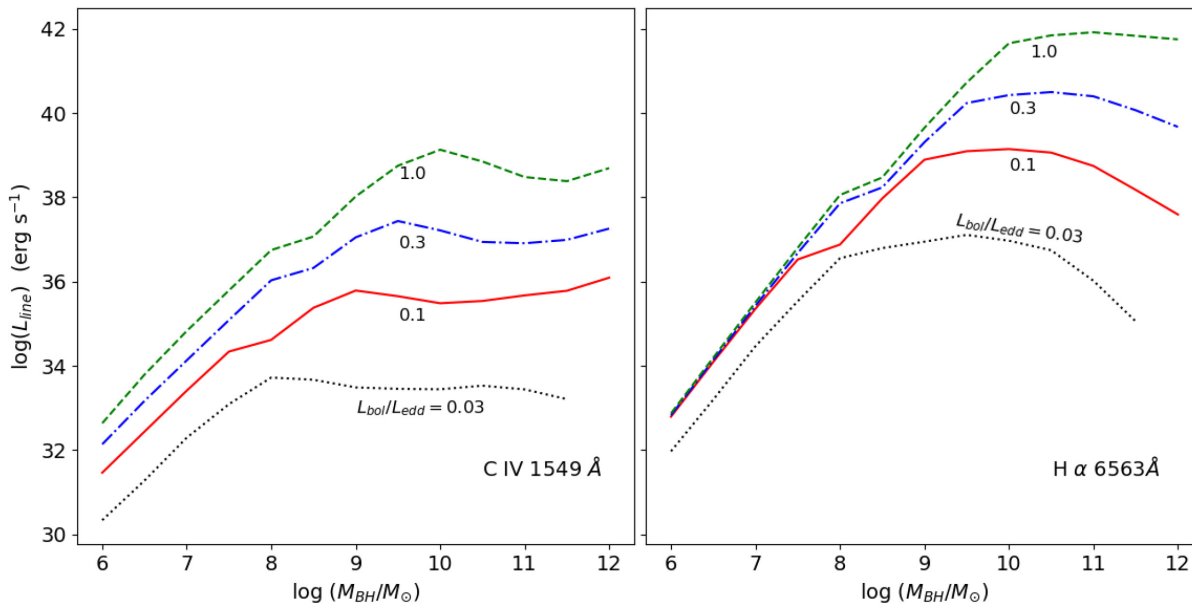


Figure 7. L_{line} of C IV 1549 Å and H α 6563 Å as a function of M_{BH}/M_{\odot} calculated using equation (13).

lower energies with an increase in BH mass. Thus, at the corresponding BH mass, the H α and H β \mathcal{EW} s start dropping. This discussion thus illustrates the fine sensitivity that line strengths have on the shape of the illuminating SED. Further, this sensitivity becomes evident in our study because we are probing a mass range of BHs where the SEDs transition through the energy range of the relevant IPs and line energies – a very fortunate natural coincidence indeed!

Fig. 6 further shows that the turnaround of $\log(\mathcal{EW})$ in O VI 1034 Å, C IV 1549 Å for higher masses makes it impossible to determine the mass of the HMBH accurately using just $\log(\mathcal{EW})$ of these strong BELs. For the other emission lines, similar degeneracy exists at the lower mass end. Hence, to remove this degeneracy we have calculated line ratios which we discuss in Section 7.2.

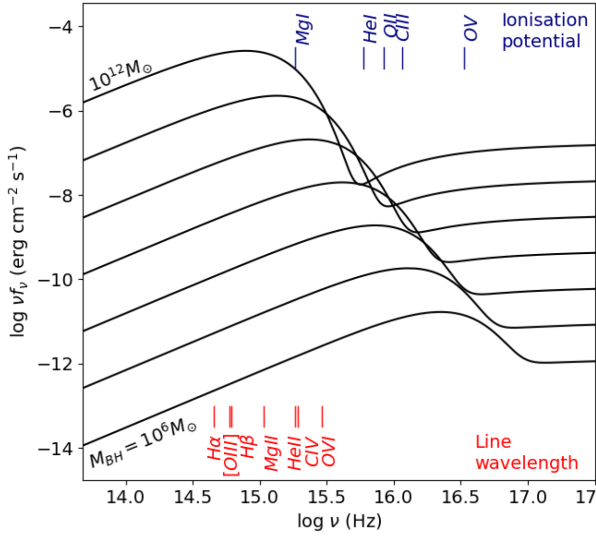


Figure 8. The line wavelength of the five strongest BELs (marked at the bottom) and the ionization potentials of the lower ions (marked on the top) are compared against the shape of the broad-band SEDs of different BHs, for $L_{\text{bol}}/L_{\text{Edd}} = 0.1$.

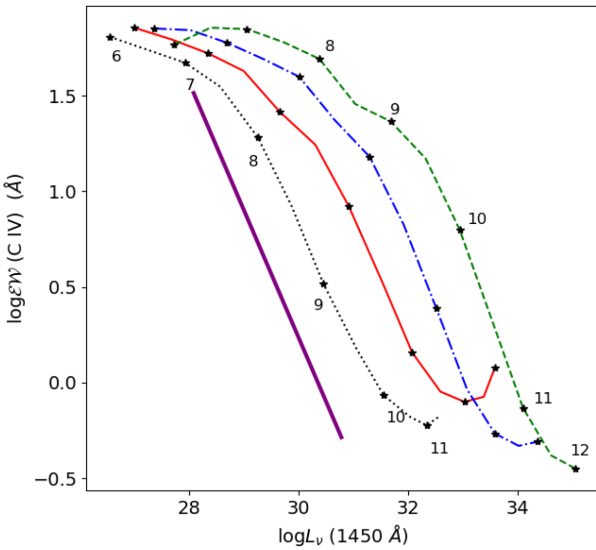


Figure 9. Demonstration of the Baldwin effect using the C IV 1549 Å emission line. The left-most thick solid magenta line is the predicted Baldwin effect relationship $\mathcal{E}\mathcal{W} \sim L_{\nu}^{-2/3}(1450\text{\AA})$, with arbitrary normalization. The rest of the lines are the (EW) profiles of the C IV line, having the same line-colour description as in Fig. 6 – from accretion rate of 0.03 to 1.0, from left to right. The numbers on each profile indicate the mass of the BH, in $\log(M_{\text{BH}}/M_{\odot})$.

We are in a position to investigate if the Baldwin Effect (Baldwin 1977; Zheng & Malkan 1993; Shemmer & Lieber 2015) holds true for the HMBHs and gain some insight on the mass range or range of accretion rates for which this effect remains valid. Hence, we plot the $\mathcal{E}\mathcal{W}$ of C IV 1549 Å as a function of $L_{\nu}(1450\text{\AA})$ in Fig. 9. The left-most thick solid magenta line in Fig. 9 shows the relationship, $\mathcal{E}\mathcal{W} \sim L_{\nu}^{-2/3}(1450\text{\AA})$, predicted by Baldwin (1977) between the C IV line strength and the luminosity at 1450 Å. Clearly, the low-mass BHs ($M_{\text{BH}} < 10^7 M_{\odot}$) do not obey this relationship. However, for higher masses ($10^8 \leq M_{\odot} \leq 10^{11}$), the match with the slope of $-2/3$

($= -0.66$) is good and improves for higher accretion rates; albeit the mass range where the match is better, also shifts to the higher values with the increase in accretion rate. For $L_{\text{bol}}/L_{\text{Edd}} = 0.03$, the slope is -0.51 for mass range 10^7 – $10^{10} M_{\odot}$, for 0.1, the slope is -0.53 for 10^8 – 10^{11} , for 0.3, the slope is -0.66 for 10^9 – 10^{11} and finally, for 1.0, the slope is -0.63 for 10^9 – 10^{12} . Beyond $10^{11} M_{\odot}$, the Baldwin effect disappears as the $\mathcal{E}\mathcal{W}$ of the C IV line starts to strengthen again, especially, at low accretion rates. Thus, we show that the Baldwin effect is a natural result of the changing accretion disc SED with BH mass over 2–4 orders of magnitude.

Note that the discussion of the behaviour of emission-line strengths in this section is for non-spinning BHs. To understand how BH spin may play a role (particularly for the O VI and the C IV lines) in this discussion, refer to Section 8.

6 NARROW EMISSION LINES

We want to know if the NELs will have different observable properties as mass of the BH rises. Hence, we conducted CLOUDY simulations of the NELs, as well. In the left-hand panel of Fig. 10, we show the isocontours of calculated EWs (in log) for the [O III] 5700 Å line in the $\log n_{\text{H}}$ – $\log r$ plane for $M_{\text{BH}} = 10^{8.0} M_{\odot}$ and $L_{\text{bol}}/L_{\text{Edd}} = 0.1$. As mentioned in Section 3 (Table 4), we are using a different range of Φ and n_{H} for NELs (as opposed to the right-hand panel of Fig. 3). As NLRs are situated further away from the BLRs, the range of $\Phi(\text{H}) = Q(\text{H})/4\pi r^2$ for which NELs are efficiently produced is lesser than that of BELs (Peterson 1997). The EWs are measured relative to the incident continuum at 4860 Å which is then normalized to the central wavelength of each line. We see that our contour plots match closely with the contours presented in Ferguson et al. (1997) for $\log M_{\text{H}} = 23$. The small differences are because of the slightly different SED that we use. In the right-hand panel of Fig. 10, we represent the contour for $M_{\text{BH}} = 10^{11} M_{\odot}$ to compare the efficiency of line emission at higher masses. While the highest EW achieved for the $M_{\text{BH}} = 10^8 M_{\odot}$ SED is $10^{3.75}$, that for the $M_{\text{BH}} = 10^{11} M_{\odot}$ SED is $10^{1.25}$. Thus, everything else remaining the same, the line becomes fainter by 2.5 dex.

Over the entire range of parameter space, we used CLOUDY to calculate the line strengths for almost all of the lines discussed in Ferguson et al. (1997). However, for the scope of this paper, we use results of six of them, namely H β 4861 Å, [O III] 5007 Å, [O I] 6300 Å, H α 6563 Å, [N II] 6584 Å, and [S II] 6720 Å. The individual EWs were then used in equations (12) and (13) to calculate L_{line} and $\mathcal{E}\mathcal{W}$. The sensitivity of γ and β of equation (12) in case of NELs are presented in detail in Ferguson et al. (1997) and shows that for dust-free models like ours, $\gamma = -1.25$ and $\beta = -1.4$ fits the observational spectra the best. Hence, we use these indices for our calculations. In the case of BELs, we had used an upper limit for $r(= R_{\text{Keplerian}})$ corresponding to $v_{\text{min}} = 1000 \text{ km s}^{-1}$. To make a clear distinction between BLR and NLR, we use a similar idea, but this time for lower limit of $r(= R_{\text{Keplerian}})$ corresponding to $v_{\text{max}} = 500 \text{ km s}^{-1}$. The results are shown in Fig. 11 (main panel). Note that unlike some of the BELs (O VI 1036 Å, C IV 1549 Å, and He 1640 Å), the EW of [O III] 5007 Å line decreases monotonically with the increase in the mass of the BH. $\mathcal{E}\mathcal{W}$ of [O III] 5007 Å drops by ~ 1.5 dex from $M_{\text{BH}} = 10^8$ to $10^{10} M_{\odot}$. This amplitude is similar to those seen for most of the BELs. The same behaviour holds for all six NELs that we are discussing in this paper.

To understand the evolution of the [O III] 5007 Å line $\mathcal{E}\mathcal{W}$, we again refer to Fig. 8. The ionization potential of O II is similar to that of He I, but the corresponding [O III] line does not exhibit a turnover in EW, similar to that of He II 1640 Å BEL. The EW profile is rather

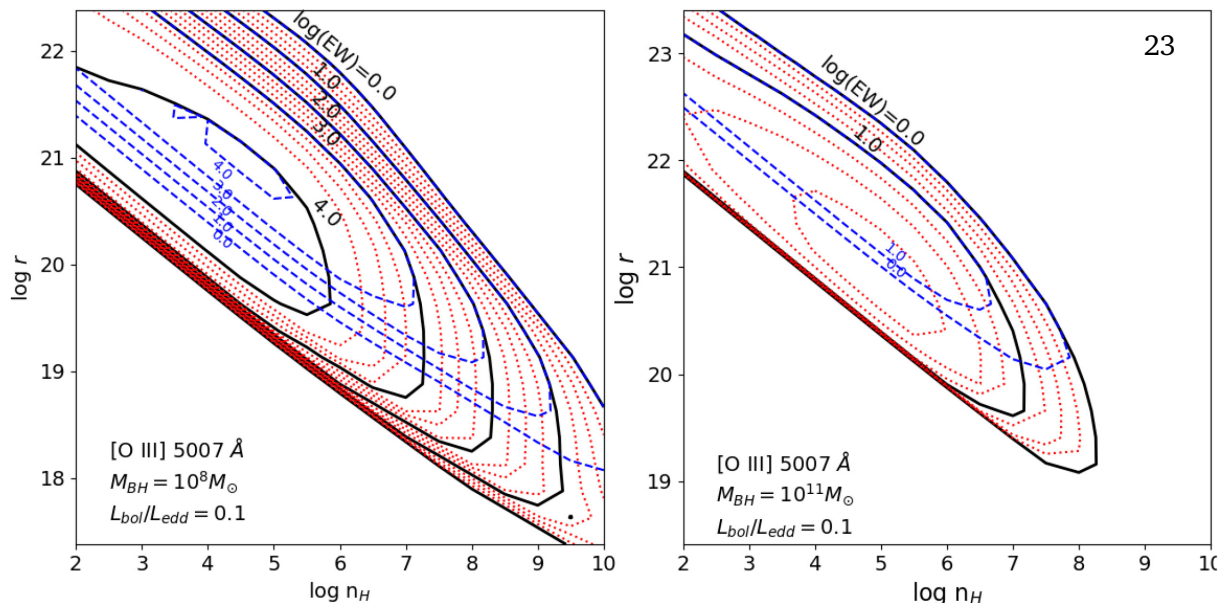


Figure 10. Contour plot for EW of [O III] 5007 Å in the $n_{\text{H}}-r$ plane for $M_{\text{BH}} = 10^8$ (left-hand panel) and $10^{11} M_{\odot}$ (right-hand panel). The solid black lines are contours at steps of 1 dex and dotted red lines are at the steps of 0.25 dex, for $\log N_{\text{H}} = 23$. The dashed blue lines are contours at steps of 1 dex, for $\log N_{\text{H}} = 21$. It is evident that the efficiency of the line emission has decreased greatly in $M_{\text{BH}} = 10^{11} M_{\odot}$ when compared to $M_{\text{BH}} = 10^8 M_{\odot}$.

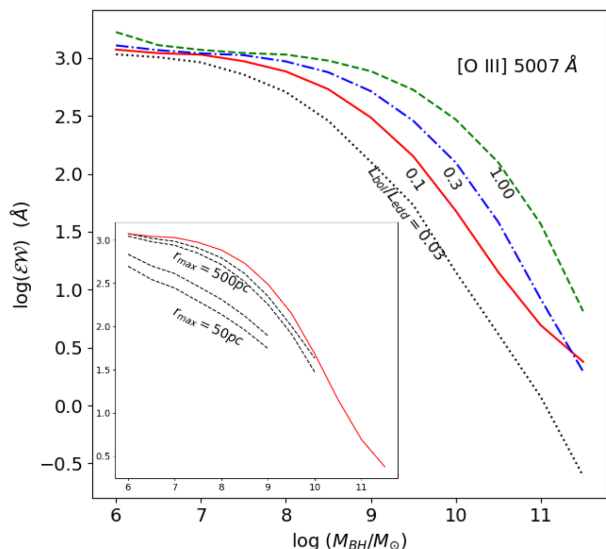


Figure 11. $\log \mathcal{E}W$ of [O III] 5007 Å as a function of $\log M_{\text{BH}}/M_{\odot}$ for different $L_{\text{bol}}/L_{\text{Edd}}$. In the inset panel, we have compared, for accretion rate 0.1, modified $\mathcal{E}W$ s where the LOC integration was done up to $r = 1000, 500, 100, 50$ pc (dashed black lines, from top to bottom, respectively).

similar to that of the Hydrogen lines $\text{H}\alpha$ and $\text{H}\beta$, indicating that it is the shape of the SED at the energy range of the [O III] line’s central wavelength, that determines the strength of the line. Because [O III] 5007 Å, is a forbidden line, it is the energy (of the illuminating SED) at the central wavelength of the line, that is of more importance than the energy at the IP of O II, as explained by the Stoy energy balance temperature indicator (see section 5.10 of Osterbrock & Ferland 2006). The evolution of the $\mathcal{E}W$ of all the other five NELs would be similar to that of [O III] 5007 Å, because they too are forbidden lines.

The $\mathcal{E}W$ s of O III 5007 Å $\mathcal{E}W$ s are higher from that usually observed for the O III line ($\lesssim 100$ – fig. 1 of Risaliti, Salvati & Marconi

2011 shows a distribution; also see Shen et al. 2011). One reason for the discrepancy is because we did not put any constraint on the upper limit of r in the LOC integration of NELs. We demonstrate the effect of incorporating this constrain in the inset of Fig. 11. Notice the comparison, with the solid red curve, of the modified $\mathcal{E}W$ s as the upper limit on r is varied from 1000 to 50 pc, through 500 and 100 pc. For the $r_{\text{max}} = 100$ pc profile, we see that for the $10^8 M_{\odot}$ BH, $\log(\mathcal{E}W) \sim 2.5$, which yields a value about 0.5–1 dex higher from the predictions of Risaliti et al. (2011). While we understand that the sample in Risaliti et al. (2011) can have BHs with higher mass and/or lower accretion rate, the second reason for the discrepancy is the use of the uniform/constant covering factor of 0.24, a value that is motivated by the study of broad lines and satisfies the BEL $\mathcal{E}W$ s, as we have seen in Section 5. Baskin & Laor (2005) show that this value for covering factor for [O III] 5007 Å line ranges between 0.02 and 0.2. If we account for this additional factor of 10 (drop in $\mathcal{E}W$), we reach a good agreement with the observed values reported in Risaliti et al. (2011). That we rely on r_{max} to be 100 pc, or lower, is an indication, that we usually observe more compact NLRs. This initial analysis shows here, that there is scope of discerning the nature of NLRs (and also BLRs) if a rigorous, systematic analysis of the variations of the LOC parameters are conducted for NLRs, a study beyond the scope of this paper.

7 LINE RATIOS

7.1 Narrow lines and BPT diagrams

Unlike BELs, NELs are not direct signatures of AGN activity. For example, SFRs also emit NELs (of the order of 100 km s^{-1}). So, making the distinction between the two becomes very important. That is where the BPT diagrams become very useful. BPT diagrams were first plotted by Baldwin et al. (1981) to classify galaxies based on their excitation mechanisms. They found an empirical method of separating AGNs from SFRs based on line ratios.

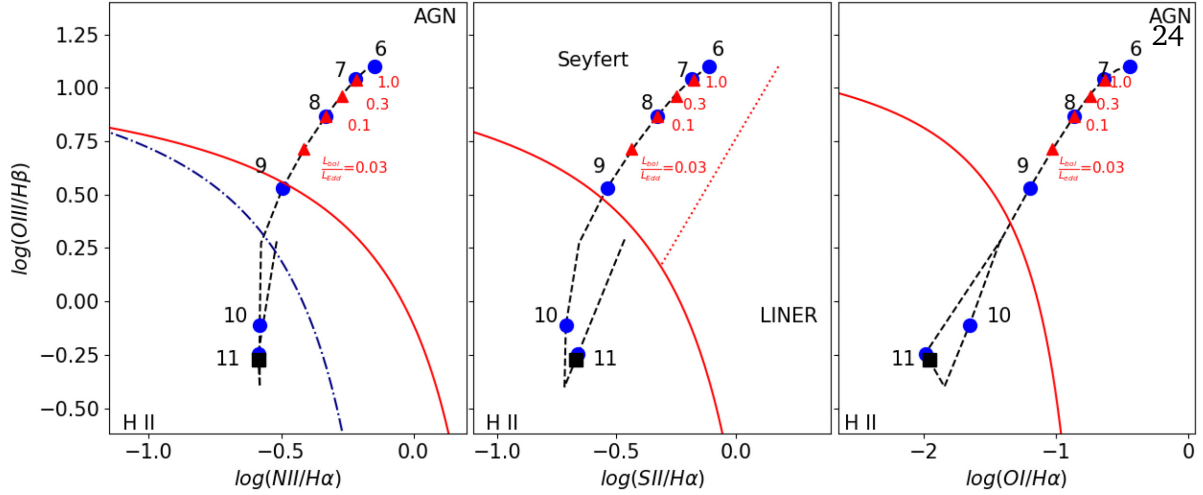


Figure 12. Line luminosity ratios of few observable prominent NELs as a function of BH mass for $L_{\text{bol}}/L_{\text{Edd}} = 0.1$ is plotted on Kewley et al. (2001, 2006) plots (red line) and is marked in blue circles and are labelled with $\log(M_{\text{BH}}/M_{\odot})$ adjacent to them. Line luminosity ratios as a function of accretion rates, but only for $M_{\text{BH}} = 10^8 M_{\odot}$ is marked in red triangles. We have plotted a black square corresponding to the AGN whose total luminosity is $10^{47} \text{ erg cm}^{-2} \text{ s}^{-1}$ to indicate the position of brightest known quasars on our plot.

Kewley et al. (2001) used theoretical pure star photoionization models to give a maximum starburst line for some of the important BPT line ratios to distinguish AGNs from SFRs more cleanly. We use the same line ratio planes as Kewley et al. (2001). The maximum starburst lines given by Kewley et al. (2001) are plotted as the solid red lines in each panel of the Fig. 12.

The equations for these lines were as follows:

$$\log([\text{O III}]/\text{H}\beta) > 0.61/[\log([\text{N II}]/\text{H}\alpha) - 0.47] + 1.19, \quad (15)$$

$$\log([\text{O III}]/\text{H}\beta) > 0.72/[\log([\text{S II}]/\text{H}\alpha) - 0.32] + 1.30, \quad (16)$$

$$\log([\text{O III}]/\text{H}\beta) > 0.73/[\log([\text{O I}]/\text{H}\alpha) + 0.59] + 1.33. \quad (17)$$

There have been other schemes of demarcation as well. For example, the semi-empirical line given by Kauffmann et al. (2003) is marked as a dotted and dashed blue line in the left-hand panel of Fig. 12. As predicted by Kewley et al. (2001), the region below the solid red lines is expected to be the part of the plane populated by SFR line ratios, while the region above represents the AGN activity. As such, these line ratios have also become a method to look for AGNs. Our theoretical predictions as a function of M_{BH} in the line ratio planes are traced by the dashed black lines in Fig. 12, for $L_{\text{bol}}/L_{\text{Edd}} = 0.1$. We see that for the higher mass BHs ($10^{8.5} M_{\odot} \lesssim M_{\text{BH}} \lesssim 10^{10.75} M_{\odot}$), the line ratios of NELs move into the SFRs of Kewley et al. (2001) plots. Hence these higher mass BHs will be incorrectly detected as SFR using these diagrams. We have further plotted the line luminosity ratios for different accretion rates $L_{\text{bol}}/L_{\text{Edd}}$ (but only, for $M_{\text{BH}} = 10^8 M_{\odot}$) with red triangles in Fig. 12. Note that, the less luminous BHs (even for lesser mass $\sim 10^8 M_{\odot}$) also start to seep into the SFR. This change is due to the disc SED being cooler, comparable to O-star temperatures, and so produce similar emission lines to H II regions. *Therefore, by using this method to distinguish AGNs from SFRs, we are losing low accretion rate and high-mass BHs.*

7.2 Line ratios for BELs

As seen in Fig. 6, for some emission lines a particular $\log(\mathcal{E}\mathcal{W})$ corresponds to two different BH masses. O VI 1034 Å, C IV 1549

Å, and to some extent He II 1640 Å show degeneracy at the high-mass end whereas Mg II 2798 Å, H β 4861 Å, and H α 6563 Å show degeneracy at the low-mass end. Therefore, if we try to estimate the BH mass using just the observed line strengths, we might end up with two very different values for BH masses agreeing to the observed line strengths. To remove this degeneracy, we plot the line luminosity ratios on a multiline plane as a counterpart to the BPT diagrams for NELs (Fig. 13). Blue circles in Fig. 13 are line luminosity ratios for different masses for accretion rate $L_{\text{bol}}/L_{\text{Edd}} = 0.1$ traced by a black dashed line. The red triangles are line luminosity ratios for different accretion rates $L_{\text{bol}}/L_{\text{Edd}}$, but only for $M_{\text{BH}} = 10^8 M_{\odot}$. Such plots will be of use to determine the BH mass just by using the observed line ratios. This may be a new tool for selecting HMBHs.

8 SPINNING BLACK HOLES

BHs are known to have spin associated with them (Reynolds 2014, 2019). Our analysis in the previous sections was motivated to look at the influence of mass variation on the changes in the line emission strengths. Just as the change in mass varies the SED, so does the variation in the spin of the BH (see Bertemes et al. 2016 for a detailed discussion). Hence, in this section, we look into the effect of the spin of the BHs. We do the same rigorous analysis of emission-line strengths, as in previous sections, but comparing, only, the ‘maximally spinning’ BHs to the zero spin ones (analysed in the previous sections), because they will show the maximum deviation from the spin zero case. Results for any intermediate spin is beyond the scope of this paper – it is expected that results for the intermediate spin BHs will simply, lie in between. The more quantitative rigorous analysis will be conducted in future publications where we intend to compare theoretical predictions with observations.

DISKBB is a SED package that does not have spin as an explicit input parameter. However, since all SED generation in the previous sections relied on DISKBB, we find a way to tweak and use the same package, for BHs with spin, for the sake of uniformity. We know that the innermost stable circular orbit of the accretion disc of a spinning BH moves relatively closer (compared to that of a

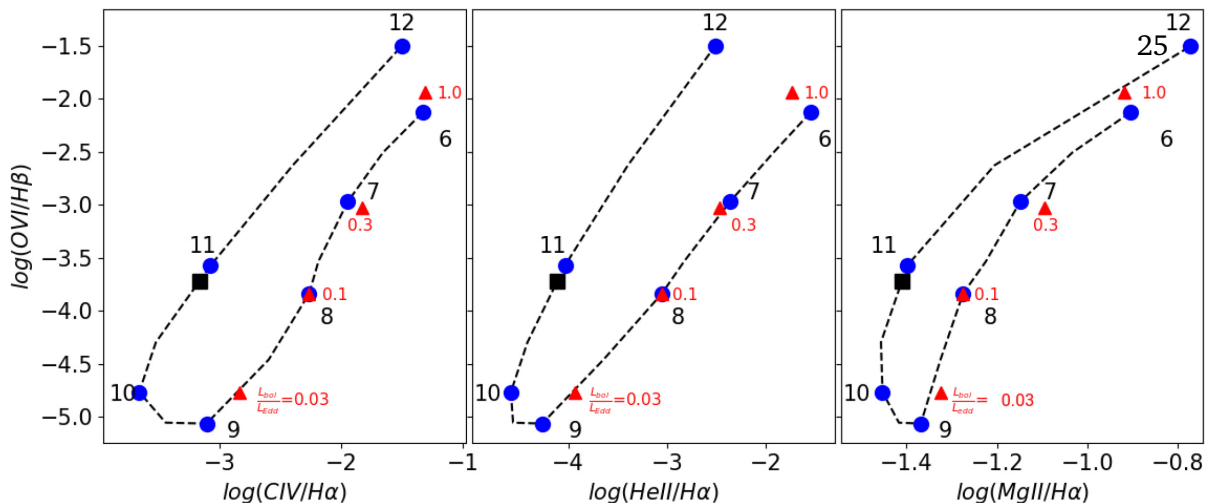


Figure 13. Line luminosity ratios of few observable prominent BELs as a function of BH mass for $L_{\text{bol}}/L_{\text{Edd}} = 0.1$ is marked in blue circles and are labelled with $\log(M_{\text{BH}}/M_{\odot})$ adjacent to them. Note that we use the line 1640 Å He II emission line in the middle panel, here, and in all subsequent figures of line ratios of BELs. We see that the degeneracy is lost when we plot the ratios on multiline plane. Line luminosity ratios as a function of accretion rates, but only for $M_{\text{BH}} = 10^8 M_{\odot}$ is marked in red triangles. We have plotted a black square corresponding to the AGN whose total luminosity is $10^{47} \text{ erg cm}^{-2} \text{ s}^{-1}$ to indicate the position of brightest known quasars on our plot.

non-spinning or less spinning one) to the BH. Thus, in equations (1) and (3), if we opt for a smaller value of R_{in} , while correctly adjusting for η , then we can mimic the SED of a spinning BH, even while using the package DISKBB. To understand what will be a reasonable R_{in} modification to assume, we compare with an SED generated by the package OPTXAGN (Done et al. 2012), from XSPEC version 12.10. In OPTXAGN, we generated the accretion disc SED of a maximally spinning ($a^* = 0.998$) BH of mass $10^8 M_{\odot}$, accreting at $L_{\text{disc}} = 0.1 L_{\text{Edd}}$. Keeping the mass and the accretion rate constant for the BH, when we used DISKBB input parameters, we found a very good match of the SED, for $R_{\text{in}} = R_s = 2R_G$ (resulting in $\eta = 0.75$), while comparing $L_{\nu}(2500 \text{ Å})$ and the energy where the SED peaks (two important aspects relevant to the analysis in this paper). Hence, we proceed to make this a norm for SEDs in this section (and the paper) for BHs with spin – we use DISKBB, with R_{in} set to $R_s = 2R_G$. We understand that for a non-spinning BH, $R_{\text{in}} = R_s$ (or $\eta = 0.75$) is less than the allowed limit of $3 R_s$. Thus, for DISKBB, which is a package for spin zero BHs, using $R_{\text{in}} = R_s$ is unphysical – we made this choice as an artificial fix in the package which cannot include the effects of spin, in any other way. Fig. 14 shows the comparisons of the resultant SEDs for $10^8 M_{\odot}$, accreting at $L_{\text{bol}} = 0.1 L_{\text{Edd}}$ ($\theta = 30^\circ$). Compared to the Schwarzschild SED (red, dotted and dashed line), the peak of the SED for the maximally spinning BH is shifted by 0.25 dex (and 0.15 dex), higher in frequency, for the DISKBB (and the OPTXAGN) SED. At the He II ionization edge (at 228 Å), the maximally spinning DISKBB (and OPTXAGN) SED is 0.2 dex (and 0.16 dex) higher in normalization than the Schwarzschild SED. We generate SEDs corresponding to a range of $10^6 \leq M_{\text{BH}} \leq 10^{11}$, but, this time, with an interval of 1.0 dex. These SEDs are then used through CLOUDY to predict emission-line strengths for both BELs and NELs, in the same way that have been discussed in the previous sections, for the Schwarzschild BHs. The results of this analysis is presented in Figs 15 through 17.

We see that in the case of spinning BHs (of same mass $M_{\text{BH}} = 10^8 M_{\odot}$), $\mathcal{E}\mathcal{W}$ for C IV 1549 Å is higher (by 0.45 dex) than that for the Schwarzschild BHs and this factor decreases for HMBHs (Fig. 15). However, the overall trend of declining $\mathcal{E}\mathcal{W}$, for all the lines, as a function of mass, still remains true even in the extreme case of

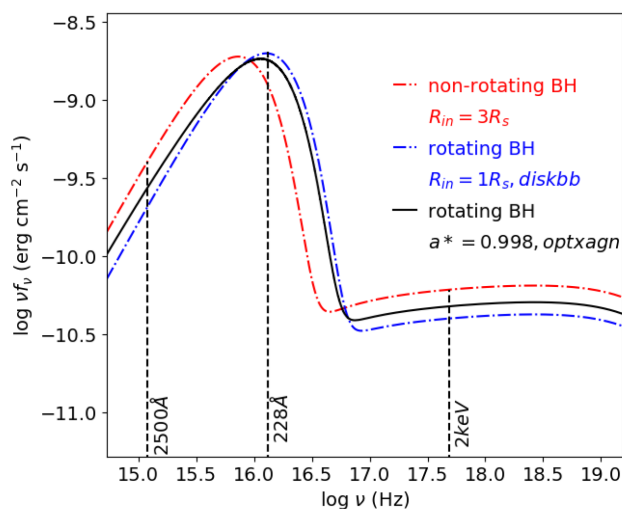


Figure 14. Comparison of SEDs of maximally spinning and non-spinning BH for $M_{\text{BH}} = 10^8 M_{\odot}$. Note that the peak of DISKBB is more energetic and power-law component is less prominent for spinning BHs.

maximum spin. We had noted earlier that for the O VI and C IV lines, the $\mathcal{E}\mathcal{W}$ turns over at the high-mass end, for Schwarzschild BHs with $L_{\text{bol}}/L_{\text{Edd}} \leq 0.1$. However, we do not see such turnover for the spinning BHs. This is not surprising, because, for the same mass, the SED of the spinning BH has the same effect as the SED of BH with a higher accretion rate (see Fig. 6). On the other hand, the $\mathcal{E}\mathcal{W}$ for H α drops much less, for spinning BHs!

Fig. 16 demonstrates that the Baldwin effect, for the C IV line holds fort, for spinning BHs; in fact, higher the spin, better would be the match of the slope of the profile with the value $-2/3$ (-0.66), since the Baldwin effect is $\mathcal{E}\mathcal{W} \sim L_{\nu}^{-2/3}$ (1450 Å). For the non-spinning BH, the slope is -0.53 for the mass range $10^8 - 10^{11} M_{\odot}$ and for the spinning BH, the slope is -0.67 , for the mass range $10^9 - 10^{12}$.

Fig. 17 shows the line ratios for the BELs (top panels) and NELs (bottom panels). There are clearly quantitative differences

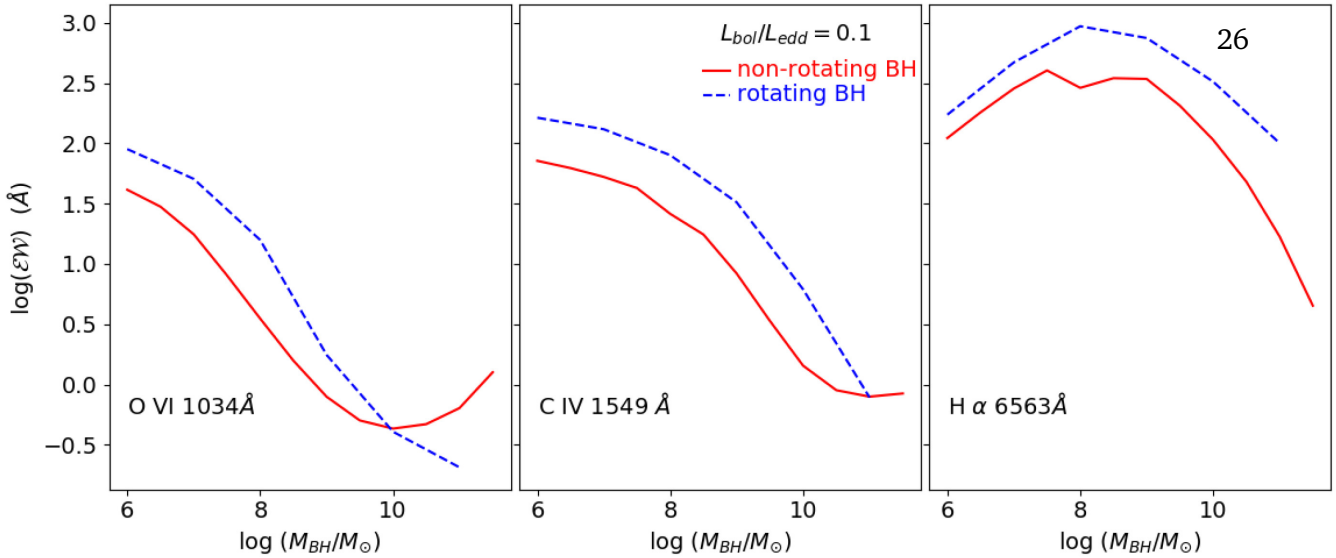


Figure 15. Evolution of some of the $\mathcal{E}\mathcal{W}$ as an extension from Fig. 6. Even though the $\mathcal{E}\mathcal{W}$ of spinning BHs are stronger than the non-spinning BHs, the trend remains.

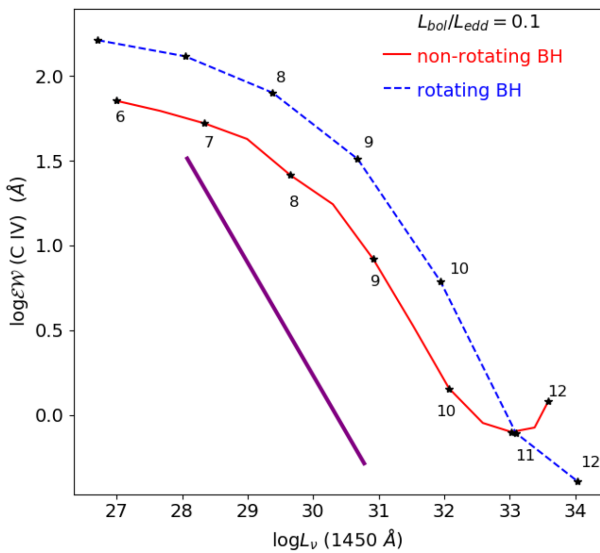


Figure 16. The Baldwin effect demonstrated for the zero spin and highly spinning BH.

in the line ratios, but the overall trend remains the same even for the spinning BHs. Even though higher mass spinning BHs fall into H II region of Kewley plots, it happens only for $M_{\text{BH}} \geq 10^{10} M_{\odot}$ (as opposed to $M_{\text{BH}} \geq 10^9 M_{\odot}$ in the case of non-spinning BHs).

9 EMISSION-LINE STRENGTHS IN LOWER MASS SCHWARZSCHILD BLACK HOLES

We have mainly focused in this paper on the super to hyper massive BHs, with the motivation to see how emission-line strengths evolve as this transition is made. In Chakravorty et al. (2014), on the other hand, the authors had concentrated their efforts on the low-mass BHs. Since, accretion discs of lower mass ($\leq 10^6 M_{\odot}$) peak at EUV, the part of the SED which ionizes the line emitting gas, is entirely dominated by the disc SED. Hence, in Chakravorty et al. (2014) had

ignored the power-law component. Reconstructing a disc plus power-law SED for the low-mass BHs would require involved analysis of observations, and such an exercise is beyond the scope of this paper. However, following the cue of Chakravorty et al. (2014), we can rely on ‘approximate’ SEDs for the lower mass Schwarzschild BHs, where the disc is the only component. After construction of these SEDs, for $L_{\text{bol}}/L_{\text{Edd}} = 0.1$, and $10^2 \leq M_{\text{BH}}/M_{\odot} \leq 10^5$ (at steps of 1.0 dex) we run them through CLOUDY to calculate the emission-line strengths. Following the same methods, on the line emissions, as for the higher mass BHs, we try to build a ‘continuum’ of emission-line properties across the entire mass range $10^2 \leq M_{\text{BH}}/M_{\odot} \leq 10^{12}$. While, the SEDs for the lower masses, may not be accurate, we get a few interesting insights.

Fig. 18 shows that there is a ‘sweet spot’ in BH mass range $10^6 - 10^9 M_{\odot}$, where the strong emission lines like C IV and H α peak and their $\mathcal{E}\mathcal{W}$ drop sharply, on both sides of this mass range! This is a striking result, because this gives us an insight into the resultant selection bias that all emission-line surveys must have in favour of $10^6 - 10^9 M_{\odot}$ BHs. This is in fact where most AGN BH masses are found (e.g. in Shen et al. 2011, and references therein). Given this bias, it could be that the true range of BH masses is much broader than has been supposed. O VI seems to have a constant strength down to masses, as low as $10^4 M_{\odot}$. So, in the search for intermediate-mass BHs, this would be the best emission line to target. O VI is hard to detect, however, as it requires far-UV spectroscopy at low redshifts, as from FUSE (Kriss 2004), while at high redshifts it is almost always absorbed by the Lyman alpha forest.

Fig. 19 shows the line ratios for the entire mass range, for BELs (top panels) and NELs (bottom panels). The BPT diagrams of the ratios of the different NELs is a common tool, now, not only to distinguish AGNs from SFRs but even to distinguish Seyfert-like AGNs from LINER-like AGNs. Note that Chakravorty et al. (2014) had presented some results about how the $\mathcal{E}\mathcal{W}$ of BELs will look like, albeit with much less rigour than has been used in this paper. However, there has been no investigation of the evolution of the BPT diagrams, concentrating on the low-mass end. In Kewley et al. (2006), the authors had introduced a dividing line between Seyferts and LINERS, shown as the dotted red line on the (middle) $\log([\text{O III}]/\text{H } \beta)$ versus $\log([\text{S II}]/\text{H } \alpha)$ and the (right) $\log([\text{O III}]/\text{H } \beta)$

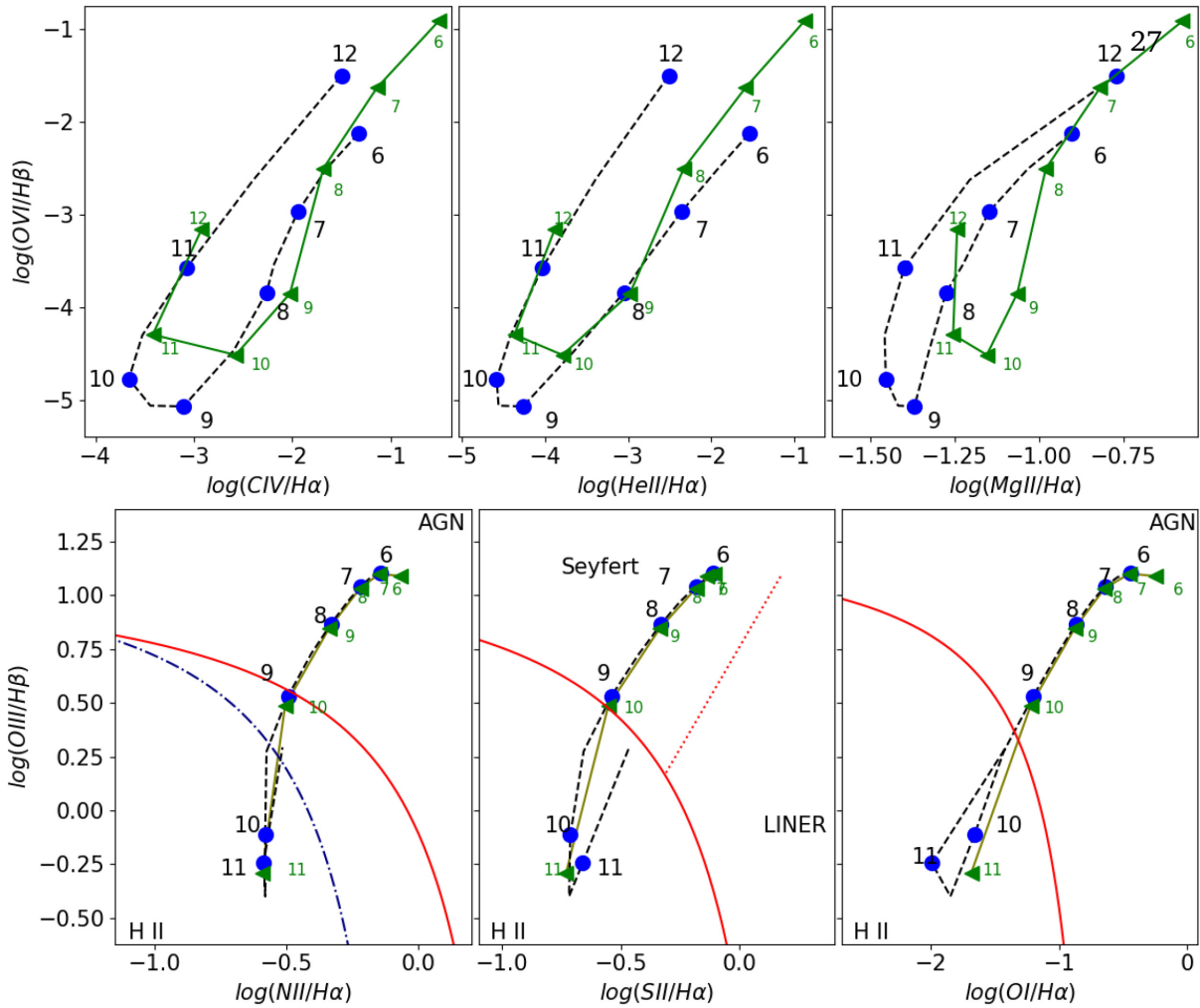


Figure 17. Extending Figs 13 and 12, we compare the BEL (top panels) and NEL (bottom panels) ratios of spinning BHs. Green triangles joined by the solid green line, in the figure, correspond to spinning BHs and are labelled with $\log(M_{\text{BH}}/M_{\odot})$ adjacent to them (smaller green fonts). For comparison, we retain the line ratio profiles for the non-spinning BHs through the black dashed curves joining the blue circles.

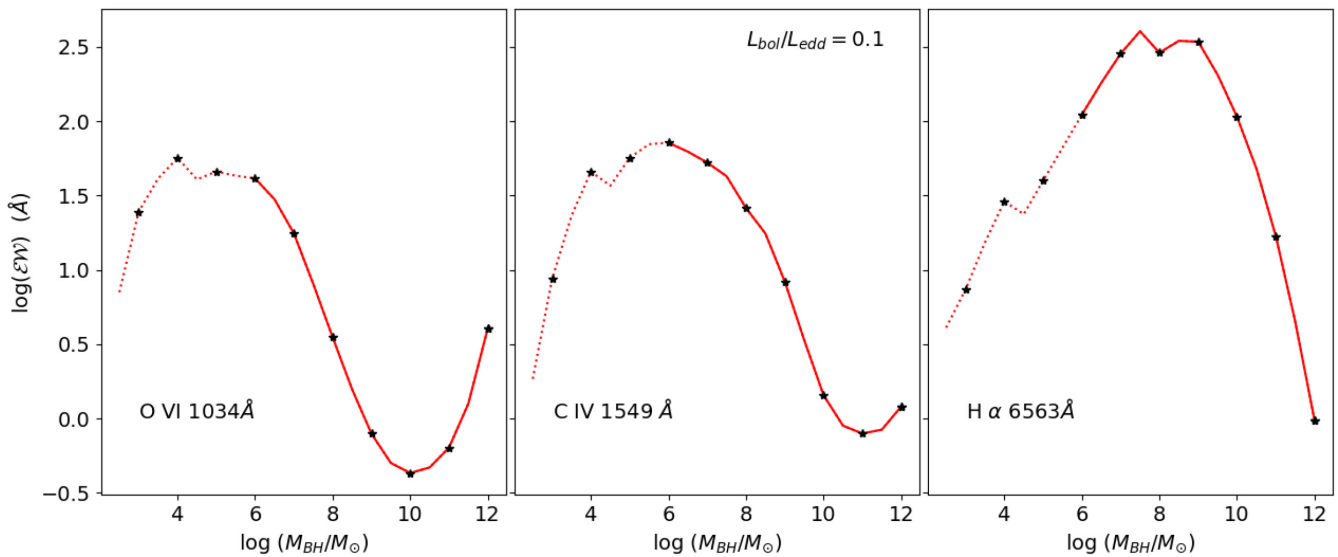


Figure 18. Evolution of some of the $\mathcal{E}\mathcal{W}$ as an extension from Fig. 6. The $\mathcal{E}\mathcal{W}$ for the lower mass BHs (traced by red dotted lines joining the stars) are added to show the variation across the entire BH mass range.

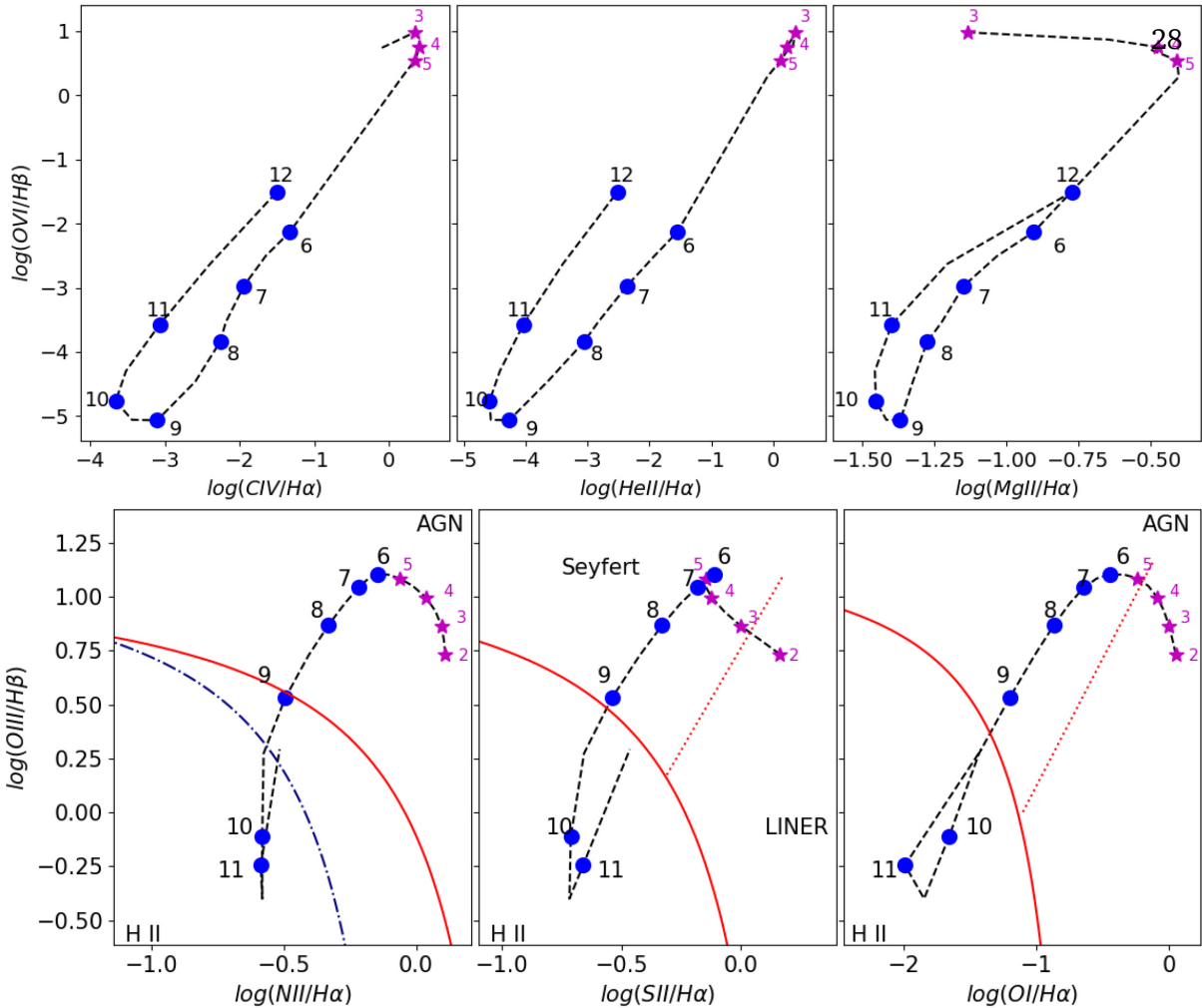


Figure 19. As an extension from Fig. 12, we have calculated the line ratios for lower mass BHs, $10^2 M_{\odot} < M_{\text{BH}} < 10^6 M_{\odot}$ (extended black dashed line, studded with magenta star symbols) at a steps of 1 dex. We have used just the DISKBB component of the SED.

versus $\log([\text{O I}]/\text{H}\alpha)$ line ratio planes. In Fig. 19, bottom panels, while in the middle panel even the low-mass BHs are consistent with Seyfert-like line ratios (except for $\log(M_{\text{BH}}/M_{\odot}) \lesssim 2$), in the right-hand panel, BH with masses lower than $10^{4.5} M_{\odot}$ are consistent with being LINERS.

A more rigorous calculation about the low-mass BH NELs is beyond the scope of this paper, because this paper deals with HMBHs.

10 DISCUSSION

10.1 On truncated discs and radiatively inefficient accretion flows

To model the radiation from the accretion disc, we have used the ‘thin disc paradigm’ and used the Shakura–Sunyaev model (Shakura & Sunyaev 1973; Frank et al. 2002) where $L \sim \dot{m}$, however, when the accretion rate decreases below $\dot{m} < 0.01$, $L \sim \dot{m}^2$. The accretion flow close to the BH becomes very different, the disc becomes optically thin and geometrically thick and radiatively inefficient. We are pursuing the calculations for such radiatively inefficient accretion flow (RIAF) in a separate analysis. In such cases, there are often signatures that the innermost parts of the accretion disc are truncated, where the radiatively inefficient flow dominates, and

there is an outer thin disc. SEDs, corresponding to such scenarios are different flavours of the may be similar to the RIAF SEDs. We will address such SEDs, also, in the RIAF paper. Since these SEDs are predicted to be ‘dim’ in UV and optical but bright in X-rays, in addition to looking at the emission-line properties, we will also look into the properties of the X-ray warm absorbers for SMBH harbouring RIAFs.

10.2 On the 150 eV soft excess component of AGN SEDs

X-ray observations from *ROSAT* and *XMM-Newton* show the presence of unaccounted excess intensity at $E < 1$ keV known as the *soft excess* component, in the observed spectra of type1 AGNs. (Elvis, Wilkes & Tananbaum 1985; Brinkmann 1992; Buehler et al. 1995; Pounds & Reeves 2002). This component is usually by a blackbody with temperature $T_{\text{se}} \sim 100 - 200$ eV (i.e. peaking at $\sim 282 - 564$ eV) (Matsumoto, Leighly & Marshall 2004; Porquet et al. 2004; Vignali et al. 2004; Piconcelli et al. 2005; , and references therein). The ratio of the *soft excess* luminosity to power-law luminosity (between 0.1 and 10 keV) is independent for each object, for e.g. it is 0.04 in Mkn 304 (Piconcelli et al. 2005) and $\gtrsim 1.0$ in Ark 564 (Vignali et al. 2004). The DISKBB model, though represents UV SED of the observed AGN spectra satisfactorily,

cannot model the *soft excess* component because centres of SMBHs are too cold to reach the peak temperature at ~ 0.5 keV. *Soft excess* component can be explained only by making modifications to the DISKBB model (Czerny & Elvis 1987; Korista, Ferland & Baldwin 1997) or by introducing an additional spectral component.

In this paper, we have ignored the *soft excess* as a component of the AGN SED. Because the physical origin of the *soft excess* component is not certain, hence it is not easy to relate it, in a systematic way, to either the accretion disc component or the power law. There is no empirical relation that will guide us to find the evolution of the *soft excess* component as a function of the BH mass. The task of finding the correct prescription to relate these components is beyond the scope of this paper. In our future attempts at deriving more physically motivated SED, we can use (for example) OPTXAGN to generate the *soft excess* as a function of the disc component (which will have a dependence on the mass of the BH).

The *soft excess* component could be further ignored, for this paper, because of the energy range where it dominates. As mentioned above, *soft excess* peaks at $\sim 282 - 564$ eV. The ions emitting the BELs and NELs, discussed in this paper, are unlikely to be influenced by photons with such high energies – for example, the IP of O V is ~ 114 eV and the central wavelengths of all the lines are in the UV range. So, for the purpose of this paper, the *soft excess* would have been a redundant component.

11 CONCLUSIONS

(i) The motivation of this paper was to test, for Schwarzschild BHs, (i) if there is a higher mass cut-off above which BHs cannot efficiently produce typical BELs such as O VI 1034 Å, C IV 1549 Å, He II 1640 Å, Mg II 2798 Å, H β 4861 Å, and H α 6563 Å used to detect AGNs, (ii) how would ratios of the NELs evolve for the HMBH ($\gtrsim 10^9 M_\odot$), in the standard BPT diagrams involving H β 4861 Å, [O III] 5007 Å, [O I] 6300 Å, H α 6563 Å, [N II] 6584 Å, and [S II] 6720 Å.

(ii) We wanted to probe the HMBHs with mass $\geq 10^8 M_\odot$. The first step in the analysis was to build a method of producing systematic mass-dependent AGN SEDs for the range $10^6 - 10^{12} M_\odot$. For HMBHs, the peak of the disc component moves to lower energies and hence the important conventional wavelength of 2500 Å sees a different part of the disc radiation in case of the most massive HMBHs. We used the latest empirical results known, for the SMBHs and used judicious extrapolations to form a suite of SEDs for all BHs in the aforementioned mass range.

(iii) These suites of SEDs were used in CLOUDY to calculate emission-line strength for gas clouds with a wide range of densities and placed over a wide range of distance from the BH. This exercise was done for both the (popularly known) BEL and NELs. The CLOUDY calculated EWs of the individual clouds were then suitably added and averaged using the ‘LOC’ model to predict the final effective EW \mathcal{EW} and luminosity of the emission lines. These emission-line strengths and their ratios were then used to predict observables for the HMBHs.

(iv) We found that the optical BELs, like H β 4861 Å and H α 6563 Å are not the best tracers to look for HMBHs because these lines’ \mathcal{EW} drop by about a factor of ~ 100 as mass increases from 10^8 to $10^{10} M_\odot$. This is a very important point to note because large optical surveys like SDSS use these optical broad lines to look for AGN activity. If we want to look for HMBHs, the UV line O VI 1034 Å would be the most useful because its strength undergoes a significant and interesting turnover, from their drop, in intensity, for the highest mass BHs.

(v) The Baldwin effect is clearly reproduced by the changing SEDs in our calculations. C IV \mathcal{EW} scales as $\sim L_\nu^{-2.9}$ (1450 Å) for the super to hypermassive BHs ($\sim 10^8 - 10^{10} M_\odot$). It approximately holds for accretion rate, as low as 0.03, but the relationship matches better for higher accretion rate (or higher spin of the BH), and also spans a larger mass range (up to $\sim 10^{11} M_\odot$).

(vi) Studying the BPT diagrams for the NELs, reveals that BHs with the highest mass with/or low accretion rate may have line ratios consistent with SFRs, thus making it very difficult to find them in this way. This, further, implies that the number of actively SFRs are being overestimated in large survey samples like SDSS and the number of massive BHs are being underestimated. This effect adds to the above-mentioned bias against HMBHs in broad-line detection. Such a realization should have a profound effect on the luminosity functions of both these classes of objects, namely AGNs and normal (but actively star-forming) galaxies.

(vii) Following the principles of BPT diagrams, we have proposed line ratio diagrams for the BELs, too. The $\log(\mathcal{EW})$ profile is often degenerate in mass, which can be broken, by using the line ratio plots for BELs. Note that above-mentioned degeneracy is pronounced and noticeable because we are dealing with a much wider mass range here.

(viii) After considering mass and accretion rates as two main BH parameters which alter the SED of the accretion disc, we also paid attention to the spin of the BH. Since maximally spinning BHs will have the most different SEDs, compared to Schwarzschild ones, we compared these two, for the super to hyper massive BH mass range, while holding the accretion rate constant at 0.1. The effect of the spin turned out to be similar to the effect of the accretion rate, for the BH of same mass. Both of these parameters tend to increase the peak energy E_{\max} where the SED has a maxima. The drastic fall off of the line \mathcal{EW} with increasing mass cannot be arrested, for even the spinning BHs, they also satisfy the Baldwin effect. The spinning HMBHs also plunge into the SFR region of the BPT diagram, only for relatively higher masses. Only, if we have a maximally spinning high accretion rate (~ 1.0), HMBHs, then they may be populating the AGN region of the BPT diagrams.

(ix) We have further, investigated the change of \mathcal{EW} for lower masses ($\leq 10^6 M_\odot$). We find that the strong observable emission lines like the C IV and H α favour a mass range $10^6 - 10^9 M_\odot$ and drop off sharply, in EW, on both sides of this mass range! This is a striking result, because this gives us an insight into the resultant selection bias that all emission line surveys must have in favour of $10^6 - 10^9 M_\odot$ BHs. This is in fact where most AGN BH masses are found. Given this bias, it could be that the true range of BH masses is much broader than has been supposed. O VI is the best emission line to look for intermediate-mass BHs as it maintains a constant \mathcal{EW} down to $10^4 M_\odot$. The BPT diagrams for lower masses show that for some line ratios, they tend to behave like LINERS.

(x) Our results show that weak emission lines from HMBHs would be very difficult to detect using the current optical facilities. However, these same results establish a benchmark which can be used by future 30 m class optical telescopes to look for HMBHs.

ACKNOWLEDGEMENTS

We thank the anonymous reviewer for useful comments and suggestions that helped us improve the quality of this manuscript significantly. HB acknowledges support from IISc, where a major fraction of this work was done during her project. SC was supported by the SERB National Postdoctoral Fellowship (File No.

PDF/2017/000841). NR acknowledges support from the Infosys Foundation through the Infosys Young Investigator grant.

DATA AVAILABILITY

There are no new data associated with this article.

REFERENCES

- Arnaud K. A., 1996, in Jacoby G. H., Barnes J., eds, ASP Conf. Ser. Vol. 101, Astronomical Data Analysis Software and Systems V. Astron. Soc. Pac., San Francisco, p. 17
- Baldwin J. A., 1977, *ApJ*, 214, 679
- Baldwin J. A., 1997, in Peterson B. M., Cheng F.-Z., Wilson A. S., eds, ASP Conf. Ser. 113, IAU Coll. 159: Emission Lines in Active Galaxies: New Methods and Techniques. Astron. Soc. Pac., San Francisco, p. 80
- Baldwin J. A., Phillips M. M., Terlevich R., 1981, *PASP*, 93, 5
- Baldwin J., Ferland G., Korista K., Verner D., 1995, *ApJ*, 455, L119
- Baskin A., Laor A., 2005, *MNRAS*, 358, 1043
- Beloborodov A. M., 1999, in Poutanen J., Svensson R., eds, ASP Conf. Ser. Vol. 161, High Energy Processes in Accreting Black Holes. Astron. Soc. Pac., San Francisco, p. 295
- Bertemes C., Trakhtenbrot B., Schawinski K., Done C., Elvis M., 2016, *MNRAS*, 463, 4041
- Brightman M. et al., 2013, *MNRAS*, 433, 2485
- Brinkmann W., 1992, in Brinkmann W., Truemper J., eds, X-ray Emission from Active Galactic Nuclei and the Cosmic X-ray Background. Proc. Max-Planck-Institut für Extraterrestrische Physik Conf., Garching, MPE report 235, p. 143
- Buehler P., Courvoisier T. J. L., Staubert R., Brunner H., Lamer G., 1995, *A&A*, 295, 309
- Chakravorty S., Elvis M., Ferland G., 2014, *MNRAS*, 437, 740
- Coppi P. S., 1992, *MNRAS*, 258, 657
- Coppi P. S., 1999, in Poutanen J., Svensson R., eds, ASP Conf. Ser. Vol. 161, High Energy Processes in Accreting Black Holes. Astron. Soc. Pac., San Francisco, p. 375
- Czerny B., Elvis M., 1987, *ApJ*, 321, 305
- Done C., Davis S. W., Jin C., Blaes O., Ward M., 2012, *MNRAS*, 420, 1848
- Elvis M., Wilkes B. J., Tananbaum H., 1985, *ApJ*, 292, 357
- Fan X. et al., 2001, *AJ*, 122, 2833
- Ferguson J. W., Korista K. T., Baldwin J. A., Ferland G. J., 1997, *ApJ*, 487, 122
- Ferland G. J. et al., 2017, *Rev. Mex. Astron. Astrofis.*, 53, 385
- Frank J., King A., Raine D. J., 2002, *Accretion Power in Astrophysics*, 3rd edn. Cambridge Univ. Press, Cambridge
- Gierlinski M., Zdziarski A. A., Poutanen J., Coppi P. S., Ebisawa K., Johnson W. N., 1999, *MNRAS*, 309, 496
- Haardt F., Maraschi L., 1993, *ApJ*, 413, 507
- Hamann F., Korista K. T., Ferland G. J., Warner C., Baldwin J., 2002, *ApJ*, 564, 592
- Ichikawa K., Inayoshi K., 2017, *ApJ*, 840, L9
- Johnson J. L., Whalen D. J., Fryer C. L., Li H., 2012, *ApJ*, 750, 66
- Kauffmann G. et al., 2003, *MNRAS*, 346, 1055
- Kewley L. J., Dopita M. A., Sutherland R. S., Heisler C. A., Trevena J., 2001, *ApJ*, 556, 121
- Kewley L. J., Groves B., Kauffmann G., Heckman T., 2006, *MNRAS*, 372, 961
- King A., 2015, in Gandhi P., Hoening S. F., eds, Proc. TORUS2015 :The AGN Unification Scheme After 30 Years. University of Southampton, Winchester
- Korista K., Baldwin J., Ferland G., Verner D., 1997a, *ApJ*, 108, 401
- Korista K., Ferland G., Baldwin J., 1997b, *ApJ*, 487, 555
- Kriss G. A., 2004, preprint ([astro-ph/0411380](https://arxiv.org/abs/astro-ph/0411380))
- Kwan J., Krolik J. H., 1981, *ApJ*, 250, 478
- Laor A., Davis S. W., 2011, *MNRAS*, 417, 681
- Latif M. A., Ferrara A., 2016, *Publ. Astron. Soc. Aust.*, 33, 51
- Leighly K., Casebeer D., 2007, in Ho L., Wang J.-M., eds, ASP Conf. Ser. 373, The Central Engine of Active Galactic Nuclei. Astron. Soc. Pac., San Francisco, p. 365
- Lightman A. P., Zdziarski A. A., 1987, *ApJ*, 319, 643
- Lu Y., Yu Q., 1999, *ApJ*, 526, L5
- Lusso E., Risaliti G., 2016, 819, 154
- Makishima K., Maejima Y., Mitsuda K., Bradt H. V., Remillard R. A., Tuohy I. R., Hoshi R., Nakagawa M., 1986, *ApJ*, 308, 635
- Matsumoto C., Leighly K. M., Marshall H. L., 2004, *ApJ*, 603, 456
- Mitsuda K. et al., 1984, *PASJ*, 36, 741
- Mortlock D. J., 2011, *Nature*, 474, 616
- Natarajan P., 2014, *Gen. Relativ. Gravit.*, 46, 1702
- Natarajan P., Treister E., 2009, *MNRAS*, 393, 838
- Netzer H., 2015, *ARA&A*, 53, 365
- Netzer H., Laor A., Gondhalekar P. M., 1992, *MNRAS*, 254, 15
- Osterbrock D. E., Ferland G. J., eds, 2006, *Astrophysics of Gaseous Nebulae and Active Galactic Nuclei*, 2nd edn. University Science Books, Sausalito, CA
- Peterson B. M., 1997, *An Introduction to Active Galactic Nuclei*. Cambridge Univ. Press, Cambridge
- Piconcelli E., Guainazzi M., Cappi M., Jimenez-Bailon E., Schartel N., 2005, *A&A*, 432, 835
- Porquet D., Reeves J. N., O'Brien P., Brinkmann W., 2004, *A&A*, 422, 85
- Pounds K., Reeves J., 2002, preprint ([astro-ph/0201436](https://arxiv.org/abs/astro-ph/0201436))
- Reynolds C. S., 2014, *Space Sci. Rev.*, 183, 277
- Reynolds C. S., 2019, *Nat. Astron.*, 3, 41
- Risaliti G., Salvati M., Marconi A., 2011, *MNRAS*, 411, 2223
- Shakura N. I., Sunyaev R. A., 1973, *A&A*, 24, 337
- Shemmer O., Lieber S., 2015, *ApJ*, 805, 124
- Shemmer O., Brandt W. N., Netzer H., Maiolino R., Kaspi S., 2006, *ApJ*, 646, L29
- Shen Y., 2011, *ApJS*, 194, 45
- Tananbaum H. et al., 1979, *ApJ*, 234, L9
- Trakhtenbrot B. et al., 2017, *MNRAS*, 470, 800
- Vignali C., Brandt W. N., Boller Th., Fabian A. C., Vaughan S., 2004, *MNRAS*, 347, 854
- Volonteri M., 2012, *Science*, 337, 544
- Wang J.-M., Watarai K.-Y., Mineshige S., 2004, *ApJ*, 607, L107
- Wu X.-B. et al., 2015, *Nature*, 518, 512
- Zdziarski A. A., Johnson W. N., Magdziarz P., 1996, *MNRAS*, 283, 193
- Zheng W., Malkan M. A., 1993, *ApJ*, 415, 517
- Zimmerman E. R., Naraya R., McClintock J. E., Miller J. M., 2005, *ApJ*, 618, 832
- Życki P. T., Done C., Smith D. A., 1999, *MNRAS*, 309, 561

APPENDIX A: ADDING DISC AND POWER LAW WITHOUT EXTRAPOLATION RELATION FOR HMBHS

In Section 2.3, we have described that to build our SEDs, we use a method of extrapolation to scale the $L_{\text{pl}}/L_{\text{disc}}$ for HMBH, while using equation (8) for the SMBHs. This is the method, which has been used throughout the paper and we call this method as ‘extrapolated ratio’ in this section. One might argue that equation (8) does not distinguish between SMBHs and HMBHs and so this equation should be used directly, even for the HMBHs and should not be extrapolated. However, these extrapolations, which become important only for the HMBHs, are based on the physics of accretion discs. However, in this section, we show that if we directly used equation (8) for the highest masses, to scale the power law with respect to the disc, and add the two components, the differences in the results would be minor, and effectively has no difference in the qualitative inferences. We call this second method of creating the SED (relevant in the context of the HMBHs, only) as ‘Lusso ratio’, in this section.

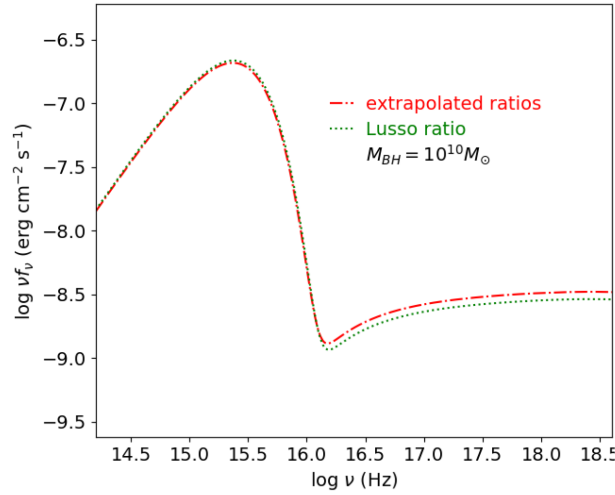


Figure A1. Comparison of SED (called ‘Lusso ratio’) constructed using ‘just’ equation (5) (Lusso & Risaliti 2016) versus SED (called ‘extrapolated ratio’) using our more rigorous method using Fig. 2 and equation (6), for black hole of mass $10^{10} M_{\odot}$ and $L_{\text{bol}}/L_{\text{Edd}} = 0.1$.

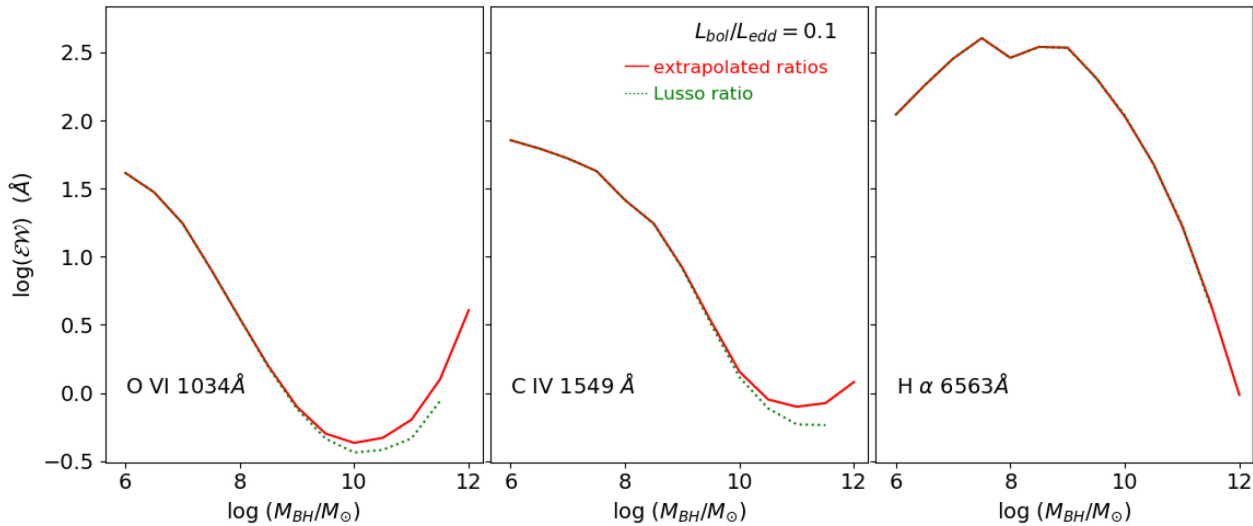


Figure A2. Comparison of some of the $\mathcal{E}\mathcal{W}$ as an extension from Fig. 6. The SED generation schemes are marked in the Figure.

(i) In Fig. A1, we show the SEDs of BHs of same mass $10^{10} M_{\odot}$ and $L_{\text{bol}}/L_{\text{Edd}} = 0.1$, but different schemes of SED generation, as labelled. We demonstrate that the variation in SED is minor. Such SEDs were generated for $L_{\text{bol}}/L_{\text{Edd}} = 0.1$, but only for BHs whose SEDs were generated using ‘extrapolated ratio’ method, namely the mass range $>10^{8.25} M_{\odot}$. Note that BHs

with lower mass, the ‘Lusso ratio’ method was anyway, used. So whatever differences arise because of the variation of scheme of SED creation, will affect the results for only the higher mass BHs.

(ii) Referring to Figs A2 and A3 we see that there is absolutely no qualitative difference to the results.

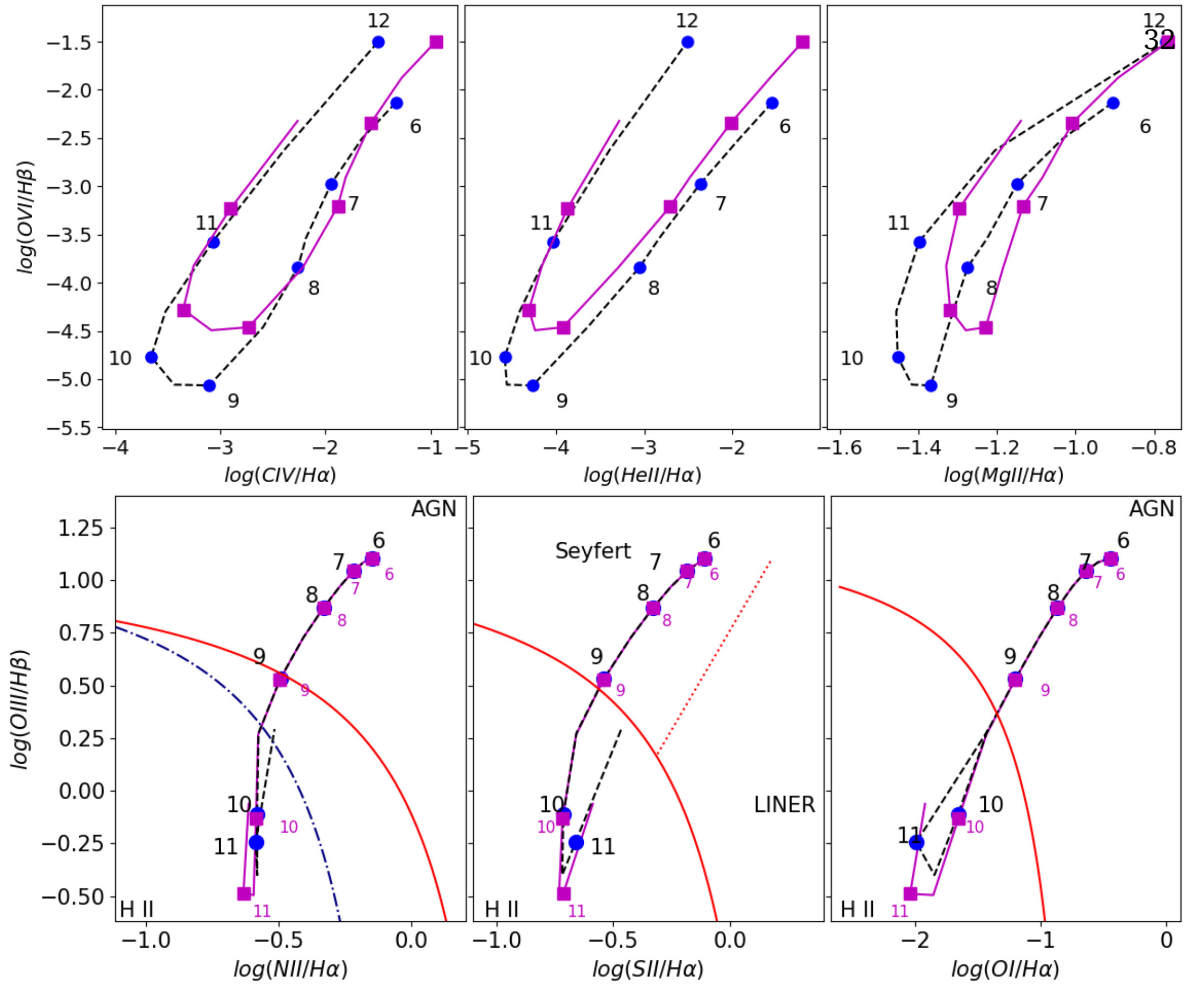


Figure A3. As an extension from Figs 12 and 13, we have calculated the line ratios for BELs (top panels) and NELs (bottom panels), to show the comparison of effects of SEDs, in Fig. A1, but for all the higher masses, for $L_{\text{bol}}/L_{\text{Edd}} = 0.1$. The solid magenta curves represent the results of the ‘Lusso ratio’ method.

This paper has been typeset from a $\text{\TeX}/\text{\LaTeX}$ file prepared by the author.

Paper II - Mid-Infrared observations of Galactic Centre

The GC is an exciting region to study star formation as the environmental factors there are quite extreme. High-angular resolution observations close to the SMBH (Sgr A*) at the GC have shown the presence of a ring (~1.5-7 pc) of clumpy molecular gas and warm dust called CND. A system of three ionized clumpy streamers called mini-spiral extends from the inner edge of CND up to a few arcseconds from the Sgr A*. There are several pieces of observational evidence for outflows in this region e.g. mini-cavity, several bow-shock sources, etc and this lets only a small fraction of the available material reach and accrete onto the SMBH. The dynamics, as well as the physical properties of gaseous-dusty structures within the sphere of the gravitational influence of Sgr A*, are crucial for the understanding of the mass and the momentum transport from larger to smaller scales ultimately leading to Sgr A*.

In this work, we have looked into the physical processes in this turbulent region of GC. We present the proper motions of the largest consistent set of resolved and reliably determined dusty sources. In addition to stellar orbital motions, we identify a stream-like motion of extended clumps along the mini-spiral. We also delve into the structures and origins of the dusty sources.

The results are reported in the following peer-reviewed article published in *The Astrophysical Journal*.

Credit: H. K. Bhat, N. B. Sabha, M Zajacek et. al., ApJ 929, 178 (2022).
Reproduced with the permission of ©American Astronomical Society.

Mid-infrared Studies of Dusty Sources in the Galactic Center

Harshitha K. Bhat^{1,2} , Nadeen B. Sabha^{1,3} , Michal Zajaček^{1,4} , Andreas Eckart^{1,2} , Rainer Schödel⁵ ,
S. Elahé Hosseini^{1,2} , Florian Peißker¹ , and Anton Zensus² 

¹ I. Physikalisches Institut der Universität zu Köln, Zùlpicher Str. 77, D-50937 Köln, Germany

² Max-Planck-Institut für Radioastronomie (MPIfR), Auf dem Hügel 69, D-53121 Bonn, Germany

³ Institut für Astro- und Teilchenphysik, Universität Innsbruck, Technikerstrasse 25/8, A-6929 Innsbruck, Austria

⁴ Department of Theoretical Physics and Astrophysics, Faculty of Science, Masaryk University, Kotlářská 2, 611 37 Brno, Czech Republic

⁵ Instituto de Astrofísica de Andalucía (CSIC), Glorieta de la Astronomía s/n, E-18008 Granada, Spain

Received 2021 November 29; revised 2022 March 21; accepted 2022 March 23; published 2022 April 27

Abstract

Mid-infrared (MIR) images of the Galactic center show extended gas and dust features along with bright infrared sources (IRS). Some of these dust features are a part of ionized clumpy streamers orbiting Sgr A*, known as the mini-spiral. We present their proper motions over a 12 yr time period and report their flux densities in *N*-band filters and derive their spectral indices. The observations were carried out by VISIR at the ESO's Very Large Telescope. High-pass filtering led to the detection of several resolved filaments and clumps along the mini-spiral. Each source was fit by a 2D Gaussian profile to determine the offsets and aperture sizes. We perform aperture photometry to extract fluxes in two different bands. We present the proper motions of the largest consistent set of resolved and reliably determined sources. In addition to stellar orbital motions, we identify a stream-like motion of extended clumps along the mini-spiral. We also detect MIR counterparts of the radio tail components of the IRS 7 source. They show a clear kinematical deviation with respect to the star. They likely represent Kelvin–Helmholtz instabilities formed downstream in the shocked stellar wind. We also analyze the shape and orientation of the extended late-type IRS 3 star that is consistent with the Atacama Large Millimeter/submillimeter Array submillimeter detection of the source. Its puffed-up envelope with a radius of $\sim 2 \times 10^6 R_{\odot}$ could be the result of the red-giant collision with a nuclear jet, which was followed by tidal prolongation along the orbit.

Unified Astronomy Thesaurus concepts: Galactic center (565); Infrared photometry (792); Galaxy kinematics (602)

1. Introduction

High-angular-resolution observations of the vicinity of the compact radio source Sgr A* in the Galactic center (GC), which is associated with the supermassive black hole (SMBH; Eckart et al. 2002; Genzel et al. 2010; Falcke & Markoff 2013; Eckart et al. 2017), showed the presence of a ring of dense clumpy molecular and neutral gas and warm dust, called the circumnuclear disk (CND), extending from ~ 1.5 to ~ 7 pc (Vollmer et al. 2004; Christopher et al. 2005; Mills et al. 2013; Hsieh et al. 2021). The CND surrounds an ionized central cavity which has a much lower mean gas density within ~ 1 – 1.5 pc radius with a total mass of $\sim 60 M_{\odot}$ (Lo & Claussen 1983; Blank et al. 2016). At the Bondi radius, $r_B \sim 0.14(k_B T/1.3 \text{ keV})^{-1}$ pc, the mean electron number density is $n_e = 26 f_V^{-1/2} \text{ cm}^{-3}$ (Baganoff et al. 2003), where f_V is the filling factor of 1.3 keV plasma, while the CND density reaches $\sim 10^6$ – 10^8 cm^{-3} in molecular cores (Jackson et al. 1993; Shukla et al. 2004; Christopher et al. 2005). Mossoux & Eckart (2018) found a depression in the X-ray surface brightness at the position of the CND, which could be attributed to the CND acting as a barrier for the hot and diluted plasma in the central cavity. A system of orbiting ionized clumpy streamers and gas filaments extending inwards from the inner edge of the CND is denoted as the mini-spiral (Lo & Claussen 1983; Nitschai et al. 2020, and references therein). The western arc of the mini-spiral appears to have a circular orbit similar to the neutral gas in the CND. However, the northern and

the eastern arms penetrate deep into the ionized cavity on eccentric orbits and reach up to a few arcseconds from Sgr A*, possibly colliding in the Bar region (Becklin et al. 1982; Jackson et al. 1993; Christopher et al. 2005; Zhao et al. 2009).

There have been several studies on the kinematics of the mini-spiral. Vollmer & Duschl (2000) derived a 3D kinematic model of gas streams that describes the bulk motion of the mini-spiral in three different planes based on a data cube of the [Ne II] line ($12.8 \mu\text{m}$), with the main plane coinciding with the inner rim of the CND. Paumard et al. (2006) performed a kinematic study and showed that the northern arm consists of a weak continuous surface that is drawn into a narrow stream near Sgr A*. Using *L'*-band data ($3.8 \mu\text{m}$), Mužić et al. (2007) provided proper motions of a number of thin dusty filaments along the mini-spiral and considered a central, partially collimated outflow as the possible explanation for their formation and motion along the mini-spiral, with some deviations from a purely Keplerian rotation. Based on radio observations using the H92 α and H30 α lines, Zhao et al. (2009) and Zhao et al. (2010) determined the 3D velocity field of the mini-spiral. The ionized streamers can dynamically be modeled as a system of three bundles of quasi-Keplerian orbits in the potential dominated by the central mass of $\lesssim 10^7 M_{\odot}$, i.e., dominated by Sgr A* (Zhao et al. 2009, 2010). The orbital planes of the northern arm and the western arc are nearly coplanar, while the eastern arm plane is perpendicular to them.

In the central parsec, there is a nuclear stellar cluster (NSC) that consists predominantly of the nearly spherical old cluster of late-type stars as well as the cusp of ~ 100 massive young OB/Wolf–Rayet (WR) stars that supply about $3 \times 10^{-3} M_{\odot} \text{ yr}^{-1}$ in the form of stellar winds (Najarro et al. 1997; Moultaqa et al. 2004;

Schödel et al. 2014). However, less than 1% of the Bondi accretion rate is accreted by Sgr A* (Bower et al. 2003; Marrone et al. 2006; Wang et al. 2013). Blandford & Begelman (1999) proposed a solution for the low accretion rate with the adiabatic inflow-outflow model, in which most of the gas that is accreted has positive energy and is lost through winds and only a small fraction is accreted onto the SMBH. Observational evidence for the outflow first emerged with the detection of the “mini-cavity” region on radio maps by Yusef-Zadeh et al. (1990). The detection of a strong [Fe III] bubble surrounding Sgr A* (Eckart et al. 1992; Lutz et al. 1993) has led to the conclusion that the fast wind originating within the central few arcseconds blows into the orbiting streamers creating an expanding gas bubble. This has also been supported by Peißker et al. (2020b), who found that some identified dusty sources located to the west within the S cluster exhibit Doppler-shifted [Fe III] multiplet lines that could be excited by the collimated wind outflowing in their direction toward the mini-cavity. The extended region of low excitation centered on Sgr A* (Schödel et al. 2007) and the mass-losing envelope, along with the extended tail of IRS 7 (Yusef-Zadeh & Melia 1992), could also be influenced by a strong central wind coming from the central few arcseconds. Closer to Sgr A*, the orientation of infrared-excess, comet-shaped sources X7, X3, and X8 suggests the presence of a fast, collimated outflow that originates in the Sgr A* accretion flow or in the collective wind of OB/WR stars (Mužić et al. 2010; Peißker et al. 2019; Yusef-Zadeh et al. 2020; Peißker et al. 2021). The nuclear outflow that nearly balances the inflow is also consistent with the flat number density profile of hot plasma, $n_e \propto r^{-0.5}$, inside the Bondi radius, as inferred from the analysis of the X-ray bremsstrahlung surface-density profile (Wang et al. 2013). In a broader context, the past active jet of Sgr A* could have contributed to the depletion of bright red giants in the GC due to the intense stripping and truncation of their extended envelopes (Zajaček et al. 2020a, 2020b; Karas et al. 2021).

To fully understand the dynamics of these processes, it becomes important to get proper motions or tangential velocities of the various parts of the CNB as well as the mini-spiral. The dynamics as well as the physical properties of gaseous-dusty structures within the sphere of the gravitational influence of Sgr A* are crucial for the understanding of the mass and the momentum transport from larger to smaller scales all the way to Sgr A*.

In this work, we analyze mid-infrared (MIR) images of the central parsec at two wavelengths in the *N* band, the 8.59 μm (PAH1 filter) and the 13.04 μm (Ne II_2 filter), over the course of 12 yr. This allows us to study the proper motions of infrared-excess sources of the NSC as well as of identified extended objects in the mini-spiral region. The photometric information at two wavelengths enables us to infer the spectral indices that in turn shed light on the properties of the identified sources. We manage to identify MIR components associated with the circumstellar material of two late-type stars, IRS 7 and IRS 3, which manifest their interaction with the circumnuclear medium.

The paper is structured as follows. In Section 2, we describe the data set used and the imaging tools that were applied. Subsequently, in Section 3, we describe the main results of the analysis, including the MIR differential map, tangential velocities, and the photometry, including spectral indices. In particular, we focus on the identification of the MIR components of IRS 7, the extended circumstellar structure of

Table 1
Details of the Observed VISIR Images at Each Epoch

Year	Pixel Scale	FOV of a Single Image
2006	0".075	19".2 \times 19".2
2007	0".075	19".2 \times 19".2
2010	0".127	32".5 \times 32".5
2016	0".045	38".0 \times 38".0
2018	0".045	38".0 \times 38".0

IRS 3, and the general characteristics of the identified dusty sources. We discuss the results in Section 4, and subsequently conclude with Section 5.

2. Data and Observations

2.1. VISIR

Observations were carried out at the ESO’s Very Large Telescope (VLT, UT3) using the VLT Imager and Spectrometer for the mid-InfraRed (VISIR) at five different epochs covering a total time from 2006 to 2018 in the *N*-band PAH1 (8.59 μm) and Ne II_2 (13.04 μm). Depending on the atmospheric conditions, VISIR provides 0".25–0".4 angular resolution imaging with high sensitivity. The data used here were obtained as a part of a larger survey (N. B. Sabha et al. 2022, in preparation). The field of view (FOV) and spatial pixel size at each epoch is listed in Table 1. To increase the signal-to-noise ratio (S/N), jittered images with different offsets were added to create a mosaic with a slightly larger FOV. To reduce the bright and varying MIR background, differential observations with the chop/nod mode were executed.

2.2. High-pass Filter

MIR images generally show dusty structures, dust-embedded sources, stellar sources, and even emission from the mini-spiral. Overlapping wings of point-spread functions (PSFs) can create artificial sources and together with noise can complicate the identification of extended objects of interest, especially in a crowded FOV as in the central few arcseconds of the GC. In order to obtain high-angular-resolution information and to highlight the structures of the extended sources, we produce high-pass filter maps. High-pass filters can be used as a sharpener and to resolve the objects that are close to the detection limit while preserving the shape of the extended objects. This filtering technique and its significance are described in detail in Mužić et al. (2007); see also Peißker et al. (2020a, 2021).

First, the Gaussian-smoothed (3–9 pixel Gaussian, corresponding to 0".375–0".405) version of the input image is subtracted from itself. After removing the negatives, the resulted image is smoothed again using a Gaussian whose size is adjusted depending on the required angular resolution and sensitivity. In Figure 1, we show the effectiveness of this technique for isolating the signals and thereby reducing the chance of confusion between nearby objects.

3. Results

3.1. Differential Map

To get a general idea of the direction of the bulk motion, we produce a differential map using the smooth-subtracted images from the 2006 and 2018 epochs. As illustrated in Figure 2,

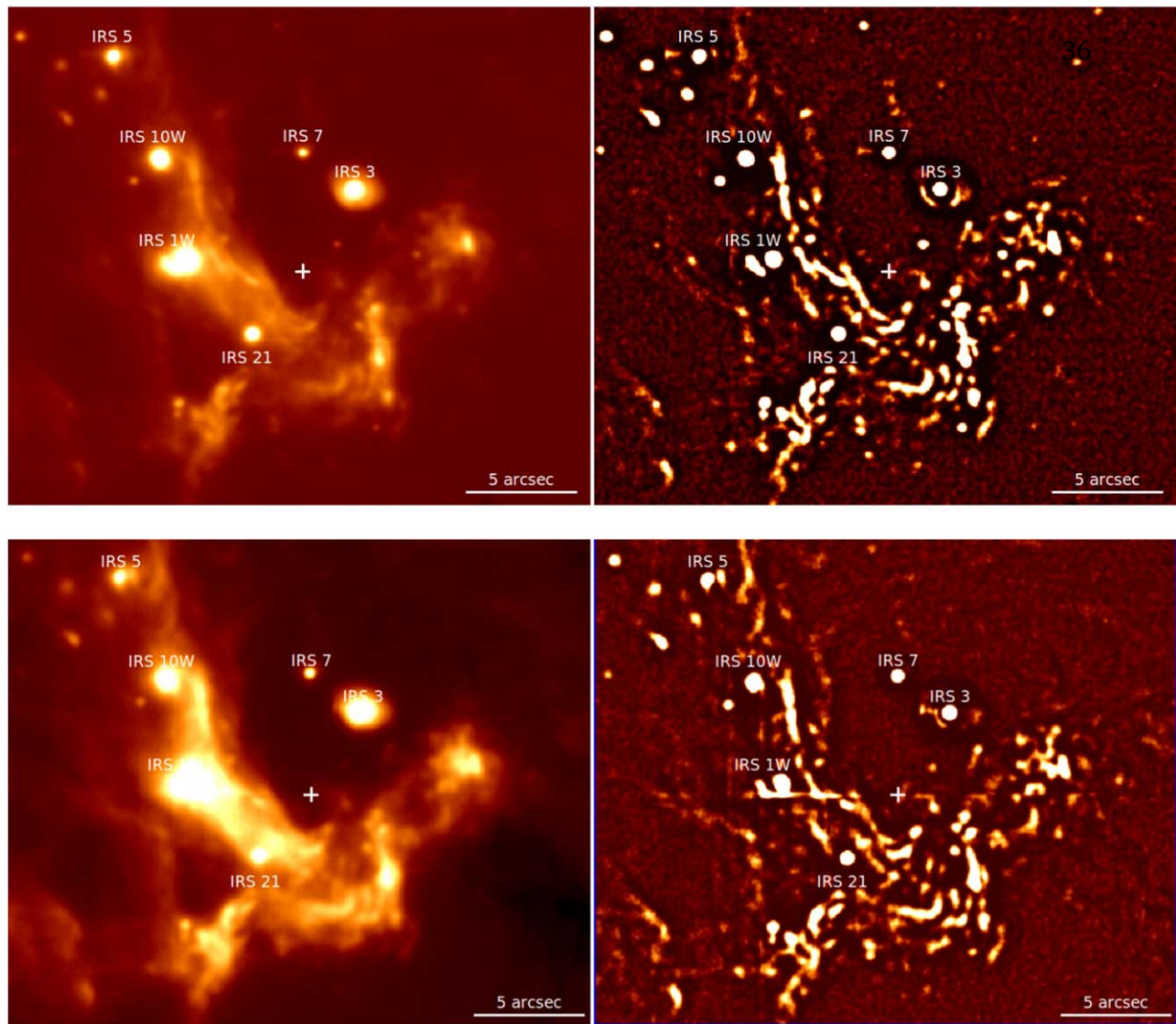


Figure 1. Central $24'' \times 24''$ region of the Milky Way in the PAH1 filter ($8.59 \mu\text{m}$) in the top panel and in the Ne II_2 filter ($13.04 \mu\text{m}$) in the bottom panel. The north is up and the east is to the left. The right panel displays the high-pass-filtered version of the left image. All the dusty-filament-like structures and infrared-excess stars are resolved and enhanced through the high-pass filter.

subtracting the images separated by large timescales essentially represents the subtraction of two slightly shifted Gaussian profiles. The result is a crude but clear indication of the direction of the bulk motion. We first scaled (rebinned) and transformed all PAH1 image frames into the common coordinate system of the 2018 epoch using the positions of IRS 10EE, IRS 9, and IRS 7 (and Ne II_2 image frames using the positions of IRS 10EE, IRS 7, IRS 12N, IRS 15NE, and IRS 17) to calculate the transformation matrix. These positions were corrected for stellar velocities, as reported in the K band by Schödel et al. (2009) and Genzel et al. (2000). The resulting image (differential map) is presented in Figure 3 along with the derived proper motions of the stellar sources, which are discussed in subsequent subsections.

3.2. Proper Motions

We first identified the infrared sources (IRS) in N -band images by comparing them with the K and L' bands. To make sure the proper motions that we calculate are reliable, we make

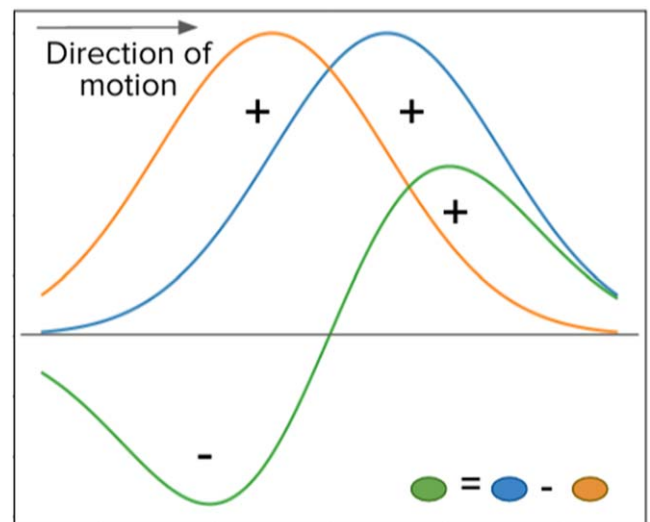


Figure 2. Difference of shifted Gaussian profiles as an indicator of the direction of motion.

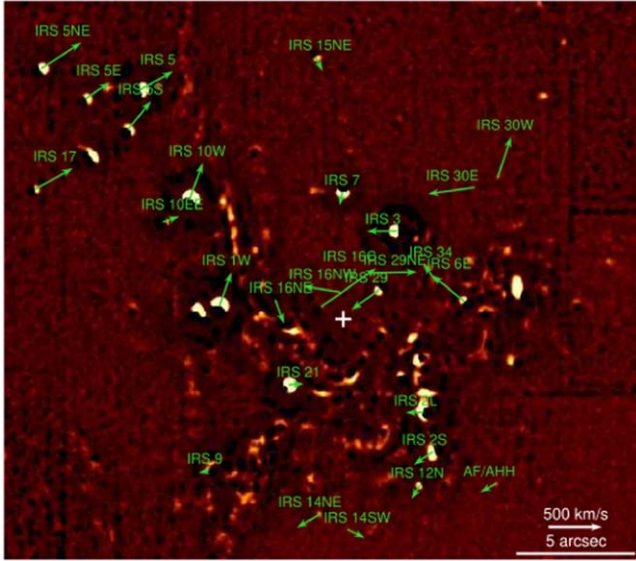


Figure 3. Differential map produced by subtracting the PAH1 2006 image from the PAH1 2018 image. The arrows correspond to velocities obtained by measuring offset positions and velocities w.r.t. IRS 10EE, 9, and 7.

similar calculations for IRS sources in the K band and compare them both with the velocities reported by Schödel et al. (2009) and Genzel et al. (2000). We chose IRS 10EE, IRS 9, IRS 12N, and IRS 7 as calibrators for PAH1 images (and IRS 10EE, IRS 7, IRS 12N, IRS 15NE, and IRS 17 for Ne II₂ images) as they were unambiguously identifiable in both N and K bands and had velocities, v_α and v_δ , from Schödel et al. (2009). We measure the offsets of each source of interest from these IRS sources. We calculate relative velocities w.r.t. each of them and then add their respective velocities (as given by Schödel et al. 2009), before averaging them to get the proper motions w.r.t. Sgr A*. By doing so, we are minimizing the errors introduced during the process of offset measurements. As an example, we show in Figure 4 the v_α and v_δ plots for the source IRS 1W. Multiplying the proper motions with the distance to the GC, $D_{GC} = 8.1$ kpc, gives the tangential velocity. We compare tangential velocities in the N band and K band with Schödel et al. (2009) and Genzel et al. (2000) in Appendix A. Table 5 in Appendix A contains the calculated velocities in various bands along with the literature values. Figures 12 and 13 in Appendix A depict the deviations from Schödel et al. (2009). It is important to note that the uncertainties in the fainter sources could be larger than in the brighter sources due to the possibility of unresolved background sources blending with our target sources. While the uncertainties of the Gaussian fits for the positions is typically of the order of a few hundredth of a pixel, we conservatively assume an uncertainty of 0.25 pixels for that quantity. The mean absolute difference between the velocities in the two filters is about 100 km s^{-1} and standard deviation of the angle difference is about 40° .

We then move on to calculate the tangential velocities of all the extended sources in the FOV, concentrating especially on the inner edge of the northern arm. We determine the positions of each resolved source by fitting an elliptical Gaussian using the data visualization tool QFitsView (Ott 2012). We derive tangential velocities as described above and tabulate them in Table 2. We only report velocities of those sources that are free from confusion in at least three epochs. The uncertainties in the

combined R.A./decl. velocities are about $\pm 120 \text{ km s}^{-1}$ and the uncertainties in the flight direction are about $\pm 30^\circ$. Figure 5 shows the source labels and the apertures used in the left panel and their derived proper motion vectors in the right panel. We have removed the velocity vectors belonging to the IRS sources to get a clear indication of any bulk motion. We see a clear stream-like motion along the inner edge of the northern arm toward the southwest direction, which changes direction sharply as it crosses the Sgr A* to move in the northwest direction (blue dashed arrow in Figure 6).

We assume that within the area of the mini-spiral's northern arm we find N_{NA} sources that truly belong to the northern arm. The number of sources in that region which belong to the underlying cluster is N_C . We assume that N_C is a fraction of N_{NA} , i.e.,

$$N_C = f \times N_{NA}. \quad (1)$$

The total number of sources detected within the area of the mini-spiral's northern arm is then given by

$$N_{\text{tot}} = N_C + N_{NA} = N_{NA} \times (1 + f). \quad (2)$$

Therefore, even if all the N_{NA} sources move downstream one would not expect that all sources observed in that region follow that trend. While we assume that all the N_{NA} sources in the northern arm will be headed downstream along the mini-spiral arm, we also assume in a very simplistic way that half of the cluster sources, N_C , in that area will be moving downstream and half of them upstream. This implies that the ratio, R , between the sources moving up- and downstream is

$$R = \frac{N_{NA} + 0.5 N_C}{0.5 N_C} = \frac{N_C/f + 0.5 N_C}{0.5 N_C} = \frac{2}{f} + 1. \quad (3)$$

As can be seen in Figure 5, we find that in the mini-spiral region 11 sources move downstream and four sources move upstream, implying $R = 11/4 = 2.75$. Hence, we find that

$$R = \frac{2}{f} + 1 = 2.75. \quad (4)$$

Therefore, that fraction, f , turns out to be just above unity, with

$$f = \frac{2}{2.75 - 1} = 1.14, \quad (5)$$

just as expected for an additional contribution of dusty infrared-excess sources due to the northern arm on top of a cluster contribution with conceivably almost the same number density in dusty, stellar infrared-excess sources. For an equal contribution from the northern arm and the cluster in the region of the northern arm, we would have expected $R = 3$.

3.3. Photometry

Even though there have been many photometric studies on stars in the GC in various other wavelengths, they are limited in the MIR (e.g., Blum et al. 1996; Ott et al. 1999; Tanner et al. 2002; Viehmann et al. 2005, 2006). We carry on these studies on the extended dusty sources that we have identified.

Viehmann et al. (2006) report flux densities in various filters including the N band. In the MIR regime, they performed relative aperture photometry while relying on Tanner et al. (2002) for flux calibration. Contrary to what is mentioned in Viehmann et al. (2006), it appears that the reported N -band flux densities are not extinction-corrected. For example,

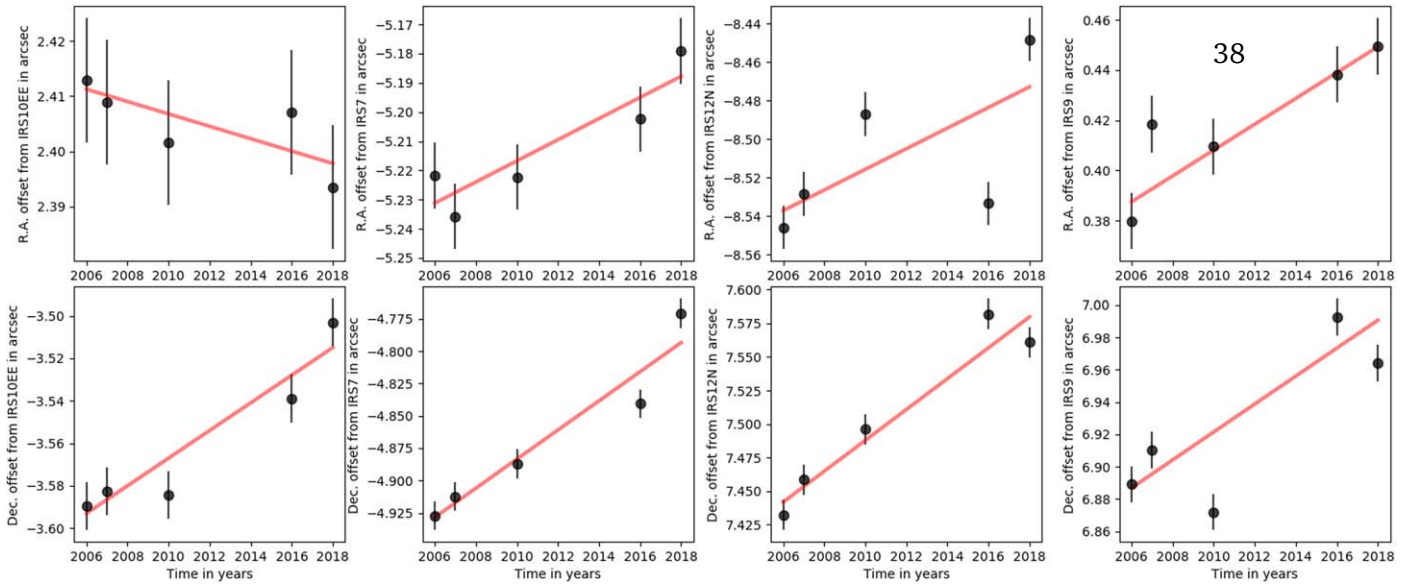


Figure 4. Proper motion, v_α and v_δ , of an example source IRS 1W. Relative velocities w.r.t. IRS 10EE, 7, 12N, and 9 were determined using offset measurements. Error bars correspond to 0.25 pixels.

Viehmman et al. (2006) report IRS 21’s flux density as 4.56 Jy at $8.6 \mu\text{m}$, which is consistent with 3.6 Jy by Stolovy et al. (1996) at $8.7 \mu\text{m}$ and 3.6 by Tanner et al. (2002) at $8.8 \mu\text{m}$. Stolovy et al.’s (1996) results are based on the zero-point measurements made with SpectroCam-10 on the 200 inch Hale telescope. As both of these previous studies did not report dereddened fluxes, if Viehmman et al.’s (2006) values were, in fact, extinction-corrected we would expect it to be about 5 times higher. This finding is further confirmed by two other independent studies by N. B. Sabha et al. (2022, in preparation) and R. Schödel et al. (2022, in preparation; through private communication), both based on zero-point measurements provided by the ESO.

The flux densities were extracted via aperture photometry using elliptical apertures to match the shape of extended or filamentary sources (see Figure 5). Aperture sizes were determined by fitting a 2D Gaussian along the semimajor and semiminor axes of the source. We selected IRS 5NE, IRS 10W, IRS 7, and IRS 1W as calibrators using a source aperture and background similar to Viehmman et al. (2006). As all the elliptical apertures we use do not have the same area, we measured the surface density of background contribution at various apertures in the uncrowded regions of the image and multiplied it by the area of each ellipse to get their background contributions. An extinction correction of $A_\lambda \sim 2.04$ for PAH1 and $A_\lambda \sim 1.34$ for Ne II (Fritz et al. 2011) was applied to obtain dereddened flux densities.

Table 6 in Appendix B lists the flux density values by Viehmman et al. (2006), our results when we use similar apertures and background as Viehmman et al. (2006), and our results when we use aperture sizes determined by the FWHM of the 2D Gaussian that we fit (our results in the table are before extinction correction). The table shows that our calibration approach results in source flux densities that are in good agreement with the results from Viehmman et al. (2006). It is to be noted that the central wavelength of the Ne II_2 filter used for our images is $13.04 \mu\text{m}$ (Ne II_2), while that of Viehmman et al.’s (2006) images is $12.81 \mu\text{m}$ (Ne II). For $\alpha_s \pm 1$ this difference corresponds to a 2% variation in flux densities.

Table 3 lists both the reddened (F) and dereddened (F') flux densities of all the reliable sources at both PAH1 ($8.59 \mu\text{m}$) and Ne II_2 ($13.04 \mu\text{m}$), along with their spectral indices, which were calculated using

$$\alpha_s = \frac{\log(F'_{13.04}/F'_{8.59})}{\log(8.59/13.04)}, \quad (6)$$

i.e., using the convention $F \propto \nu^{+\alpha_s}$ or $F \propto \lambda^{-\alpha_s}$. In particular, hotter sources (nonembedded stars) are characterized by a positive spectral index in this convention, while dust-enshrouded stars, colder dusty filaments, or potential compact objects powered by nonthermal synchrotron emission (neutron stars) exhibit a steep power-law spectrum with a negative spectral index in the MIR domain.

In Figure 7, we depict the spectral indices of each source. The color and the size of each source indicate the spectral index and the flux density at the PAH1 band, respectively. In Figure 7, it is apparent that the brightest infrared-excess sources are also warm and blue, while the fainter and colder dust sources are along the mini-spiral.

3.4. Cometary Tail of IRS 7

IRS 7 (about $5''.5$ north of Sgr A*) is one of the brightest IR sources in the region and is classified as a pulsating M1/M2 red supergiant (Carr et al. 2000; Paumard et al. 2014; Gravity Collaboration et al. 2021). Radio (Yusef-Zadeh & Morris 1991; Yusef-Zadeh & Melia 1992) and MIR (Serabyn et al. 1991) observations of IRS 7 have revealed a bow-shock feature toward the north and a cometary-tail-like structure pointed directly away from Sgr A*. Recently, Tsuboi et al. (2020) also reported the shell-like structure surrounding IRS 7 and its northern extension in the H30 α recombination line. They measured line-of-sight velocities and concluded that the tail is the gas stream flowing from the shell around IRS 7. As IRS 7 moves southward, the pulsating release of gas as a stellar wind (Paumard et al. 2014) is left behind and is ionized by far-UV radiation coming from the NSC.

Table 2
List of Tangential Velocities

39

Source	Name	$\Delta\alpha$ (arcsec)	$\Delta\delta$ (arcsec)	v_α	PAH1	Ne II_2	
					v_δ	v_α	v_δ
(all velocities are in km s ⁻¹)							
1	IRS 5NE	12.71	10.55	-374	243	-167	-167
2	IRS 5E	10.87	9.27	-232	155	-216	-211
3	IRS 5S	9.07	7.97	-218	268	-75	97
4	IRS 5	8.53	9.67	-303	167	-71	-145
5		10.60	6.87	-223	286	-226	1
6	IRS 17	12.97	5.45	-351	198	-238	-83
7		6.75	12.08	-151	-345	-187	-279
8		6.68	9.95	-350	-472	-55	-52
9		5.00	8.10	-210	-96		
10	IRS 15NE	1.17	11.04	-67	-133	-6	-308
11	IRS 10EE	7.60	4.07	-157	54	-186	142
12	IRS 10W	6.45	5.08	-118	331	120	148
13	IRS 7	0.03	5.34	27	-125	232	-250
14	IRS 3	-2.26	3.70	282	-2	412	-13
15		4.90	4.41	-77	-3	-7	-182
16		4.69	2.97	-180	-132	-215	-215
17		6.10	0.24	159	178	20	-51
18	IRS 1W	5.21	0.57	-113	307	53	275
19		3.67	0.22	-221	-337	301	-218
20		2.34	-0.40	-360	-330	163	-205
21		3.54	-1.67	-136	-162	-25	-303
22	IRS 21	2.29	-2.78	-137	8	-65	3
23		1.47	-2.07	38	-93	196	17
24		-1.57	-0.53	-116	218	-170	39
25		-0.78	-1.61	-108	207	-180	255
26		-0.33	-2.44	-61	-225	-395	-33
27		10.00	-8.83	-21	-181	-62	-159
28		7.10	-7.83	-184	-80	173	-277
29		5.70	-7.86	-74	-120	-259	-455
30		5.60	-5.89	-16	-138	63	-175
31		4.82	-6.39	-89	-228	316	37
32		14.38	-5.71	-128	61	-72	-161
33		11.07	-5.41	-191	-160	-44	-267
34		10.47	-5.97	103	-313	-135	-7
35		6.61	-1.80	-142	-126	-141	-195
36		6.35	-2.96	20	-157	64	-193
37		2.84	-5.14	-126	63	-185	7
38		3.66	-5.29	-53	-70	55	-3
39		0.26	-3.57	-51	-209	-189	-198
40		-1.14	-4.07	-98	-52	-57	-353
41		-1.41	-3.06	-139	166	6	-209
42		-2.47	-2.42	86	180	76	175
43		0.58	-1.94	-50	5	-295	-7
44	IRS 29	-1.50	1.22	256	-186	585	-205
45		-3.54	2.05	-71	374	-89	502
46		-3.19	-1.67	41	144	93	122
47	IRS 2L	-3.39	-3.94	173	-2	293	191
48		-5.44	2.50	198	92	362	74
49		-5.39	1.39	36	138	699	92
50		-5.90	0.33	-74	104	418	92
51		-6.00	-1.03	202	-87	100	185
52		-4.34	-1.70	-61	-21	185	180
53		-5.24	-0.11	-27	45	546	-85
54		-7.12	-1.73	329	206	368	-79
55		-7.75	-0.19	203	-81	273	158
56		-8.30	1.38	-297	20	98	181
57		-9.82	0.67	-32	438	123	179
58		-7.36	1.28	96	234	15	160
59		2.66	-4.41	-46	93	-84	357
60	IRS 2S	-3.78	-5.59	180	-124	82	-230
61		-2.81	-5.53	27	-168	-255	-15
62		-2.23	-5.60	-230	-137	168	-139

Table 2
(Continued)

40

63		-3.10	-4.81	-79	-13	331	36
64		-2.45	-4.47	30	166	-71	287
65		-1.63	-5.04	-49	-149	-366	145
66		-4.24	-7.01	-222	132	-100	-24
67	IRS 12N	-3.24	-6.99	80	-133	-5	-106
68		-3.01	-6.11	-39	-50	-127	123
69		-1.97	-6.56	91	-310	-326	-66
70		-4.52	-5.99	-191	-52	1	343
71		4.42	1.53	351	259	132	-271
72		3.55	1.47	-72	-68	-150	-244
73		3.85	3.01	-373	-419	334	-96
74		3.26	3.35	48	220	-21	-593
75		3.77	7.10	-16	188		
76		3.60	6.23	-22	261	-146	-338
77		3.24	5.16	47	105	108	173
78		0.02	8.46	302	231		
79		-0.09	7.73	297	211	516	126
80		-0.27	7.16	268	-301	990	250
81		-2.30	8.38	-193	340	970	-529
82		10.44	1.18	-90	189		
83		8.87	0.49	-27	207		
84		4.25	1.91	41	-273		
85	IRS 16NE	2.87	0.81	-83	-224		
86		1.27	0.85	-289	-79		
87	IRS 16C	0.93	0.51	-513	358		
88	IRS 16NW	0.12	1.13	351	54		
89	IRS 29NE	-1.15	1.93	-435	7		
90	IRS 9	5.66	-6.40	97	-22		
91		1.59	-0.53	-227	-289		
92		1.13	-1.39	88	102		
93		-1.89	-2.02	-95	42		
94		-2.53	-1.41	150	220		
95		-2.92	-0.88	114	247		
96	IRS 34	-3.91	1.56	119	166		
97		-6.37	2.97	-36	112		
98		-6.98	2.90	237	-133		
99		-6.72	2.42	-60	118		
100		1.69	-4.39	-88	-190	-100	-91
101		0.87	-3.12	-335	-538		
102		-0.39	-3.15	-258	81	-105	-43
103		-0.69	-3.69	-342	-47		
104		-1.90	-3.22	24	166	-205	13
105		1.35	-6.69	80	-113	112	100
106		1.30	-7.13	-65	-157		
107	IRS 14NE	0.95	-8.22	223	-130	153	-91
108		-1.25	-8.69	-47	-546		
109		3.66	-11.41	-3	-456		
110		4.24	-8.74	5	-164		
111		4.28	-7.38	-20	-195		
112		3.75	-7.31	82	-316		
113		3.00	-7.70	-213	-235		
114		2.68	-7.26	-367	-5		
115		3.07	-6.62	-24	-84	-458	338
116		3.08	-5.82	77	18		
117	IRS 30E	-5.52	5.53	435	-59		
118	IRS 30W	-6.50	5.94	-125	384		
119	IRS 6E	-5.07	0.76	294	234	398	181
120	AF/AHH	-6.46	-6.93	152	-85		
121	IRS 14SW	-0.18	-8.88	-162	-80		

Note. The positions are offsets from Sgr A* (in 2018) in arcsecs and all the velocities are in km s^{-1} . We chose a conservative 0.25 pixel uncertainty for proper motion calculations, which corresponds to about 45 km s^{-1} .

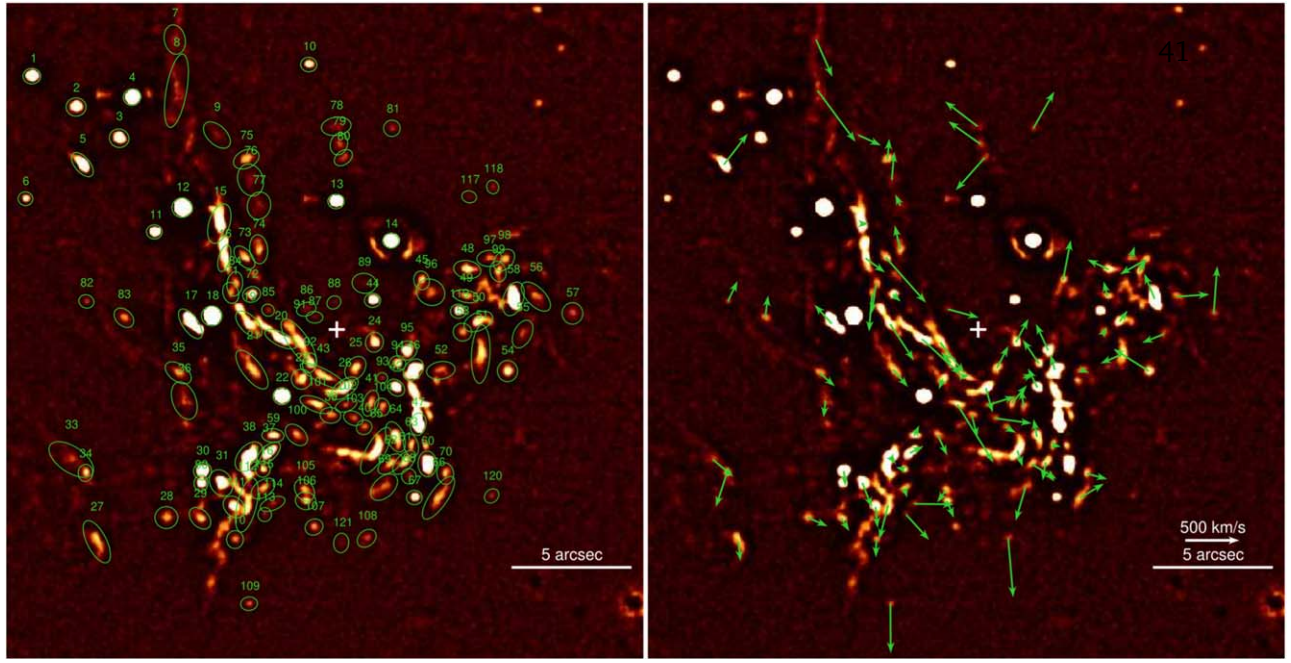


Figure 5. Left: the PAH1 image with the identification for each source and the apertures used to perform photometry. Right: proper motion of all the labeled sources. Arrows corresponding to IRS sources are removed for a better visualization of the stream-like motion.

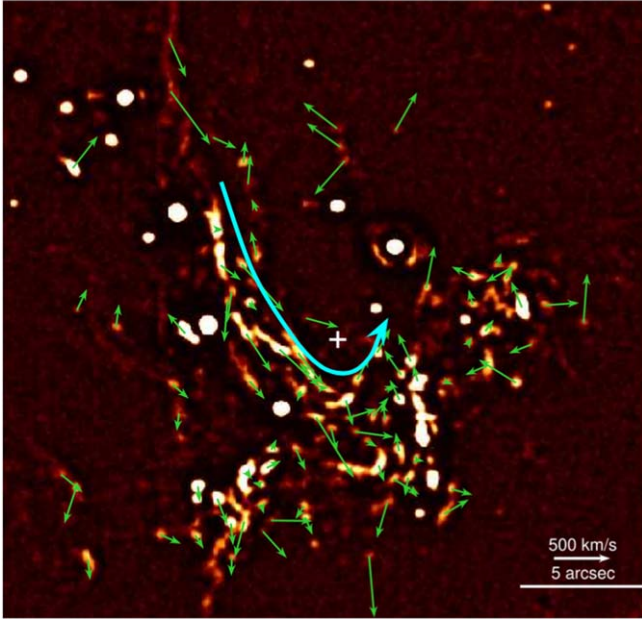


Figure 6. Presence of a stream-like motion along the inner edge of the northern arm toward the southwest direction, which changes direction sharply as it crosses the Sgr A* to move in the northwest direction (blue dashed arrow).

In the right panel of Figure 8, we show the PAH1 ($8.59 \mu\text{m}$) image of IRS 7 and its extended tail in comparison with the $\lambda = 2 \text{ cm}$ contour map from Yusef-Zadeh & Melia (1992), which is on the left. Contours of individual substructures of the tail in both wavelengths seem to match well with each other, which is an indication of the quality of our data and filtering techniques. The tail extends from $1''$ to $3''6$ north of IRS 7 and has three major substructures. Blue arrows mark the proper motions and gray lines mark their error boundaries. The slight discrepancy in the direction of the transverse velocity in the MIR/near-IR bands (see Appendix A), and by using SiO maser astrometry

(Reid et al. 2003; Borkar et al. 2020), could be caused by the fact that they probe different layers of the star. The proper-motion measurements of the substructures of the tail reveal the dominant influences on each of them. The northern two, which have detached from IRS 7 earliest, have almost similar velocities. This could mean that they are driven by a nuclear outflow coming from the inner few arcseconds.

In addition, the proper-motion distribution of the three components reflects the combination of the downstream fluid motion in the IRS 7 tail and the development of hydrodynamic instabilities, such as Kelvin–Helmholtz (KH) instabilities, which are manifested as propagating waves moving transverse along the south–north direction of the flow, i.e., they introduce an additional turbulent velocity field to the predominant south–north downstream bow-shock flow. The development of the KH instability is expected due to the velocity shear between the shocked stellar wind of IRS 7 and the surrounding hot medium. Assuming that the MIR–radio tail clumps formed due to the KH instability, we adopt their typical length scale, $\lambda_{\text{tail}} \sim 0''.5 \sim 0.02 \text{ pc}$, from Figure 8. The density and the temperature of the tail components, $n_{\text{tail}} \sim 6 \times 10^4 \text{ cm}^{-3}$ and $T_{\text{tail}} \sim 4650 \text{ K}$, respectively, can be inferred from H30 α recombination-line observations (Tsuboi et al. 2020). These tail components are approximately in pressure equilibrium with the surrounding hot medium, under the assumption of the extrapolation of the Bondi-radius values, $T_a \sim 10^7 \text{ K}$ and $n_a \sim 26 \text{ cm}^{-3}$ (Baganoff et al. 2003), i.e., $n_{\text{tail}} T_{\text{tail}} \sim n_a T_a$. This implies a density ratio between the ambient medium and the IRS 7 tail of $r = n_a/n_{\text{tail}} \sim 4.3 \times 10^{-4}$. For the shear velocity, we take the mean of the IRS 7 stellar motions, $v_{\text{shear}} \simeq v_* \sim 180 \text{ km s}^{-1}$, according to Table 5. The growth timescale of KH instabilities of the size λ_{tail} can be estimated as

$$\tau_{\text{KH}} \sim \frac{\lambda_{\text{tail}}}{v_{\text{shear}}} \frac{1+r}{\sqrt{r}} \sim 111 \text{ yr}. \quad (7)$$

Since the crossing timescale of the IRS 7 for the total length of the tail, $l_{\text{tail}} \sim 3''$, is $\tau_{\text{cross}} \sim l_{\text{tail}}/v_* \sim 652 \text{ yr} \gtrsim \tau_{\text{KH}}$, the KH

Table 3
List of Reliable Flux Densities in PAH1 and Ne II₂ Filters

Source	Name	$F_{8.59}$ (Jy)	$\Delta F_{8.59}$ (Jy)	$F'_{8.59}$ (Jy)	$\Delta F'_{8.59}$ (Jy)	$F_{13.04}$ (Jy)	$\Delta F_{13.04}$ (Jy)	$F'_{13.04}$ (Jy)	$\Delta F'_{13.04}$ (Jy)	α_s	$\Delta\alpha_s$
1	IRS 5NE	0.57	0.09	3.75	0.58	1	0.09	3.43	0.3	0.21	0.43
2	IRS 5E	0.49	0.08	3.22	0.50	1.99	0.17	6.84	0.58	-1.80	0.42
3	IRS 5S	0.61	0.09	4.01	0.62	2.35	0.2	8.07	0.69	-1.68	0.42
4	IRS 5	3.92	0.60	25.64	3.90	4.54	0.38	15.58	1.32	1.19	0.42
5		0.54	0.08	3.50	0.54	1.83	0.16	6.3	0.54	-1.41	0.42
6	IRS 17	0.02	0.01	0.11	0.02	0.27	0.02	0.94	0.09	-5.14	0.49
7		0.33	0.05	2.18	0.34	3.47	0.29	11.91	1.01	-4.07	0.43
8		1.38	0.21	9.02	1.39	6.33	0.54	21.73	1.84	-2.11	0.42
9		0.21	0.03	1.38	0.22	5.36	0.46	18.43	1.56	-6.21	0.43
10	IRS 15NE	0.04	0.01	0.26	0.05	0.09	0.01	0.3	0.03	-0.34	0.52
11	IRS 10EE	0.46	0.07	3.02	0.47	1.22	0.1	4.19	0.36	-0.78	0.43
12	IRS 10W	8.33	1.27	54.51	8.28	11.61	0.98	39.87	3.36	0.75	0.42
13	IRS 7	1.15	0.18	7.54	1.15	2.04	0.17	7	0.6	0.18	0.42
14	IRS 3	8.65	1.31	56.59	8.60	11.75	0.99	40.37	3.4	0.81	0.42
15		4.00	0.61	26.17	3.99	9.39	0.79	32.26	2.72	-0.50	0.42
16		1.64	0.25	10.73	1.64	9.27	0.78	31.83	2.69	-2.60	0.42
17		6.67	1.01	43.64	6.63	11.87	1	40.76	3.44	0.16	0.42
18	IRS 1W	16.14	2.45	105.66	16.05	21.97	1.85	75.47	6.36	0.81	0.42
19		3.99	0.61	26.15	3.98	12.64	1.07	43.44	3.67	-1.22	0.42
20		3.03	0.46	19.85	3.02	5.28	0.45	18.14	1.53	0.22	0.42
21		3.54	0.54	23.19	3.53	12.48	1.05	42.86	3.62	-1.47	0.42
22	IRS 21	4.79	0.73	31.39	4.77	6.92	0.58	23.77	2.01	0.67	0.42
23		2.37	0.36	15.52	2.36	11.58	0.98	39.79	3.36	-2.26	0.42
24		0.49	0.08	3.24	0.50	1.49	0.13	5.11	0.44	-1.09	0.42
25		0.81	0.12	5.28	0.81	2.34	0.2	8.02	0.68	-1.00	0.42
26		1.86	0.28	12.18	1.86	6.16	0.52	21.15	1.79	-1.32	0.42
27		0.42	0.07	2.74	0.43	2.78	0.24	9.54	0.81	-2.99	0.43
28		0.33	0.05	2.13	0.33	1.78	0.15	6.12	0.52	-2.53	0.42
29		0.74	0.11	4.82	0.74	3.61	0.31	12.39	1.05	-2.26	0.42
30		1.10	0.17	7.18	1.10	2.95	0.25	10.14	0.86	-0.83	0.42
31		2.26	0.35	14.81	2.26	6.09	0.52	20.92	1.77	-0.83	0.42
32		0.60	0.09	3.91	0.61	4.45	0.38	15.28	1.3	-3.27	0.43
33		0.49	0.08	3.19	0.50	3.44	0.29	11.83	1.01	-3.14	0.43
34		0.18	0.03	1.15	0.18	1.89	0.16	6.48	0.55	-4.14	0.43
35		0.59	0.09	3.87	0.60	2.99	0.25	10.28	0.87	-2.34	0.42
36		0.59	0.09	3.86	0.60	2.65	0.23	9.11	0.78	-2.06	0.43
37		1.32	0.20	8.65	1.32	3.72	0.32	12.79	1.08	-0.94	0.42
38		3.05	0.47	19.98	3.04	8.05	0.68	27.67	2.34	-0.78	0.42
39		0.96	0.15	6.29	0.96	4.24	0.36	14.56	1.23	-2.01	0.42
40		0.58	0.09	3.78	0.58	2.25	0.19	7.72	0.66	-1.71	0.42
41		0.81	0.12	5.30	0.81	2.05	0.17	7.04	0.6	-0.68	0.42
42		1.06	0.16	6.92	1.06	2.26	0.19	7.77	0.66	-0.28	0.42
43		2.33	0.36	15.24	2.33	6.6	0.56	22.68	1.92	-0.95	0.42
44	IRS 29	0.13	0.02	0.85	0.14	0.14	0.01	0.48	0.05	1.37	0.47
45		0.14	0.02	0.94	0.15	0.61	0.05	2.09	0.18	-1.91	0.43
46		2.41	0.37	15.80	2.41	4.08	0.35	14	1.19	0.29	0.42
47	IRS 2L	3.28	0.50	21.49	3.27	5.52	0.47	18.98	1.6	0.30	0.42
48		0.64	0.10	4.20	0.65	1.48	0.13	5.09	0.44	-0.46	0.42
49		0.57	0.09	3.72	0.57	2.5	0.21	8.6	0.73	-2.01	0.42
50		1.33	0.20	8.71	1.33	4.11	0.35	14.14	1.2	-1.16	0.42
51		1.60	0.25	10.49	1.61	5.88	0.5	20.21	1.71	-1.57	0.42
52		0.97	0.15	6.34	0.97	7.58	0.64	26.04	2.21	-3.38	0.42
53		0.46	0.07	3.01	0.46	1.51	0.13	5.17	0.44	-1.30	0.42
54		0.34	0.05	2.24	0.35	1.39	0.12	4.79	0.41	-1.82	0.43
55		0.55	0.09	3.61	0.56	2.09	0.18	7.19	0.61	-1.65	0.42
56		0.82	0.13	5.38	0.83	3.65	0.31	12.55	1.07	-2.03	0.42
57		0.03	0.01	0.22	0.04	0.47	0.04	1.61	0.14	-4.77	0.48
58		4.07	0.62	26.65	4.06	7.26	0.61	24.95	2.11	0.16	0.42
59		0.66	0.10	4.34	0.67	2.77	0.23	9.5	0.81	-1.88	0.42
60	IRS 2S	1.93	0.29	12.64	1.93	3.67	0.31	12.61	1.07	0.01	0.42
61		1.68	0.26	11.00	1.68	4.4	0.37	15.1	1.28	-0.76	0.42
62		1.37	0.21	8.97	1.37	5.63	0.48	19.36	1.64	-1.84	0.42
63		1.73	0.26	11.36	1.73	3.83	0.32	13.17	1.12	-0.35	0.42

Table 3
(Continued)

43

Source	Name	$F_{8.59}$ (Jy)	$\Delta F_{8.59}$ (Jy)	$F'_{8.59}$ (Jy)	$\Delta F'_{8.59}$ (Jy)	$F_{13.04}$ (Jy)	$\Delta F_{13.04}$ (Jy)	$F'_{13.04}$ (Jy)	$\Delta F'_{13.04}$ (Jy)	α_s	$\Delta\alpha_s$
64		2.34	0.36	15.34	2.34	7.67	0.65	26.37	2.23	-1.30	0.42
65		3.86	0.59	25.27	3.85	9.92	0.84	34.1	2.88	-0.72	0.42
66		0.73	0.11	4.75	0.73	1.03	0.09	3.54	0.31	0.70	0.42
67	IRS 12N	0.16	0.03	1.05	0.17	0.42	0.04	1.46	0.13	-0.79	0.44
68		0.42	0.07	2.77	0.43	1.03	0.09	3.55	0.3	-0.59	0.42
69		0.80	0.12	5.21	0.80	5.9	0.5	20.28	1.72	-3.26	0.42
70		0.36	0.06	2.36	0.37	1	0.09	3.44	0.3	-0.90	0.43
71		2.02	0.31	13.20	2.01	5.43	0.46	18.64	1.58	-0.83	0.42
72		1.04	0.16	6.82	1.04	1.94	0.17	6.68	0.57	0.05	0.42
73		1.08	0.17	7.09	1.08	1.98	0.17	6.82	0.58	0.09	0.42
74		0.64	0.10	4.18	0.65	2.09	0.18	7.18	0.61	-1.30	0.42
75		0.39	0.06	2.56	0.40	1.12	0.1	3.85	0.33	-0.98	0.43
76		0.50	0.08	3.27	0.51	1.22	0.11	4.2	0.36	-0.60	0.43
77		0.30	0.05	1.98	0.31	0.78	0.07	2.69	0.23	-0.73	0.43
78		0.01	0.01	0.05	0.02	0.08	0.01	0.27	0.03	-4.04	0.99
79		0.02	0.01	0.14	0.03	0.1	0.01	0.35	0.04	-2.20	0.58
80		0.02	0.01	0.16	0.03	0.09	0.01	0.3	0.03	-1.51	0.51
81						0.01	0.01	0.03	0.01		
82		0.01	0.01	0.09	0.02						
83		0.30	0.05	1.96	0.31						
84		1.69	0.26	11.05	1.69						
85	IRS 16NE	0.50	0.08	3.26	0.50						
86		0.02	0.01	0.12	0.02						
87	IRS 16C	0.01	0.01	0.05	0.01						
88	IRS 16NW										
89	IRS 29NE	0.01	0.01	0.04	0.02						
90	IRS 9	0.78	0.12	5.14	0.79						
91		3.73	0.57	24.39	3.72	9.83	0.83	33.77	2.86	-0.78	0.42
92		1.15	0.18	7.54	1.15						
93		0.19	0.03	1.22	0.19	1.24	0.11	4.27	0.37	-3.00	0.43
94		0.85	0.13	5.55	0.85	3.28	0.28	11.26	0.96	-1.69	0.42
95		1.15	0.18	7.50	1.15	4.24	0.36	14.58	1.24	-1.59	0.42
96	IRS 34	0.44	0.07	2.86	0.45						
97		0.50	0.08	3.25	0.50	0.97	0.08	3.33	0.29	-0.06	0.42
98		0.57	0.09	3.74	0.58	2.29	0.2	7.87	0.67	-1.78	0.42
99		0.85	0.13	5.57	0.85	2.43	0.21	8.34	0.71	-0.97	0.42
100		0.88	0.13	5.76	0.88	6.17	0.52	21.19	1.79	-3.12	0.42
101		1.94	0.30	12.67	1.93	6.48	0.55	22.26	1.88	-1.35	0.42
102		0.72	0.11	4.72	0.72	3.14	0.27	10.8	0.92	-1.98	0.42
103		0.56	0.09	3.68	0.57	2.03	0.17	6.98	0.59	-1.53	0.42
104		0.52	0.08	3.42	0.53	1.61	0.14	5.52	0.47	-1.15	0.42
105		0.46	0.07	3.01	0.47	3.54	0.3	12.15	1.03	-3.34	0.43
106		0.29	0.05	1.92	0.30	1.5	0.13	5.14	0.44	-2.36	0.43
107	IRS 14NE	0.01	0.01	0.07	0.02						
108						0.14	0.01	0.47	0.05		
109											
110		0.43	0.07	2.80	0.43	1.84	0.16	6.31	0.54	-1.95	0.42
111		2.18	0.33	14.24	2.17	5.94	0.5	20.41	1.73	-0.86	0.42
112		3.85	0.59	25.22	3.84						
113		0.15	0.02	1.00	0.16	0.76	0.07	2.6	0.22	-2.29	0.43
114		0.24	0.04	1.54	0.24	0.96	0.08	3.28	0.28	-1.81	0.43
115		0.88	0.14	5.78	0.89	2.45	0.21	8.41	0.72	-0.90	0.42
116		0.76	0.12	4.96	0.76	1.13	0.1	3.87	0.33	0.59	0.42
117	IRS 30E										
118	IRS 30W										
119	IRS 6E	0.39	0.06	2.53	0.39	1.22	0.1	4.19	0.36	-1.21	0.42
120	AF/AHH										
121	IRS 14SW										

instabilities of the length scale of the observed clumps could have developed as IRS 7 plows through the hot medium. The KH instabilities of the radius $R_{\text{tail}} \sim 0.5\lambda_{\text{tail}}$ can also survive

long enough in the surrounding hot medium to be observed. For the pressure-confined colder clumps of the constant mass density ρ_{tail} that have a mass of $m_{\text{tail}} = 4/3\pi R_{\text{tail}}^3 \rho_{\text{tail}}$, the

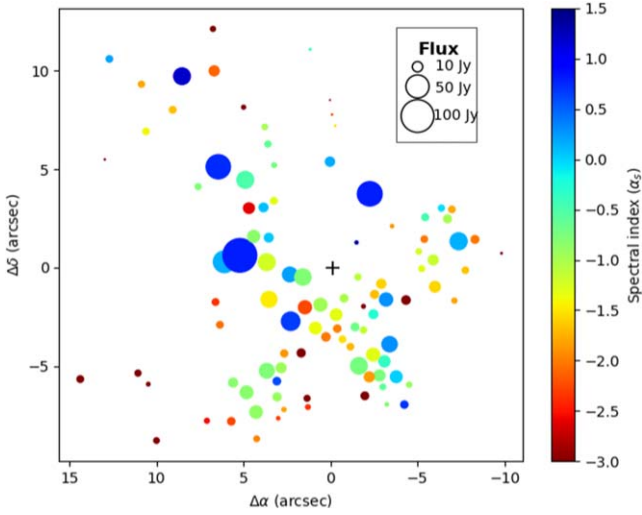


Figure 7. Spectral indices using the dereddened flux density measurements in the PAH1 and Ne II₂ filters. The positions are offsets from Sgr A* and the sizes correspond to the flux density in the PAH1 filter. The figure also shows the positive correlation between the PAH1 flux density and the spectral index (α_s): the larger the PAH1 flux density (larger circles), the greater the spectral index (bluer colors).

evaporation timescale is given by Cowie & McKee (1977) and Karas et al. (2021):

$$\begin{aligned} \tau_{\text{evap}} &= \frac{25k_B n_{\text{tail}} R_{\text{tail}}^2}{8\kappa_{\text{H}}} \\ &\simeq 4067 \left(\frac{n_{\text{tail}}}{6 \times 10^4 \text{ cm}^{-3}} \right) \left(\frac{R_{\text{tail}}}{0.02 \text{ pc}} \right)^2 \text{ yr}, \end{aligned} \quad (8)$$

where κ_{H} is the conductivity of the hot ambient medium, and its value can be calculated as $\kappa_{\text{H}} = 1.92 \times 10^{11} \text{ erg s}^{-1} \text{ K}^{-1} \text{ cm}^{-1}$. Since $\tau_{\text{KH}} < \tau_{\text{cross}} < \tau_{\text{evap}}$, the KH instabilities can properly explain the tail components of IRS 7.

3.5. Extended Emission of IRS 3

IRS 3 is the brightest and the most extended stellar source at the GC. Although it is a stellar core, the extended source is not circularly symmetric, which has been a topic of interest. Viehmann et al. (2005) suggests that this morphology is due to a bow shock generated by winds from the massive central stellar cluster or an outflow from Sgr A*. However, Yusef-Zadeh et al. (2017) suggests a tidal distortion scenario as IRS 3 orbits around Sgr A*. In Figure 9, we compare the contour maps around IRS 3 with a 226 GHz image from Yusef-Zadeh et al. (2017).

By comparing the 226 GHz emission and the PAH1 image in Figure 9, the IRS3 circumstellar envelope exhibits similar structures at both wavelengths, in particular the extension in the northeast/southwest direction as well as another brighter extension to the southeast. Since the circumstellar material of IRS 3 has an enormous radius of $R_{\text{IRS3}} \sim 1'' \sim 0.04 \text{ pc} \sim 2 \times 10^6 R_{\odot}$, i.e., a thousand times bigger than a red supergiant or an asymptotic giant branch (AGB) star, it could be a signature of tidal elongation along the proper-motion direction as suggested by Yusef-Zadeh et al. (2017). The question arises: What could have caused the expansion of the IRS 3 envelope beyond its tidal (Hill) radius? If we consider the upper limit on the distance of IRS 3 from Sgr A* based on its mean stellar velocity of

$v_* \sim 266 \text{ km s}^{-1}$ (see Table 5), we obtain

$$d_{\text{IRS3}} \lesssim 0.24 \text{ pc}. \quad (9)$$

Then we can estimate the upper limit on the tidal radius of IRS 3:

$$\begin{aligned} R_{\text{tidal}} &\lesssim d_{\text{IRS3}} \left(\frac{m_{\text{IRS3}}}{3M_*} \right)^{1/3} \\ &\sim 10^5 \left(\frac{d_{\text{IRS3}}}{0.24 \text{ pc}} \right) \left(\frac{m_{\text{IRS3}}}{10 M_{\odot}} \right)^{1/3} \left(\frac{M_*}{4 \times 10^6 M_{\odot}} \right)^{-1/3} R_{\odot}. \end{aligned} \quad (10)$$

Hence, even the largest red supergiants or AGB stars should have photospheres well inside their tidal radii at the distance of IRS 3; see Equation (9). One possibility of the perturbation of the atmosphere of IRS 3 is its ongoing or recent past interaction with the fast nuclear outflow or the jet, which led to shock propagation inside the red supergiant's envelope. This could effectively lead to atmosphere ablation by the jet (Zajaček et al. 2020a). As a consequence, after one jet crossing, the IRS 3 envelope adiabatically puffed up beyond the tidal (Hill) radius of the host star. The shocked envelope would expand adiabatically up to the tidal radius on the timescale given by the sound speed,

$$\begin{aligned} \tau_{\text{exp}} &\sim \frac{R_{\text{tidal}}}{c_s} \\ &\simeq 172 \left(\frac{R_{\text{tidal}}}{10^5 R_{\odot}} \right) \left(\frac{T_{\text{atm}}}{10^4 \text{ K}} \right)^{-1/2} \text{ yr}, \end{aligned} \quad (11)$$

where T_{atm} is the temperature of the shocked red-giant envelope or the temperature of the red-giant photosphere after the jet ablation.

Subsequently, after the short envelope expansion up to the tidal radius, the red-giant circumstellar material further undergoes tidal prolongation along the orbital direction. The tidal stretching generally takes place on a timescale that is a fraction of the orbital timescale. The prolongation of an envelope of a radius R_{tidal} by a factor of $m = 10$ is expected to occur in

$$\begin{aligned} \tau_{\text{tidal}} &= \sqrt{m} \frac{d_{\text{IRS3}}^{3/2}}{\sqrt{GM_*}}, \\ &= 2772 \left(\frac{m}{10} \right)^{1/2} \left(\frac{d_{\text{IRS3}}}{0.24 \text{ pc}} \right)^{3/2} \left(\frac{M_*}{4 \times 10^6 M_{\odot}} \right)^{-1/2} \text{ yr}. \end{aligned} \quad (12)$$

Hence, the current extended state of IRS 3 is likely the result of its atmosphere's perturbation by the fast outflow or the jet, which led to a propagating shock inside the red-giant envelope. This was followed by fast envelope expansion up to the tidal radius, and subsequently tidal prolongation along IRS 3's orbital motion took place. Both processes are characterized by timescales shorter than the orbital timescale, $P_{\text{IRS3}} \sim 5508 (d_{\text{IRS3}}/0.24 \text{ pc})^{3/2} \text{ yr}$. Hence, the current extended state of IRS 3 is the result of a recent interaction a few thousand years ago.

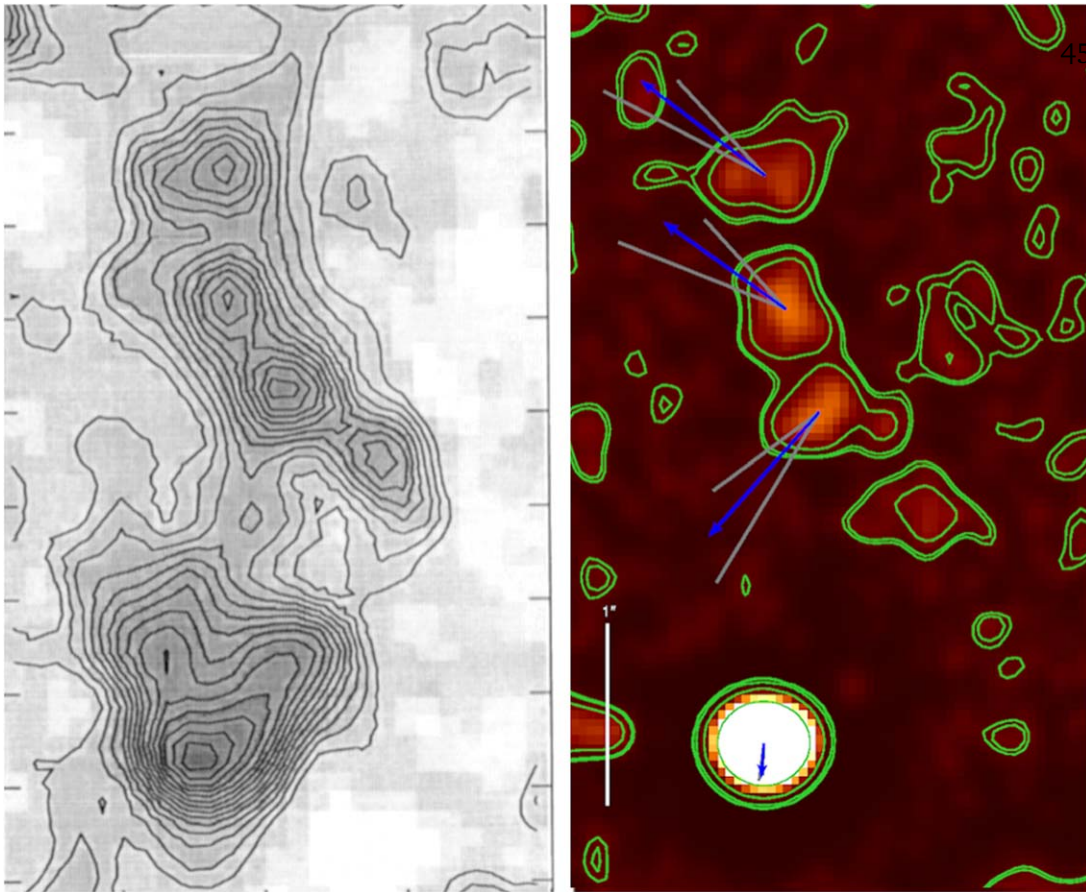


Figure 8. On the left is an image of IRS 7 and its extended tail at 2 cm from Yusef-Zadeh & Melia (1992), and on the right is a smooth-subtracted image with the same FOV in the PAH1 filter. The tail has three prominent substructures and their proper motions are indicated by blue arrows with gray lines as their error boundaries.

3.6. Nature of Dusty Sources

To get a better understanding of the nature of the dusty sources in the GC, it becomes important to perform statistical analysis of all their physical properties. We fit a 2D Gaussian on each source to determine its length and width (major and minor axes of the elliptical aperture). In the top-left image of Figure 10, we show a histogram of these measurements.

The distribution of position angles, measured anticlockwise from the west, is plotted in the top-right image of Figure 10. The sources along the northern arm have a smaller dispersion, which is expected given the fact they form a streamer-like structure.

The ellipticity, defined as $(a - b)/a$, where a and b are the major and minor axes (length and width here), is plotted in the bottom-left image of Figure 10. Lastly, the bottom-right image is a distribution of spectral indices. A large number of sources with negative indices reiterates the fact that the MIR region is dominated by dust-covered stars and colder dusty filaments.

In Figure 11, we try to find correlations between several fundamental physical properties of the dusty sources. In Table 4, we list the Spearman correlation coefficient, s , as well as the corresponding p -value for all possible combinations of parameters, in 21 pairs total. We find five significant positive correlations with sufficiently low p -values ($p < 10^{-3}$): length–ellipticity, flux (Ne II₂)–length, flux (Ne II₂)–ellipticity, flux (PAH1)–flux (Ne II₂), and flux (PAH1)–spectral index. The positive correlation between the length and the ellipticity is expected due to the definition of ellipticity, while no significant

correlation between the width and the ellipticity is caused by the narrow width distribution, which is caused by the lower cutoff due to the angular resolution, while the higher cutoff is likely determined rather by the physical process of the clump formation and evolution. The positive correlation between the flux densities at both wavelengths is also expected based on the spectral energy distribution for most of the dusty sources: with increasing wavelength, the flux density increases in the MIR domain. The positive correlation between the flux (PAH1) and the spectral index indicates that the differences among spectral energy distributions are mainly due to the flux density at $8.59 \mu\text{m}$ (PAH1) rather than due to the flux density at $13.04 \mu\text{m}$ (Ne II₂). The flatter spectrum is caused by the higher PAH1 flux density, while the Ne II₂ filter flux density is not significantly correlated with the spectral index. This is also visible in Figure 7, where the most luminous sources in the PAH1 filter have a clear tendency toward the positive spectral index (the bigger the symbol, the bluer the color). This is also in line with the last two significant positive correlations: flux density (Ne II₂) and the length of the filaments, i.e., the longer the filament, the larger the flux density in the Ne II₂ filter. On the other hand, the correlation between the PAH1 flux density and the length is weaker and less significant. The positive correlation between the Ne II₂ flux density and the filament ellipticity then stems from the definition of the ellipticity that includes the length.

The origin of the elongated blobs and filaments in the mini-spiral is uncertain. They could have arisen due to several processes, which we list below:

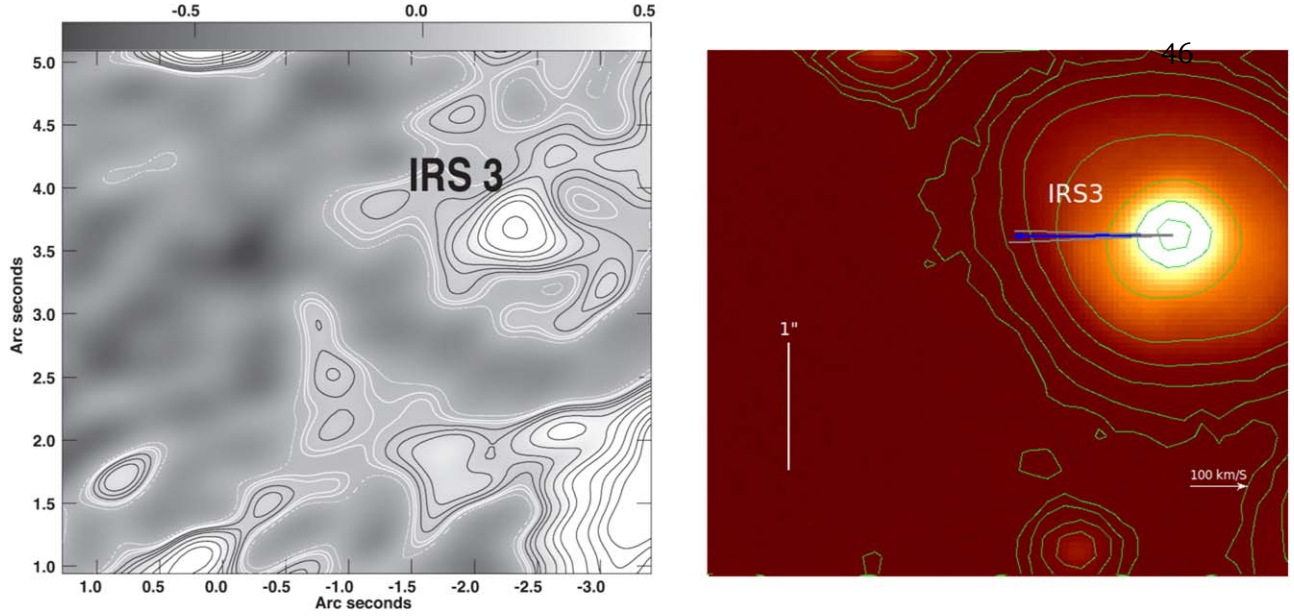


Figure 9. On the left is a 226 GHz emission of IRS 3 and its surroundings from Yusef-Zadeh et al. (2017) and on the right is an untreated PAH1 (8.6 μm) image.

- (a) Compression by the ram pressure produced by the collective stellar wind of the cluster of OB/WR stars within the NSC. For a simple estimate, we assume the mass range of the clumps to be $m_{\text{clump}} \approx 10^{-2} - 10^{-4} M_{\odot}$. We further assume an ambient number density of $n_a \sim 10 \text{ cm}^{-3}$, i.e., close to the Bondi-sphere value, and an outflow stellar wind velocity of $v_w \sim 1000 \text{ km s}^{-1}$ (Najarro et al. 1997). For the stationary setup, in which the MIR filaments are pressure-confined by the wind pressure acting on the mini-spiral clumps moving with the orbital velocity of $v_{\text{clump}} \sim 100 \text{ km s}^{-1}$ (Zhao et al. 2009), we can obtain their characteristic length scale using

$$\lambda_{\text{clump}} \sim \left(\frac{m_{\text{clump}} k_B T_{\text{clump}}}{\mu m_H [\mu m_H (v_{\text{clump}}^2 + v_w^2) - B^2/8\pi]} \right)^{1/3}, \quad (13)$$

where the ram pressure is balanced by the thermal pressure as well as the magnetic field inside the filaments. For a clump temperature of $T_{\text{clump}} \sim 10^4 \text{ K}$ (Zhao et al. 2010) and a negligible magnetic field, the characteristic length scale is $\lambda_{\text{clump}} \sim 10,500\text{--}2300 \text{ au}$, which captures the range for the inferred length and the width of the MIR filaments; see Figure 10 (top-left panel). An aligned magnetic field in the northern arm (see, e.g., Aitken et al. 1998; Roche et al. 2018), has a tendency to increase the length scale of the clumps.

- (b) The blobs are the manifestation of the KH instability that arises due to the streaming motion of the mini-spiral in the surrounding hot plasma. This is especially the case for the northern and the eastern arms, which have more radial, elliptical orbits in comparison with the western arm (Zhao et al. 2009). For the estimate of the characteristic growth timescale of the KH instabilities of a certain size, $\lambda_{\text{clump}} \sim 1000\text{--}10,000 \text{ au} \sim 1.5 \times 10^{16} - 1.5 \times 10^{17} \text{ cm}$, we will assume a shearing velocity given by the terminal stellar wind velocity that is approximately perpendicular to the mini-spiral orbital motion, i.e., $v_w \sim 1000 \text{ km s}^{-1}$ and $v_{\text{mini}} \sim 100 \text{ km s}^{-1}$, which gives $v_{\text{shear}} \sim \sqrt{v_w^2 + v_{\text{mini}}^2} \sim 1000 \text{ km s}^{-1}$. The density of the ionized component of the mini-spiral was inferred to be $n_{\text{mini}} \sim 3 - 21 \times 10^4 \text{ cm}^{-3}$ (Zhao et al. 2010), which sets the ratio with respect to the

ambient hot plasma to $r = n_a/n_{\text{mini}} \sim 4.8 \times 10^{-5} - 3.3 \times 10^{-4}$, assuming $n_a \sim 10 \text{ cm}^{-3}$. Using Equation (7), we get a KH growth timescale of $\tau_{\text{KH}}(1000 \text{ au}) \sim 262\text{--}686 \text{ yr}$ and $\tau_{\text{KH}}(10,000 \text{ au}) \sim 2620\text{--}6860 \text{ yr}$. Since the lifetime of the mini-spiral is $\sim 6 \times 10^4 \text{ yr}$, as given by the mean orbital timescale of the arms (Zhao et al. 2009), the clumps of $\lambda_{\text{clump}} \sim 1000 \text{ au}$ are continually forming as well as disappearing along the arms since their lifetime is comparable to the formation time as given by the evaporation timescale, see Equation (8), which gives $\tau_{\text{evap}} \sim 480\text{--}3360 \text{ yr}$ for the clump size of $\lambda_{\text{clump}} \sim 1000 \text{ au}$, the density range of $n_{\text{clump}} \sim 3 - 21 \times 10^4 \text{ cm}^{-3}$, and the conductivity of the hot medium $\kappa_H \sim 1.9 \times 10^{11} T_7^{5/2} \text{ erg s}^{-1} \text{ K}^{-1} \text{ cm}^{-1}$, where T_7 is in units of 10^7 K . This is consistent with the early considerations of the transient nature of ionized clouds in Sgr A West; see Lacy et al. (1980).

- (c) The denser clumps could have formed as a result of thermal instability during past states of a higher activity of Sgr A* when its bolometric luminosity reached $\sim 10^{39}\text{--}10^{41} \text{ erg s}^{-1}$. This was proposed by Różańska et al. (2014), who studied the conditions for the thermal instability in the mini-spiral region. They concluded that the thermal instability does not operate in the current low-luminous state of Sgr A*, but during the past periods of enhanced activity the thermal instability likely operated up to $\sim 1.4 \text{ pc}$ from Sgr A*, which led to the formation of a two-phase medium. This increased the clumpiness of the mini-spiral by creating clumps of $\sim 1\text{--}100$ Earth masses, i.e., $3 \times 10^{-6}\text{--}3 \times 10^{-4} M_{\odot}$. Based on the mini-spiral clump mass estimate presented in Section 4, the thermal instability clump mass appears to be lower by at least two orders magnitude. In case the thermal instability operated a few hundred years ago and clumps with the radius of $R_{\text{clump}} \sim 10^{14}\text{--}10^{15} \text{ cm}$ and the mass of $m_{\text{clump}} \sim 3 \times 10^{-5} M_{\odot}$ formed, then the evaporation timescale according to Equation (8) is long enough ($\sim 10^3\text{--}10^4 \text{ yr}$) so that they could in principle survive until nowadays. However, by including the mechanical heating of the NSC, Różańska et al. (2017) concluded that cold

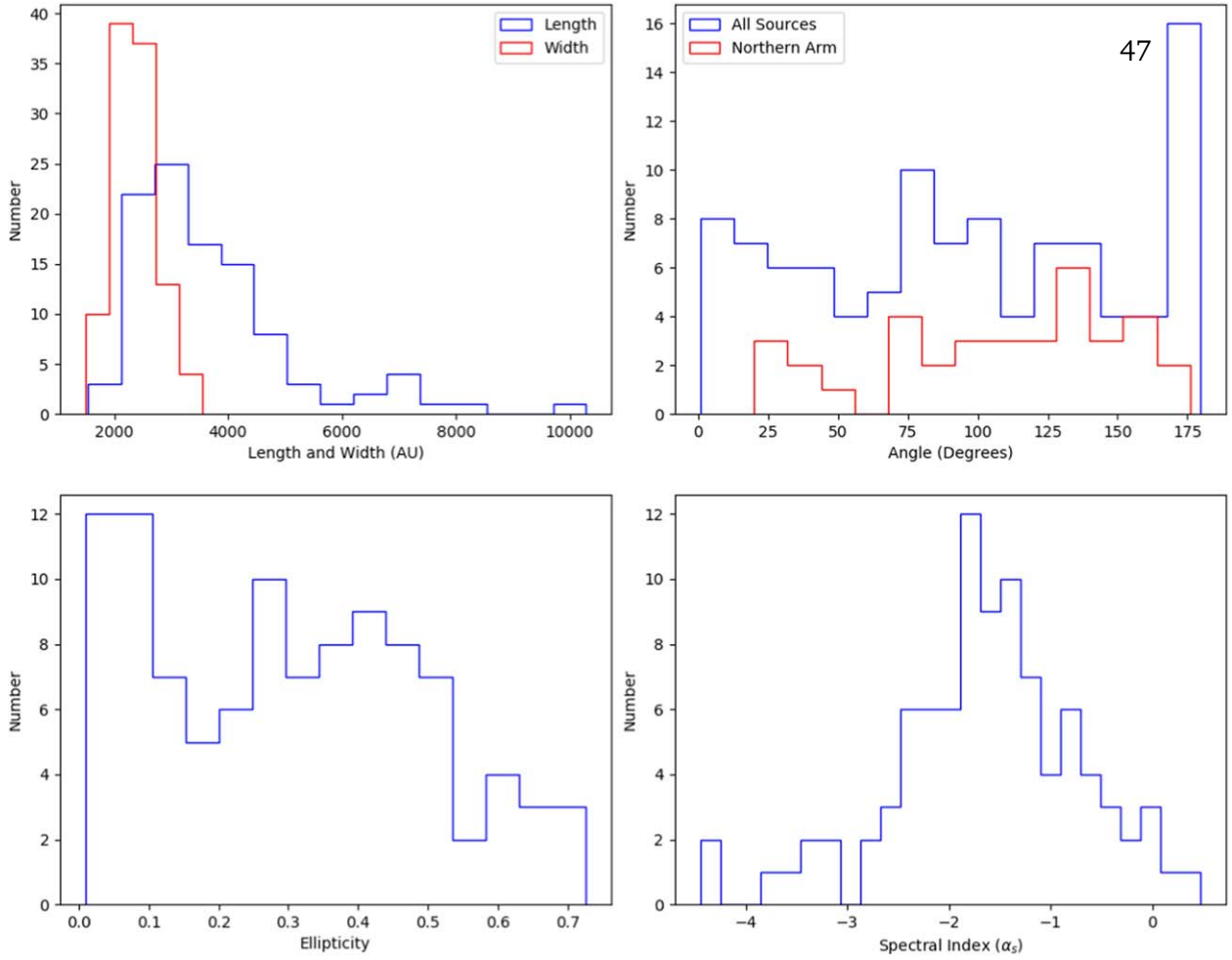


Figure 10. Histograms of the physical properties of the extended dusty sources. Most sources are about 3500–4000 au long and 2000 – 2500 au wide. Most sources are elliptic with various position angles. The sources on the northern arm seem to have a relatively tight spread of position angles compared to the rest of the sources.

clumps are not expected to form in the vicinity of Sgr A* since stellar winds induce an outflow of the hot ambient plasma. This fact, in combination with the small clump mass, renders the instability scenario less plausible to explain the formation of the elongated MIR sources, unless each MIR filament would consist of at least 100 clumps formed via the thermal instability. However, since the models of Rózańska et al. (2014) and Rózańska et al. (2017) assume a spherical symmetry it is difficult to explain the filamentary structure of the instability clumps in this framework.

Regardless of the way the denser and brighter MIR clumps formed, their shape and orientation are the result of tidal prolongation along the streaming motion of the northern arm. This stems from the tidal radius estimated for a mini-spiral clump of radius $R_{\text{clump}} \gtrsim 1000$ au and mass $m_{\text{clump}} \leq 0.1 M_{\odot}$:

$$\begin{aligned}
 r_t &\simeq R_{\text{clump}} \left(\frac{2M_{\bullet}}{m_{\text{clump}}} \right)^{1/3} \\
 &\sim 2.1 \left(\frac{R_{\text{clump}}}{1000 \text{ au}} \right) \left(\frac{m_{\text{clump}}}{0.1 M_{\odot}} \right)^{-1/3} \left(\frac{M_{\bullet}}{4 \times 10^6 M_{\odot}} \right)^{1/3} \text{ pc.}
 \end{aligned}
 \tag{14}$$

Since the mini-spiral arms are closer than 2 pc, any clump inside them is susceptible to tidal forces and prolongation parallel to the streaming (orbital) motion of the arms.

4. Discussion

Here we present, to our knowledge, the largest consistent number of individual source identifications, proper motions, and thus tangential velocities, and MIR spectral indices in the central parsec of the galaxy, covering the central stellar cluster and the immediate Sgr A* SMBH region. The MIR sources can clearly be divided into two groups: one associated with the flow along the extended mini-spiral, and one associated with dust-enshrouded stars and infrared-excess sources of the central stellar cluster.

Based on the color–temperature map derived from 12.5 to 20.3 μm maps by Cotera et al. (1999), the overall temperature in the mini-spiral is of the order of ~ 200 K. We assume that this is a good estimate of, or at least a lower limit to, the temperatures of the infrared-excess sources within the mini-spiral. A more exact estimate of the temperatures has to await multifrequency MIR data at a high angular resolution, as will be obtained, for example, with the METIS instrument at the extremely large telescope (Brandl et al. 2021).

For the sources not associated with stars, we estimate their dust masses based on PAH1 and Ne II₂ flux densities. We use

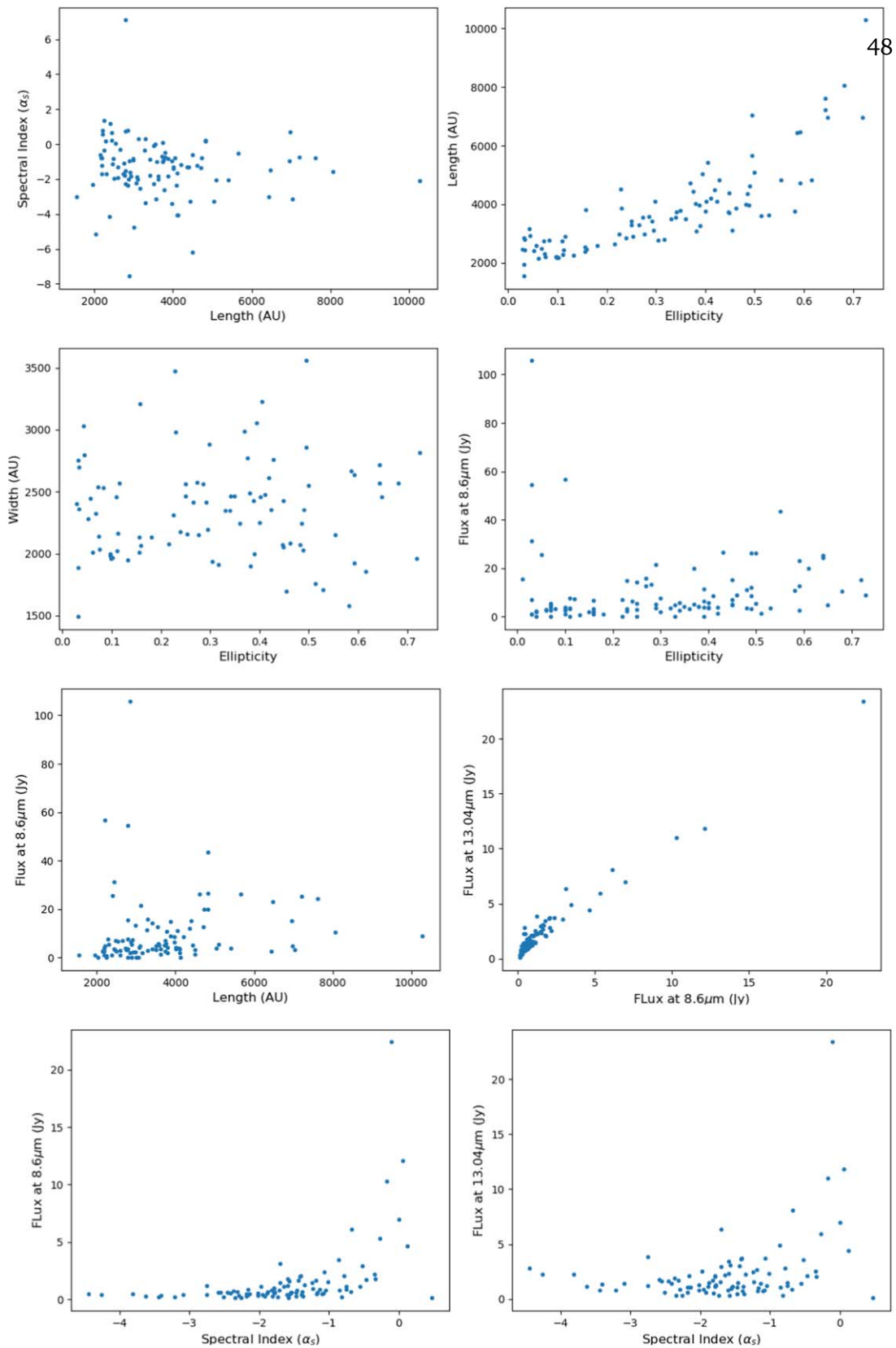


Figure 11. Correlation (or lack of it) among a few physical properties of the extended dusty sources. The spectral index (α_s , using the convention $F \propto \nu^{+\alpha_s}$) does not show a correlation with the length of the sources. Unsurprisingly, longer sources seem to be more elliptic. The flux densities at both the filters do correlate; however, the spectral index has a tighter correlation with flux at PAH1 than with flux at Ne II₂. Although flux does not correlate with ellipticity or length, a few noticeable outliers are those associated with bright IRS sources.

Table 4
Spearman Correlation Coefficients between Quantities that Characterize Compact MIR Dusty Sources

	Length	Width	Angle	Flux (PAH1)	Flux (Ne II ₂)	Spectral index	Ellipticity
Length	...	0.064 (0.524)	-0.098 (0.326)	0.260 (0.008)	0.404 (2.310×10^{-5})	-0.136 (0.171)	0.715 (2.04×10^{-17})
Width	0.064 (0.524)	...	-0.091(0.361)	0.146(0.140)	0.235(0.017)	-0.078(0.432)	0.048(0.630)
Angle	-0.098 (0.326)	-0.091(0.361)	...	-0.074(0.457)	-0.180(0.069)	0.089 (0.372)	-0.106(0.287)
Flux (PAH1)	0.260 (0.008)	0.146(0.140)	-0.074(0.457)	...	0.850(7.36×10^{-30})	0.510(3.65×10^{-8})	0.307(0.0016)
Flux (Ne II ₂)	0.404 (2.310×10^{-5})	0.235(0.017)	-0.180(0.069)	0.850(7.36×10^{-30})	...	0.081(0.419)	0.382(6.70×10^{-5})
Spectral Index	-0.136 (0.171)	-0.078(0.432)	0.089 (0.372)	0.510(3.65×10^{-8})	0.081(0.419)	...	-0.073(0.466)
Ellipticity	0.715 (2.04×10^{-17})	0.048(0.630)	-0.106(0.287)	0.307(0.0016)	0.382(6.70×10^{-5})	-0.073(0.466)	...

Note. In parentheses, we include the p -value. Five significant positive correlations were found: length flux (Ne II₂), length-ellipticity, flux (PAH1)-flux (Ne II₂), flux (PAH1)-spectral index, and flux (Ne II₂)-ellipticity.

the relation based on Rieke et al. (1978) and Kunneriath et al. (2012),

$$M_d = \frac{F(\nu) D_{GC}^2}{B(\nu, T_d)} \frac{4a}{3Q(\nu)} \rho_d, \quad (15)$$

where $F(\nu)$ is the measured flux density and $B(\nu, T_d)$ is the Planck function calculated for a dust temperature of $T_d \sim 200$ K (Cotera et al. 1999). The dust is characterized by the mean values of the radius, $a = 0.1 \mu\text{m}$, the mass density, $\rho_d = 2 \text{ g cm}^{-3}$, and the emissivity, $Q \approx 10^{-3} - 10^{-2}$ close to $10 \mu\text{m}$ (Aannestad 1975; Rieke et al. 1978). The distance to the GC is set to $D_{GC} = 8.1$ kpc. Assuming a gas-to-dust ratio of ~ 100 , we obtain a mean gas mass of the mini-spiral clump, $\overline{M}_g(\text{PAH1}) \sim 0.046 - 0.46 M_\odot$ and $\overline{M}_g(\text{Ne ii}_2) \sim 0.015 - 0.15 M_\odot$, as based on 85 dusty filaments that are not associated with stellar sources. These values are consistent within a factor of 3. Considering the peak width of the clumps, $w \sim 2000$ au, and the peak length, $l \sim 3000$ au, we obtain the characteristic clump volume of $V_{\text{clump}} \sim 3.2 \times 10^{49} \text{ cm}^3$, which yields a filament number density in the range of $n_{\text{clump}} \sim 1.1 \times 10^6 - 3.4 \times 10^7 \text{ cm}^{-3}$, which is at least one order of magnitude more than the electron number density of the ionized component, $n_e = (3-21) \times 10^4 \text{ cm}^{-3}$ (Zhao et al. 2010). The filaments could thus be overdense regions that are either pressure-confined by the stellar winds of OB/WR stars or they could stand for KH instabilities that got denser due to radiative cooling. This supports the multiphase nature of the mini-spiral streamers, with denser filaments embedded within a more diluted ionized gas (Różańska et al. 2014). Denser dusty filaments could also be the sites of the water- and CO-ice features and hydrocarbons detected within the central parsec (Moultaka et al. 2015a, 2015b). If the mean clump gas mass is in the range of $\sim 0.01 - 0.1 M_\odot$ and we have ~ 100 filaments, then their total gas mass of $\sim 1 - 10 M_\odot$ is consistent with the total ionized gas mass of $\sim 60 M_\odot$ within the central cavity (Lo & Claussen 1983). The denser filaments are currently not massive and dense enough to form stellar and substellar objects. As discussed in the previous section, they are transient features formed via the KH instability along the streaming motion and they evaporate on a timescale of $\sim 100 - 1000$ yr. The filaments are also expected to be tidally elongated along the streaming motion of the mini-spiral during their lifetime.

Mužić et al. (2007) show that the shape and motion of the mini-spiral filaments do not agree with a purely Keplerian motion of gas in the potential of the SMBH at the position of Sgr A*. The authors involve additional mechanisms that are responsible for the formation and the motion of these filaments. They assume that the filaments are affected by an outflow from the disk of young mass-losing stars around Sgr A*. In addition, an outflow from the Sgr A* black hole region itself may be responsible for the elongated shape and the motion of the filaments.

5. Summary

We studied MIR images of the central parsec of the GC in the N band (8.6 and $13.04 \mu\text{m}$). As the MIR emission is dominated by dust and extended regions around the central SMBH, we applied a high-pass filter on the images to resolve and identify the sources. We present the proper motions of these extended objects over a 12 yr time period. There are two distinct types of the observed motion: one related to infrared-excess sources of the central stellar cluster and the other a stream-like motion of extended objects along the mini-spiral streamer. We also present the flux densities of all the sources using elliptical apertures. Using the spectral indices, we infer that the MIR region is dominated by dust-enshrouded stars or colder dusty filaments and the temperature of ~ 200 K (Cotera et al. 1999) is at least the lower limit of infrared-excess sources within the mini-spiral. We detect a bow-shock feature and tail components of IRS 7 that are pointed away from Sgr A*. The proper-motion distribution of the individual tail components can be interpreted with a combination of downstream fluid motion and the development of KH instabilities. We detect and resolve the brightest MIR source in the region, IRS 3. The extended structure of the star is likely a result of its atmosphere's perturbation followed by tidal prolongation. We also report on the nature of all the dusty sources and delve into their possible origins.

This work was supported in part by SFB 956, “Conditions and Impact of Star Formation.” H.B. and E.H. are members of the International Max Planck Research School for Astronomy and Astrophysics at the Universities of Bonn and Cologne. We thank the Collaborative Research Centre 956, subproject A02, funded by the Deutsche Forschungsgemeinschaft (DFG), project ID 184018867. N.B.S. acknowledges financial support from the Austrian National Science Foundation through a FWF standalone grant No. P31154-N27. M.Z. acknowledges financial support by the GAČR EXPRO grant No. 21-13491X, “Exploring the Hot Universe and Understanding Cosmic Feedback.” R.S. acknowledges financial support from the State Agency for Research of the Spanish MCIU through the “Center of Excellence Severo Ochoa” award for the Instituto de Astrofísica de Andalucía (grant No. SEV-2017-0709) and financial support from national project PGC2018-095049-B-C21 (MCIU/AEI/FEDER, UE).

Appendix A

Tangential Velocity Comparisons between MIR and K -band Velocities

A comparison between the K -band tangential velocity (Schödel et al. 2009; Genzel et al. 2000) and our MIR velocities for the point sources (see Table 5) looks favorable. The mean absolute difference of around $\pm 100 \text{ km s}^{-1}$ is most likely affected by the larger PSF in the MIR, the limited baseline in time, and the fact that even the point sources may show some IR excess/extension or they are located on background emission that is spatially structured/variable on the scales of the PSF. Figures 12 and 13 in depict the deviations from Schödel et al. (2009).

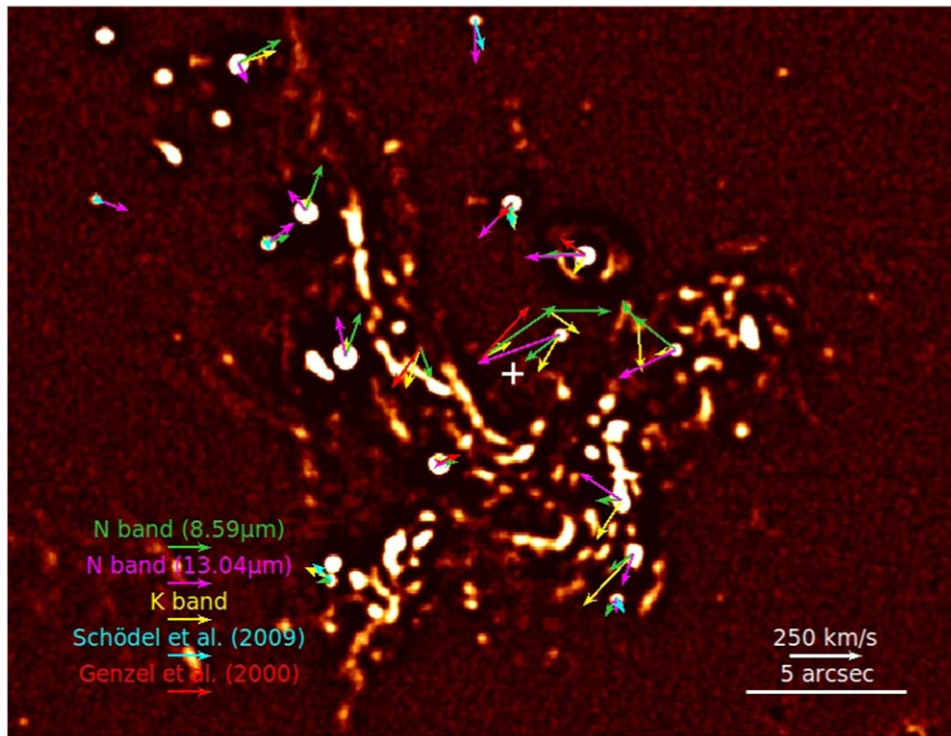


Figure 12. Comparison velocities from the *K* band and from Schödel et al. (2009) and Genzel et al. (2000).

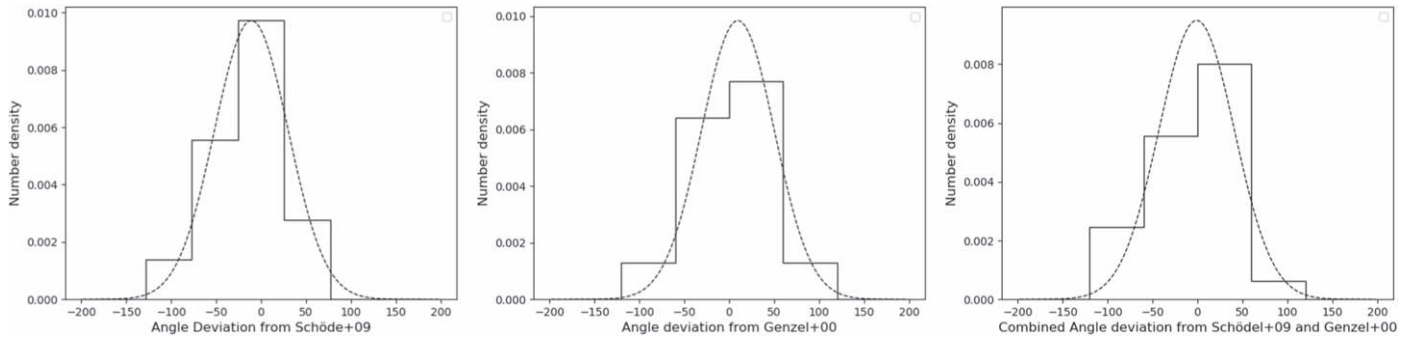


Figure 13. Angle deviations from Schödel et al. (2009) and Genzel et al. (2000) values in all the wavelengths. Mean absolute deviation in velocity (R.A.) is about 102 km s^{-1} , in velocity (decl.) is about 76 km s^{-1} , and the standard deviation of the angle difference is about 40° .

Table 5
Comparison of Stellar Tangential Velocities in PAH1 and Ne II₂ Bands with those in the K Band

Source	PAH1		Ne II		K			S09				G00				
	v_α	v_δ	v_α	v_δ	v_α	Δv_α	v_δ	Δv_δ	v_α	Δv_α	v_δ	Δv_δ	v_α	Δv_α	v_δ	Δv_δ
IRS 5	-303	167	-71	-145	-267	6	84	12								
IRS 10W	-118	331	120	148	-29	6	115	10								
IRS 10EE*	-157	54	-186	142	-44	6	-16	10	-15	7	-60	7				
IRS 1W	-113	307	53	275	-9	6	131	10								
IRS 16NE	-83	-224			104	6	-281	10					199	65	-279	21
IRS 16C	-513	358			-211	6	108	10					-330	39	353	34
IRS 21	-138	8	-65	3	-1	6	-43	10					-159	65	64	38
IRS 9*	97	-22			176	6	90	10	127	10	116	10				
IRS 2S	180	-124	82	-230	352	8	-368	14								
IRS 2L	173	-2	293	191	174	8	-273	10								
IRS 29	256	-186	585	-205	165	6	-261	10								
IRS 29NE	-435	7			-215	6	-151	10								
IRS 34	119	166			-24	8	-335	10								
IRS 6E	294	234	398	-206	141	6	-39	10								
IRS 3	282	-2	412	-13	84	8	-137	10					170	40	115	45
IRS 7*	27	-125	232	-250	-23	8	-193	12	-2	9	-176	9	100	67	-118	35
IRS 12N*	80	-133	-5	-106					-62	8	-107	8				
IRS 15NE*	-67	-133	-6	-308					-58	6	-223	6				
IRS 17*	-351	198	-238	-83					-65	5	-40	5				

Note. All velocities are in kilometers per second. S09 is the data from Schödel et al. (2009). G00 is the data from Genzel et al. (2000). Sources used as calibrators are marked with *. We chose a conservative 0.25 pixel uncertainty for PAH1 and Ne II₂ proper motions, which corresponds to about 45 km s⁻¹.

Appendix B

N-band Flux Density Comparison

Table 6 presents a comparison of our measured flux densities with Viehmann et al. (2006), using both circular apertures and elliptic apertures determined by their FWHM.

Table 6
Comparison of Measured Flux Densities (Reddened) with *N*-band Fluxes of Viehmann et al. (2006)

53

Source	F (Jy) (V+06)	PAH1 F (Jy) (Circular)	F (Jy) (FWHM)	±F (Jy)	F (Jy) (V+06)	Ne II_2 F (Jy) (Circular)	F (Jy) (FWHM)	±F (Jy)
IRS 5NE*	0.51	0.59	0.57	0.09	0.56	0.50	1.00	0.09
IRS 5E	0.59	0.38	0.49	0.08	1.54	0.57	1.99	0.17
IRS 5S	0.63	0.25	0.61	0.09	0.38	0.29	2.35	0.20
IRS 5	5.11	5.44	3.92	0.60	5.85	4.78	4.54	0.38
IRS 10W*	11.06	10.18	8.33	1.27	11.85	10.94	11.61	0.98
IRS 7*	1.47	1.26	1.15	0.18	1.75	1.95	2.04	0.17
IRS 3	13.42	16.35	8.65	1.31	12.85	11.17	11.75	0.99
IRS 1W*	20.42	22.96	16.14	2.45	22.93	25.40	21.97	1.85
IRS 21	4.56	4.95	4.79	0.73	5.44	6.27	6.92	0.58
IRS 29	0.15	0.07	0.13	0.02				
IRS 2L	5.26	4.25	3.28	0.50	7.49	6.45	5.52	0.47
IRS 9	0.21	0.58	0.39	0.06				

Note. Uncertainties in V + 06 flux densities are $\pm 30\%$. Sources used as flux calibrators are marked with *.

ORCID iDs

Harshitha K. Bhat <https://orcid.org/0000-0002-4408-0650>
 Nadeen B. Sabha <https://orcid.org/0000-0001-7134-9005>
 Michal Zajaček <https://orcid.org/0000-0001-6450-1187>
 Andreas Eckart <https://orcid.org/0000-0001-6049-3132>
 Rainer Schödel <https://orcid.org/0000-0001-5404-797X>
 S. Elaheh Hosseini <https://orcid.org/0000-0002-3004-6208>
 Florian Peißker <https://orcid.org/0000-0002-9850-2708>
 Anton Zensus <https://orcid.org/0000-0001-7470-3321>

References

- Aannestad, P. A. 1975, *ApJ*, 200, 30
 Aitken, D. K., Smith, C. H., Moore, T. J. T., & Roche, P. F. 1998, *MNRAS*, 299, 743
 Baganoff, F. K., Maeda, Y., Morris, M., et al. 2003, *ApJ*, 591, 891
 Becklin, E. E., Gatley, I., & Werner, M. W. 1982, *ApJ*, 258, 135
 Blandford, R. D., & Begelman, M. C. 1999, *MNRAS*, 303, L1
 Blank, M., Morris, M. R., Frank, A., Carroll-Nellenback, J. J., & Duschl, W. J. 2016, *MNRAS*, 459, 1721
 Blum, R. D., Sellgren, K., & Depoy, D. L. 1996, *ApJ*, 470, 864
 Borkar, A., Eckart, A., Straubmeier, C., et al. 2020, in *Multifrequency Behaviour of High Energy Cosmic Sources (Trieste: SISSA)*, 33
 Bower, G. C., Wright, M. C. H., Falcke, H., & Backer, D. C. 2003, *ApJ*, 588, 331
 Brandl, B., Bettonvil, F., van Boekel, R., et al. 2021, *Msngr*, 182, 22
 Carr, J. S., Sellgren, K., & Balachandran, S. C. 2000, *ApJ*, 530, 307
 Christopher, M. H., Scoville, N. Z., Stolovy, S. R., & Yun, M. S. 2005, *ApJ*, 622, 346
 Cotera, A., Morris, M., Ghez, A. M., et al. 1999, in *ASP Conf. Ser. 186, The Central Parsecs of the Galaxy*, ed. H. Falcke et al. (San Francisco, CA: ASP), 240
 Cowie, L. L., & McKee, C. F. 1977, *ApJ*, 211, 135
 Eckart, A., Genzel, R., Krabbe, A., et al. 1992, *Natur*, 355, 526
 Eckart, A., Genzel, R., Ott, T., & Schödel, R. 2002, *MNRAS*, 331, 917
 Eckart, A., Hüttemann, A., Kiefer, C., et al. 2017, *FoPh*, 47, 553
 Falcke, H., & Markoff, S. B. 2013, *CQGra*, 30, 244003
 Fritz, T. K., Gillessen, S., Dodds-Eden, K., et al. 2011, *ApJ*, 737, 73
 Genzel, R., Eisenhauer, F., & Gillessen, S. 2010, *RvMP*, 82, 3121
 Genzel, R., Pichon, C., Eckart, A., Gerhard, O. E., & Ott, T. 2000, *MNRAS*, 317, 348
 Gravity Collaboration, Rodríguez-Coira, G., Paumard, T., et al. 2021, *A&A*, 651, A37
 Hsieh, P.-Y., Koch, P. M., Kim, W.-T., et al. 2021, *ApJ*, 913, 94
 Jackson, J. M., Geis, N., Genzel, R., et al. 1993, *ApJ*, 402, 173
 Karas, V., Svoboda, J., & Zajaček, M. 2021, arXiv:1901.06507
 Kunneriath, D., Eckart, A., Vogel, S. N., et al. 2012, *A&A*, 538, A127
 Lacy, J. H., Townes, C. H., Geballe, T. R., & Hollenbach, D. J. 1980, *ApJ*, 241, 132
 Lo, K. Y., & Claussen, M. J. 1983, *Natur*, 306, 647
 Lutz, D., Krabbe, A., & Genzel, R. 1993, *ApJ*, 418, 244
 Marrone, D. P., Moran, J. M., Zhao, J.-H., & Rao, R. 2006, *ApJ*, 640, 308
 Mills, E. A. C., Güsten, R., Requena-Torres, M. A., & Morris, M. R. 2013, *ApJ*, 779, 47
 Mossoux, E., & Eckart, A. 2018, *MNRAS*, 474, 3787
 Moultaqa, J., Eckart, A., & Mužić, K. 2015a, *ApJ*, 806, 202
 Moultaqa, J., Eckart, A., & Sabha, N. 2015b, *MNRAS*, 448, 3363
 Moultaqa, J., Eckart, A., Viehmann, T., et al. 2004, *A&A*, 425, 529
 Mužić, K., Eckart, A., Schödel, R., et al. 2010, *A&A*, 521, A13
 Mužić, K., Eckart, A., Schödel, R., Meyer, L., & Zensus, A. 2007, *A&A*, 469, 993
 Najarro, F., Krabbe, A., Genzel, R., et al. 1997, *A&A*, 325, 700
 Nitschai, M. S., Neumayer, N., & Feldmeier-Krause, A. 2020, *ApJ*, 896, 68
 Ott, T. 2012, QFitsView: FITS file viewer, Astrophysics Source Code Library, ascl:1210.019
 Ott, T., Eckart, A., & Genzel, R. 1999, *ApJ*, 523, 248
 Paumard, T., Genzel, R., Martins, F., et al. 2006, *ApJ*, 643, 1011
 Paumard, T., Pfuhl, O., Martins, F., et al. 2014, *A&A*, 568, A85
 Peißker, F., Ali, B., Zajaček, M., et al. 2021, *ApJ*, 909, 62
 Peißker, F., Eckart, A., Sabha, N. B., Zajaček, M., & Bhat, H. 2020a, *ApJ*, 897, 28
 Peißker, F., Hosseini, S. E., Zajaček, M., et al. 2020b, *A&A*, 634, A35
 Peißker, F., Zajaček, M., Eckart, A., et al. 2019, *A&A*, 624, A97
 Reid, M. J., Menten, K. M., Genzel, R., et al. 2003, *ApJ*, 587, 208
 Rieke, G. H., Telesco, C. M., & Harper, D. A. 1978, *ApJ*, 220, 556
 Rózańska, A., Czerny, B., Kunneriath, D., et al. 2014, *MNRAS*, 445, 4385
 Rózańska, A., Kunneriath, D., Czerny, B., Adhikari, T. P., & Karas, V. 2017, *MNRAS*, 464, 2090
 Roche, P. F., Lopez-Rodriguez, E., Telesco, C. M., Schödel, R., & Packham, C. 2018, *MNRAS*, 476, 235
 Schödel, R., Eckart, A., Alexander, T., et al. 2007, *A&A*, 469, 125
 Schödel, R., Feldmeier, A., Neumayer, N., Meyer, L., & Yelda, S. 2014, *CQGra*, 31, 244007
 Schödel, R., Merritt, D., & Eckart, A. 2009, *A&A*, 502, 91
 Serabyn, E., Lacy, J. H., & Achtermann, J. M. 1991, *ApJ*, 378, 557
 Shukla, H., Yun, M. S., & Scoville, N. Z. 2004, *ApJ*, 616, 231
 Stolovy, S. R., Hayward, T. L., & Herter, T. 1996, *ApJL*, 470, L45
 Tanner, A., Ghez, A. M., Morris, M., et al. 2002, *ApJ*, 575, 860
 Tsuboi, M., Kitamura, Y., Tsutsumi, T., et al. 2020, *PASJ*, 72, 36
 Viehmann, T., Eckart, A., Schödel, R., et al. 2005, *A&A*, 433, 117
 Viehmann, T., Eckart, A., Schödel, R., Pott, J. U., & Moultaqa, J. 2006, *ApJ*, 642, 861
 Vollmer, B., Beckert, T., & Duschl, W. J. 2004, *A&A*, 413, 949
 Vollmer, B., & Duschl, W. J. 2000, *NewA*, 4, 581
 Wang, Q. D., Nowak, M. A., Markoff, S. B., et al. 2013, *Sci*, 341, 981

Yusef-Zadeh, F., & Melia, F. 1992, [ApJL](#), **385**, L41
Yusef-Zadeh, F., & Morris, M. 1991, [ApJL](#), **371**, L59
Yusef-Zadeh, F., Morris, M., & Ekers, R. D. 1990, [Natur](#), **348**, 45
Yusef-Zadeh, F., Royster, M., Wardle, M., et al. 2020, [MNRAS](#), **499**, 3909
Yusef-Zadeh, F., Wardle, M., Cotton, W., et al. 2017, [ApJ](#), **837**, 93

Zajaček, M., Araudo, A., Karas, V., et al. 2020b, arXiv:2011.12868
Zajaček, M., Araudo, A., Karas, V., Czerny, B., & Eckart, A. 2020a, [ApJ](#), **903**, 140
Zhao, J.-H., Blundell, R., Moran, J. M., et al. 2010, [ApJ](#), **723**, 1097
Zhao, J.-H., Morris, M. R., Goss, W. M., & An, T. 2009, [ApJ](#), **699**, 186

4

Paper III - Influence of Jets on [OIII] Extensions in Green Pea/Bean Galaxies

Galaxies with strong [OIII] λ 5007 emission have been associated in the literature with extreme star formation and/or AGN activity. Those located at intermediate red-shifts ($z \sim 0.1$) have been called ‘Green Peas’ and ‘Green beans’ due to their appearance in *gri* images, where their [OIII] lines (that fall in the r-band) dominate the emission. The [OIII] line emission is associated with powerful outflows and can serve as a clock for the starburst or AGN activity. It is also known that Green Beans exhibit ionization echoes (luminous extended narrow line regions with fading AGN activity) and act as fossils for rapid shutdown of the central AGN engine.

In this work, I observe 12 radio-selected Green Beans using long-slit spectroscopy and study their Extended Emission Line Regions (EELRs) using [OIII] λ 5007 and their associations with radio jets.

The results are submitted in the form of an article to *The Astrophysical Journal* which is currently under review.

Influence of Jets on [OIII] Extensions in Green Pea/Bean Galaxies

HARSHITHA K. BHAT ^{1,2} ANDREAS ECKART ^{1,2} PERSIS MISQUITTA ¹ MONICA VALENCIA-S. ^{1,3} MADELEINE YTTERGREN,⁴ AND ANTON ZENSUS ²

¹*Physikalisches Institut der Universität zu Köln, Zùlpicher Str. 77, D-50937 Köln, Germany*

²*Max-Planck-Institut für Radioastronomie (MPIfR), Auf dem Hügel 69, D-53121 Bonn, Germany*

³*Regional Computer Center (RRZK), Universität zu Köln, Weyertal 121, 50931 Köln, Germany*

⁴*Department of Space, Earth and Environment, Chalmers University of Technology, SE-412 96 Gothenburg, Sweden*

ABSTRACT

We present a study investigating the influence of jets on galaxies exhibiting strong [OIII] λ 5007 emission, known as ‘Green Peas’ and ‘Green Beans.’ Our sample comprised 12 nearby sources ($z \sim 0.04 - 0.1$, 6 with jets and 6 without jets) with high [OIII] luminosity ($L \sim 10^{40}$ erg/s), selected from a radio-selected galaxy sample observed with SDSS-FIRST surveys. We perform LBT-MODS long-slit spectroscopy at two position angles for each galaxy: one aligned with the jet direction and another perpendicular to it. By tracing the [OIII] emission along these slits, our aim was to assess the extension of the Narrow Line Region (NLR) and examine the impact of jets. Surprisingly, our analysis revealed no preferred direction for the extension of the [OIII] emission, indicating that jets have a limited influence on the Extended Emission Line Regions (EELRs). This also suggests the possibility of missed detection of conical-shaped EELRs aligned with the jets, attributable to our slit orientations. Furthermore, we compared the extension of [OII] emission, which traces star-forming regions, with that of [OIII]. We observed a significant difference, with [OII] exhibiting a considerably greater extension along the galactic plane. This suggests a stronger association of [OII] emission with stellar processes.

1. INTRODUCTION

Extended warm ionized gas, called narrow line regions (NLRs) surrounds radio-loud quasars and is primarily photoionized by the hard ionizing radiation of the Active Galactic Nuclei (AGN) (Netzer 2015). NLRs can reach up to kiloparsecs and are excited by energetic outflows. In the case of luminous, highly accreting AGNs these outflows can be driven by the radiation pressure (Alexander et al. 2010) whereas, in the case of radio-loud sources, they can be initiated by radio cores/jets (Rosario et al. 2010). In some cases, the AGN can ionize gas at larger distances forming extended emission-line regions (EELRs) and the strongest narrow emission lines (NELs, e.g., [OIII] λ 5007 can trace up to > 10 kpc (Stockton & MacKenty 1987; Schmitt et al. 2003; Stockton et al. 2006). EELRs are usually observed in Seyfert-2 galaxies and are characterized by conical or bi-conical shapes (referred to as ionization cones). The shape of EELRs depends on the luminosity and orientation of the AGN as well as the gas distribution throughout the galaxy (Mulchaey et al. 1996). The gas in the region could be the interstellar medium (ISM) of the host galaxy or gas provided by the mergers or outflows. The ionization cone is often aligned with the radio jet suggesting a strong interaction between

ISM and jet, and may even directly enhance their brightness (McCarthy et al. 1987; Wilson & Tsvetanov 1994).

Cardamone et al. (2009) reported a new class of rapidly growing emission line galaxies first noticed by volunteers in the Galaxy Zoo project and called them ‘Green Peas’ (GPs), due to their appearance in *gri* images, where their [OIII] lines (that fall in the *r*-band) dominate the emission. Amongst the 112 confirmed GPs, they find 80 star-forming galaxies with high star formation rates (SFR) and low-metallicities, 9 Seyfert-1s, 10 Seyfert-2s and 13 composite galaxies with both AGN and star-formation signatures.

Green Beans (GBs) are the galaxies first discovered by Schirmer et al. (2013) with GP colors but much larger and more luminous NLRs than GPs. They exhibit EELRs (20-40 kpc) that are ionized by radio-weak type-2 quasars (Sun et al. 2018). Even though over 98 percent of type-2 AGNs have radio luminosities larger than 10^{23} WHz^{-1} , it is less than 50 percent in the case of GBs (Mullaney et al. 2013), suggesting the significance of radiation pressure in exciting the EELRs. The current observed AGN activity is much lower than expected from the large angular extent and high [OIII] luminosities. This leads to the conclusion that GBs host recently faded AGNs whose activity has declined over timescales less than the light-crossing time of the NLR, resulting in strong light echoes/ionization echoes (Lintott et al. 2009; Knese et al. 2020; Saade et al. 2022). This was further confirmed using X-ray luminosities by Davies et al. (2015); Schirmer et al. (2016).

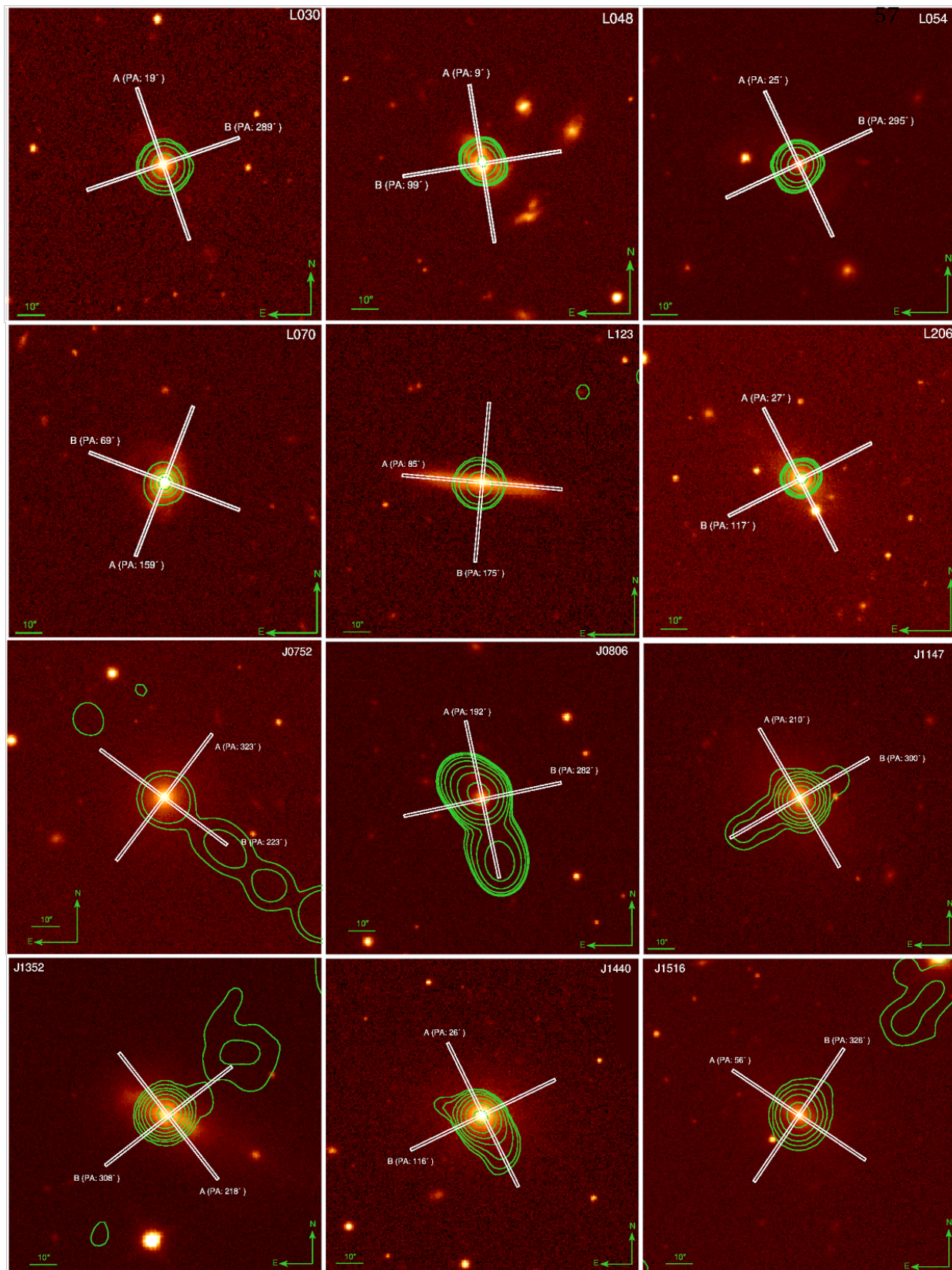


Figure 1. SDSS r-band images of all the galaxies in our sample overplotted with FIRST (1.4 GHz) contours. The contour levels are chosen arbitrarily. Observations were made at two perpendicular slit positions (marked A & B) using a 1'' slit.

It is believed that the radio jets can compress the circumnuclear ISM, which leads to enhanced emissions in the NLR. This idea is supported by studies such as Schmitt et al. (2003) and Riffel et al. (2006), where a correlation between radio emissions and NLR distributions was observed. However, other studies such as Kaiser et al. (2000) have not found this correlation. Barbosa et al. (2009) report that only a subset of their sample shows signatures of this interaction, and they acknowledge the possibility of other mechanisms for NLR outflows such as accretion disc winds. Leipski et al. (2006) found a correlation between radio and NLR sizes but suggested that this could also be due to the influence of the central engine on both parameters. Jarvis et al. (2019) demonstrate a strong relationship between radio emissions and ionized gas kinematics in the 1-25 kpc scales using high-resolution VLA observations. Our research aims to build on these findings to examine the influence of jets on NLRs and EELRs in GB/GPs, providing insights into a distinct phase of fading AGNs.

In the sample of SDSS narrow emission-line galaxies which are also detected in the FIRST radio survey, we chose objects with high [OIII] luminosity ($L \sim 10^{40}$ erg/s) and equivalent width ($EW \sim 10 - 30$ Å). From these, we selected the 12 galaxies (6 jetted and 6 non-jetted) within the redshift range $0.04 < z < 0.1$, and studied the extension of [OIII] and [OII]. We aim to determine the extension of the [OIII] emission and the role of radio jets on the EELRs in these sources.

2. DATA & OBSERVATIONS

2.1. Source selection

Vitale et al. (2012) studied a large sample of optical-radio galaxy population by cross-identifying Sloan Digital Sky Survey (SDSS) galaxies with Faint Images of the Radio Sky at Twenty-centimeters (FIRST) survey. From this sample, a subsample of 119 high-radio flux galaxies (integrated flux density at 1.4 GHz $F_{1.4} > 100$ mJy) was collected and observed at Effelsberg 100-m radio telescope at two frequencies (4.8 GHz and 10.45 GHz) by Vitale et al. (2015)). Additionally, Zajaček et al. (2019) observed low-radio flux galaxies ($F_{1.4} > 50$ mJy; 298 sources at 4.85 GHz, 90 sources at 10.45 GHz) at Effelsberg and studied the radio spectral index distribution of the combined subsample. The redshifts of the Effelsberg sample were restricted to $0.04 < z < 0.4$, to avoid aperture effects. In Table 1, we present the radio fluxes and the spectral indices calculated between 1.4 GHz (FIRST) and 4.85 GHz (and 10.45 GHz). Here the radio loudness (R) is defined as $L_{4.85}/L_O$ where $L_{4.85}$ is the integrated radio flux density at 4.85 GHz and L_O is the flux density in SDSS r -band in Jy. Sources with $\log(R) > 2.4$ are considered radio loud whereas $\log(R) \leq 2.4$ is considered radio quiet (Panessa et al. 2007).

In this SDSS-FIRST-Effelsberg sample, we have encountered objects with characteristically high [OIII] luminosity ($L \sim 10^{40}$ erg/s) and equivalent width ($EW \sim 10 - 30$ Å). We chose 12 such galaxies, 6 with jets and 6 without jets, and Fig. 1 shows the SDSS r -band images of the galaxies with

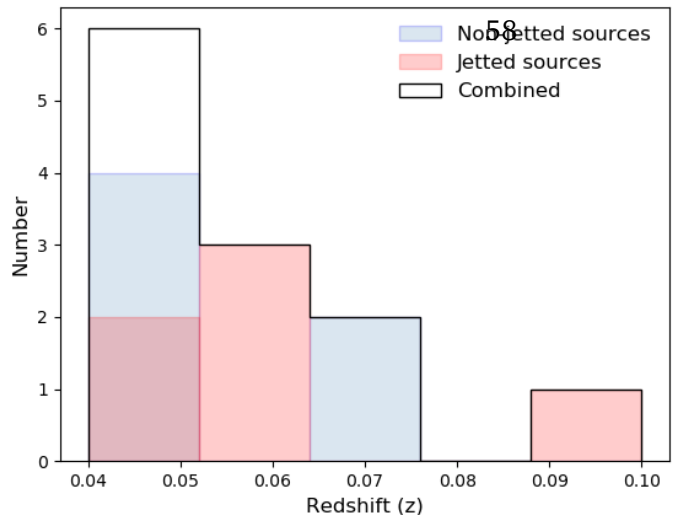


Figure 2. Redshift distribution of the selected GB galaxy sample. The selected GB galaxy sample shows a redshift distribution that mostly falls at the lower end of the range. However, there is no noticeable difference in the distribution between the jetted and non-jetted sets of galaxies.

FIRST contours. The sample galaxies are located within the redshift range $0.04 < z < 0.1$ (Fig. 2) to ensure resolving spatial scales of < 200 pc on the source and performed optical long-slit spectroscopy.

2.2. Observations

Optical long-slit spectrometry was carried out at the Large Binocular Telescope (LBT) located at Mt. Graham International Observatory in Arizona, USA. LBT has a binocular design with two circular 8.4 m wide mirrors, making the combined collecting area equivalent to a single circular mirror with a diameter of 11.8 m. Observations were made from 09-02-2019 to 27-04-2022 using the Multi-Object Double Spectrograph (MODS) mounted at the direct Gregorian foci of the mirrors. MODS are a pair of low- to medium-resolution, identical spectrographs covering the UV to near-IR wavelengths (320 nm-1100 nm), with a field-of-view of $6'' \times 6''$. A dichroic placed below each slit splits the beam at a wavelength of 565 nm into red and blue optimized channels.

We used the grating spectroscopy mode with a long $1''$ wide slit, which provides a spectral resolution of about 150 km s^{-1} and spatial resolution of 0.12 arcsec.

Each source was observed at two perpendicular slit positions, one along the jet and another perpendicular to it (or along and perpendicular to the galactic plane in the case of non-jetted sources; A & B respectively in Fig. 1). At each position, we took two exposures, one with the source at the center of the slit and another with $10''$ dithering along the slit direction. Whenever additional telescope time was available, we made multiple exposures at these angles and positions. All the observational details are provided in Table 2.

2.3. Reduction

Table 1. Radio fluxes and indices. Radio loud galaxies ($\log(R) = \log(L_{4.85}/L_O) > 2.4$) are highlighted. 59

Source	$S_{1.4GHz}$	$S_{4.85GHz}$	$S_{10.45GHz}$	$\alpha_{(1.4/4.85)}$	$\alpha_{(1.4/10.45)}$	$\log(R)$
L030	0.099	0.023	0.014	-1.176	-0.700	2.61
L048	0.012	0.136	0.008	1.983	-3.700	3.40
L054	0.021	0.009		-0.727		2.19
L070	0.011	0.006		-0.496		2.03
L123	0.068	0.026		-0.792		2.66
L206	0.010	0.006		-0.362		2.07
J0752 / L181	0.050	0.276	0.094	1.373	-1.400	3.72
J0806 / H068	0.113	0.077	0.051	-0.312	-0.525	3.13
J1147 / H070	0.615	0.223	0.225	-0.816	0.011	3.62
J1352 / H074	3.709	1.853	1.067	-0.558	-0.719	4.56
J1440 / H059	0.134	0.135	0.114	0.008	-0.219	3.41
J1516 / H119	0.756	1.191	1.034	0.366	-0.184	4.35

Table 2. Observational details. Project PI Name: Andreas Eckart

Source	Proposal ID	R.A.	Dec	Redshift	Date	Exposure time	Position Angle	
		(α)	(δ)	(z)		s	A	B
L030	LBT-2020A-I0002-0	07:57:56.71	39:59:36.13	0.0657	20-01-2020	4800	19	289
	MPIA-2021B-099				27/28-02.2022	4800		
L048	MPIA-2020B-099	01:25:16.38	-08:52:25.23	0.0490	20-10-2020	4800	9	99
L054	MPIA-2020B-099	01:37:06.95	-09:08:57.46	0.0697	20-10-2020	6000	25	295
L070	MPIA-2021A-099	11:47:21.61	52:26:58.50	0.0488	20-04-2021	4800	159	69
L123	MPIA-2021B-099	09:50:58.69	37:57:58.87	0.0414	27/29-01-2022	4800	85	175
L206	MPIA-2020B-099	07:52:38.95	18:19:17.75	0.0451	20-10-2020	5400	27	117
J0752 / L181	LBT-2018A-I0062-0	07:52:44.19	45:56:57.41	0.0518	09-02-2019	3200	234	144
	MPIA-2021B-099				28-01-2022	4800		
J0806 / H068	MPIA-2021B-099	08:06:01.51	19:06:14.71	0.0976	08-11-2021	4800	192	282
J1147 / H070	LBT-2018A-I0062-0	11:47:22.13	35:01:07.56	0.0631	09-02-2019	3200	210	300
J1352 / H074	LBT-2018A-I0062-0	13:52:17.88	31:26:46.49	0.0452	09-02-2019	4800	218	308
J1440 / H059	MPIA-2021A-099	14:40:17.98	05:56:34.03	0.0613	15/16-05-2021	4800	26	116
J1516 / H119	RDS-2022A-011	15:16:40.21	00:15:01.89	0.0527	27-04-2022	4800	56	326

Notes: 1. Nomenclature by Vitale et al. (2015); Zajaček et al. (2019) is followed here. 2. Redshifts were estimated using the observed $H\alpha$ line. 3. Whenever a galaxy was observed on more than one day, each spectrum was reduced separately and then combined accordingly.

Observed spectral frames were flat-corrected, bias-corrected, and combined using MODS CCD Reduction pipeline (Pogge 2019). Calibrations, background subtraction, and 1-D spectra extraction were done using Pyraf scripts adapted from IRAF routines based on ‘A User’s Guide to Reducing Slit Spectra with IRAF’ by Massey, Valdes & Barnes. Along with science observations, wavelength and flux calibration spectra were also observed. The wavelength was calibrated using Ne, Hg, Kr, Xe, and Ar lamps. Spectroscopic standard stars were observed for each observational run and used for flux calibration. All calibration spectra underwent similar reduction processes. Spectra from MODS1

and MODS2 channels and different dithered positions were reduced and then combined accordingly.

3. SPECTRA

We extract 1-D spectra for the central 1” aperture from both the position angles and average them to get the spectral lines (Fig. 3) at the galactic nuclei. The prominent spectral emission lines are marked in each of the spectra.

We derive flux densities and Full Width at Half Maximum (FWHM) by fitting one or more Gaussian functions for each emission line using the Levenberg- Markwardt algorithm, non-linear least-squares minimization and curve-fitting for Python (LMFIT; Markwardt (2009); Newville et al. (2016)).

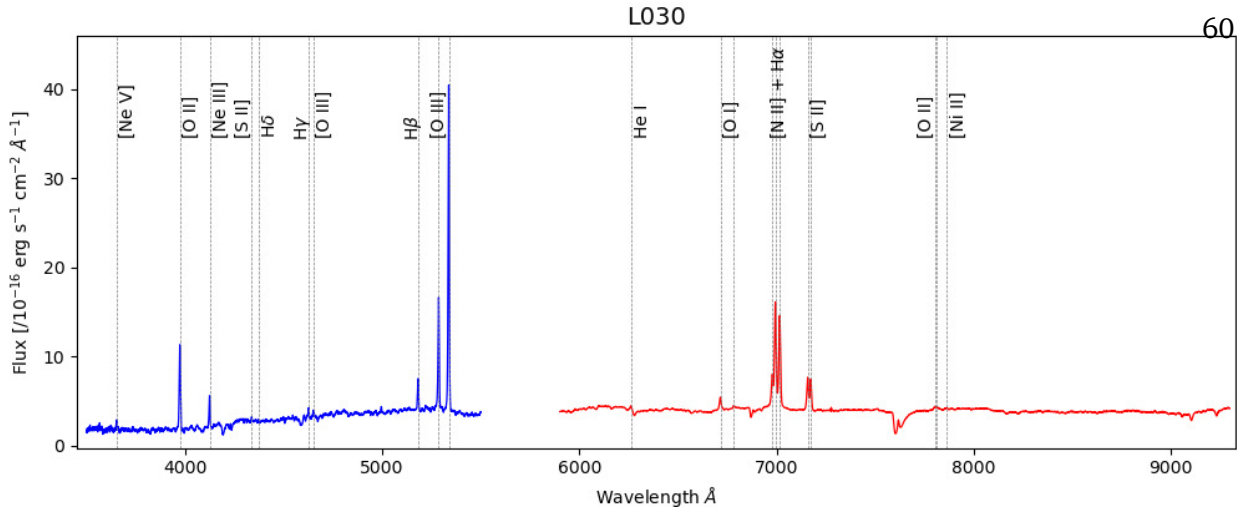


Figure 3. The averaged one-dimensional optical spectrum of the central arcsec of L030. The prominent observed emission lines are marked by dashed lines. The complete figure set for all the galaxies (12 images) is available in the online journal.

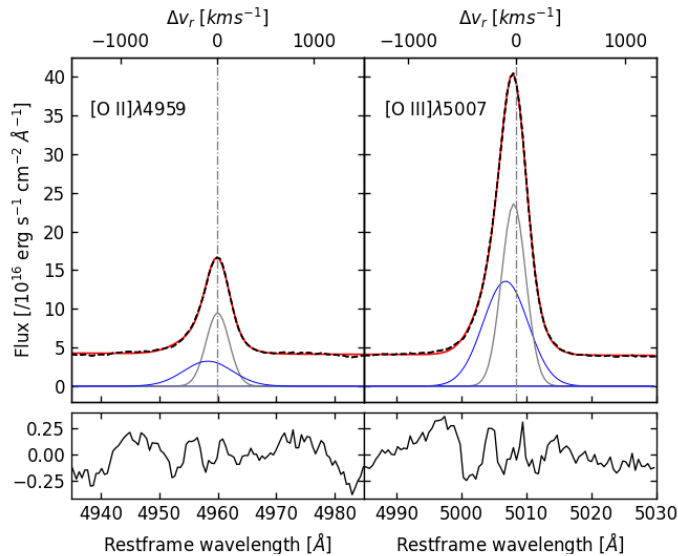


Figure 4. [O III] λ 4959,5007 region from the central 1'' spectrum of L030. Black dashed line: Continuum with emission lines around [O III] λ 4959,5007. Grey solid line: Gaussian fit at the line center. Blue solid line: Gaussian fit to account the blue wing in the emission line. Red solid line: Model spectra produced by combining both the Gaussians at each emission line. The lower panel shows the observed minus model residuals.

The derived flux densities, FWHM, and the wavelength at which the lines were observed are all presented in Tables. 3. We have calculated and reported the redshifts in Table. 2 using the observed central wavelengths of the H α line and the formula $z = (\lambda_o - \lambda_l)/\lambda_l$, where λ_o refers to the observed central wavelength, while λ_l is the laboratory wavelength of H α , 6562.81 Å. In the following subsections, we give a brief introduction to each galaxy in the sample.

3.1. L030

We cross-identify L030 as B3 0754+401, WISEA J075756.71+395936.1, 2MASX J07575670+3959363, 2MASXi J0757567+395936 and 2MASS J07575671+3959361 using NASA/IPAC Extragalactic Database¹. It has been previously classified as Seyfert 2 by Toba et al. (2014). L030 is one of the non-jetted sources with compact radio emission. The nucleus exhibits several strong emission lines, and the emission in [OIII] λ 5007 is particularly very high. Flux densities and FWHM of the strong emission lines are presented in Table 3. The striking feature of L030 spectrum is the blue-ward asymmetries in narrow, high-ionization emission lines, [OIII] λ 4959 and [OIII] λ 5007 as shown in Fig. 4. As these forbidden lines trace the low-density ionized gas, the blueshift in the emission line indicates the Doppler effect caused by the gas moving towards us and hence widely used as the outflow signatures in AGNs (Whittle 1985; Leighly & Moore 2004; Crenshaw et al. 2015). By fitting the blue wing with a separate Gaussian, we find that the outflow velocities are 318 km/s and 232 km/s when derived from [OIII] λ 4959 and [OIII] λ 5007, respectively. L030 also has [Ne V] λ 3427 and [N III] λ 3869, which suggests a hard ionizing spectrum.

3.2. L048

L080 was cross-identified as MCG -02-04-045, WISEA J012516.37-085225.0, 2MASX J01251637-0852250, 2MASS J01251638-0852251 and SDSS J012516.37-085225.2 using NASA/IPAC Extragalactic Database². It has been classified as Low-power Radio Galaxy by Lin et al. (2018) and as an AGN by Ge et al. (2012); Toba et al. (2014). We see several strong emission lines, with broad components in both H α λ 6563 and H β λ 4861. The blue-wing component is present in high-ionization emission lines, [OIII] λ 4959 and

¹ https://ned.ipac.caltech.edu/byname?objname=B3+0754%2B401&hconst=67.8&omegam=0.308&omegav=0.692&wmap=4&corr_z=1

² https://ned.ipac.caltech.edu/byname?objname=MCG+-02-04-045&hconst=67.8&omegam=0.308&omegav=0.692&wmap=4&corr_z=1

Table 3. Central Emission Lines of L030. Tables for all 12 galaxies are published in its entirety in the machine-readable format. An example for L030 is shown here for guidance regarding its form and content.

Emission line	Observed wavelength (λ_o) (Å)	$\Delta\lambda_o$ (Å)	Flux (F) ($10^{-16}\text{ergs}^{-1}\text{cm}^{-2}$)	ΔF ($10^{-16}\text{ergs}^{-1}\text{cm}^{-2}$)	$FWHM$ (kms^{-1})	$\Delta FWHM$ (kms^{-1})
[Ne V] λ 3426	3652.7	0.19	6.31	0.41	466.0	34.0
[O II] λ 3729	3973.09	0.02	66.35	0.44	489.0	4.0
[Ne III] λ 3869	4124.31	0.2	8.6	3.97	276.0	44.0
H γ λ 4340	4626.36	0.25	5.52	0.5	340.0	36.0
[O III] λ 4363	4651.22	0.39	4.93	0.57	427.0	56.0
H β λ 4861	5181.62	0.04	20.32	0.32	321.0	6.0
[O III] λ 4959 _{blue}	5280.64	0.45	12.55	1.46	401.0	85.0
[O III] λ 4959	5286.25	0.05	68.14	1.69	303.0	4.0
[O III] λ 5007 _{blue}	5333.3	0.96	43.21	13.12	397.0	90.0
[O III] λ 5007	5337.43	0.06	184.02	13.01	291.0	4.0
He I λ 5876	6260.77	0.74	2.65	0.59	306.0	79.0
[O I] λ 6300	6714.75	0.26	13.57	0.72	423.0	26.0
[N II] λ 6548	6978.25	0.22	19.97	2.79	333.0	26.0
H α λ 6563	6994.16	0.05	78.76	3.45	329.0	7.0
H α λ 6563 _{broad1}	6992.25	1.27	42.96	8.77	1102.0	157.0
H α λ 6563 _{broad2}	6994.23	1.46	70.42	6.8	3129.0	237.0
[N II] λ 6583	7016.22	0.04	87.69	1.34	368.0	4.0
[S II] λ 6716	7158.18	0.11	37.3	0.85	412.0	11.0
[S II] λ 6731	7173.37	0.11	32.35	0.81	365.0	11.0
[O II] λ 7320	7801.61	0.37	1.34	0.28	262.0	40.0
[O II] λ 7331	7811.62	0.64	8.7	0.46	13.0	0.0
[Ni II] λ 7378	7861.51	0.45	2.79	0.2	514.0	39.0

[OIII] λ 5007 as well as [OII] λ 3729 and [SII] λ 6716. The outflow velocity corresponding to the blue-winged [OIII] λ 5007 line is around 450 km/s.

3.3. L054

We cross-identify L054 as GIN 086, WISEA J013706.94-090857.3, 2MASX J01370694-0908575, 2MASS J01370694-0908575 and SDSS J013706.94-090857.5 using NASA/IPAC Extragalactic Database³. It has been classified as Seyfert 1 by Oh et al. (2015) and as Seyfert 2 by Toba et al. (2014). Upon analyzing the central spectrum of L054, we observed strong emission lines with broad components in both H α and H β . Additionally, there are strong outflow signatures in NeIII λ 3869, [OIII] λ 4959 and [OIII] λ 5007, with respective outflow velocities of 214 km/s, 111 km/s, and 248 km/s.

3.4. L070

L070 can be cross-identified as MRK 1457, MRK 1456 GROUP NED02, SBS 1144+527B, KUG 1144+527B and

CGCG 268-083 using NASA/IPAC Extragalactic Database⁴. L070 is a compact radio galaxy. Its spectrum shows extremely high [OIII] λ 5007 along with [OIII] λ 4959 emission with blue-winged components indicating outflow velocities reaching upto 200 km/s. Even though it is classified as Seyfert 2 (Toba et al. 2014), we see broad H α components. It also shows [NeV] λ 3426 and [ArIII] λ 7136 indicating a hard ionizing spectrum.

3.5. L123

We cross-identified L123 as FGC 0955, RFGC 1643, 2MFGC 07622, WISEA J095058.73+375758.3 and 2MASX J09505867+3757584 using NASA/IPAC Extragalactic Database⁵. It is an edge-on galaxy with an elongated morphology. L123 is classified as Seyfert 1 (Toba et al. 2014) and shows a broad H α component. We see that [OII] λ 3729 is greatly extended along the galactic plane upto 2 kpc from the center, as it can be produced by star formation regions in the galaxy. L123 also shows outflow signatures

³ https://ned.ipac.caltech.edu/byname?objname=GIN+086&hconst=67.8&omegam=0.308&omegav=0.692&wmap=4&corr_z=1

⁴ https://ned.ipac.caltech.edu/byname?objname=MRK+1457&hconst=67.8&omegam=0.308&omegav=0.692&wmap=4&corr_z=1

⁵ https://ned.ipac.caltech.edu/byname?objname=FGC+0955&hconst=67.8&omegam=0.308&omegav=0.692&wmap=4&corr_z=1

in [OIII] λ 4959,5007 with respective outflow velocities of 185 km/s and 135 km/s.

3.6. L206

We cross-identified L206 as WISEA J075238.95+181917.7, 2MASX J07523897+1819180, 2MASXi J0752389+181918, 2MASS J07523895+1819178 and SDSS J075238.95+181917.7⁶. It is also classified as Seyfert 2 by Toba et al. (2014). It shows several strong narrow lines and has blue-winged outflow signature in [OIII] λ 4959 line and by fitting a blue-winged component we derive the outflow velocity to be 267 km/s. It is a compact low energy radio source and shows extension in [OIII] and [OII] along the galactic plane.

3.7. J0752

J0752 can be cross-identified as B3 0749+460A, WISEA J075244.20+455657.4, 2MASX J07524421+4556576, 2MASXi J0752442+455657 and 2MASS J07524421+4556575⁷. It is a BL Lac object (D’Abrusco et al. 2019) with high X-ray emission (Cusumano et al. 2010). Its spectrum shows several strong narrow emission lines, and is dominated by [OIII] λ 5007 emission in the blue channel and [NII] λ 6583 emission in the red channel. It has a radio jet on one direction extending upto 3’. The outflow signatures in [OIII] λ 4959,5007 indicate respective velocities of 225 km/s and 94 km/s.

3.8. J0806

We cross-identified J0806 as WISEA J080601.54+190614.6, 2MASX J08060148+1906142, 2MASS J08060153+1906148, SDSS J080601.51+190614.7 and SDSS J080601.52+190614.7⁸. It is a Seyfert 2 (Toba et al. 2014) with compact high energy radio emission. Its spectrum is dominated by [OIII] λ 5007 emission, and has weaker H α and H β emission but no outflow signatures.

3.9. J1147

J1147 was cross-identified as CGCG 186-048, CGCG 1144.7+3518, B2 1144+35B, 2MASX J11472209+3501071 and 2MASXi J1147220+350107⁹. It has been classified as a BL Lac object by D’Abrusco et al. (2019), as Seyfert 1 by Oh et al. (2015) and as Seyfert 2 by Toba et al. (2014). It is a compact radio source with relatively smaller jets extending upto 30’’ on either side. Its spectrum is dominated by extremely high [OIII] λ 5007 emission with an outflow signature whose velocities reach up to 178 km/s. It is known to have

⁶ https://ned.ipac.caltech.edu/byname?objname=WISEA+J075238.95%2B181917.7&hconst=67.8&omegam=0.308&omegav=0.692&wmap=4&corr_z=1

⁷ https://ned.ipac.caltech.edu/byname?objname=B3+0749%2B460A&hconst=67.8&omegam=0.308&omegav=0.692&wmap=4&corr_z=1

⁸ https://ned.ipac.caltech.edu/byname?objname=WISEA+J080601.54%2B190614.6&hconst=67.8&omegam=0.308&omegav=0.692&wmap=4&corr_z=1

⁹ https://ned.ipac.caltech.edu/byname?objname=CGCG+186-048&hconst=67.8&omegam=0.308&omegav=0.692&wmap=4&corr_z=1

high X-ray emission (Malizia et al. 2016) which confirms the presence of AGN.

3.10. J1352

We cross-identified J1352 as UGC 08782, VV 369, CGCG 162-021, CGCG 1350.0+3142 and MCG +05-33-012¹⁰. It has been classified as a BL Lac object by D’Abrusco et al. (2019). Its 1-D spectrum shows several emission lines including a broad H α line. Interestingly, [OII] λ 3729 emission dominates the blue channel, indicating softer ionizing spectra. Blue-winged components are evident in [OII] λ 3729, [OIII] λ 4959, [OIII] λ 5007 and [SII] λ 6716 indicates strong outflows upto 278 km/s in the central regions of the galaxy. J1352 also has X-ray emission (Ueda et al. 2005). FIRST radio contours show highly extended jets in both the direction, however, the one pointing North-West (Fig. 1) is much brighter.

3.11. J1440

We cross-identified J1440 as 2MASX J14401795+0556341, GALEXASC J144017.93+055633.9, GALEXMSC J144018.03+055634.6, SPIDER J220.07493+05.94279 and SDSS J144017.98+055634.0¹¹. It has been classified as Seyfert 2 by Toba et al. (2014). We see several narrow emission lines, however, H α is very weak and H β could not be detected. We also see a blue-winged outflow signature in [OIII] λ 5007 with outflow velocity of around 590 km/s. Radio contours show a jet-like morphology on one side of the galaxy.

3.12. J1516

J1516 was cross-identified with several other objects such as CGCG 021-063, CGCG 1514.1+0025, 4C +00.56, PKS 1514+00 and WISEA J151640.21+001501.9¹². According to Oh et al. (2015), it is classified as a Seyfert 1 object, while D’Abrusco et al. (2019) classify it as a BL Lac object. J1516 also shows X-ray emission (Nisbet & Best 2016). The 1-Dimensional spectrum of central 1’’ shows strong emission lines including [OIII] λ 4959,5007 and [NII] λ 6548,6583+H α λ 6563 complex, but no noticeable outflow signatures in [OIII] λ 4959,5007 lines. The spectrum also reveals a stellar continuum. The FIRST images (green contours in Fig. 1) show the jets in both directions extending over 4’.

4. RESULTS

4.1. Diagnostic diagrams

¹⁰ https://ned.ipac.caltech.edu/byname?objname=UGC+08782&hconst=67.8&omegam=0.308&omegav=0.692&wmap=4&corr_z=1

¹¹ https://ned.ipac.caltech.edu/byname?objname=2MASX+J14401795%2B0556341&hconst=67.8&omegam=0.308&omegav=0.692&wmap=4&corr_z=1

¹² https://ned.ipac.caltech.edu/byname?objname=CGCG%20021-063&hconst=67.8&omegam=0.308&omegav=0.692&wmap=4&corr_z=1

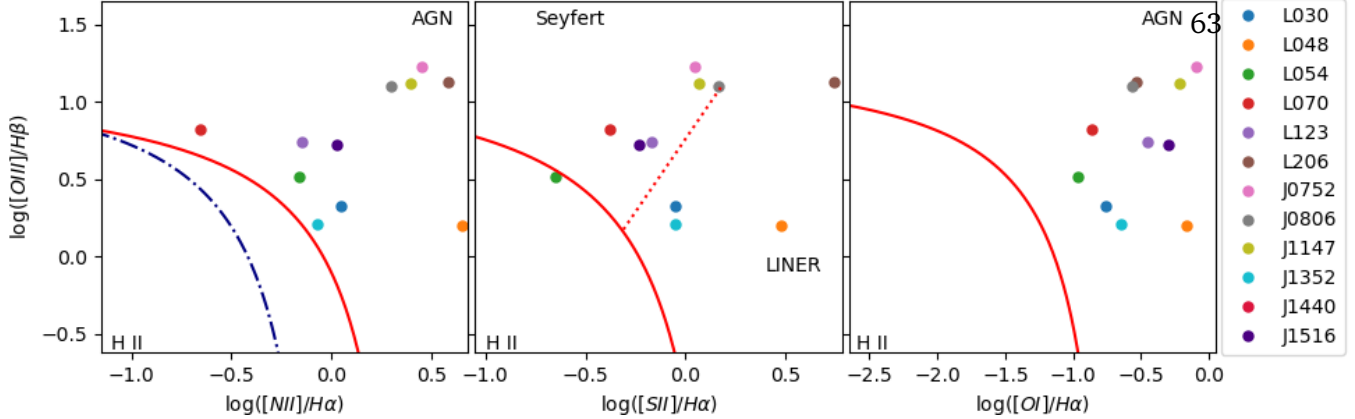


Figure 5. BPT diagram using the flux ratios of central 1". All the galaxies fall at the higher end of $\log([OIII]/H\beta)$ ratio, indicating the presence of AGN.

Unlike BLRs, NLRs do not directly indicate nuclear activity. As our spectra consist of dominant NELs, we use the diagnostic diagrams devised by Baldwin et al. (1981) to categorize our sources based on their primary ionizing source. The BPT diagram along with the diagnostic diagrams introduced by Veilleux & Osterbrock (1987), use emission line ratios ($[OIII]/H\beta$, $[NII]/H\alpha$, $[SII]/H\alpha$ and $[OI]/H\alpha$) to classify galaxies into star-burst galaxies or active galaxies. Kewley et al. (2001) proposed theoretical models to predict the maximum star-formation contribution, represented by red solid lines in Fig. 5 and Kauffmann et al. (2003) empirically moved this line (blue dot-dashed line) based on extensive observational data. The objects that fall between the two lines are considered transition objects, with both ongoing star formation and AGN. Fig. 5 shows that all the sources in our sample have AGNs as their dominant ionizing source and some may even be classified as LINERs (Low-Ionization Nuclear Emission-Line Regions).

4.2. Mid-IR vs. $[OIII]\lambda 5007$ Luminosities

Low-luminosity AGNs are believed to represent the initial or final stages of the galaxies' active phases. Thermal emission from the warm dusty torus is strongest in MIR, and the observed MIR luminosities represent the re-processed UV/X-ray radiation from the dusty clouds inside the torus. MIR emission also correlates with the X-ray brightness over a wide range of luminosities and hence can be used as a proxy for AGN activity (Lutz et al. 2004; Horst et al. 2009; Asmus et al. 2011).

Schirmer et al. (2013) compared MIR- $[OIII]$ relation of a set of Green Beans with a larger sample of type-2 galaxies from Reyes et al. (2008); Greene et al. (2011). They plot the *WISE* luminosities at $24\ \mu\text{m}$ (W4 filter, as it is not affected by dust absorption) against $[OIII]\lambda 5007$ luminosities and conclude that the $24\ \mu\text{m}$ luminosities of GBs are in the same range as of other obscured type-2 galaxies however their $[OIII]$ emission was 5-50 times greater. This could be explained by the light echo scenario where the NLR is re-

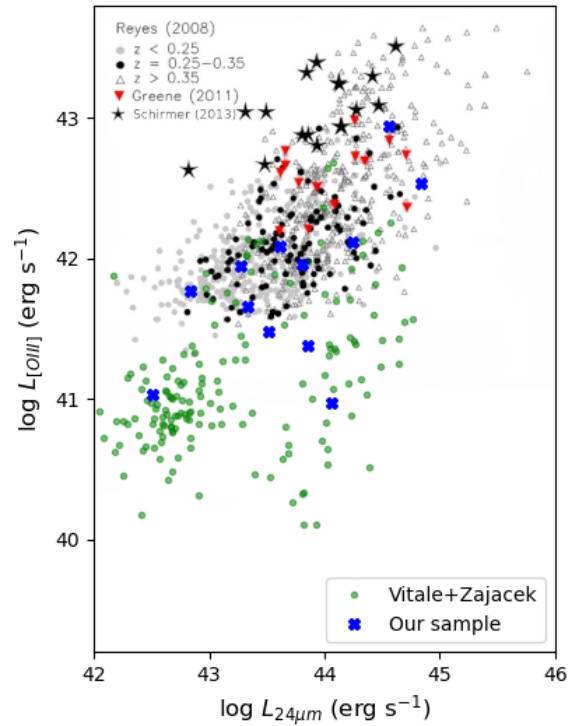


Figure 6. *WISE* $24\ \mu\text{m}$ vs. $[OIII]\lambda 5007$ luminosities from Schirmer et al. (2013) overplotted with Vitale et al. (2015); Zajaček et al. (2019) sources in the range $0.04 < z < 0.1$. Due to the difference in selection processes, VZ sources exhibit both lower $L_{[OIII]}$ and lower $L_{[24\mu\text{m}]}$ values. However, among these radio-selected VZ sources, our GB sample (blue crosses) stands out with higher $[OIII]$ luminosities.

flecting an earlier active state of AGN which has declined significantly in less than the light crossing time.

We overplot MIR and $[OIII]$ luminosities of Vitale et al. (2015); Zajaček et al. (2019) sources over Schirmer et al. (2013) plot in Fig. 6. It is to be noted that the redshift range of radio-selected galaxies was constrained to $0.04 < z < 0.1$ to match the galaxy sample considered in this paper. We see a general trend of lower $[OIII]$ luminosities in radio-

selected galaxies, compared to the type-2 galaxies covered in Reyes et al. (2008); Greene et al. (2011). However, among the radio-selected galaxies, our GB sample stands out with higher [OIII] luminosities even though the two are indistinguishable in MIR.

When compared with Schirmer et al. (2013), we find that the radio selection does not particularly increase the number of sources with strong [OIII] line emission. Only two out of twelve sources in our sample fell within the [OIII] luminosity range of Schirmer et al. (2013).

Strong radio emission can indicate recent activity (by feeding the central black hole) or enhanced high-mass star formation. We find that despite stronger non-thermal radio emission, there was no significant decline in line emission during bulge crossing time scales. This may be obvious in jetted sources, as the presence of a jet with expansion speeds less than the speed of light suggests prolonged ongoing quasi-continuous activity. However, in non-jetted sources, such an argument is less obvious but indicates nuclear activity on time scales that exceed bulge crossing time scales.

4.3. Extended emission

To examine the relationship between NELs and the distance from the galactic center, we made a cut across the 2D spectrum at the line position. Our cut was carefully chosen to encompass the velocity dispersion of the galaxy while ensuring no overlap from neighboring lines. The resulting plot in Fig. 7 illustrates the normalized flux of [OIII] λ 5007 across the galaxy, alongside the continuum fluxes. This representation allows for a fair comparison of line extensions along and perpendicular to the radio jets. A similar plot for [OII] λ 3729 is presented in Fig. 8.

To investigate whether there is a preferred direction for the extended [OIII] emission, we measured the full widths at 50% and 90% of the maximum flux in both directions, as shown in Fig. 9. We conducted a two Kolmogorov-Smirnov test (KS-Test) between the distributions in either direction (i. 50% of maximum flux - \parallel plane vs \perp plane; ii. 90% of maximum flux - \parallel plane vs \perp plane) to compare the extended widths along the parallel and perpendicular planes. The resulting p-values of 0.249 and 0.518, respectively, indicate no significant systematic difference between the samples, suggesting the absence of a preferred direction for the [OIII] emission.

In contrast, when comparing the extended [OII] emission, we observed a distinct pattern. The p-value of approximately 0.034 obtained from FWHM along the parallel plane versus the perpendicular plane suggests two different distributions between the samples. Specifically, [OII] exhibits systematic extensions primarily along the galactic plane. This behavior can be attributed to the lower ionizing potential of [OII] and its production by stellar photons.

To estimate the impact of jet presence on the observed extensions, we conducted separate tests for jetted and non-jetted sources. The corresponding p-values are presented in Table 4, indicating no significant difference in the extensions between the two groups. However, it is worth noting that the

conical shape of the ionized NLR implies a potential misalignment between the slit position and the EELR associated with the jets. Therefore, the observed lack of extended [OIII] emission in those regions could be attributed to this misalignment.

In summary, our study examined the extensions of NELs about the galactic center. The analysis revealed no preferred direction for the extended [OIII] emission while demonstrating the systematic extensions of [OII] predominantly along the galactic plane. Furthermore, the lack of significant differences in extensions between jetted and non-jetted sources suggests the need for careful consideration of the alignment between the slit position and the EELR in future studies.

5. SUMMARY

In this study, we focused on galaxies exhibiting strong [OIII] λ 5007 emission, which has been associated with extreme star formation and/or active galactic nuclei in the literature. These galaxies, often referred to as ‘Green Peas’ and ‘Green Beans,’ display a prominent appearance in *gri* images due to the dominance of their [OIII] lines (which fall in the r-band). From a larger radio-selected galaxy sample observed with SDSS-FIRST, we selected 12 nearby sources (with redshifts approximately ranging from 0.04 to 0.1), characterized by high [OIII] luminosity ($L \sim 10^{40}$ erg/s).

To investigate the potential impact of jets on the EELRs, we conducted LBT-MODS long-slit spectroscopy at two different position angles for each selected galaxy. One slit was aligned along the direction of the jet, while the other was oriented perpendicular to it. By tracing the [OIII] emission along both slit positions, we aimed to estimate the extension of the Narrow Line Region (NLR).

Our analysis revealed that there is no preferential direction for the extension of the [OIII] emission, suggesting that the presence of jets does not significantly affect the EELRs. This finding implies that if the EELRs are conical in shape with their axes aligned with the jets, we may have missed their detection by placing the slits parallel or perpendicular to the jet directions.

Furthermore, we also plotted the extension of [OII] emission, which traces the star-forming regions within the galaxy. Interestingly, we observed that [OII] exhibits a much greater extension along the galactic plane compared to [OIII]. This disparity could be due to the lower ionization potential of [OII] and its association with stellar processes.

In summary, our study of high [OIII] emitting galaxies selected from a radio-selected sample demonstrated no preferential direction for the extension of [OIII] emission, suggesting a limited impact of jets on the EELRs. We highlighted the possibility of missing conical-shaped EELRs aligned with the jets by using slits along or perpendicular to the jet directions. Moreover, the significant extension of [OII] emission along the galactic plane emphasized its association with star-forming regions within the galaxies.

Acknowledgements: We would like to thank the reviewer for their constructive suggestions and feedback that helped us improve the quality of this manuscript significantly. This work was supported in part by SFB

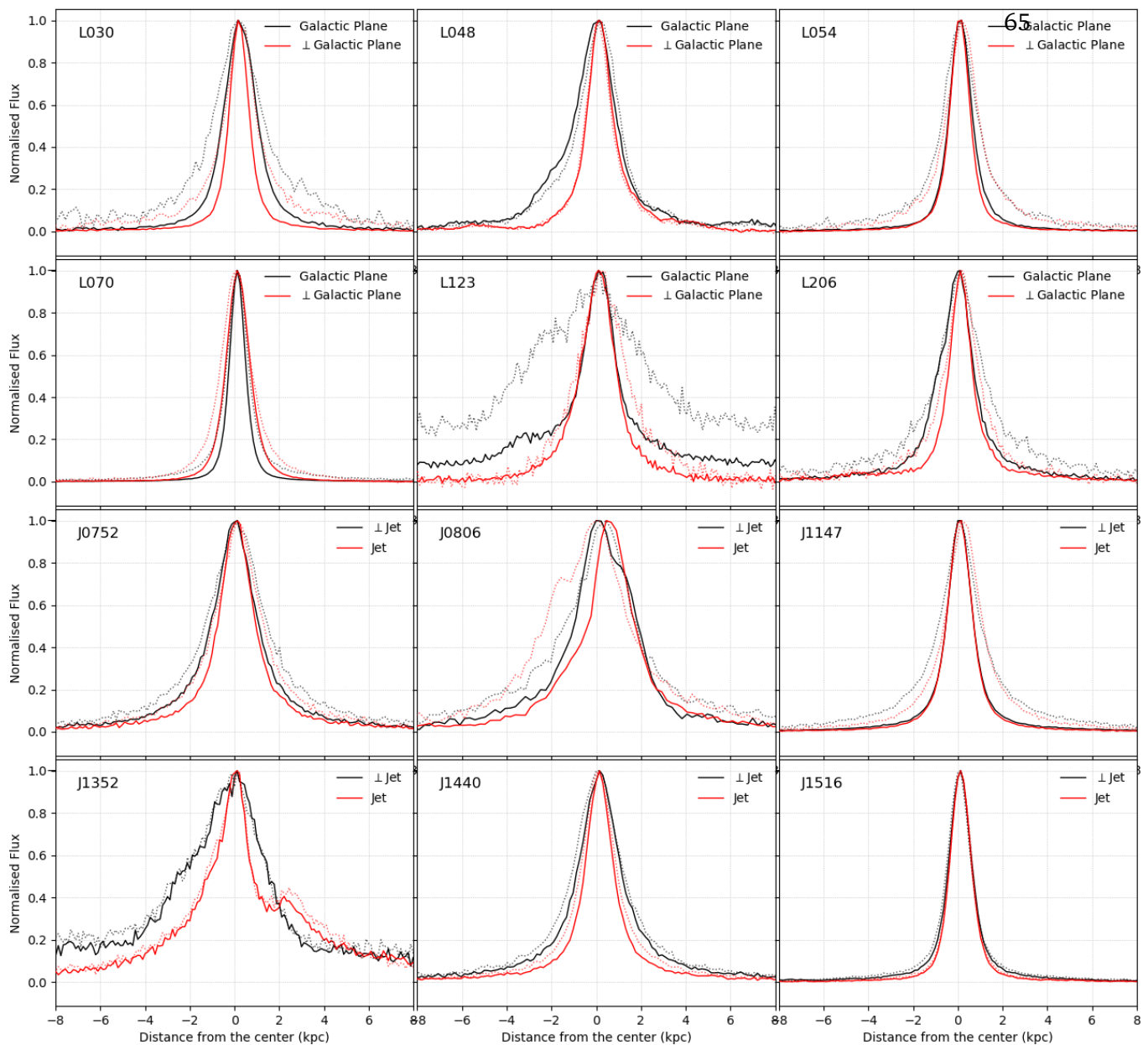


Figure 7. Extension of $[OIII]\lambda 5007$: Normalised flux is plotted as a function of distance from the center of the galaxy. The top 6 panels correspond to non-jetted compact radio sources and the bottom 6 panels correspond to the jetted source. The black solid line represents $[OIII]\lambda 5007$ flux along the galactic plane (or perpendicular to the jet for jetted sources) whereas the black dotted line is the continuum flux in the same direction. Similarly, the red solid line represents $[OIII]\lambda 5007$ in the direction perpendicular to the galactic plane (or along the jet for the jetted sources) and the red dotted line is the continuum flux from the same 2D spectrum.

956—Conditions and Impact of Star Formation. We thank the Collaborative Research Centre 956, sub-project A02, funded by the Deutsche Forschungsgemeinschaft (DFG) – project ID 184018867. Harshitha Bhat was a member

of the International Max Planck Research School for Astronomy and Astrophysics at the Universities of Bonn and Cologne and has received financial support for this research from IMPRS.

REFERENCES

- Alexander, D. M., Swinbank, A. M., Smail, I., McDermid, R., & Nesvadba, N. P. H. 2010, *MNRAS*, 402, 2211, doi: [10.1111/j.1365-2966.2009.16046.x](https://doi.org/10.1111/j.1365-2966.2009.16046.x)
- Asmus, D., Gandhi, P., Smette, A., Hönic, S. F., & Duschl, W. J. 2011, *A&A*, 536, A36, doi: [10.1051/0004-6361/201116693](https://doi.org/10.1051/0004-6361/201116693)

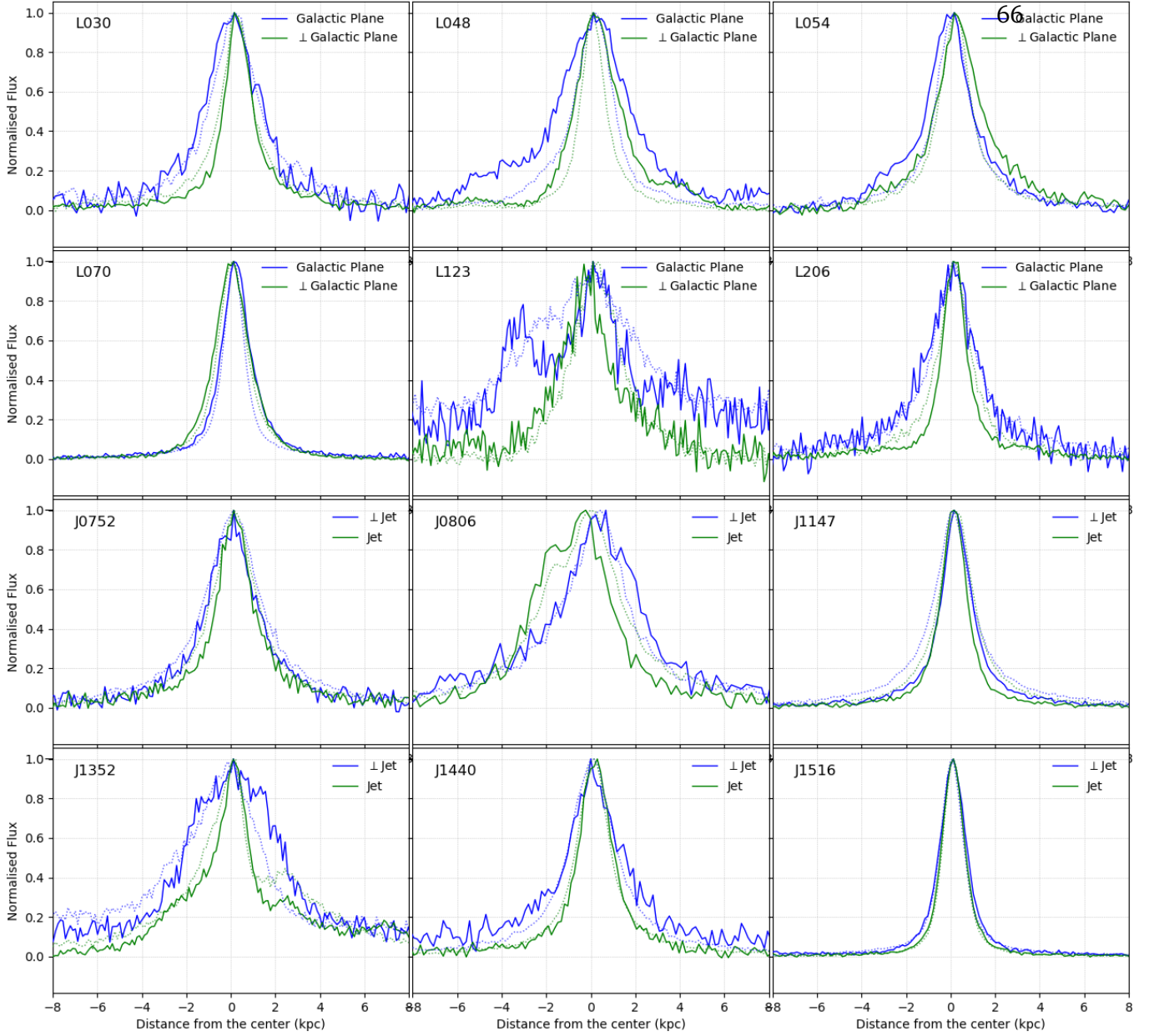


Figure 8. *Extension of [OIII] λ 3729:* Normalised flux is plotted as a function of distance from the center of the galaxy. The top 6 panels correspond to non-jetted compact radio sources and the bottom 6 panels correspond to the jetted source. The blue solid line represents [OIII] λ 3729 flux along the galactic plane (or perpendicular to the jet for jetted sources) whereas the blue dotted line is the continuum flux in the same direction. Similarly, the green solid line represents [OIII] λ 3729 in the direction perpendicular to the galactic plane (or along the jet for the jetted sources) and the green dotted line is the continuum flux from the same 2D spectrum.

Baldwin, J. A., Phillips, M. M., & Terlevich, R. 1981, *PASP*, 93, 5, doi: [10.1086/130766](https://doi.org/10.1086/130766)

Barbosa, F. K. B., Storchi-Bergmann, T., Cid Fernandes, R., Winge, C., & Schmitt, H. 2009, *MNRAS*, 396, 2, doi: [10.1111/j.1365-2966.2009.14485.x](https://doi.org/10.1111/j.1365-2966.2009.14485.x)

Cardamone, C., Schawinski, K., Sarzi, M., et al. 2009, *MNRAS*, 399, 1191, doi: [10.1111/j.1365-2966.2009.15383.x](https://doi.org/10.1111/j.1365-2966.2009.15383.x)

Crenshaw, D. M., Fischer, T. C., Kraemer, S. B., & Schmitt, H. R. 2015, *ApJ*, 799, 83, doi: [10.1088/0004-637X/799/1/83](https://doi.org/10.1088/0004-637X/799/1/83)

Cusumano, G., La Parola, V., Segreto, A., et al. 2010, *A&A*, 524, A64, doi: [10.1051/0004-6361/201015249](https://doi.org/10.1051/0004-6361/201015249)

D'Abrusco, R., Álvarez Crespo, N., Massaro, F., et al. 2019, *ApJS*, 242, 4, doi: [10.3847/1538-4365/ab16f4](https://doi.org/10.3847/1538-4365/ab16f4)

Davies, R. L., Schirmer, M., & Turner, J. E. H. 2015, *MNRAS*, 449, 1731, doi: [10.1093/mnras/stv343](https://doi.org/10.1093/mnras/stv343)

Ge, J.-Q., Hu, C., Wang, J.-M., Bai, J.-M., & Zhang, S. 2012, *ApJS*, 201, 31, doi: [10.1088/0067-0049/201/2/31](https://doi.org/10.1088/0067-0049/201/2/31)

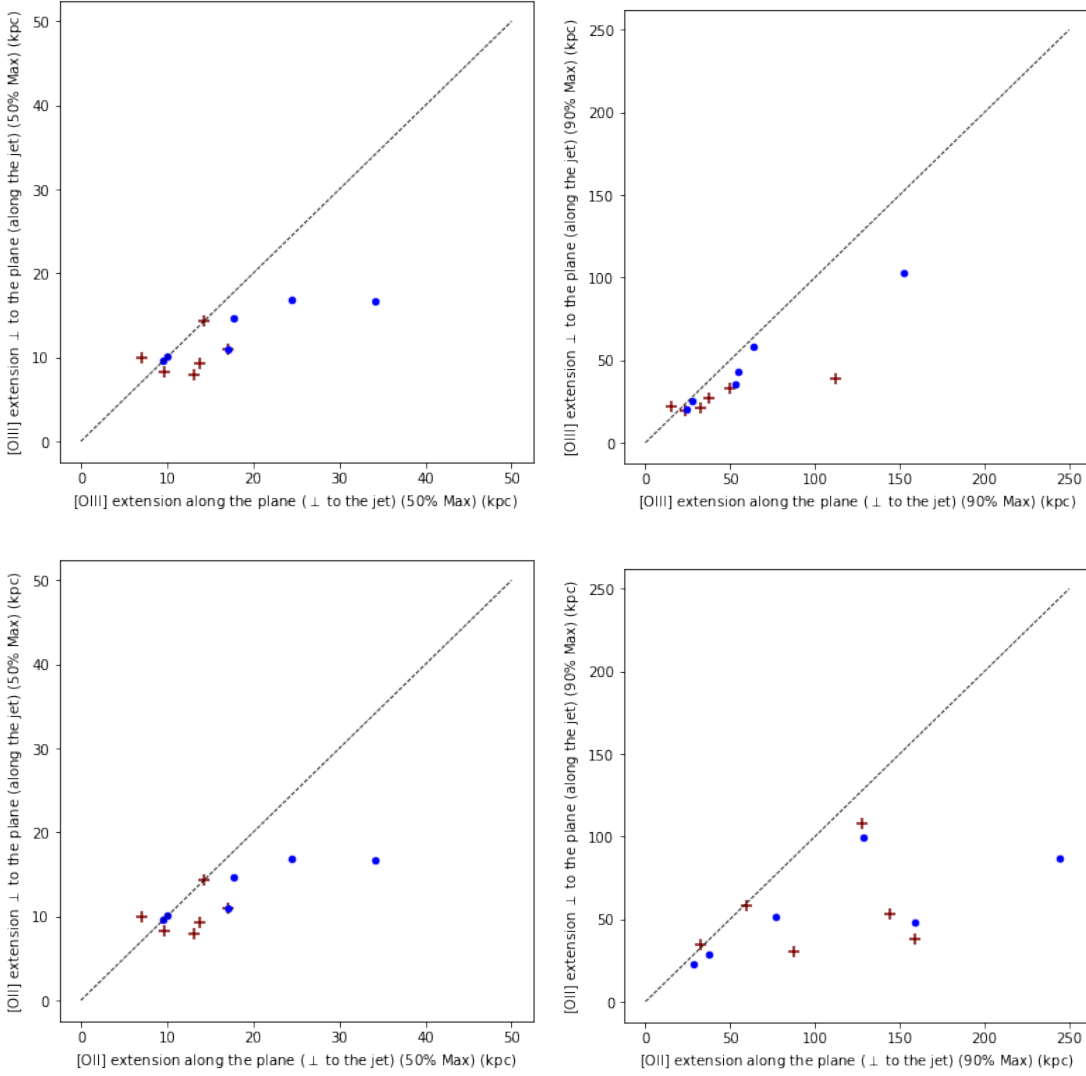


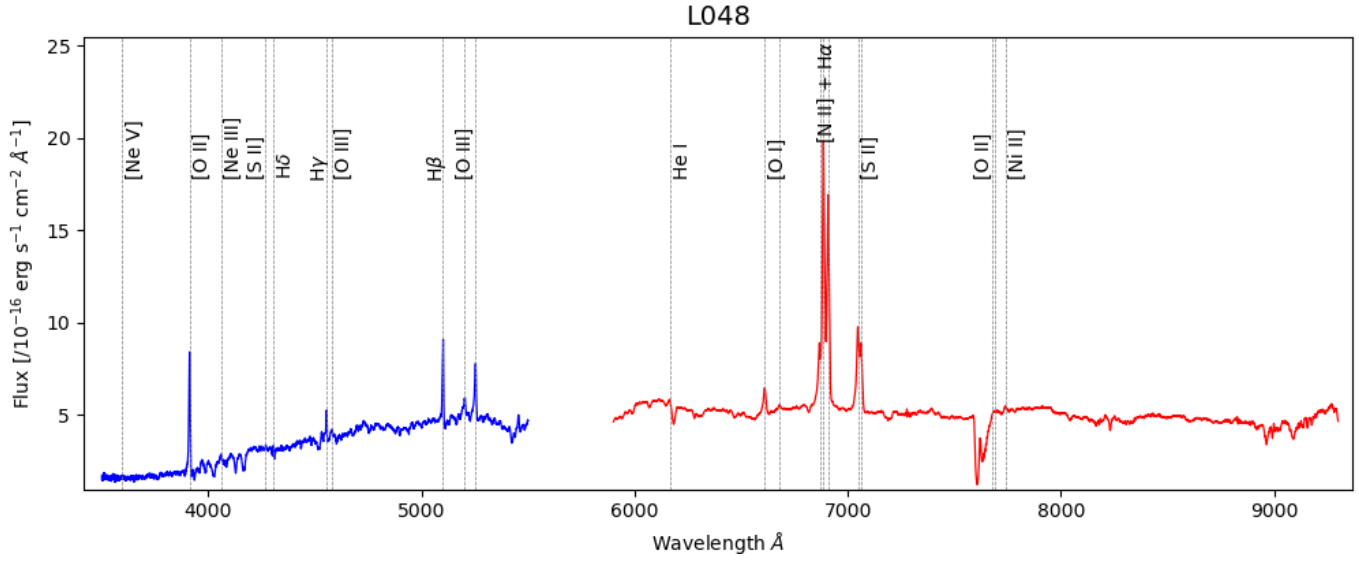
Figure 9. We conducted a comparison of the extensions of [OIII] and [OII] plots in parallel and perpendicular planes. The non-jetted sources are marked with maroon ‘+’ markers while jetted sources are marked with blue ‘.’ markers. The dashed black line represents the point where the widths along both directions would be equal. In all the figures except the bottom right figure ([OII] widths at 90% max), the plot points cluster around the dashed line, indicating no preferential direction. However, in the bottom right figure, we observed that the extension widths along the galactic plane were significantly more compared to the perpendicular plane. The K-S test confirmed this finding.

Table 4. The p -values from the KS-test for comparison between different categories of extension widths.

	[OIII]	[OII]
FWHM (entire sample) - plane vs \perp plane	0.249	0.034
90% of maxima (entire sample) - plane vs \perp plane	0.518	0.100
FWHM plane - non-jetted vs jetted	0.139	0.893
FWHM \perp plane - non-jetted vs jetted	0.441	0.441
FWHM plane / FWHM \perp plane - non-jetted vs jetted	1.000	0.893

- Greene, J. E., Zakamska, N. L., Ho, L. C., & Barth, A. J. 2011, *ApJ*, 732, 9, doi: [10.1088/0004-637X/732/1/9](https://doi.org/10.1088/0004-637X/732/1/9)
- Horst, H., Duschl, W. J., Gandhi, P., & Smette, A. 2009, *A&A*, 495, 137, doi: [10.1051/0004-6361:200809878](https://doi.org/10.1051/0004-6361:200809878)
- Jarvis, M. E., Harrison, C. M., Thomson, A. P., et al. 2019, *MNRAS*, 485, 2710, doi: [10.1093/mnras/stz556](https://doi.org/10.1093/mnras/stz556)
- Kaiser, M. E., Bradley, L. D., I., Hutchings, J. B., et al. 2000, *ApJ*, 528, 260, doi: [10.1086/308143](https://doi.org/10.1086/308143)
- Kauffmann, G., Heckman, T. M., Tremonti, C., et al. 2003, *MNRAS*, 346, 1055, doi: [10.1111/j.1365-2966.2003.07154.x](https://doi.org/10.1111/j.1365-2966.2003.07154.x)
- Kewley, L. J., Dopita, M. A., Sutherland, R. S., Heisler, C. A., & Trevena, J. 2001, *ApJ*, 556, 121, doi: [10.1086/321545](https://doi.org/10.1086/321545)
- Knese, E. D., Keel, W. C., Knese, G., et al. 2020, *MNRAS*, 496, 1035, doi: [10.1093/mnras/staa1510](https://doi.org/10.1093/mnras/staa1510)
- Leighly, K. M., & Moore, J. R. 2004, *ApJ*, 611, 107, doi: [10.1086/422088](https://doi.org/10.1086/422088)
- Leipski, C., Falcke, H., Bennert, N., & Hüttemeister, S. 2006, *A&A*, 455, 161, doi: [10.1051/0004-6361:20054311](https://doi.org/10.1051/0004-6361:20054311)
- Lin, Y.-T., Huang, H.-J., & Chen, Y.-C. 2018, *AJ*, 155, 188, doi: [10.3847/1538-3881/aab5b4](https://doi.org/10.3847/1538-3881/aab5b4)
- Lintott, C. J., Schawinski, K., Keel, W., et al. 2009, *MNRAS*, 399, 129, doi: [10.1111/j.1365-2966.2009.15299.x](https://doi.org/10.1111/j.1365-2966.2009.15299.x)
- Lutz, D., Maiolino, R., Spoon, H. W. W., & Moorwood, A. F. M. 2004, *A&A*, 418, 465, doi: [10.1051/0004-6361:20035838](https://doi.org/10.1051/0004-6361:20035838)
- Malizia, A., Landi, R., Molina, M., et al. 2016, *MNRAS*, 460, 19, doi: [10.1093/mnras/stw972](https://doi.org/10.1093/mnras/stw972)
- Markwardt, C. B. 2009, in *Astronomical Society of the Pacific Conference Series*, Vol. 411, *Astronomical Data Analysis Software and Systems XVIII*, ed. D. A. Bohlender, D. Durand, & P. Dowler, 251. <https://arxiv.org/abs/0902.2850>
- McCarthy, P. J., van Breugel, W., Spinrad, H., & Djorgovski, S. 1987, *ApJL*, 321, L29, doi: [10.1086/185000](https://doi.org/10.1086/185000)
- Mulchaey, J. S., Wilson, A. S., & Tsvetanov, Z. 1996, *ApJS*, 102, 309, doi: [10.1086/192261](https://doi.org/10.1086/192261)
- Mullaney, J. R., Alexander, D. M., Fine, S., et al. 2013, *MNRAS*, 433, 622, doi: [10.1093/mnras/stt751](https://doi.org/10.1093/mnras/stt751)
- Netzer, H. 2015, *ARA&A*, 53, 365, doi: [10.1146/annurev-astro-082214-122302](https://doi.org/10.1146/annurev-astro-082214-122302)
- Newville, M., Stensitzki, T., Allen, D. B., et al. 2016, *Lmfit: Non-Linear Least-Square Minimization and Curve-Fitting for Python*, *Astrophysics Source Code Library*, record ascl:1606.014. <http://ascl.net/1606.014>
- Nisbet, D. M., & Best, P. N. 2016, *MNRAS*, 455, 2551, doi: [10.1093/mnras/stv2450](https://doi.org/10.1093/mnras/stv2450)
- Oh, K., Yi, S. K., Schawinski, K., et al. 2015, *ApJ*, 821, 1, doi: [10.1088/0067-0049/219/1/1](https://doi.org/10.1088/0067-0049/219/1/1)
- Panessa, F., Barcons, X., Bassani, L., et al. 2007, *A&A*, 467, 519, doi: [10.1051/0004-6361:20066943](https://doi.org/10.1051/0004-6361:20066943)
- Pogge, R. 2019, *rwpgge/modsCCDRed 2.0, 2.0*, Zenodo, Zenodo, doi: [10.5281/zenodo.2550741](https://doi.org/10.5281/zenodo.2550741)
- Reyes, R., Zakamska, N. L., Strauss, M. A., et al. 2008, *AJ*, 136, 2373, doi: [10.1088/0004-6256/136/6/2373](https://doi.org/10.1088/0004-6256/136/6/2373)
- Riffel, R. A., Storchi-Bergmann, T., Winge, C., & Barbosa, F. K. B. 2006, *MNRAS*, 373, 2, doi: [10.1111/j.1365-2966.2006.11050.x](https://doi.org/10.1111/j.1365-2966.2006.11050.x)
- Rosario, D. J., Shields, G. A., Taylor, G. B., Salviander, S., & Smith, K. L. 2010, *ApJ*, 716, 131, doi: [10.1088/0004-637X/716/1/131](https://doi.org/10.1088/0004-637X/716/1/131)
- Saade, M. L., Brightman, M., Stern, D., Malkan, M. A., & García, J. A. 2022, *ApJ*, 936, 162, doi: [10.3847/1538-4357/ac88cf](https://doi.org/10.3847/1538-4357/ac88cf)
- Schirmer, M., Diaz, R., Holhjem, K., Levenson, N. A., & Winge, C. 2013, *ApJ*, 763, 60, doi: [10.1088/0004-637X/763/1/60](https://doi.org/10.1088/0004-637X/763/1/60)
- Schirmer, M., Malhotra, S., Levenson, N. A., et al. 2016, *MNRAS*, 463, 1554, doi: [10.1093/mnras/stw1819](https://doi.org/10.1093/mnras/stw1819)
- Schmitt, H. R., Donley, J. L., Antonucci, R. R. J., et al. 2003, *ApJ*, 597, 768, doi: [10.1086/381224](https://doi.org/10.1086/381224)
- Stockton, A., Fu, H., & Canalizo, G. 2006, *NewAR*, 50, 694, doi: [10.1016/j.newar.2006.06.024](https://doi.org/10.1016/j.newar.2006.06.024)
- Stockton, A., & MacKenty, J. W. 1987, *ApJ*, 316, 584, doi: [10.1086/165227](https://doi.org/10.1086/165227)
- Sun, A.-L., Greene, J. E., Zakamska, N. L., et al. 2018, *MNRAS*, 480, 2302, doi: [10.1093/mnras/sty1394](https://doi.org/10.1093/mnras/sty1394)
- Toba, Y., Oyabu, S., Matsuhara, H., et al. 2014, *ApJ*, 788, 45, doi: [10.1088/0004-637X/788/1/45](https://doi.org/10.1088/0004-637X/788/1/45)
- Ueda, Y., Ishisaki, Y., Takahashi, T., Makishima, K., & Ohashi, T. 2005, *ApJS*, 161, 185, doi: [10.1086/468187](https://doi.org/10.1086/468187)
- Veilleux, S., & Osterbrock, D. E. 1987, *ApJS*, 63, 295, doi: [10.1086/191166](https://doi.org/10.1086/191166)
- Vitale, M., Fuhrmann, L., García-Marín, M., et al. 2015, *A&A*, 573, A93, doi: [10.1051/0004-6361/201423993](https://doi.org/10.1051/0004-6361/201423993)
- Vitale, M., Zuther, J., García-Marín, M., et al. 2012, *A&A*, 546, A17, doi: [10.1051/0004-6361/201219290](https://doi.org/10.1051/0004-6361/201219290)
- Whittle, M. 1985, *MNRAS*, 213, 1, doi: [10.1093/mnras/213.1.1](https://doi.org/10.1093/mnras/213.1.1)
- Wilson, A. S., & Tsvetanov, Z. I. 1994, *AJ*, 107, 1227, doi: [10.1086/116935](https://doi.org/10.1086/116935)
- Zajaček, M., Busch, G., Valencia-S., M., et al. 2019, *A&A*, 630, A83, doi: [10.1051/0004-6361/201833388](https://doi.org/10.1051/0004-6361/201833388)

APPENDIX

**Figure 10.****Table 5.** Emission Lines L048

Emission line	Observed wavelength (λ_o) (Å)	$\Delta\lambda_o$ (Å)	Flux (F) ($10^{-16} \text{ ergs}^{-1} \text{ cm}^{-2}$)	ΔF ($10^{-16} \text{ ergs}^{-1} \text{ cm}^{-2}$)	$FWHM$ (kms^{-1})	$\Delta FWHM$ (kms^{-1})
[O II] λ 3729 _{blue}	3905.98	2.98	7.46	4.7	739.0	281.0
[O II] λ 3729	3911.87	0.09	38.87	4.54	441.0	16.0
H γ λ 4340	4554.33	0.14	6.27	0.4	281.0	21.0
H β λ 4861 _{broad}	5098.56	1.08	14.22	5.35	371.0	57.0
H β λ 4861	5101.44	0.11	11.7	5.14	214.0	29.0
[O III] λ 4959 _{blue}	5199.97	0.55	22.49	1.14	1359.0	72.0
[O III] λ 4959	5203.23	0.45	1.99	0.67	250.0	70.0
[O III] λ 5007 _{blue}	5245.66	0.98	19.16	1.83	1157.0	74.0
[O III] λ 5007	5253.03	0.11	18.43	1.43	393.0	19.0
[O I] λ 6300	6609.71	0.31	17.27	0.87	576.0	32.0
[N II] λ 6548	6866.15	0.18	19.24	2.58	415.0	28.0
H α λ 6563	6884.28	0.12	25.58	3.74	266.0	14.0
H α λ 6563 _{broad1}	6884.43	0.7	106.69	10.41	2234.0	116.0
H α λ 6563 _{broad2}	6886.42	0.11	116.29	6.94	525.0	16.0
[N II] λ 6583	6907.49	0.04	115.39	2.62	471.0	5.0
[S II] λ 6716 _{blue}	7043.93	2.69	35.1	8.7	1068.0	94.0
[S II] λ 6716	7047.05	0.08	34.17	3.64	426.0	12.0
[S II] λ 6731	7061.79	0.21	42.78	4.93	526.0	17.0
[Ni II] λ 7378	7740.02	0.44	3.09	0.28	417.0	40.0

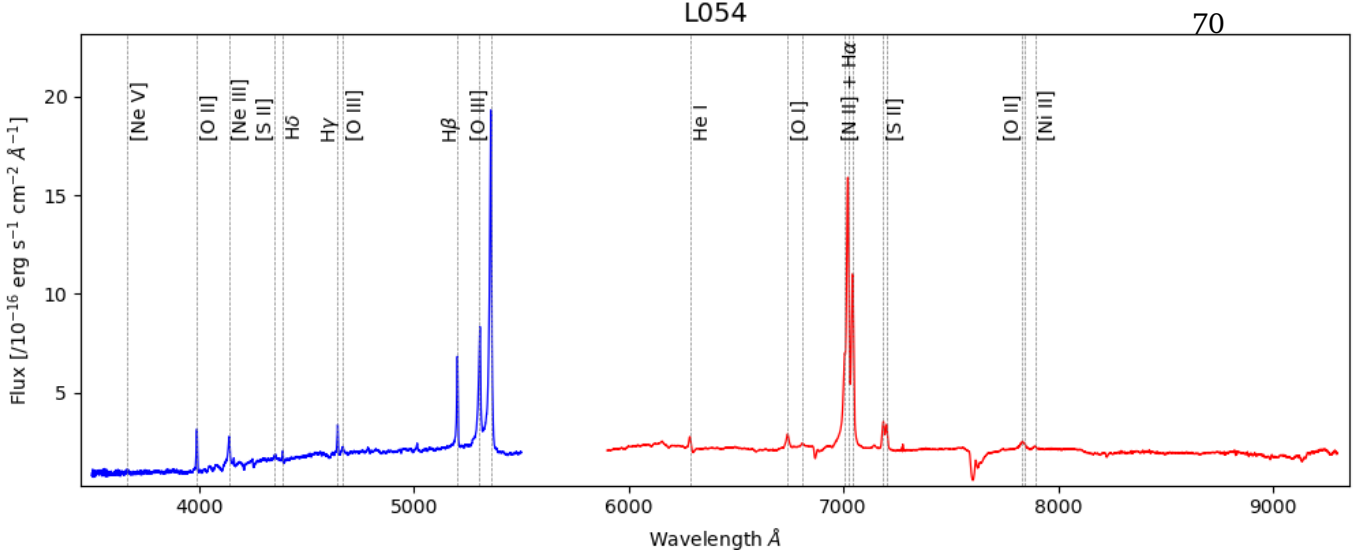


Figure 11.

Table 6. Emission Lines L054

Emission line	Observed wavelength (λ_o) (Å)	$\Delta\lambda_o$ (Å)	Flux (F) ($10^{-16} \text{ ergs}^{-1} \text{ cm}^{-2}$)	ΔF ($10^{-16} \text{ ergs}^{-1} \text{ cm}^{-2}$)	$FWHM$ (kms^{-1})	$\Delta FWHM$ (kms^{-1})
[O II] λ 3729	3989.32	0.05	12.2	0.23	413.0	9.0
[Ne III] λ 3869 _{blue}	4136.77	0.61	11.17	0.77	1574.0	105.0
[Ne III] λ 3869	4139.72	0.14	6.57	0.69	470.0	32.0
H δ λ 4102	4389.57	0.18	1.4	0.17	201.0	28.0
H γ λ 4340	4644.93	0.08	6.58	0.21	297.0	11.0
[O III] λ 4363	4668.51	0.39	2.44	0.26	454.0	56.0
H β λ 4861 _{broad}	5197.12	0.53	10.14	0.84	753.0	38.0
H β λ 4861	5202.67	0.03	21.89	0.67	291.0	5.0
[O III] λ 4959 _{blue}	5304.87	0.73	42.14	4.05	1332.0	208.0
[O III] λ 4959	5306.83	0.15	29.46	3.35	401.0	27.0
[O III] λ 5007 _{blue}	5354.31	0.25	118.81	5.11	914.0	23.0
[O III] λ 5007	5358.74	0.06	71.73	3.58	355.0	10.0
He I λ 5876	6284.95	0.21	5.47	0.26	425.0	22.0
[O I] λ 6300	6740.35	0.25	14.14	0.41	838.0	26.0
[N II] λ 6548	7005.4	0.13	28.26	1.29	433.0	13.0
H α λ 6563	7020.42	0.09	129.78	2.95	473.0	5.0
H α λ 6563 _{broad1}	7016.95	0.39	118.98	3.26	2290.0	40.0
H α λ 6563 _{broad2}	7023.21	0.23	5.84	2.33	236.0	33.0
[N II] λ 6583	7042.94	0.03	89.12	1.02	467.0	3.0
[S II] λ 6716	7185.95	0.1	15.62	0.28	461.0	9.0
[S II] λ 6731	7201.22	0.1	13.34	0.27	424.0	9.0
[O II] λ 7320	7834.42	0.19	10.51	0.18	1054.0	18.0
[Ni II] λ 7378	7891.56	0.39	2.19	0.12	601.0	34.0

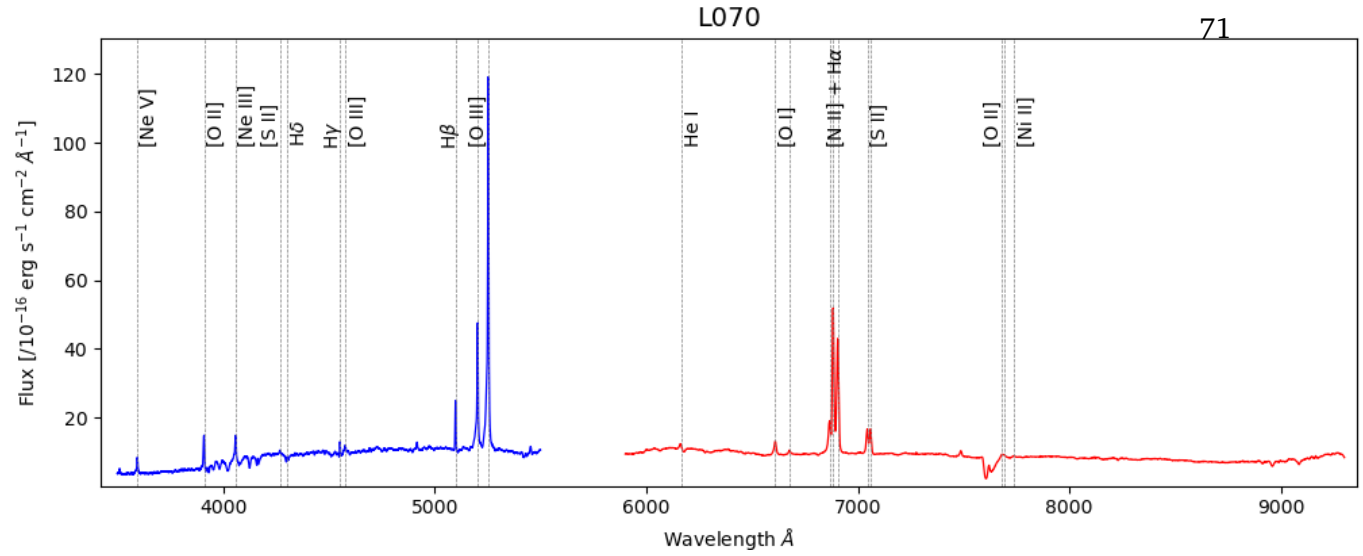


Figure 12.

Table 7. Emission Lines L070

Emission line	Observed wavelength (λ_o) (Å)	$\Delta\lambda_o$ (Å)	Flux (F) ($10^{-16} \text{ ergs}^{-1} \text{ cm}^{-2}$)	ΔF ($10^{-16} \text{ ergs}^{-1} \text{ cm}^{-2}$)	$FWHM$ (kms^{-1})	$\Delta FWHM$ (kms^{-1})
[Ne V] λ 3426	3594.82	0.16	32.77	1.51	603.0	31.0
[O II] λ 3729	3909.58	0.06	58.12	1.27	428.0	11.0
[Ne III] λ 3869 _{blue}	4055.25	0.5	68.5	3.56	1602.0	81.0
[Ne III] λ 3869	4059.41	0.1	30.47	2.14	350.0	20.0
H γ λ 4340	4552.37	0.1	8.53	0.64	165.0	14.0
[O III] λ 4363	4577.35	0.28	13.92	1.09	463.0	164.0
H β λ 4861	5098.58	0.04	59.66	1.12	236.0	5.0
[O III] λ 4959 _{blue}	5199.64	0.19	161.24	3.27	1163.0	24.0
[O III] λ 4959	5203.04	0.02	133.67	2.06	245.0	3.0
[O III] λ 5007 _{blue}	5249.84	0.06	417.41	3.38	995.0	8.0
[O III] λ 5007	5253.36	0.01	398.92	2.27	243.0	1.0
He I λ 5876	6161.04	0.29	19.42	1.32	528.0	35.0
[O I] λ 6300	6609.12	0.08	47.94	0.69	558.0	8.0
[O I] λ 6364	6677.23	0.25	13.07	0.69	500.0	27.0
[N II] λ 6548	6865.98	0.1	76.94	4.94	420.0	15.0
H α λ 6563	6882.84	0.11	347.54	43.54	370.0	10.0
H α λ 6563 _{broad1}	6891.31	5.83	38.28	52.83	582.0	608.0
H α λ 6563 _{broad2}	6880.89	1.03	156.59	14.62	2360.0	147.0
[N II] λ 6583	6865.98	0.1	76.94	4.94	420.0	15.0
[S II] λ 6716	7044.17	0.04	75.05	0.69	436.0	5.0
[S II] λ 6731	7059.46	0.04	70.57	0.66	402.0	4.0
[Ar III] λ 7136	7486.33	0.09	17.04	0.39	411.0	9.0

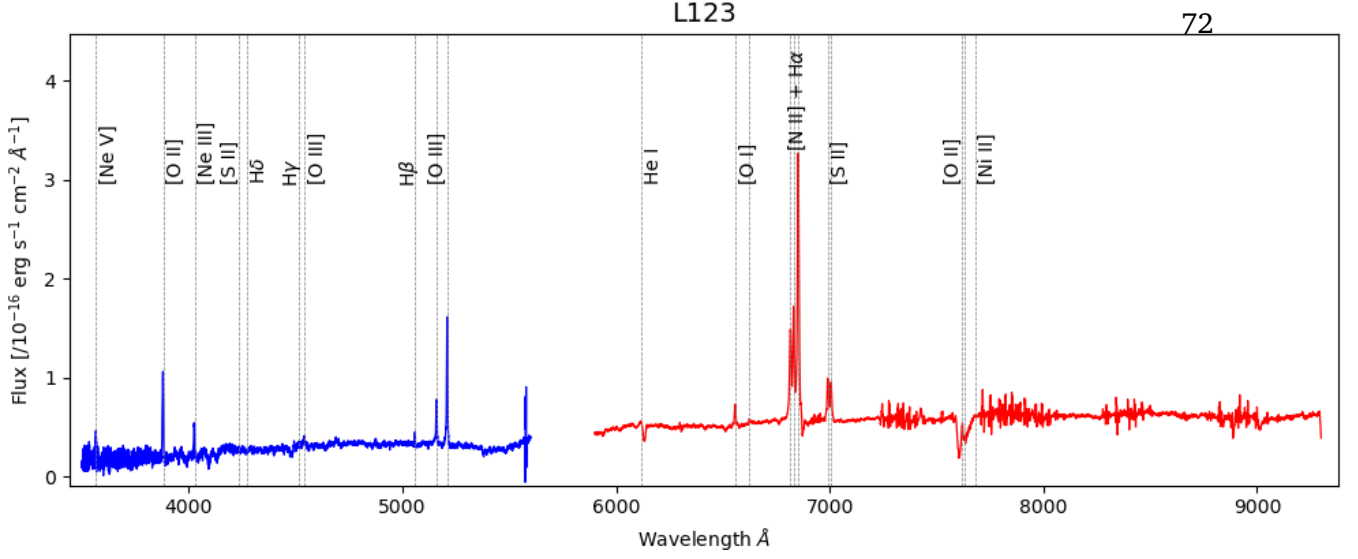


Figure 13.

Table 8. Emission Lines L123

Emission line	Observed wavelength (λ_o) (\AA)	$\Delta\lambda_o$ (\AA)	Flux (F) ($10^{-16} \text{ erg s}^{-1} \text{ cm}^{-2}$)	ΔF ($10^{-16} \text{ erg s}^{-1} \text{ cm}^{-2}$)	$FWHM$ (kms^{-1})	$\Delta FWHM$ (kms^{-1})
[Ne V] λ 3426	3567.45	0.24	0.89	0.14	290.0	47.0
[O II] λ 3729	3881.26	0.05	4.92	0.1	424.0	9.0
[Ne III] λ 3869	4027.78	0.12	1.79	0.09	376.0	22.0
H β λ 4861	5060.79	0.14	0.39	0.03	205.0	19.0
[O III] λ 4959 _{blue}	5159.23	0.58	1.56	0.1	1145.0	79.0
[O III] λ 4959	5162.41	0.04	1.88	0.07	255.0	7.0
[O III] λ 5007 _{blue}	5209.93	0.24	2.53	0.12	737.0	29.0
[O III] λ 5007	5212.28	0.02	5.26	0.11	249.0	3.0
[O I] λ 6300	6560.45	0.12	1.64	0.06	324.0	13.0
[N II] λ 6548	6818.96	0.1	5.38	0.26	315.0	12.0
H α λ 6563	6834.53	0.07	5.54	0.26	270.0	10.0
H α λ 6563 _{broad1}	6836.03	0.9	16.05	0.76	1888.0	72.0
[N II] λ 6583	6855.93	0.03	21.01	0.26	348.0	4.0
[S II] λ 6716	6994.72	0.1	3.59	0.09	359.0	11.0
[S II] λ 6731	7009.27	0.11	3.56	0.1	381.0	12.0

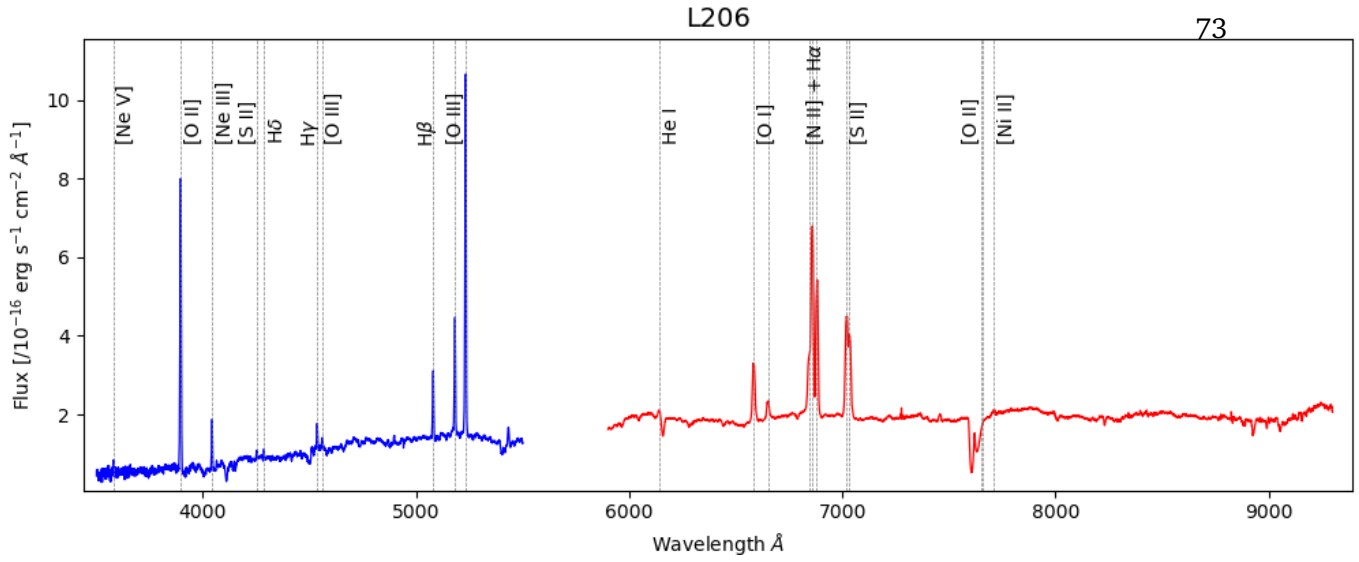


Figure 14.

Table 9. Emission Lines L206

Emission line	Observed wavelength (λ_o) (Å)	$\Delta\lambda_o$ (Å)	Flux (F) ($10^{-16} \text{ erg s}^{-1} \text{ cm}^{-2}$)	ΔF ($10^{-16} \text{ erg s}^{-1} \text{ cm}^{-2}$)	$FWHM$ (kms^{-1})	$\Delta FWHM$ (kms^{-1})
[O II] λ 3729	3895.3	0.02	45.83	0.26	443.0	3.0
[Ne III] λ 3869	4042.71	0.09	5.33	0.22	310.0	14.0
[S II] λ 4069	4251.89	0.17	0.92	0.08	301.0	28.0
H δ λ 4102	4286.25	0.13	0.75	0.07	214.0	21.0
H γ λ 4340	4535.61	0.07	3.25	0.11	306.0	11.0
[O III] λ 4363	4559.32	0.21	1.96	0.15	460.0	35.0
H β λ 4861	5079.96	0.06	9.29	0.21	308.0	8.0
[O III] λ 4959 _{blue}	5177.48	1.48	3.39	0.75	819.0	114.0
[O III] λ 4959	5182.09	0.04	14.92	0.59	289.0	7.0
[O III] λ 5007	5232.06	0.01	50.91	0.23	307.0	1.0
[O I] λ 6300	6583.77	0.05	21.32	0.18	585.0	5.0
[O I] λ 6364	6650.74	0.16	6.61	0.17	602.0	17.0
[N II] λ 6548	6843.83	0.7	24.63	2.31	691.0	58.0
H α λ 6563	6858.71	0.15	59.87	2.13	495.0	11.0
[N II] λ 6583	6880.47	0.08	42.63	0.9	476.0	10.0
[S II] λ 6716	7019.16	0.1	36.71	0.57	564.0	8.0
[S II] λ 6731	7034.45	0.12	26.97	0.56	526.0	9.0
[Ar III] λ 7136	7457.43	0.2	1.72	0.08	393.0	19.0
[Ni II] λ 7378	7708.24	0.44	1.65	0.21	528.0	50.0

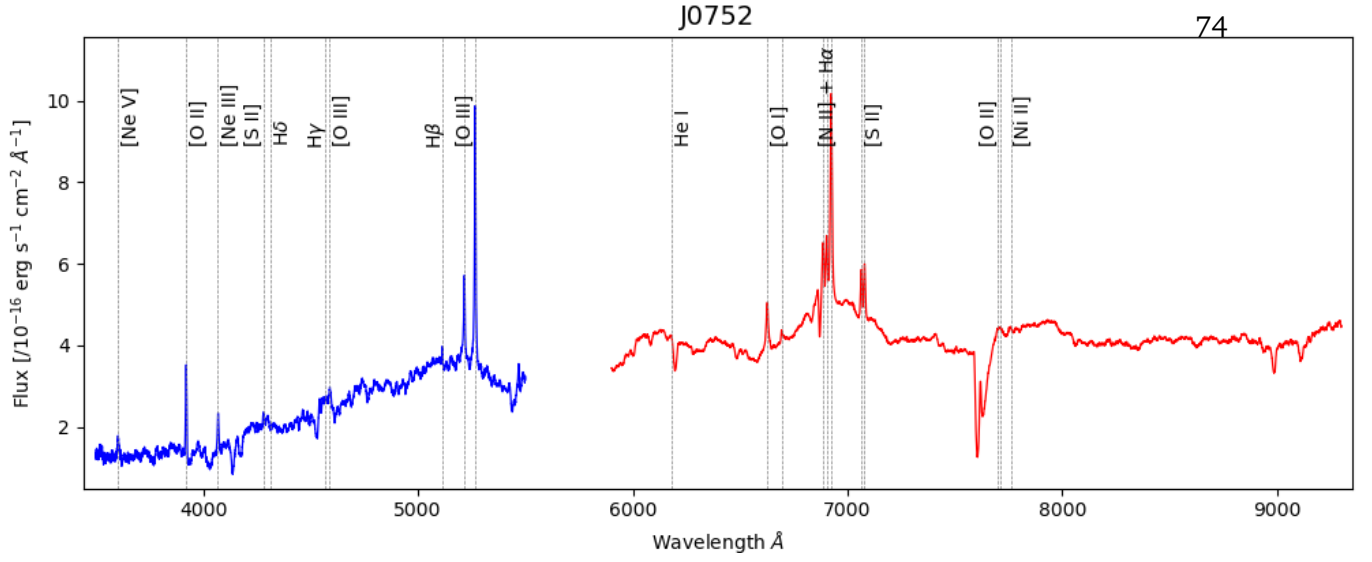


Figure 15.

Table 10. Emission Lines J0752

Emission line	Observed wavelength (λ_o) (Å)	$\Delta\lambda_o$ (Å)	Flux (F) ($10^{-16} \text{ erg s}^{-1} \text{ cm}^{-2}$)	ΔF ($10^{-16} \text{ erg s}^{-1} \text{ cm}^{-2}$)	$FWHM$ (kms^{-1})	$\Delta FWHM$ (kms^{-1})
[Ne V] λ 3426	3603.94	0.53	3.93	0.46	801.0	101.0
[O II] λ 3729	3920.74	0.07	13.08	0.32	427.0	12.0
[Ne III] λ 3869	4069.4	0.2	7.07	0.39	556.0	34.0
H β λ 4861	5113.23	0.23	1.54	0.2	209.0	31.0
[O III] λ 4959 _{blue}	5212.05	0.55	20.89	0.76	1979.0	82.0
[O III] λ 4959	5215.96	0.07	9.73	0.37	308.0	10.0
[O III] λ 5007 _{blue}	5264.7	0.17	28.27	0.69	1026.0	28.0
[O III] λ 5007	5266.35	0.02	25.86	0.59	277.0	4.0
[O I] λ 6300	6625.92	0.13	14.97	0.33	592.0	14.0
[O I] λ 6364	6694.76	0.54	2.54	0.27	469.0	55.0
[N II] λ 6548	6885.58	0.27	14.99	0.98	385.0	28.0
H α λ 6563	6902.72	0.3	18.63	1.08	485.0	33.0
[N II] λ 6583	6923.7	0.09	52.28	0.96	430.0	9.0
[S II] λ 6716	7063.88	0.03	9.7	0.1	327.0	3.0
[S II] λ 6731	7078.94	0.03	11.14	0.1	340.0	3.0

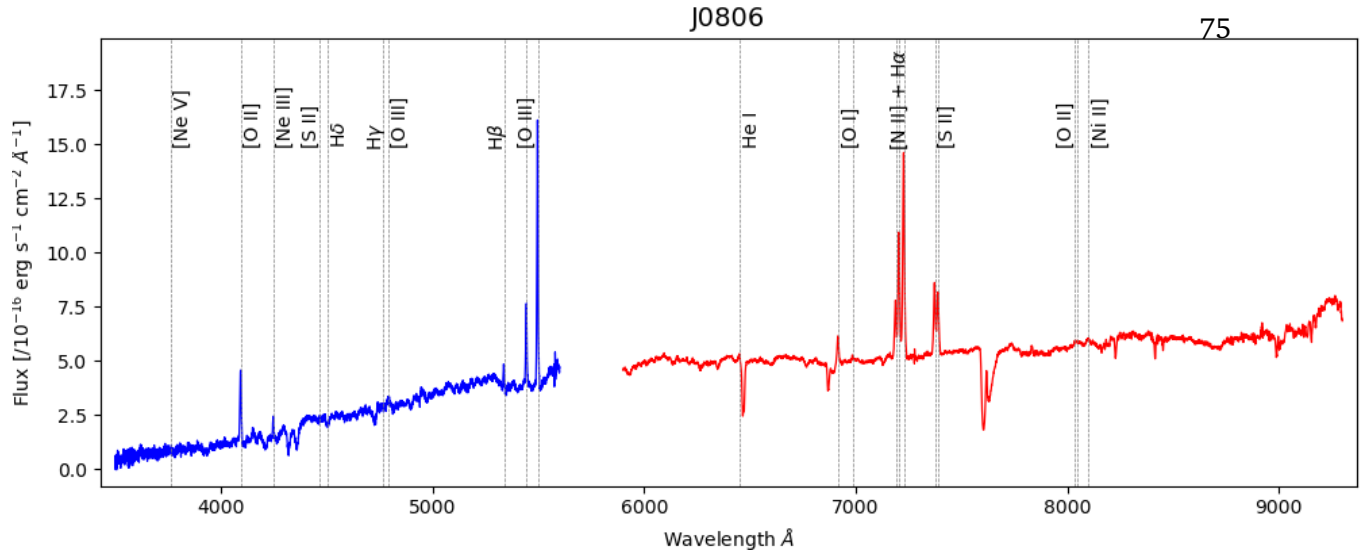


Figure 16.

Table 11. Emission Lines J0806

Emission line	Observed wavelength (λ_o) (Å)	$\Delta\lambda_o$ (Å)	Flux (F) ($10^{-16} \text{ erg s}^{-1} \text{ cm}^{-2}$)	ΔF ($10^{-16} \text{ erg s}^{-1} \text{ cm}^{-2}$)	$FWHM$ (kms^{-1})	$\Delta FWHM$ (kms^{-1})
[O II] λ 3729	4092.56	0.07	23.45	0.46	489.0	11.0
[Ne III] λ 3869	4246.53	0.25	5.22	0.45	414.0	39.0
H β λ 4861	5335.95	0.19	5.11	0.47	235.0	23.0
[O III] λ 4959	5442.94	0.07	21.06	0.52	307.0	8.0
[O III] λ 5007	5495.62	0.02	64.83	0.54	290.0	3.0
[O I] λ 6300	6915.53	0.57	10.3	1.46	341.0	54.0
[N II] λ 6548	7187.08	0.09	18.69	1.17	318.0	13.0
H α λ 6563	7203.05	0.05	37.79	1.05	296.0	5.0
H α λ 6563 _{broad1}	7209.97	1.75	30.88	2.7	1470.0	165.0
[N II] λ 6583	7225.97	0.03	74.96	0.85	331.0	3.0
[S II] λ 6716	7372.16	0.04	28.42	0.41	342.0	4.0
[S II] λ 6731	7387.8	0.05	26.43	0.37	372.0	5.0
[Ar III] λ 7136	7832.08	0.28	3.11	0.29	295.0	26.0

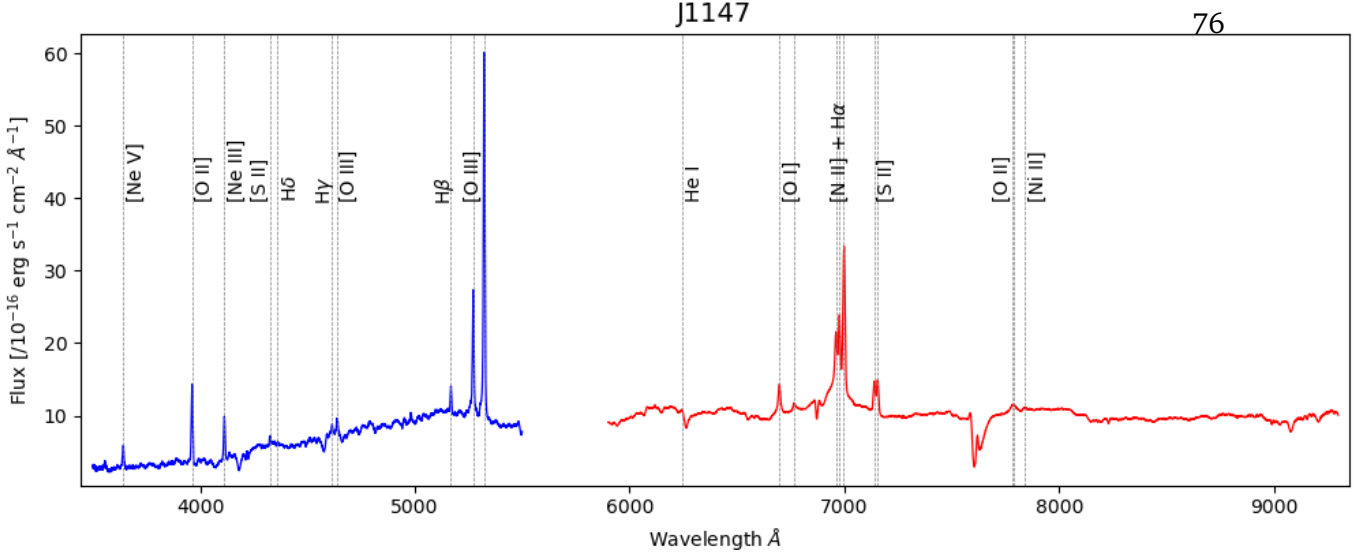


Figure 17.

Table 12. Emission Lines J1147

Emission line	Observed wavelength (λ_o) (Å)	$\Delta\lambda_o$ (Å)	Flux (F) ($10^{-16} \text{ ergs}^{-1} \text{ cm}^{-2}$)	ΔF ($10^{-16} \text{ ergs}^{-1} \text{ cm}^{-2}$)	$FWHM$ (kms^{-1})	$\Delta FWHM$ (kms^{-1})
[Ne V] λ 3426	3642.11	0.13	22.62	0.78	607.0	24.0
[O II] λ 3729	3962.56	0.03	81.97	0.76	532.0	6.0
[Ne III] λ 3869	4112.99	0.06	43.52	0.77	506.0	10.0
[S II] λ 4069	4326.28	0.19	9.05	0.53	497.0	31.0
H γ λ 4340	4614.83	0.31	21.23	2.13	918.0	66.0
[O III] λ 4363	4638.9	0.15	32.64	1.3	799.0	26.0
H β λ 4861	5168.12	0.05	23.03	0.46	357.0	7.0
[O III] λ 4959 _{blue}	5270.27	0.3	59.3	3.05	1307.0	72.0
[O III] λ 4959	5271.95	0.01	95.84	1.65	347.0	4.0
[O III] λ 5007 _{blue}	5319.78	0.15	110.33	3.06	1099.0	25.0
[O III] λ 5007	5322.97	0.01	301.33	1.73	353.0	1.0
[O I] λ 6300	6697.5	0.08	47.99	0.89	549.0	9.0
[O I] λ 6364	6768.04	0.37	13.62	0.88	635.0	40.0
[N II] λ 6548	6960.94	0.14	56.95	2.96	407.0	16.0
H α λ 6563	6976.76	0.1	79.83	3.32	397.0	12.0
H α λ 6563 _{broad1}	6970.5	0.63	361.47	8.88	3040.0	120.0
[N II] λ 6583	6998.58	0.04	198.17	2.87	419.0	5.0
[S II] λ 6716	7139.99	0.1	45.29	0.95	436.0	10.0
[S II] λ 6731	7155.16	0.09	47.59	0.92	408.0	9.0
[O II] λ 7331	7786.4	0.21	33.1	0.8	39.0	1.0

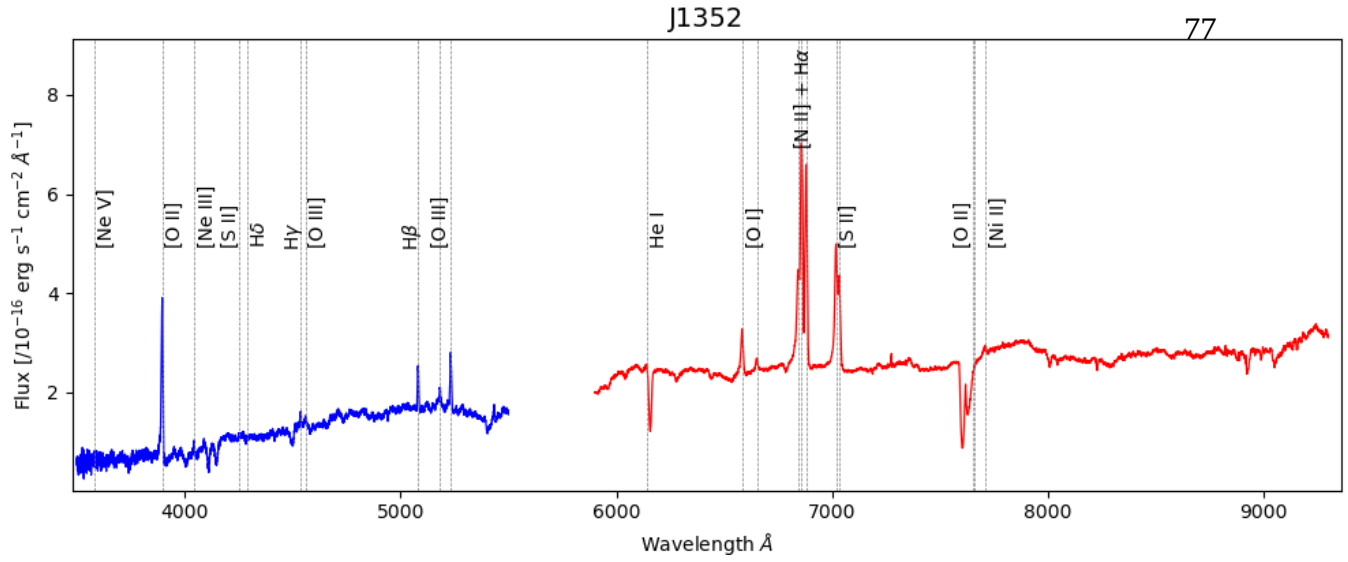


Figure 18.

Table 13. Emission Lines J1352

Emission line	Observed wavelength (λ_o) (Å)	$\Delta\lambda_o$ (Å)	Flux (F) ($10^{-16} \text{ ergs}^{-1} \text{ cm}^{-2}$)	ΔF ($10^{-16} \text{ ergs}^{-1} \text{ cm}^{-2}$)	$FWHM$ (kms^{-1})	$\Delta FWHM$ (kms^{-1})
[O II] λ 3729 _{blue}	3887.78	2.4	5.59	2.12	979.0	275.0
[O II] λ 3729	3896.25	0.1	23.57	1.99	546.0	18.0
[Ne III] λ 3869	4043.05	0.54	1.48	0.28	435.0	92.0
H β λ 4861	5081.86	0.06	5.23	0.13	339.0	9.0
[O III] λ 4959 _{blue}	5178.47	0.76	5.63	0.39	1656.0	109.0
[O III] λ 4959	5183.27	0.2	1.48	0.17	298.0	30.0
[O III] λ 5007 _{blue}	5220.11	0.68	1.78	0.24	660.0	99.0
[O III] λ 5007	5233.21	0.07	8.44	0.2	412.0	9.0
[O I] λ 6300	6582.65	0.1	11.27	0.22	561.0	11.0
[O I] λ 6364	6650.75	0.35	2.95	0.21	504.0	38.0
[N II] λ 6548	6842.91	0.27	24.84	2.34	661.0	34.0
H α λ 6563	6859.23	0.09	49.96	1.92	478.0	10.0
H α λ 6563 _{broad1}	6853.34	2.31	22.06	4.53	2533.0	366.0
[N II] λ 6583	6879.94	0.06	42.41	1.18	437.0	8.0
[S II] λ 6716 _{blue}	7013.49	1.29	15.53	1.45	1330.0	59.0
[S II] λ 6716	7018.44	0.04	24.04	0.66	469.0	6.0
[S II] λ 6731	7033.28	0.06	20.21	0.79	492.0	8.0
[Ni II] λ 7378	7706.48	0.52	2.27	0.25	620.0	56.0

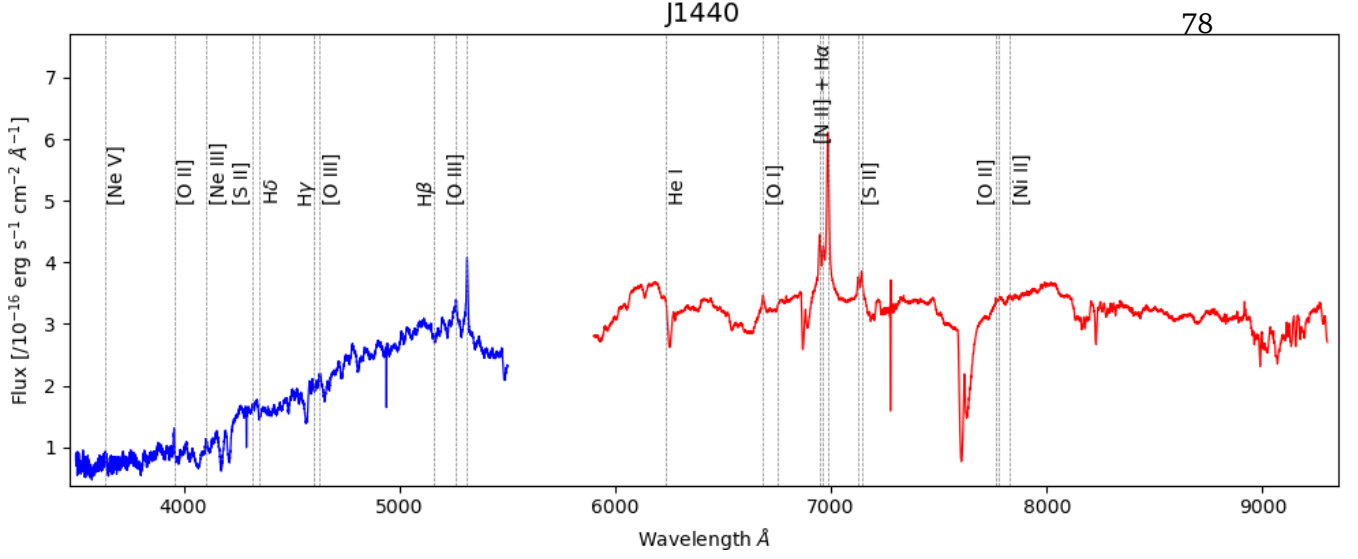


Figure 19.

Table 14. Emission Lines J1440

Emission line	Observed wavelength (λ_o) (\AA)	$\Delta\lambda_o$ (\AA)	Flux (F) ($10^{-16} \text{ erg s}^{-1} \text{ cm}^{-2}$)	ΔF ($10^{-16} \text{ erg s}^{-1} \text{ cm}^{-2}$)	$FWHM$ (kms^{-1})	$\Delta FWHM$ (kms^{-1})
[O II] λ 3729	3955.94	0.15	2.79	0.16	446.0	26.0
[Ne III] λ 3869	4104.87	0.32	1.4	0.15	541.0	58.0
[O III] λ 4959	5259.04	0.39	12.51	0.69	1614.0	68.0
[O III] λ 5007 _{blue}	5303.86	1.05	3.6	0.65	666.0	103.0
[O III] λ 5007	5314.32	0.17	9.57	0.61	452.0	16.0
[O I] λ 6300	6685.49	0.18	3.6	0.15	602.0	21.0
[N II] λ 6548	6947.93	0.27	9.03	0.54	463.0	27.0
H α λ 6563	6965.21	0.37	8.36	0.58	556.0	46.0
[N II] λ 6583	6985.94	0.08	30.72	0.48	520.0	8.0
[S II] λ 6716	7125.05	0.92	4.71	0.9	517.0	70.0
[S II] λ 6731	7142.88	0.92	9.5	0.99	758.0	78.0

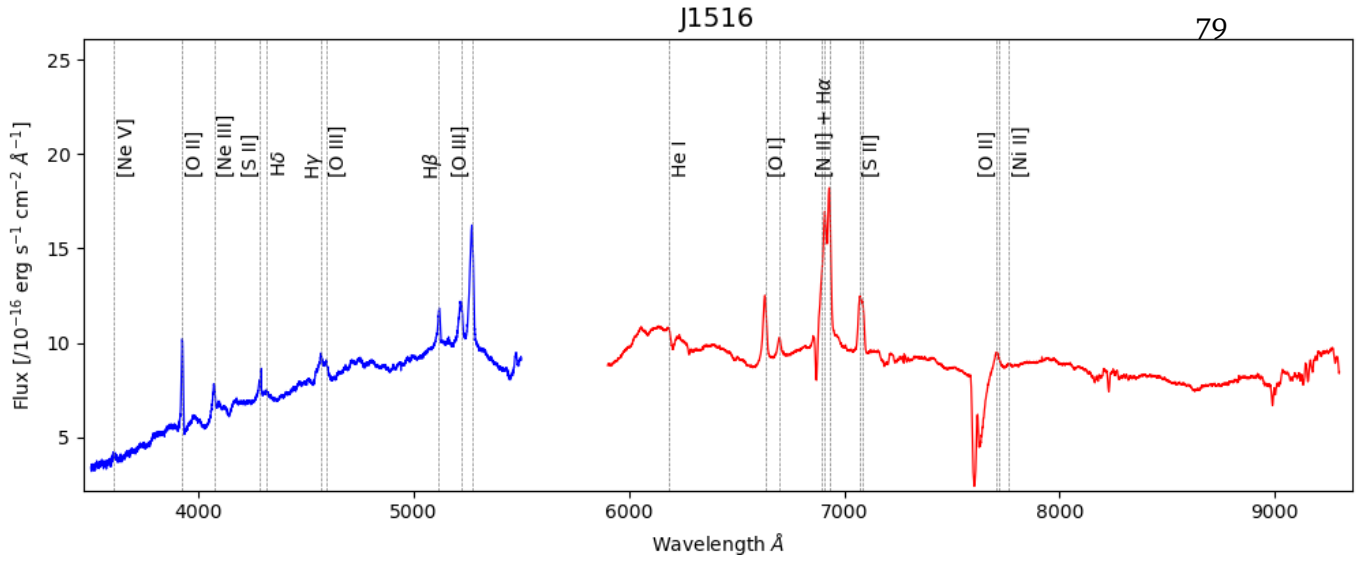


Figure 20.

Table 15. Emission Lines J1516

Emission line	Observed wavelength (λ_o) (\AA)	$\Delta\lambda_o$ (\AA)	Flux (F) ($10^{-16} \text{erg s}^{-1} \text{cm}^{-2}$)	ΔF ($10^{-16} \text{erg s}^{-1} \text{cm}^{-2}$)	$FWHM$ (kms^{-1})	$\Delta FWHM$ (kms^{-1})
[O II] λ 3729	3924.21	0.07	42.99	0.7	665.0	12.0
[Ne III] λ 3869	4072.24	0.29	23.12	0.91	1115.0	49.0
[S II] λ 4069	4284.11	0.42	11.22	0.86	824.0	65.0
H γ λ 4340	4567.93	0.54	49.32	3.13	2435.0	125.0
[O III] λ 4363	4595.2	0.45	8.91	1.32	947.0	82.0
H β λ 4861	5117.27	0.21	24.11	0.94	742.0	30.0
[O III] λ 4959	5217.95	0.24	53.31	1.35	1333.0	34.0
[O III] λ 5007	5268.05	0.08	128.19	1.37	1112.0	11.0
[O I] λ 6300	6630.51	0.08	66.29	0.62	843.0	8.0
[O I] λ 6364	6697.61	0.27	19.27	0.63	852.0	29.0
[N II] λ 6548	6890.51	1.36	39.35	9.72	620.0	83.0
H α λ 6563	6908.69	0.47	130.4	14.68	785.0	84.0
[N II] λ 6583	6930.25	0.37	137.51	7.17	699.0	27.0
[S II] λ 6716	7072.28	0.23	50.01	1.39	702.0	15.0
[S II] λ 6731	7086.99	0.22	26.96	1.34	522.0	13.0
[O II] λ 7331	7707.45	0.19	29.22	1.16	38.0	1.0

5 Summary and Conclusions

In my thesis, I conducted a study on the physical processes and interactions within three unique black hole environments. These environments include [AGNs](#) with Hypermassive Black Holes, the Galactic Center, and the Green Bean galaxies with fading [AGNs](#). Each of these projects focused on different physical processes due to the varying scales of the environments. To provide a comprehensive summary of my work, I have prepared a chapter-wise summary in the following section.

Chapter-wise Summary

Paper I: Observational Diagnostics for [HMBHs](#)

In this paper, we try to test if there is a higher mass cut-off above which our current methods of detecting [AGNs](#) become less effective. We predicted the observable emission line ratios and/or their detection limits for [AGNs](#) with [HMBHs](#) ($M_{BH} > 10^9 M_{\odot}$) to see how these line strengths evolve as we move from the usually observed mass range to the hyper-massive ones.

Since we wanted to probe the [BH](#) with mass $\geq 10^8 M_{\odot}$, we first built a systematic method to build mass-dependant [AGN SEDs](#) for the range $10^6 - 10^{12} M_{\odot}$. We use the classical *disc-blackbody* model from XSPEC to simulate the radiation from the accretion disc. However, there is an additional power-law component in the X-ray regime (due to inverse Compton scattering) that can photoionize the [BLR](#) and [NLR](#) and produce high-excitation emission lines. As the conventional methods of adding the disk and the power-law component (e.g. using standard scaling relation $\alpha_{OX} = -0.384 \log(L_{2keV}/L_{2500\text{\AA}})$, [Tananbaum et al. \(1979\)](#)) proved inadequate, we used the latest empirical results known, for the [SMBHs](#) and used suitable extrapolations to form a range of [SEDs](#) for all [BHs](#) in the aforementioned mass range and over a range of accretion rates and spins

of the BHs.

The constructed SEDs were then used as inputs for the photo-ionization code CLOUDY. We calculate emission line strength for a grid of gas cloud parameters; a wide range of gas densities and placed over a wide range of distances from the black hole. The estimated equivalent widths of the individual clouds were then integrated and averaged using the ‘*Locally Optimally Emitting Cloud*’ model to predict the final effective equivalent width $\mathcal{E}W$ and the observable luminosity of each of the emission lines.

We found that the typical optical Broad Emission Lines (BELs) that are used to identify AGNs, like $H\beta$ 4861 Å and $H\alpha$ 6563 Å are not the best tracers to look for HMBHs. The $\mathcal{E}W$ of these lines decrease by a factor of ~ 100 as the mass increases from 10^8 to $10^{10}M_{\odot}$. Instead, the UV lines O VI 1034 Å, C IV 1549 Å would be the most suited as they undergo a significant and interesting turnover from their drop in intensity and regain strength for the highest mass black holes.

Estimated Narrow Emission Line (NEL) ratios reveal an interesting fact that BHs with the highest mass with/or low accretion rate may have line ratios consistent with star-forming regions on the BPT diagnostic diagrams. This further suggests that the number of massive black holes in large survey samples like SDSS is being underestimated.

Paper II: MIR studies of Galactic Centre

Through this project, we tried to make a comprehensive study of all the dusty sources along the mini-spiral. We analyzed the MIR images of the central parsec in detail and examined the motion and physical properties of the extended gas and dust features along with bright Infrared Sources (IRS). The GC is illuminated in MIR due to the presence of dust, dominated by Polycyclic Aromatic Hydrocarbons (PAH) emission and NeII emission from ionized gas. We studied the MIR images at two wavelengths in the N-band – 8.59 μm (PAH1 filter) and 13.04 μm (NeII_2 filter) observed at VLT/VISIR – over 12 years. We produced high-pass filter maps to resolve and highlight the structures of extended sources by removing the effects of overlapping Point Spread Functions (PSFs). We performed astrometry and photometry to present the proper motions and flux densities of the largest set of resolved and reliably determined sources.

We have looked into the physical processes in this turbulent region of GC. We detect a bow-shock feature and tail components of IRS 7 (a pulsating red giant) that are pointed away from Sgr A*. The proper motion distribution of the individual tail components can be interpreted with a combination of downstream fluid motion and the development of Kelvin-Helmholtz (KH) instabilities. We detect and resolve the brightest MIR source in the region, IRS 3. The extended (puffed-up) structure of the star is likely a result of its atmosphere’s perturba-

tion followed by tidal prolongation. We also deduce that the structures and origins of the dusty sources in the region can be explained in combination with ram-pressure compression due to radiation from the NSC and KH instabilities, making the clumps form and fragment as they move along the mini-spiral.

Paper III: Influence of Jets on [OIII] Extensions in Green Pea/Bean Galaxies

In this paper, we study the impact of relativistic jets on the EELRs in a particular sample of high [OIII] 5007Å emitting galaxies. From the larger sample of SDSS narrow emission-line galaxies cross-identified with FIRST radio galaxies, we chose objects with characteristically high [OIII] luminosity ($L \sim 10^{40} \text{ erg/s}$) and equivalent width ($EW \sim 10\text{-}30 \text{ \AA}$). Among these, we chose the 12 closest sources ($z \sim 0.04\text{-}0.1$, 6 with jets and 6 without jets) in order to ensure resolving spatial scales $< 200 \text{ pc}$ on the source. We carried out MODS long-slit spectroscopy at LBT at two position angles for each source, one along the jet direction and one orthogonal to the jet direction.

We extracted the [OIII] 5007Å flux densities along both the slit direction and compare their normalised fluxes. We observed no significant disparity between extension among jetted and non-jetted sources. In the cases of jetted sources, we observed no preferential direction for [OIII] extension. For comparison, we also extracted [OII]λ3729 as a function of distance from the centre. [OII]λ3729 has a much lower ionizing potential than [OIII]λ5007 and therefore probes the star-forming regions of the galaxy. As a result, we see [OII]λ3729 being much more extended especially along the galactic plane, confirming our validity of data, reduction and analysis methods. Lack of extended [OIII]λ5007 could also mean that the ionised NLR region is conical in shape and the slit positioned along the jets did not align with the possible EELR.

Estimating the line flux densities and line ratios, shows that the sample is mostly populated by low-luminosity AGNs which are believed to represent the initial or final stages of the galaxies' active phases. In dust-obscured galaxies, X-ray brightness is severely diminished and cannot be used as an indicator of nuclear activity. However, the thermal emission from the warm dusty torus is strongest in MIR and represents the re-processed UV/X-ray radiation from inner regions. MIR emission also correlates with the X-ray brightness over a wide range of luminosities and can be used as a proxy to estimate the AGN activity.

The plot of MIR vs [OIII]λ5007 luminosities Schirmer et al. (2013) show that the Green Beans are less luminous in MIR compared to the larger sample of dust-obscured galaxies of similar [OIII]λ5007 fluxes. This leads to the conclusion that Green Beans host recently faded AGNs whose activity has declined over timescales less than the light-crossing time of the NLR, resulting in strong *ionisation echoes*. In addition, our radio-selected galaxies did not entirely coin-

cide with the brightest [OIII] λ 5007 emitting galaxies. Radio detections can act as signatures of recently enhanced activity leading to jet emission or bursts of star formation and hence no pronounced line emission decay on bulge crossing time scales.

Bibliography

- Alexander, T. (2005). Stellar processes near the massive black hole in the Galactic center [review article]. *Phys. Rep.*, 419(2-3):65–142.
- Balick, B. and Brown, R. L. (1974). Intense sub-arcsecond structure in the galactic center. *ApJ*, 194:265–270.
- Becklin, E. E., Gatley, I., and Werner, M. W. (1982). Far-infrared observations of Sagittarius A - The luminosity and dust density in the central parsec of the Galaxy. *ApJ*, 258:135–142.
- Becklin, E. E. and Kleinmann, D. E. (1968). Infrared Observations of the Crab Nebula. *ApJ*, 152:L25.
- Becklin, E. E. and Neugebauer, G. (1975). High-resolution maps of the galactic center at 2.2 and 10 microns. *ApJ*, 200:L71–L74.
- Beckmann, V., Soldi, S., Ricci, C., Alfonso-Garzón, J., Courvoisier, T. J. L., Domingo, A., Gehrels, N., Lubiński, P., Mas-Hesse, J. M., and Zdziarski, A. A. (2009). The second INTEGRAL AGN catalogue. *A&A*, 505(1):417–439.
- Blank, M., Morris, M. R., Frank, A., Carroll-Nellenback, J. J., and Duschl, W. J. (2016). The inner cavity of the circumnuclear disc. *MNRAS*, 459(2):1721–1736.
- Bolton, J. G., Stanley, G. J., and Slee, O. B. (1949). Positions of Three Discrete Sources of Galactic Radio-Frequency Radiation. *Nature*, 164(4159):101–102.
- Christopher, M. H., Scoville, N. Z., Stolovy, S. R., and Yun, M. S. (2005). HCN and HCO⁺ Observations of the Galactic Circumnuclear Disk. *ApJ*, 622(1):346–365.

- Eckart, A. and Genzel, R. (1996). Observations of stellar proper motions near the Galactic Centre. *Nature*, 383(6599):415–417.
- Eckart, A. and Genzel, R. (1997). Stellar proper motions in the central 0.1 PC of the Galaxy. *MNRAS*, 284(3):576–598.
- Eckart, A., Schödel, R., and Straubmeier, C. (2005). *The black hole at the center of the Milky Way*.
- Event Horizon Telescope Collaboration, Akiyama, K., Alberdi, A., Alef, W., Algaba, J. C., Anantua, R., Asada, K., Azulay, R., Bach, U., Baczko, A.-K., Ball, D., Baloković, M., Barrett, J., Bauböck, M., Benson, B. A., Bintley, D., Blackburn, L., Blundell, R., Bouman, K. L., Bower, G. C., Boyce, H., Bremer, M., Brinkerink, C. D., Brissenden, R., Britzen, S., Broderick, A. E., Brogiere, D., Bronzwaer, T., Bustamante, S., Byun, D.-Y., Carlstrom, J. E., Ceccobello, C., Chael, A., Chan, C.-k., Chatterjee, K., Chatterjee, S., Chen, M.-T., Chen, Y., Cheng, X., Cho, I., Christian, P., Conroy, N. S., Conway, J. E., Cordes, J. M., Crawford, T. M., Crew, G. B., Cruz-Osorio, A., Cui, Y., Davelaar, J., Laurentis, M. D., Deane, R., Dempsey, J., Desvignes, G., Dexter, J., Dhruv, V., Doeleman, S. S., Dougal, S., Dzib, S. A., Eatough, R. P., Emami, R., Falcke, H., Farah, J., Fish, V. L., Fomalont, E., Ford, H. A., Fraga-Encinas, R., Freeman, W. T., Friberg, P., Fromm, C. M., Fuentes, A., Galison, P., Gammie, C. F., García, R., Gentaz, O., Georgiev, B., Goddi, C., Gold, R., Gómez-Ruiz, A. I., Gómez, J. L., Gu, M., Gurwell, M., Hada, K., Haggard, D., Haworth, K., Hecht, M. H., Hesper, R., Heumann, D., Ho, L. C., Ho, P., Honma, M., Huang, C.-W. L., Huang, L., Hughes, D. H., Ikeda, S., Impellizzeri, C. M. V., Inoue, M., Issaoun, S., James, D. J., Jannuzi, B. T., Janssen, M., Jeter, B., Jiang, W., Jiménez-Rosales, A., Johnson, M. D., Jorstad, S., Joshi, A. V., Jung, T., Karami, M., Karuppusamy, R., Kawashima, T., Keating, G. K., Kettenis, M., Kim, D.-J., Kim, J.-Y., Kim, J., Kim, J., Kino, M., Koay, J. Y., Kocherlakota, P., Kofuji, Y., Koch, P. M., Koyama, S., Kramer, C., Kramer, M., Krichbaum, T. P., Kuo, C.-Y., Bella, N. L., Lauer, T. R., Lee, D., Lee, S.-S., Leung, P. K., Levis, A., Li, Z., Lico, R., Lindahl, G., Lindqvist, M., Lisakov, M., Liu, J., Liu, K., Liuzzo, E., Lo, W.-P., Lobanov, A. P., Loinard, L., Lonsdale, C. J., Lu, R.-S., Mao, J., Marchili, N., Markoff, S., Marrone, D. P., Marscher, A. P., Martí-Vidal, I., Matsushita, S., Matthews, L. D., Medeiros, L., Menten, K. M., Michalik, D., Mizuno, I., Mizuno, Y., Moran, J. M., Moriyama, K., Moscibrodzka, M., Müller, C., Mus, A., Musoke, G., Myserlis, I., Nadolski, A., Nagai, H., Nagar, N. M., Nakamura, M., Narayan, R., Narayanan, G., Natarajan, I., Nathanail, A., Fuentes, S. N., Neilsen, J., Neri, R., Ni, C., Noutsos, A., Nowak, M. A., Oh, J., Okino, H., Olivares, H., Ortiz-León, G. N., Oyama, T., Özel, F., Palumbo, D. C. M., Paraschos, G. F., Park, J., Parsons, H., Patel, N., Pen, U.-L., Pesce, D. W., Piétu, V., Plambeck, R., PopStefanija, A., Porth, O., Pötzl, F. M., Prather, B., Preciado-López, J. A., Psaltis, D., Pu, H.-Y., Ramakrishnan, V., Rao, R., Rawlings, M. G., Raymond, A. W., Rezzolla, L., Ricarte, A., Ripperda, B., Roelofs, F., Rogers, A., Ros, E., Romero-Cañizales, C., Roshanineshat, A., Rottmann,

H., Roy, A. L., Ruiz, I., Ruzsczyk, C., Rygl, K. L. J., Sánchez, S., Sánchez-Argüelles, D., Sánchez-Portal, M., Sasada, M., Satapathy, K., Savolainen, T., Schloerb, F. P., Schonfeld, J., Schuster, K.-F., Shao, L., Shen, Z., Small, D., Sohn, B. W., SooHoo, J., Souccar, K., Sun, H., Tazaki, F., Tetarenko, A. J., Tiede, P., Tilanus, R. P. J., Titus, M., Torne, P., Traianou, E., Trent, T., Trippe, S., Turk, M., van Bemmell, I., van Langevelde, H. J., van Rossum, D. R., Vos, J., Wagner, J., Ward-Thompson, D., Wardle, J., Weintroub, J., Wex, N., Wharton, R., Wielgus, M., Wiik, K., Witzel, G., Wondrak, M. F., Wong, G. N., Wu, Q., Yamaguchi, P., Yoon, D., Young, A., Young, K., Younsi, Z., Yuan, F., Yuan, Y.-F., Zensus, J. A., Zhang, S., Zhao, G.-Y., Zhao, S.-S., Agurto, C., Allardi, A., Amestica, R., Araneda, J. P., Arriagada, O., Berghuis, J. L., Bertarini, A., Berthold, R., Blanchard, J., Brown, K., Cárdenas, M., Cantzler, M., Caro, P., Castillo-Domínguez, E., Chan, T. L., Chang, C.-C., Chang, D. O., Chang, S.-H., Chang, S.-C., Chen, C.-C., Chilson, R., Chuter, T. C., Ciechanowicz, M., Colin-Beltran, E., Coulson, I. M., Crowley, J., Degenaar, N., Dornbusch, S., Durán, C. A., Everett, W. B., Faber, A., Forster, K., Fuchs, M. M., Gale, D. M., Geertsema, G., González, E., Graham, D., Gueth, F., Halverson, N. W., Han, C.-C., Han, K.-C., Hasegawa, Y., Hernández-Rebollar, J. L., Herrera, C., Herrero-Illana, R., Heyminck, S., Hirota, A., Hoge, J., Hostler Schimpf, S. R., Howie, R. E., Huang, Y.-D., Jiang, H., Jinchi, H., John, D., Kimura, K., Klein, T., Kubo, D., Kuroda, J., Kwon, C., Lacasse, R., Laing, R., Leitch, E. M., Li, C.-T., Liu, C.-T., Liu, K.-Y., Lin, L. C. C., Lu, L.-M., Mac-Auliffe, F., Martin-Cocher, P., Matulonis, C., Maute, J. K., Messias, H., Meyer-Zhao, Z., Montaña, A., Montenegro-Montes, F., Montgomerie, W., Moreno Nolasco, M. E., Muders, D., Nishioka, H., Norton, T. J., Nystrom, G., Ogawa, H., Olivares, R., Oshiro, P., Pérez-Beaupuits, J. P., Parra, R., Phillips, N. M., Poirier, M., Pradel, N., Qiu, R., Raffin, P. A., Rahlin, A. S., Ramírez, J., Ressler, S., Reynolds, M., Rodríguez-Montoya, I., Saez-Madain, A. F., Santana, J., Shaw, P., Shirkey, L. E., Silva, K. M., Snow, W., Sousa, D., Sridharan, T. K., Stahm, W., Stark, A. A., Test, J., Torstensson, K., Venegas, P., Walther, C., Wei, T.-S., White, C., Wieching, G., Wijnands, R., Wouterloot, J. G. A., Yu, C.-Y., Yu (), W., and Zeballos, M. (2022). First Sagittarius A* Event Horizon Telescope Results. I. The Shadow of the Supermassive Black Hole in the Center of the Milky Way. *ApJ*, 930(2):L12.

Fath, E. A. (1909). The spectra of some spiral nebulae and globular star clusters. *Lick Observatory Bulletin*, 149:71–77.

Ferland, G. J., Korista, K. T., Verner, D. A., Ferguson, J. W., Kingdon, J. B., and Verner, E. M. (1998). CLOUDY 90: Numerical Simulation of Plasmas and Their Spectra. *PASP*, 110(749):761–778.

Genzel, R., Eisenhauer, F., and Gillessen, S. (2010). The Galactic Center massive black hole and nuclear star cluster. *Reviews of Modern Physics*, 82(4):3121–3195.

- Genzel, R., Hollenbach, D., and Townes, C. H. (1994). The nucleus of our Galaxy. *Reports on Progress in Physics*, 57(5):417–479.
- Genzel, R., Thatte, N., Krabbe, A., Kroker, H., and Tacconi-Garman, L. E. (1996). The Dark Mass Concentration in the Central Parsec of the Milky Way. *ApJ*, 472:153.
- Ghez, A. M., Klein, B. L., Morris, M., and Becklin, E. E. (1998). High Proper-Motion Stars in the Vicinity of Sagittarius A*: Evidence for a Supermassive Black Hole at the Center of Our Galaxy. *ApJ*, 509(2):678–686.
- Gillessen, S., Plewa, P. M., Eisenhauer, F., Sari, R., Waisberg, I., Habibi, M., Pfuhl, O., George, E., Dexter, J., von Fellenberg, S., Ott, T., and Genzel, R. (2017). An Update on Monitoring Stellar Orbits in the Galactic Center. *ApJ*, 837(1):30.
- Goss, W. M., Brown, R. L., and Lo, K. Y. (2003). The Discovery of Sgr A*. *Astronomische Nachrichten Supplement*, 324(1):497–504.
- Guesten, R., Genzel, R., Wright, M. C. H., Jaffe, D. T., Stutzki, J., and Harris, A. I. (1987). Aperture Synthesis Observations of the Circumnuclear Ring in the Galactic Center. *ApJ*, 318:124.
- Haardt, F. and Maraschi, L. (1991). A Two-Phase Model for the X-Ray Emission from Seyfert Galaxies. *ApJ*, 380:L51.
- Herrnstein, R. M. and Ho, P. T. P. (2002). Hot Molecular Gas in the Galactic Center. *ApJ*, 579(2):L83–L86.
- Khachikian, E. Y. and Weedman, D. W. (1974). An atlas of Seyfert galaxies. *ApJ*, 192:581–589.
- Krabbe, A., Genzel, R., Eckart, A., Najarro, F., Lutz, D., Cameron, M., Kroker, H., Tacconi-Garman, L. E., Thatte, N., Weitzel, L., Drapatz, S., Geballe, T., Sternberg, A., and Kudritzki, R. (1995). The Nuclear Cluster of the Milky Way: Star Formation and Velocity Dispersion in the Central 0.5 Parsec. *ApJ*, 447:L95.
- Lo, K. Y. and Claussen, M. J. (1983). High-resolution observations of ionized gas in central 3 parsecs of the Galaxy: possible evidence for infall. *Nature*, 306(5944):647–651.
- Lo, K. Y., Schilizzi, R. T., Cohen, M. H., and Ross, H. N. (1975). VLBI observations of the compact radio source in the center of the Galaxy. *ApJ*, 202:L63–L65.
- Lynden-Bell, D. (1969). Galactic Nuclei as Collapsed Old Quasars. *Nature*, 223(5207):690–694.

- Lynden-Bell, D. and Rees, M. J. (1971). On quasars, dust and the galactic centre. *MNRAS*, 152:461.
- Martins, F., Genzel, R., Hillier, D. J., Eisenhauer, F., Paumard, T., Gillessen, S., Ott, T., and Trippe, S. (2007). Stellar and wind properties of massive stars in the central parsec of the Galaxy. *A&A*, 468(1):233–254.
- Montero-Castaño, M., Herrnstein, R. M., and Ho, P. T. P. (2009). Gas Infall Toward Sgr A* from the Clumpy Circumnuclear Disk. *ApJ*, 695(2):1477–1494.
- Mužić, K., Eckart, A., Schödel, R., Meyer, L., and Zensus, A. (2007). First proper motions of thin dust filaments at the Galactic center. *A&A*, 469(3):993–1002.
- Najarro, F., Krabbe, A., Genzel, R., Lutz, D., Kudritzki, R. P., and Hillier, D. J. (1997). Quantitative spectroscopy of the HeI cluster in the Galactic center. *A&A*, 325:700–708.
- Netzer, H. (2013). *The Physics and Evolution of Active Galactic Nuclei*.
- Padovani, P., Alexander, D. M., Assef, R. J., De Marco, B., Giommi, P., Hickox, R. C., Richards, G. T., Smolčić, V., Hatziminaoglou, E., Mainieri, V., and Salvato, M. (2017). Active galactic nuclei: what’s in a name? *A&A Rev.*, 25(1):2.
- Panda, S. (2021). *Physical Conditions in the Broad-line Regions of Active Galaxies*. PhD thesis, Polish Academy of Sciences, Institute of Physics.
- Parsa, M., Eckart, A., Shahzamanian, B., Karas, V., Zajaček, M., Zensus, J. A., and Straubmeier, C. (2017). Investigating the Relativistic Motion of the Stars Near the Supermassive Black Hole in the Galactic Center. *ApJ*, 845(1):22.
- Paumard, T., Maillard, J. P., and Morris, M. (2004). Kinematic and structural analysis of the <ASTROBJ>Minispiral</ASTROBJ> in the Galactic Center from BEAR spectro-imagery. *A&A*, 426:81–96.
- Peiřker, F., Eckart, A., Sabha, N. B., Zajaček, M., and Bhat, H. (2020). Near- and Mid-infrared Observations in the Inner Tenth of a Parsec of the Galactic Center Detection of Proper Motion of a Filament Very Close to Sgr A*. *ApJ*, 897(1):28.
- Peiřker, F., Zajaček, M., Eckart, A., Sabha, N. B., Shahzamanian, B., and Parsa, M. (2019). New bow-shock source with bipolar morphology in the vicinity of Sgr A*. *A&A*, 624:A97.
- Peterson, B. M. (1997). *An Introduction to Active Galactic Nuclei*.
- Schirmer, M., Diaz, R., Holhjem, K., Levenson, N. A., and Winge, C. (2013). A Sample of Seyfert-2 Galaxies with Ultraluminous Galaxy-wide Narrow-line Regions: Quasar Light Echoes? *ApJ*, 763(1):60.

- Schmidt, M. (1963). 3C 273 : A Star-Like Object with Large Red-Shift. *Nature*, 197(4872):1040.
- Seyfert, C. K. (1943). Nuclear Emission in Spiral Nebulae. *ApJ*, 97:28.
- Shakura, N. I. and Sunyaev, R. A. (1973). Reprint of 1973A&A....24..337S. Black holes in binary systems. Observational appearance. *A&A*, 500:33–51.
- Slipher, V. M. (1917). The spectrum and velocity of the nebula N.G.C. 1068 (M 77). *Lowell Observatory Bulletin*, 3:59–62.
- Tananbaum, H., Avni, Y., Branduardi, G., Elvis, M., Fabbiano, G., Feigelson, E., Giacconi, R., Henry, J. P., Pye, J. P., Soltan, A., and Zamorani, G. (1979). X-ray studies of quasars with the Einstein Observatory. *ApJ*, 234:L9–L13.
- Tanner, A., Figer, D. F., Najarro, F., Kudritzki, R. P., Gilmore, D., Morris, M., Becklin, E. E., McLean, I. S., Gilbert, A. M., Graham, J. R., Larkin, J. E., Levenson, N. A., and Teplitz, H. I. (2006). High Spectral Resolution Observations of the Massive Stars in the Galactic Center. *ApJ*, 641(2):891–904.
- Tanner, A., Ghez, A. M., Morris, M. R., and Christou, J. C. (2005). Stellar Bow Shocks in the Northern Arm of the Galactic Center: More Members and Kinematics of the Massive Star Population. *ApJ*, 624(2):742–750.
- Vollmer, B. and Duschl, W. J. (2000). The Minispiral in the Galactic Center revisited. *New Ast.*, 4(8):581–590.
- Wright, M. C. H., Coil, A. L., McGary, R. S., Ho, P. T. P., and Harris, A. I. (2001). Molecular Tracers of the Central 12 Parsecs of the Galactic Center. *ApJ*, 551(1):254–268.
- Yusef-Zadeh, F., Roberts, D. A., and Biretta, J. (1998). Proper Motions of Ionized Gas at the Galactic Center: Evidence for Unbound Orbiting Gas. *ApJ*, 499(2):L159–L162.
- Zhao, J.-H., Blundell, R., Moran, J. M., Downes, D., Schuster, K. F., and Marone, D. P. (2010). The High-density Ionized Gas in the Central Parsec of the Galaxy. *ApJ*, 723(2):1097–1109.
- Zhao, J.-H., Morris, M. R., Goss, W. M., and An, T. (2009). Dynamics of Ionized Gas at the Galactic Center: Very Large Array Observations of the Three-dimensional Velocity Field and Location of the Ionized Streams in Sagittarius A West. *ApJ*, 699(1):186–214.

List of Figures

1.1	Composite image of the Galactic Centre using images from the Spitzer Space Telescope, the Hubble Space Telescope, and the Chandra X-ray observatory. The bright spot in the middle of the image is where the SMBH is situated. Image credit: NASA/JPL-Caltech/ESA/CXC/STScI	2
1.2	The very first image of the SMBH ‘shadow’ at the center of Milky Way produced by Event Horizon Telescope Collaboration. Image credit: EHT collaboration	3
1.3	Multi-wavelength image (using H, K, L’ bands) of the central parsec of GC observed at NACO/ESO VLT. Image credit: University of Cologne	4
1.4	Multi-wavelength image of the inner few pc of the Galactic centre. Integrated line emission in HCN 4-3 (green: SMA, Montero-Castaño et al. (2009)) and HCN 1-0 (blue: OVRO, Christopher et al. (2005)), highlight the neutral gas in CNB whereas the 6 cm radio continuum emission (red: Lo and Claussen (1983)) highlights the ionised gas in the mini-spiral. Image credit: Genzel et al. (2010)	5
1.5	The 3-D view of the kinematics and structure of the mini-spiral around the Sgr A* (black sphere) as discussed in Zhao et al. (2010) . The arrows indicate the direction of the streamers along the orbits and the colour represents the radial velocity and the grey shadow indicates their projection onto the sky plane.	6
1.6	A schematic representation of the Unified model of the AGN. Image credit: https://fermi.gsfc.nasa.gov/science/eteu/agn	8
1.7	A schematic representation of AGN SED along with individual components that correspond to different physical processes. Image credit: Panda (2021) , adapted from Padovani et al. (2017)	9
1.8	Chopping and nodding technique on observations. Image credit:ESO VISIR user manual.	11

List of Acronyms

AGB	Asymptotic Giant Branch
AGN	Active Galactic Nucleus
AO	Adaptive Optics
BH	Black Hole
BEL	Broad Emission Line
BLR	Broad Line Region
CND	Circum-nuclear disc
EELR	Extended Emission Line Region
ESO	European Southern Observatory
FoV	Field of View
GC	Galactic center
HMBH	Hypermassive Black Hole
IMBH	intermediate-mass Black Hole
IR	Infrared
IRS	Infrared Sources
ISM	Interstellar Medium
KH	Kelvin-Helmholtz
LBT	Large Binocular Telescope
MIR	Mid-Infrared
NEL	Narrow Emission Line
NLR	Narrow Line Region
NIR	Near Infrared

NSC	Nuclear stellar cluster
PAH	Polycyclic Aromatic Hydrocarbons
PSF	Point Spread Function
QSO	Quasar
SED	Sepctral Energy Distribution
SMBH	Supermassive Black Hole
UT	Unit Telescope
UV	ultraviolet
VISIR	VLT Imager and Spectrometer for the mid-InfraRed
VLA	Very Large Array
VLBI	Very Long Baseline Interferometry
VLT	Very Large Telescope
VLTI	Very Large Telescope Interferometer
WR	Wolf-Rayet
ZAMS	Zero-Age Main-Sequence

Acknowledgements

I feel fortunate to have so many kind people around me to whom I can express my gratitude for their support throughout my life, both in and outside of science.

First and foremost, I would like to express my immense gratitude to my supervisor, Prof. Andreas Eckart, for providing me with the opportunity to work in his group and for his unwavering guidance and support throughout my Ph.D. I have always been inspired by his extensive knowledge and diverse interests, both in academia and beyond.

I also want to thank Prof. Lukas Labadaie and Prof. Anton Zensus for agreeing to be my second and third reviewers, and Prof. Berenike Maier for being the chair of my Thesis Defense Committee. My sincere thanks go to Dr. Nadeen Sabha, who has always been a supportive collaborator and a part of my Thesis Advisory Committee.

I am grateful to the Max Planck Institute for Radio Astronomy (MPIfR) for the financial support they provided during my doctoral studies. I extend my thanks to the International Max-Planck Research School and its coordinators Ms. Simone Pott and Dr. Rainer Mauersberger.

I am very thankful to the members of our workgroup, Elaheh, Persis, Lukas, Basel, Matthias, Florian, and Maria, for creating such a supportive and welcoming environment at the institute. I have so many fond memories of our whiteboard discussions, Christmas and birthday dinners, and memorable trips to Prague-Brno. I would especially like to express my deep appreciation towards Elaheh and Persis, for being the most empathetic and supportive office mates I could ask for. I am grateful for all the celebrations - big and small, deep discussions, and great memories we have shared.

I want to express my gratitude to Dr. Susmita Chakravorty for being my mentor throughout my years in academia. I truly believe that her support and encouragement during a crucial period of my life have played a significant role in shaping my academic career.

I would like to thank all the DPs, especially Vani, Anantha, Raksha, and Anantha, for making the pandemic bearable and providing me with a sense of familiarity far from home.

And finally, I want to express my deep gratitude to my amazing parents. I owe everything to your love and support, which have helped me become the person I am today. I am forever thankful for everything you have done for me!

Selbständigkeitserklärung

Hiermit versichere ich an Eides statt, dass ich die vorliegende Dissertation selbstständig und ohne die Benutzung anderer als der angegebenen Hilfsmittel und Literatur angefertigt habe. Alle Stellen, die wörtlich oder sinngemäß aus veröffentlichten und nicht veröffentlichten Werken dem Wortlaut oder dem Sinn nach entnommen wurden, sind als solche kenntlich gemacht. Ich versichere an Eides statt, dass diese Dissertation noch keiner anderen Fakultät oder Universität zur Prüfung vorgelegen hat; dass sie - abgesehen von unten angegebenen Teilpublikationen und eingebundenen Artikeln und Manuskripten - noch nicht veröffentlicht worden ist sowie, dass ich eine Veröffentlichung der Dissertation vor Abschluss der Promotion nicht ohne Genehmigung des Promotionsausschusses vornehmen werde. Die Bestimmungen dieser Ordnung sind mir bekannt. Darüber hinaus erkläre ich hiermit, dass ich die Ordnung zur Sicherung guter wissenschaftlicher Praxis und zum Umgang mit wissenschaftlichem Fehlverhalten der Universität zu Köln gelesen und sie bei der Durchführung der Dissertation zugrundeliegenden Arbeiten und der schriftlich verfassten Dissertation beachtet habe und verpflichte mich hiermit, die dort genannten Vorgaben bei allen wissenschaftlichen Tätigkeiten zu beachten und umzusetzen. Ich versichere, dass die eingereichte elektronische Fassung der eingereichten Druckfassung vollständig entspricht.

Teilpublikationen/eingebundene Artikel:

- *Hypermassive black holes have faint broad and narrow emission lines*; **H. K. Bhat**, S. Chakravorty, D. Sengupta, M. Elvis, S. R. Datta, N. Roy, C. Bertemes, G. Ferland, and S. H. Ezhikode; MNRAS 497(3), 2992 (2020).
- *Mid-infrared Studies of Dusty Sources in the Galactic Center*; **H. K. Bhat**, N. B. Sabha, M. Zajacek, A. Eckart, R. Schödel, S. E. Hosseini, F. Peißker, and

A. Zensus; ApJ 929(2):178 (2022).

Eingebundene Manuskripte in Vorbereitung:

- *Influence of Jets on [OIII] Extensions in Green Pea/Bean Galaxies* ; **H. K. Bhat**, A. Eckart, P. Misquitta, M. Valencia-S, M. Yttergren and A. Zensus; submitted to ApJ and currently under review.

Weitere Publikationen

- *Near and Mid-infrared Observations in the Inner Tenth of a Parsec of the Galactic Center Detection of Proper Motion of a Filament Very Close to Sgr A**; F. Peißker, A. Eckart, N. B. Sabha, M. Zajacek, and **H. Bhat**; ApJ, 897(1):28 (2020).
- *Detection of a new object close to Sgr A**”; F. Peissker, A. Eckart, N. B. Sabha, M. Zajacek, and **H. Bhat**; ATel 13794 (2020).

Köln, den 19.12.2022,



(Harshitha K Bhat)

Lebenslauf

Persönliche Angaben

Name: Harshitha Krishna Murthy Bhat

Anschrift: I. Physikalisches Institut, Universität zu Köln
Zülpicher Str. 77, 50937 Köln

Email: bhat@ph1.uni-koeln.de

Geburtsdatum und -ort: 25.04.1995 in Kundapur, India

Staatsangehörigkeit: Indien

Ausbildung und Berufserfahrung

Seit Sept. 2019 Promotionsstudium (Experimentalphysik),
Universität zu Köln &
Max-Planck Institut für Radioastronomie
wiss. Betreuer: Prof. Dr. Andreas Eckart

2016-2018 Master of Science (Physics)
St. Joseph's College, Bangalore, Indien

2013-2016 Bachelor of Science (Physics, Chemistry, Mathematics)
St. Joseph's College, Bangalore, Indien

2011-2013 Pre-University College
Vidya Mandir Ind. PU College, Bangalore, Indien

2001-2011 Soundarya School
Bangalore, Indien